DUCT FLOW OF POLYMER SOLUTIONS

Thesis submitted in accordance with the requirements of the University of Liverpool
for the degree of Doctor in Philosophy

by

Azuraien Jaafar

December 2009

UNIVERSITY OF
LIVERPOOL

ABSTRACT

The drag-reducing ability of a rigid "rod-like" polymer solution, scleroglucan, in a circular-pipe geometry together with the drag-reducing behaviour of a semi-rigid polymer, xanthan gum, in a concentric annular pipe have been investigated experimentally via pressure-drop measurements and using laser Doppler anemometry. The laminar and transitional flow in the annular pipe, with particular attention placed on the transitional regime, of two different polymers - a xanthan gum and a polymer known to exhibit a yield stress, carbopol - are also investigated in this work and compared to that of a Newtonian fluid, a glycerine-water mixture.

Complete rheological characterization of the different polymer solutions investigated showed that scleroglucan, xanthan gum and carbopol, exhibited increased shear-thinning with increasing solution concentration. Wall slip occurred in the carbopol solutions and was minimized using a roughened parallel-plate geometry for the steady-shear viscosity measurements producing a very high first Newtonian region at very low shear stresses, typical of a "yield stress" fluid. Capillary break-up extensional viscosity measurements conducted for scleroglucan and xanthan gum showed Newtonian-like linear filament-thinning behaviour with a Trouton ratio (>>3) confirming the non-Newtonian nature of these polymers in extensional flow.

The drag-reduction study for scleroglucan was carried out in a glass pipe-flow facility. A concentric annular-flow facility (radius ratio κ=0.506) was utilized for the drag-reduction and transitional flow study of xanthan gum and carbopol. For all fluids, pressure-drop and detailed mean flow and turbulence characteristics were obtained at axial distances from the inlet sufficient for the Newtonian and non-Newtonian flows to reach fully-developed conditions.

The drag-reduction effectiveness of scleroglucan was observed to increase with solution concentration but found to be only mildly dependent on the Reynolds number. The mean axial velocity and turbulence structure data of scleroglucan exhibit trends typical of a low drag-reducing flexible polymer solution. The drag-reduction study of xanthan gum in the concentric annular pipe-flow facility shows that the 40% drag-reduction limit proposed by Warholic et. al. (1999) for channel flows, to distinguish between the low drag-reducing and high drag-reducing flows, is also applicable to annular flows but the results exhibit slightly different turbulent structure.

In the transitional flow studies within the annular pipe a larger Reynolds number range for the transitional flow regime is observed for the more shear-thinning fluid. Contrary to what is observed for the Newtonian fluid, glycerine, the higher shear stress on the inner wall compared to the outer wall does not lead to earlier transition for shear thinning and yield stress fluids where higher turbulent activity is observed at the outer wall region. The mean axial velocity profiles show a slight shift (~5%) of the maximum velocity location towards the outer pipe wall within the transitional regime only for the Newtonian fluid.

I dedicate this thesis to my husband, Mohd Shiraz Aris, and my dear sons, Ilman, Hakim and Hafiy. Thank you for your love, support and understanding even when Mama has to constantly work and not always around to be part of your growing experience. I will surely make it up to you.

ACKNOWLEDGEMENTS

My sincerest thanks and appreciation to Dr Robert J. Poole for his patient guidance and thought provoking discussions as my first supervisor throughout the project, without whom, this research experience would not be as valuable. I would also like to thank Professor Ieuan Owen and Professor Marcel Escudier for their knowledge and constructive feedbacks given, with regards to the research work and this thesis, without limits.

To all the technical staff, I appreciate your invaluable assistance in the design and construction of the experimental rig and your endless help in overcoming the (endless) problems of technical nature throughout my research work, especially Mr. John Curran, Mr. John McCulloch, Mr. Steven Bode and Mr. Derek Neary.

A big thank you to my colleagues from the Mechanical Engineering Department, particularly Dr Fiona Keegan, Dr Sergio Rosa and Dr Keith Nickson, and my Malaysian friends who were always there throughout the highs and lows of my research experience.

My gratitude to my sponsor, Universiti Teknologi Petronas for the financial support provided for the postgraduate study.

And last but not least to my family back home in Malaysia especially my father, Hj Jaafar Ahmad, my mother, Hjh Nasriah Talib, my siblings, Anisah, Akmal, Annas and Amirah Aswan, and not forgetting my in-laws for their constant understanding, support, motivation and du'a, and also to them I dedicate this thesis.

TABLE OF CONTENTS

1 – Introduction

2 – Literature review

3 – Rheology

4 – Experimental arrangement and procedure

5 – Pipe flow

6 – Annular flow

7 – Conclusions

Japper-Jaafar, A., Poole, R.J., 2007, "Steady shear, small amplitude oscillatory shear (SAOS) and capillary break-up extensional rheology (CaBER) measurements of rod-like polymers", Fourth Annual European Rheology Conference, Italy, Poster presentation.

Japper-Jaafar, A., Escudier, M.P., Poole, R.J., 2008, "Turbulent pipe flow of rod-like polymer solutions", XVth International Congress on rheology – The Society of Rheology 80th annual meeting, 1027, 282-284.

Japper-Jaafar, A., Escudier, M.P., Poole, R.J., 2009, "Turbulent pipe flow of a drag-reducing rigid "rod-like" polymer solution", Journal of Non-Newtonian Fluid Mechanics, 161, 2009, 86-93.

NOMENCLATURE

a	Carreau-Yasuda parameter
A	Cross-sectional area (m^2)
b	Diameter of CaBER plates ($\equiv$4 mm)
c	Polymer concentration (% w/w)
c^*	Critical overlap concentration (% w/w)
d_L	Laminar equivalent diameter (m)
d_{vol}	LDA measurement volume diameter (μm)
D	Pipe diameter (m)
D_{CaBER}	Midpoint filament diameter in CaBER (mm)
$D_{o,\,CaBER}$	Midpoint filament diameter in CaBER following cessation of stretch deformation (mm)
D_H	Hydraulic diameter (mm), $\left(\equiv 4A/P\right)$
DR	Drag reduction (%), $\left(\equiv \left(\left(f_n - f_p\right)/f_n\right)\times 100\right)$
D_l	Fitting parameter in Equation [3.18] (mm)
e_r	Relative error (%)
f	Fanning friction factor, $\left(\equiv 2\tau_W / \rho U_B^2\right)$
f_x, f_y, f_z	Body forces (N/m^3)
g	Gravitational acceleration ($\equiv$9.81 m/s^2)
G'	Storage modulus (Pa)
G''	Loss modulus (Pa)
h	Distance between plates in CaBER (mm)
HB	Herschel-Bulkley number, $\left(\equiv \tau_y / K\left(U_B / R\right)^n\right)$
k	Power law consistency index (Pa.s^n)

k_1	Fitting parameter in Equation [3.18] (mm)
K	Herschel-Bulkley consistency index (Pa.s^n)
L	Pipe length over which the pressure drop was measured (m)
m	Slope of linear fitting to CaBER data (mm/s)
n	Power-law exponent
n	Refractive index
N_s	Velocity sample size collected by LDA
N_1	First normal stress difference (Pa), $\left(\equiv \tau_{xx} - \tau_{yy}\right)$
N_2	Second normal stress difference (Pa), $\left(\equiv \tau_{xx} - \tau_{zz}\right)$
p	Pressure (Pa)
Δp	Pressure drop (Pa)
P	Wetted perimeter (m)
q	End-to-end vector
Q	Volumetric flow rate (m^3/s)
r	Radial location (m)
R	Pipe radius (m)
r_{max}	Point of maximum velocity (m)
r_p	Extent of plug region (m)
$r_{\tau 0}$	Radial location of zero shear stress (m)
Re	Reynolds number based on viscosity at the wall, ($\equiv \rho U_B D/\eta_W$)
Re_{crit}	Critical Reynolds number obtained from time traces of the mean axial velocity
Re_{MR}	Metzner and Reed Reynolds number, $\left(\equiv 8\left(\rho U_B^{2-n}/k\right)\left(n/(6n+2)\right)^n\right)$
Re_{PL}	Power-law Reynolds number, $\left(\equiv \rho U_B^{2-n} D_H^n/k\right)$
Re_1	First Reynolds number limit representing onset of transition

Re_2	Second Reynolds number limit representing offset of transition
Re_τ	Friction Reynolds number, $\left(\equiv \rho u_\tau D/\eta_W\right)$
t	Time (s)
t_i	Transit time of particle crossing the LDA measuring volume (s)
t_1	Fitting parameter in Equation [3.18] (s)
t_2	Fitting parameter in Equation [3.18] (s)
T_B	Filament break-up time in CaBER (ms)
Tr	Trouton ratio, ($\equiv \eta_E\left(\sqrt{3}\dot{\varepsilon}\right)/\eta(\dot{\gamma})$)
u	Mean axial velocity (m/s)
u_i	Individual velocity from LDA measurement (m/s)
u_τ	Friction velocity (m/s), $\left(\equiv \sqrt{\tau_W/\rho}\right)$
u'	Rms axial velocity fluctuation (m/s)
U_B	Bulk velocity (m/s), $\left(\equiv 4Q/\left(\pi D^2\right)\right)$ for circular pipe or $\left(\equiv Q/\left(\pi\left(R_o^2 - R_i^2\right)\right)\right)$ for annular pipe
U_{local}	Local mean velocity (m/s)
U_{max}	Maximum velocity (m/s)
v	Mean radial velocity (m/s)
v'	Rms radial velocity fluctuation (m/s)
V_2	Capillary velocity in Equation [3.18] (m/s)
w	Mean tangential velocity (m/s)
w	Mean velocity in the *z*-direction (m/s)
w'	Rms tangential velocity fluctuation (m/s)
x	Cartesian coordinate
$X_{an,\,ext}$	Parameter value obtained using analytical method or from using Richardson's

	extrapolation-to-the-limit technique
X_{mx}	Parameter value obtained from numerical simulation using Fluent for MX grid
y	Distance from pipe wall (m)
y	Cartesian coordinate
z	Cartesian coordinate
Z_c	Parameter introduced by Yanta and Smith (1973) to give the level of confidence in determining statistical uncertainty

Greek Letters

β	Time ratio
$\dot{\varepsilon}$	Strain rate (1/s)
ϕ^*	Shape factor
$\dot{\gamma}$	Shear rate (1/s)
η	Shear viscosity (Pa.s)
η'	Dynamic viscosity (Pa.s)
η_E	Uniaxial extensional viscosity (Pa.s)
η_{EB}	Biaxial extensional viscosity (Pa.s)
η_o	Zero-shear rate viscosity (Pa.s)
η_W	Wall shear viscosity obtained from τ_W and $\dot{\gamma}_W$ via Carreau-Yasuda fit (Pa.s)
η_∞	Infinite-shear rate viscosity (Pa.s)
l_{cap}	Capillary length (m), $\left(\equiv \sqrt{\sigma/\rho g}\right)$
κ	Radius ratio, $\left(\equiv R_i / R_o\right)$
λ	Relaxation time of fluid (s)
λ_{CY}	Carreau-Yasuda constant representing onset of shear thinning (s)

μ_s	Sample average
Λ	Aspect ratio in CaBER measurements $\left(\equiv h/b\right)$
ρ	Fluid density (kg/m^3)
$\rho\overline{u'v'}$	Reynolds shear stress (Pa)
σ	Standard deviation
σ	Surface tension of fluid (N/m)
τ	Stress (Pa)
τ_A	Average wall shear stress (Pa)
τ_{crit}	Critical shear stress (Pa)
τ_W	Wall shear stress (Pa), $\left(\equiv \Delta pD/4L\right)$
$\overline{\tau^p_{xy}}$	Polymer stress (Pa)
τ_y	Apparent yield stress (Pa)
ω	Angular frequency (rad/s)
ξ	Non-dimensional radial location in annulus, $\left(\equiv (r-R_i)/(R_o-R_i)\right)$
ψ_1, ψ_2	Normal stress coefficients (Pa.s^2)

Subscripts

e, v	Regions of pipe sections, elastic sublayer, viscous sublayer
f	Final
H	Hydraulic
i	Inner pipe
i	Initial
max	Maximum
n	Newtonian

o	Outer pipe
p	Polymer
W	Wall

Superscripts

$+$	"wall" coordinates

1 INTRODUCTION

1.1 Aim of study

The long term motivation behind the research work presented in this thesis was to better understand the flow behaviour of drilling fluid (or 'mud') which is pumped down the drill string through the drill bit and finally up the annulus during the oil and gas drilling process. The annulus can be defined as the space between the outside of the drill string to the borehole wall as illustrated in **Figure 1.1**. In conventional drilling a ratio of the inner pipe radius, R_i to the outer pipe radius, R_o of 0.5 is normally used while in slimhole drilling and coiled tube operations the radius ratio exceeds 0.8 (Escudier et. al., 2002a). The flow in the annulus is normally idealized as concentric, steady, isothermal and fully developed. In reality the annulus departs from concentricity significantly with the eccentricity found to vary with depth. The pressure and temperature inside the annulus also increase significantly with depth. The flow in the annulus is laminar in most occasions, with the shear rates of the drilling fluid normally between 50 to 150 s^{-1} (Gray and Darley, 1980), while the flow in the drill string is normally within the turbulent regime. Apart from drilling in oil wells there are numerous other applications such as in the food, chemical and pharmaceutical industries, to name only a few, that involve complex fluid flowing in circular and annular pipes. Thus, although the main motivation is related to drilling, the fundamental work described here has many applications.

The aim of the research work is to provide detailed fluid-dynamic measurements in a circular pipe, representing the drill string, and a concentric annular pipe, representing the annulus. Detailed velocity and Reynolds stress measurements are conducted using a laser Doppler anemometer (LDA) system together with pressure-drop measurements. As the utilization of the system requires the fluid to be optically clear, transparent polymer solutions having some of the rheological properties of drilling fluid are utilized.

1.2 Drilling fluid

Drilling fluid is one of the key elements in the drilling process which comprises of about six percent of the total well cost (Vinod, 1994). The main function of drilling fluid is to carry the rock fragments (or 'drill cuttings') loosened by the drill bit from the parent formation to the surface through the annulus and also to suspend the cuttings during a 'shutdown'. Other functions include cooling and cleaning the drill bit, reducing friction between the drill string and the borehole wall, maintaining stability for the uncased section of the borehole, preventing inflow of fluids from permeable rocks and forming a thin, low permeability filter cake which seals pores in formations penetrated by the drill bit (Gray and Darley, 1980). Special drilling fluids have been developed and formulated in the oil industry to meet these functions and requirements, which differ from well to well. Generally, most drilling fluids exhibit non-Newtonian properties (Alderman et. al., 1988; Hamed and Belhadri, 2009).

Drilling fluids are discussed in detail in Gray and Darley (1980). They state that there are three types of drilling fluids, water-based, oil-based and gas. Water-based drilling fluids were the first type of drilling fluids used but problems such as drill-sticking prevented further usage of this type of drilling fluid. Oil-based drilling fluid is advantageous with respect to this problem but is found to be less environmentally friendly. The least environmentally damaging oil-based drilling fluids are ester, internal olefin and paraffin-based. Gas drilling fluids are commonly in the form of mist, foam or gel foam.

1.2.1 Drill cuttings transport

Removal of drill cuttings from below the drill bit to the surface is important in ensuring a smooth drilling process. The efficiency of the drill cuttings removal depends on the drilling fluid viscosity, suspension, yield stress and velocity, apart from the density and size of the cuttings (Vinod, 1994). In a rising column of fluid, a particle will move upward if the velocity of the fluid is greater than the settling velocity of the particle. Hence, it is always critical for the fluid velocity in the annulus to exceed the downward falling rate of the cuttings.

Poor cuttings transport could result in undesirable increase of cuttings volume as the drilling proceeds. It has been reported that cuttings concentrations more than about 5% by volume can result in a narrowing of the annular gap due to the build up of cuttings. This narrowing leads to a low penetration rate and a blocked pipe when the circulation is stopped, a situation which can result in costly problems (Vinod, 1994).

One of the reasons for poor cuttings transport is that the flat cuttings tend to recycle locally, especially near the walls due to the shape of the laminar profile, which subjects a flat cutting to unequal forces. The cutting turns on edge, migrates to the sides of the annulus, descends some distance and migrates back towards the centre of the annulus as illustrated in **Figure 1.2**. Studies have shown that turbulent flow could improve the transport ratio due to the more uniform annular velocity distribution compared to that in laminar flow (Azouz and Shirazi, 1997). Better mixing of cuttings with the bulk flow and a decrease in turning moments is achieved in such flow conditions. However the cost of sustaining turbulent flow in cuttings transport is much higher due to the high frictional losses in the drill string, which increases with the square of the bulk velocity in turbulent flow, and the high shear near the borehole walls leading to wall erosion. Hence operational constraints in wells, particularly to limit the fluid pressure and high shear in order to avoid fracturing the formation surrounding the borehole, often restrict the flow in the annulus to the laminar regime (Gray and Darley, 1980; Ooms and Kampman-Reinhartz, 1996). If the flow velocity is to be maintained within the turbulent regime, one possible way to lower the frictional losses is by using polymer solutions which possess friction (or drag) reducing properties.

1.2.2 Rheological properties of drilling fluid

In general, most drilling fluids exhibit non-Newtonian properties of thixotropy, shear thinning with apparent yield stress and some degree of viscoelasticity (Escudier et. al. 2002a). In real conditions where the drill string is usually positioned eccentrically, especially in deviated wells, to achieve optimum hole cleaning the fluid should be shear thinning so that the viscosity reduces in the enlarged sections where the fluid velocities are high and increases in the narrowed sections where the velocities are low. The shear-thinning nature of the fluid will also reduce the pumping power. When the flow is stopped, the high viscosity at low shear rate (or the high yield stress) will keep the cuttings suspended.

1.3 Biopolymers as drilling fluid

A biopolymer is a type of polymer produced by a living organism. Deoxyribonucleic acid or DNA, proteins and starch are common examples of biopolymers. Detailed chemistry of biopolymers may be found in Tracy and Pecora (1992) and Lapasin and Pricl (1995), amongst others. As biopolymers are non-toxic, renewable, sustainable and biodegradable, a variety of biopolymers have been used as drilling fluids and the potential of their use have also been studied in tertiary recovery* since they pose minimal environmental problems (Kok and Alikaya, 2005).

---

* Tertiary recovery or enhanced oil recovery is a technique for increasing the amount of crude oil which can be extracted from an oilfield.

Dilute and semidilute aqueous solutions of biopolymers, xanthan and scleroglucan are currently used as drilling fluids and also for polymer flooding of oil reservoirs (Stokke et. al., 1992) where it is required to increase the viscosity and optimize the mobility ratio between the injected fluid and the displaced oils. These fluids are environmentally and economically advantageous over oil-based drilling fluids and superior to water-based drilling fluids containing cellulosic and guar gum, for example, in terms of lubricating power and carrying capacity with the gelation property of scleroglucan reported to be better (Hamed and Belhadri, 2009).

Scleroglucan has been reported to gel as standing time is increased resulting in good bearing capacity for a drilling fluid. A period of 48 hours has been established to be sufficient for gelling beyond which small changes in the gelation property is observed. Moreover, the amount of energy required to set the fluid back in motion is independent of the time for which pumping is stopped. The gelling has also been found to disappear very quickly as soon as flow takes place without over-pressuring the well (Grassi et. al., 1996; Hamed and Belhadri, 2009).

1.4 Present contribution

Studies have shown that high molecular weight, "flexible" polymers, when added to a Newtonian solvent, exhibit significantly less frictional resistance to flow in the turbulent regime compared to the solvent alone, and are therefore called "drag-reducing" (Lumley, 1973; Virk, 1975; Berman, 1978; Hoyt, 1986; Nieuwstadt and den Toonder, 2001; Graham, 2004, amongst others). The limited literature on "rigid" or "rod-like" polymers has shown that these polymer solutions are also capable of drag reduction but possibly to a lesser degree than flexible polymer solutions (Paschkewitz et. al., 2005; Ching et. al., 2006). Many biologically derived polymers are rigid or semi-rigid rod-like molecules (Tracy and Pecora, 1992) while all synthetic polymers are flexible polymer molecules (Doi and Edwards, 1986). Microscopically, the difference between flexible polymer and rigid polymer is that prior to shearing, flexible polymer can be viewed as being in a randomly coiled configuration requiring some minimal value of shear rate to stretch the molecules, while a rigid polymer is already stretched in a rod-like conformation. High molecular weight flexible polymer solutions are, however, very prone to mechanical degradation (Chung and Graebel, 1971 and Zakin et. al., 1977, amongst others). The use of these polymer solutions to reduce drag and pumping cost has to be balanced with its degradation rate and also the cost of new polymer additives should the previously added polymer found to have been degraded. Rigid polymer solutions on the other hand are more resistant to mechanical degradation (Paschkewitz et. al., 2005; Hoyt, 1985). The high resistance to mechanical degradation is believed to be due to the high structural chain rigidity; ordered, double-stranded, conformation of xanthan gum at high salt concentration or at low temperature and triple-stranded conformation scleroglucan; compared to the single stranded flexible polymers (Paschkewitz et. al., 2005; Hoyt, 1985; Lee, 2001). Hence, even though it is thought that flexible polymer solutions are more efficient drag reducers compared to rigid polymer solutions, their faster degradation rate might suppress the advantage.

There are no complete investigations, e.g. mean velocity, Reynolds normal and shear stress data ($u, u', v', w', \overline{u'v'}$), of rigid and semi-rigid polymers using LDA in circular and annular pipes. Moreover, due to the high amount of refraction near the wall for any accurate LDA measurements on a curved surface, many studies have concentrated on measurements, especially the Reynolds shear stresses, inside planar channels instead where the effects of refraction are more easily accounted for (Willmarth et. al., 1987 and Warholic et. al., 1999, amongst others conducted Reynolds shear stress measurements of flexible polymer solutions in channel flows). Hence, complete experimental data of rigid and semi-rigid polymers in circular and annular pipes are required particularly (but not exclusively) for validation of numerical simulations.

In this work, a comprehensive study is conducted on the drag-reducing behaviour of a rigid polymer solution, a scleroglucan, in circular pipe flow. Very dilute solutions (0.005%-0.01% w/w) are utilized where no molecular interactions are expected to occur and the solutions remain transparent. Due to the high degradation rate of flexible polymers at these dilute concentrations, measurements were only conducted for rigid polymers and the wide breadth of data from the literature, where available, for flexible polymers are utilized for comparison. The drag-reducing behaviour of a semi-rigid polymer, xanthan gum, at a concentration close to that of scleroglucan is studied instead in an annular pipe.

The laminar and transitional flow behaviour in the concentric annular pipe, with particular attention placed on the transitional regime, of two different polymers are also investigated in this work and compared to that of the Newtonian fluid, a glycerine-water mixture. Xanthan gum at various concentrations is utilized to represent the behaviour of a semi-rigid polymer. The laminar and transitional flow study in the same annulus was also conducted on a polymer, carbopol, which is known to exhibit a yield stress. The use of a yield stress fluid was motivated by the recent interesting findings of Peixinho et. al. (2005) in transitional pipe flow where two critical Reynolds numbers were observed.

Pressure drop, mean flow and turbulence characteristics of the fluid flows have been measured. Qualitative and quantitative comparison with the Newtonian data provide a clear understanding of how polymer rigidity affects the flow in such geometries. A complete rheological characterization of the different polymer solutions investigated has also been conducted and used to link the fluid dynamics with the rheological behaviour of these polymer solutions.

FIGURES

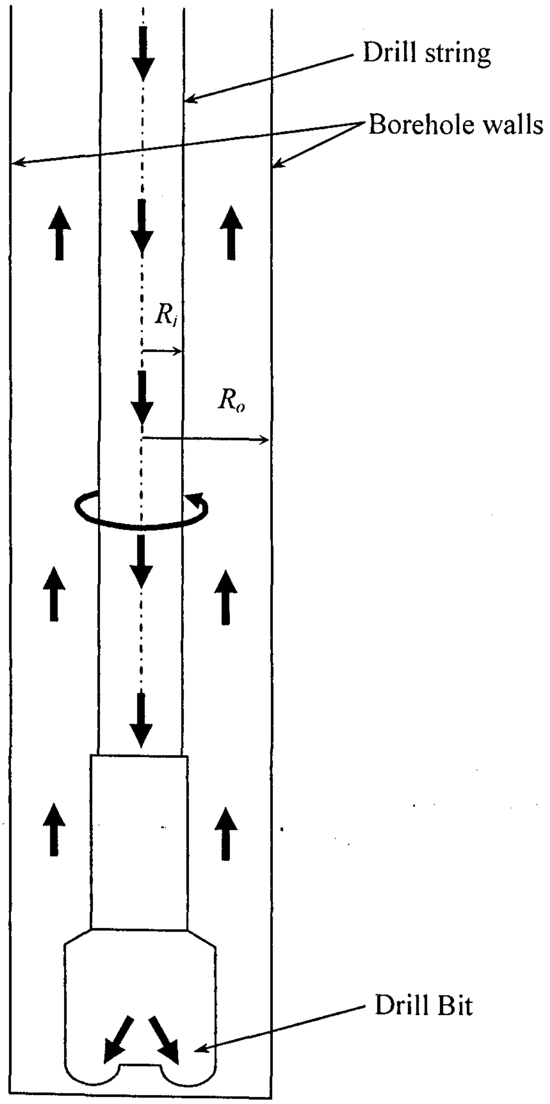

Figure 1.1: Schematic diagram of an annulus in drilling operations

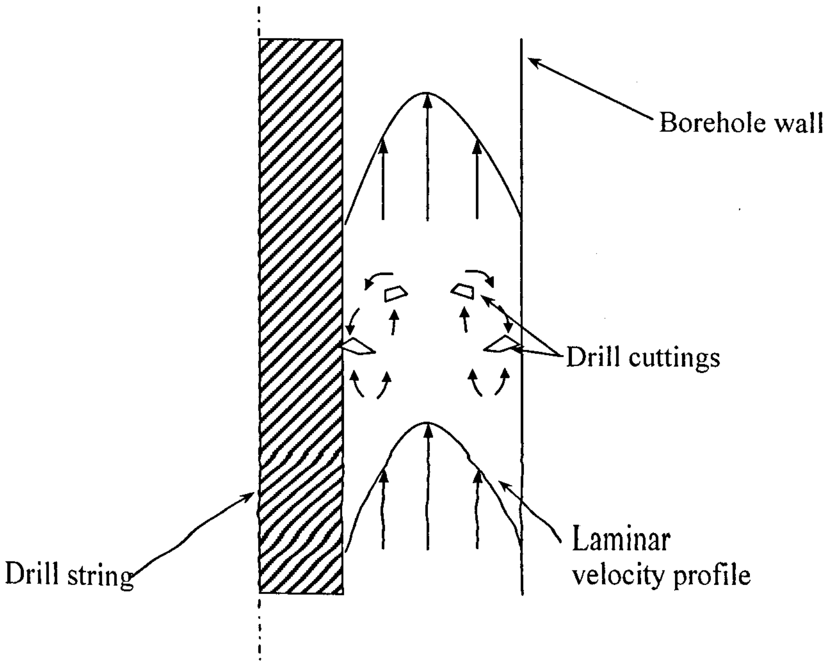

Figure 1.2: Schematic illustrating the tendency of drill cuttings to recycle locally near the walls in an annulus

2 LITERATURE REVIEW

The literature review is arranged in the following manner; the fundamentals of drag reduction are first described with the relevant scientific findings of earlier investigations in channel and pipe flows. This is followed by a literature review of annular flows of Newtonian and non-Newtonian fluids. Note that the subjects of non-Newtonian flow in pipes and drag reduction have been extensively studied for more than 50 years. As it is impossible to cite every paper on these subjects, only the most relevant papers related to the present work will be mentioned.

2.1 Drag-reduction phenomenon

The phenomenon of drag reduction is seen as a reduction of pressure drop and skin friction in turbulent flow when polymer is added to the solvent, typically water. It was initially discovered by a chemist B.A. Toms in summer 1946 and later presented at an international congress on rheology in 1949 (as discussed in Tanner and Walters (1999)). Using high molecular weight poly(methyl) methacrylate he measured the rate of flow of the polymer dissolved in monochlorobenzene across a circular pipe and observed increased flowrate with polymer concentration (Toms, 1977). Owing to his pioneering work the drag-reduction effect is now often referred to as "Tom's phenomenon" in the literature.

There are several methods of quantifying the degree of drag reduction such as based on the friction factors which are evaluated either at the same Reynolds number or at the same friction Reynolds number, $Re_\tau \left(\equiv \rho D u_\tau / \mu_W\right)$ (e.g. Escudier et. al., 2009a)

$$\%DR = \left(1 - \frac{f_p}{f_n}\right) \times 100 \qquad [2.1]$$

or based on the maximum Reynolds shear stress (e.g. Paschkewitz et. al., 2005)

$$\%DR = \left(1 - \frac{max(-\overline{u'v'_p})}{max(-\overline{u'v'_n})}\right) \times 100 . \qquad [2.2]$$

A notional limit of 40% drag reduction has been set, below which the flow is categorized as "low" drag-reducing, and above which "high" drag-reducing (e.g. Warholic et. al., 1999; Tiederman, 1990 and Escudier et. al., 2009a). There are marked differences between these two categories. For "low" drag-reducing flows, the normalized mean velocity in law-of-the-wall form $\left(u^+\right)$ remains parallel to the Newtonian data but is upshifted (Virk, 1975; Tiederman, 1990; den Toonder et. al., 1997; Warholic et. al., 1999; Ptasinski, 2002; and Escudier et. al., 2009a). In addition, the peak value of the normalized axial rms fluctuations $\left(u'^+\right)$ increases, the peak values of the radial $\left(v'^+\right)$ and tangential $\left(w'^+\right)$ rms fluctuations decrease together with a monotonic decrease of the Reynolds shear stress $\left(\rho\overline{u'v'}\right)$ (Tiederman, 1990; Warholic et. al., 1999; Ptasinski, 2002). Different trends are observed for high drag-reducing flows where there is a significant increase in the slope of the universal mean velocity profile (Tiederman, 1990; Warholic et. al., 1999; Ptasinski, 2002). At such high levels of drag reduction the normalized axial rms fluctuation levels are ultimately suppressed with further suppression of the radial and tangential components. Concomitant decreases of the Reynolds shear stress to almost zero levels close to the maximum drag reduction asymptote (Virk, 1975) are observed with corresponding increases in the so-called "polymer stress".

Drag reduction has also been the subject of extensive reviews by Lumley (1973), Virk (1975), Berman (1978), Hoyt (1986), Nieuwstadt and den Toonder (2001), Graham (2004), White and Mungal (2008) and many others. Amongst all these recent reviews the article by Virk (1975) is often discussed. As Virk describes, experimental evidence shows that drag reduction is found to be a function of the geometry of the pipe, the polymer concentration, the polymer molecular weight and the Reynolds number. Virk proposed a three-layer model for drag-reducing flow which comprises of the viscous sublayer, the buffer layer and the Newtonian core region. The polymer turbulence interaction - thought to be responsible for drag reduction - was believed to commence within the buffer layer where the axial and the radial turbulent flow fields were found to be decoupled. The polymer molecules were thought to interfere with the process of turbulent bursting within this region and the decoupling to retard the radial transport of the axial momentum. Within the Newtonian core region the profile is bound by two asymptotes; the well-known Newtonian log law, also known as the Prandtl-Kármán law, and the maximum drag reduction asymptote (Virk et. al., 1970; Virk, 1975) which is now commonly referred to as "Virk's asymptote" or maximum drag reduction asymptote (MDR). The asymptote has been established to be independent of pipe diameter, type of polymer, molecular weight and concentration. Further discussion of Virk's three-layer model and the drag reduction asymptotes will be provided in **Chapter 5**. Within the turbulent regime the friction factor, *f*, of drag-reducing flow is also bound by two asymptotes when plotted against the Reynolds number, *Re*; the Blasius approximation for fully-developed turbulent Newtonian flow and the empirical relation proposed by Virk (1975), which is further discussed in **Chapter 5**. The two asymptotes in the *f-Re* plot are as shown in **Figure 2.1**.

The polymer turbulence interaction within the buffer layer was first proposed by Lumley (1973) and further discussed by Berman (1978). Within the buffer layer, where the turbulent production and dissipation is maximum, the addition of polymer results in polymer molecule interactions with the turbulent eddies which then shifts the location of the greatest turbulence production and dissipation closer to the pipe centre resulting in an increase of the buffer layer thickness. Using flow visualization of elongated particles Hoyt (1986) proposed that the drag-reduction effect is due to the stretching of individual flexible molecules by the high deformation rate at the wall. The elongated molecules then align in the direction of flow resulting in lower frictional resistance and pressure losses.

Numerous explanations, in some cases somewhat speculative, have been proposed to elucidate the drag-reduction mechanism with most emphasis on drag reduction by flexible polymers. Pinho (1990) suggested that larger sizes of the smallest eddies and the preferential action of molecular stretching to orientate the eddies axially are the causes of turbulent structure modifications in drag-reducing flows. Many investigators have related the behaviour of drag-reducing fluid to extensional viscosity specifically tension thickening (see for example the work by Tabor and de Gennes (1986); den Toonder et. al., 1995 and the review by White and Mungal (2008)) where the ability to suppress roll-wave motion and vortex stretching in the buffer layer by the fluid has been thought to be responsible for drag reduction (Barnes et. al., 1989). Jovanovic et. al. (2006) attempted to explain the mechanism of drag reduction for flexible polymers by considering local stretching of the polymer molecules, as suggested by earlier authors, by the small scale turbulence motions near the wall. These "activated" polymer molecules then further restructure the turbulence. The analytical analysis led the authors to conclude that at the wall velocity fluctuations are predominantly one-component (i.e. anisotropic) leading to significant reduction of the turbulent dissipation rate and hence suppression of turbulence in the near wall region.

One of the most recent reviews conducted on the turbulent drag reduction mechanism of flexible polymer solutions is by White and Mungal (2008). The authors highlighted the lack of coupling between the near wall turbulence and the skin friction in the description of the drag-reduction mechanism provided so far where more work is required to understand further the process of how the restructured turbulence could reduce the skin friction. There appears to be general agreement on the criterion for drag reduction to occur : the polymer relaxation time, λ, i.e. the average time for a stretched polymer to return to a coiled configuration, must be longer than a representative viscous time scale of the near wall turbulence;

$$\lambda > \frac{\eta}{\rho u_\tau^2} \qquad [2.3]$$

where η, ρ and $u_\tau \left(\equiv \sqrt{\tau_W / \rho}\right)$ are the viscosity, density and the friction velocity respectively. Near the maximum drag reduction asymptote given by Virk (1975) the Reynolds shear stress, $\rho\overline{u'v'}$, reduces significantly and the turbulence within this regime is sustained by the polymer stress, $\overline{\tau_{xy}^p}$.

From these reviews and studies the behaviour of flexible polymer solutions as drag-reducing agents is now fairly well understood. However, the drag-reducing mechanisms of "rigid" or "rod-like" polymers are far from as well studied or understood as in the case for flexible polymers. The limited literature on these polymers has shown that the polymer solutions are also capable of drag reduction but possibly to a lesser degree than flexible polymer solutions (e.g. the boundary-layer (polymer injection) work of Paschkewitz et. al., 2005).

Berman (1978) found that rigid structures and polyelectrolyte were not effective drag reducers until the concentration was "high enough" which was also confirmed by his later study (Berman, 1980). Using collagen and carrageenan, the ratio of circumscribed volume* of the molecules to the actual volume was found to be at least 30 for the solution to be drag-reducing. Through pressure-drop measurements it was observed that the rigid polymer-solutions were drag-reducing but did not show any drag-reduction onset (i.e. there appeared to be no critical wall shear stress before drag reduction occurred) in contrast to that observed for flexible polymer solutions where a well-defined onset for drag reduction is seen (Berman and George, 1974; Virk et. al., 1997). Although exhibiting drag reduction the slopes of the friction factor, *f*, against the

---

* The lengths of the rod-like molecules were used as diameters to calculate the circumscribed volume

Reynolds number, *Re,* plotted in log-log coordinates remained parallel to that for the Newtonian fluid flow.

Bewersdorff and Singh (1988) studied the drag-reduction of xanthan gum solutions in which molecule rigidity was varied by the addition of salt to increase flexibility. Without salt addition the *f-Re* data of the xanthan gum solutions (plotted in log-log coordinates) exhibited drag reduction but the curves remained parallel to that for the Newtonian fluid. The greater flexibility due to the addition of salt resulted in greater drag reduction. These results are in disagreement with the observations of both Sasaki (1991) and Virk et. al. (1997) however. Virk et. al. (1997) found that increasing the flexibility of hydrolyzed polyacrylamide reduced the drag-reduction ability of the polymer solution. Sasaki (1991) also studied the drag-reducing ability of what he termed a "strictly rigid" polymer solution, scleroglucan, and found the trend to be in close agreement with that of a semi-rigid xanthan gum solution without salt addition.

Benzi et. al. (2005) postulated through theoretical considerations that the slope of the maximum drag reduction asymptote (*f-Re* plot) discovered by Virk (1975) applies to both flexible and rigid polymers. However, their work showed that the dynamics of these polymers upon approaching the asymptote are different. They found that the degree of drag reduction for a rigid polymer is dependent only on the concentration while it is well known that for a flexible polymer, apart from concentration, it is also a function of Reynolds number, molecular weight and the Weissenberg number (Lumley, 1973; Virk, 1975; Berman, 1978, 1980; Hoyt, 1986; Nieuwstadt and den Toonder, 2001, and White and Mungal, 2008). For flexible polymers the asymptote is reached even for low concentrations and then a crossover back to the Newtonian core is found. For rigid polymers maximum drag reduction is approached gradually as concentration is increased.

Paschkewitz et. al. (2004) conducted direct numerical simulations (DNS) of non-Brownian fibres (no elasticity) in a turbulent channel flow. At 15% drag reduction they observed an increased peak in the rms axial fluctuation $\left(u'^{+}\right)$ and decreased peaks in the radial $\left(v'^{+}\right)$ and the tangential $\left(w'^{+}\right)$ rms fluctuations that were similar to those observed in low drag-reducing flexible polymer solutions. Similar observations were made by Benzi et. al. (2008) leading the authors to conclude that elasticity is not necessary for drag reduction of rod-like polymers, also confirming the experimental observations by McComb and Chan (1985) on macroscopic fibres (chrysotile asbestos of high length-to-diameter ratio ($\sim 10^5$)). Paschkewitz et. al. (2004) also reported significant reduction of the Reynolds shear stress throughout the entire channel. The addition of fibres is found to reduce the production of turbulent kinetic energy as well as to provide an additional source for dissipation. A positive total fibre contribution to the turbulent kinetic energy is detected in the region of $10 \leq y^{+} \leq 25$, thought to be attributed to the large fluctuations in u'^{+} within the region, which further aligns the rod-like molecules in the direction of the flow. Maximum fibre stress is also observed within $y^{+} \cong 20$, corresponding to the location of the maximum streamwise velocity fluctuations. A reduced and broadened peak of the vorticity fluctuations suggests weakening of near wall vortex structures with increased vortex size resulting in lower wall shear stress. Further analysis of the stress behaviour led the authors to conclude that rod-like molecules reduce drag by interrupting the near-wall vortex structures. As drag reduction is increased, the near wall vortices become weaker and farther apart, eventually limiting the drag-reduction effectiveness of rigid, rod-like polymers. Further study by the authors using Lagrangian conditional statistics (Paschkewitz et. al., 2005) where the moments and stresses of rigid, rod-like polymers were calculated along Lagrangian pathlines confirmed the stress behaviour, which was found to be at a maximum in the buffer region. The drag-reduction effectiveness is also found to increase with increasing aspect ratio of the fibres (Berman, 1980; Paschkewitz et. al., 2004; Gillissen et. al., 2008).

2.2 Annular flow

2.2.1 Laminar and turbulent annular flow

One of the key problems in turbulent annular flow is the determination of the position of zero shear stress and hence the wall shear stresses on the inner and the outer walls which then enable the velocity representation in wall coordinates on both walls. Early investigations by Knudsen and Katz (1958), Rothfus et. al. (1950, 1955), Walker and Rothfus (1958) and Brighton and Jones (1964) assumed coincidence of the position of zero shear stress and maximum velocity. However, there are slight disagreements between the findings on the position of maximum velocity for laminar and turbulent flow where they were found to be the same (Knudsen and Katz, 1958; Rothfus et. al., 1950; Walker and Rothfus, 1958) or closer to the inner wall for turbulent flow (Rothfus et. al., 1955; Brighton and Jones, 1964) when compared to laminar flow.

Lawn and Elliott (1972) were the first to show, using hot-wire anemometry, that the position of zero shear stress and maximum velocity are non-coincident in turbulent annular flow. They found that for radius ratio, κ, of less than 0.4 the position of zero shear stress was closer to the inner pipe wall than that of the maximum velocity. The inner velocity profiles were also found to deviate from the well-known log law (derived from pipe flow data). Their findings were later supported by Rehme (1974, 1975) who studied the fully-developed turbulent flow of air using hot-wire anemometry in concentric annuli of varying radius ratio (κ=0.02, 0.04 and 0.1). The positions of zero shear stress were found to be closer to the inner wall compared to the positions of maximum velocity with the dependence of both positions on Reynolds number increasing with decreasing radius ratio. Unlike the inner wall, the outer wall profiles agree well with the well-known log law for all radius ratios. The deviations of the inner wall profile, however, increases for smaller radius ratio due to curvature effects.

Even though the regular utilization of non-intrusive laser techniques, the laser Doppler anemometer (LDA) for example, had started in the 1970s Nouri et. al. (1993) were the first authors to employ LDA for Newtonian and also non-Newtonian annular-flow measurements ($Re \geq 8900$ for Newtonian and $Re \geq 1150$ for non-Newtonian flows where $Re = \rho U_B D / \eta_W$). They measured the Reynolds shear stress of a Newtonian fluid in an annulus of radius ratio of 0.5 and found that the location of zero shear stress was within the experimental uncertainty and hence could not be distinguished from that of the maximum velocity for Newtonian concentric flow. These positions were found to be closer to the inner pipe wall and independent of the Reynolds number. In wall coordinates, the inner and outer wall profiles of Newtonian fluid flows were found to obey the well-known log law. Due to opacity of the non-Newtonian fluid utilized, carboxymethylcellulose, the Reynolds shear stress could not be measured and therefore maximum velocity and zero shear stress coincidence was assumed. The velocity profiles, normalized with the bulk velocity U_B, of the non-Newtonian fluid were observed to be flatter and less skewed compared to that of the Newtonian fluid with the transition to turbulence delayed. The rms fluctuating velocity components, when normalized with U_B, were found to be lower than those of the Newtonian fluid flow particularly in the radial and tangential components.

Performing DNS calculations of Newtonian turbulent concentric annular flow for two radius ratios of 0.1 and 0.5 at Re=8900, Chung et. al. (2002) found that the position of the zero shear stress is closer to the inner wall than those of the maximum velocity for both annuli though in the smaller radius ratio geometry the effect is more severe.

In all the experimental and numerical investigations presented so far for Newtonian flow, agreement is obtained in terms of the friction factor which was found to be higher than that in circular pipe flows for the same Reynolds number with the exception of the data presented by Jonsson and Sparrow (1966) and Quarmby (1967) which lie closer to the pipe values.

Escudier et. al. (2002a) performed LDA measurements together with numerical simulations of a power-law fluid, a xanthan gum/carboxymethylcellulose mixture in a concentric annulus with radius ratio of 0.506 within the laminar flow regime. The velocity profiles were observed to be skewed towards the inner pipe of the annulus. The velocity distributions, normalized with U_B, were found to be slightly flatter with reduced peak velocity levels when compared to the Newtonian flow.

By performing a numerical study of power-law and yield stress fluids within the laminar regime, Luo and Peden (1987) discovered that the position of maximum velocity is independent of the power-law index.

Escudier et. al. (1995a) conducted LDA measurements of three different non-Newtonian fluids - a xanthan gum, a carboxymethylcellulose and a laponite-carboxymethylcellulose blend - within the laminar, transitional and turbulent annular flow regimes (radius ratio κ=0.5). Measurements were also conducted on a control fluid, a glycerine-water mixture. At drag reduction of greater than 35%, the authors observed upward shift of the universal velocity profile with a slope greater than the well-known log law. A slight increase in the peak of the axial rms fluctuation component, normalized with U_B, compared to the Newtonian value, was seen while the tangential component was almost uniformly distributed across the annular gap significantly below the Newtonian values.

2.2.2 Transitional annular flow

Velocity profile measurements of transitional Newtonian fluid in an annulus were conducted by Rothfus et. al. (1950) using air flowing isothermally into an annulus with varying radius ratios ($\kappa = 0.162$ and 0.650) at moderate Reynolds number range covering the transitional regime ($1250 \leq Re \leq 21600$). Using a pitot tube for the measurements of velocities, the authors found that the position of maximum velocity is the same for laminar and turbulent flow in both annuli. However, within the transitional regime, the position is shifted further towards the inner pipe. The extent of the transitional regime on the Reynolds number scale was found to be a function of the radius ratio and appeared longer than in circular pipes.

Walker and Rothfus (1958) studied the behaviour of the radial location of maximum velocity r_{max}, using a pitot tube, with Reynolds number for water flowing in an annulus (κ=0.331). The Reynolds number was defined as

$$Re = \frac{2\left(R_o^2 - r_{max}^2\right)}{R_o}\frac{U_B \rho}{\eta} \qquad [2.4]$$

where R_o is the outer pipe radius. As r_{max} is not known a priori, the Reynolds number could only be calculated once this value has been determined. The values of r_{max} obtained from the velocity profiles start to deviate from the laminar flow position at Re=650. In the lower transitional regime, r_{max} appears to shift towards the inner pipe wall and then reverses its direction as the Reynolds number is further increased. The outward progression of r_{max} continues past its laminar flow value with increasing Reynolds number and stops only when a critical Reynolds number of 2200 is attained. This is the Reynolds number at which the friction factor at the outer wall reaches a minimum value before its sharp transitional increase. As Reynolds number increases further r_{max} reapproaches its laminar value.

Hanks and Bonner (1971) performed a theoretical analysis on the stability of laminar Newtonian flow within a concentric annulus. The theory predicts that the inner flow region is the least stable of the two flow regions and will undergo transition to turbulence while the flow in the outer region remains laminar. Consequently, the wall shear stress in the inner region will increase significantly due to the change in momentum transport mechanism to a turbulent mode. The increase in wall shear stress would then lead to a shift in the radius of maximum velocity to a higher value, towards the outer wall. The radius of maximum velocity will reach a maximum distance once the outer flow region undergoes transition to turbulence. Beyond this critical Reynolds number the radius of maximum velocity will decrease to a value corresponding to that in turbulent flow where $r_{max,turbulent} < r_{max,laminar}$.

Unlike the situation for Newtonian flow, there is only a very limited literature of detailed experiment and stability analysis within the transitional flow regime for non-Newtonian fluids in an annular pipe. Amongst the available literature, McEachern (1969) conducted pressure drop measurements of HEC (hydroxyethyl cellulose) within the transitional regime. Using annuli of two different radius ratios, 0.25 and 0.5, the author discovered that the end of the laminar regime occurs at different flowrates and at different axial distances from the entrance of the test section. Of course it is the critical Reynolds number which is important (not the flowrate) and, as the viscosity of HEC is shear-thinning, the laminar regime would not be expected to end at the same flowrate.

Escudier et. al. (1995a) monitored the axial turbulence intensity of Newtonian and non-Newtonian fluid (xanthan gum, carboxymethylcellulose and laponite/carboxymethylcellulose mixture) flows at the centre of the annular gap as a means to identify the onset of transitional flow. Although departure from the laminar flow regime was observed on the friction factor, f

against the Reynolds number, $Re\left(\equiv \rho U_B D_H / \eta_W\right)$ plot, a sudden increase in the normalized axial turbulence intensity, u'/U_B, above the noise level was detected at a slightly lower Reynolds number than what is observed on the *f-Re* plot for all the fluids studied. Despite the circumferential asymmetry highlighted by the authors, the mean axial velocity distribution for the Newtonian control case showed a slight shift of the location of maximum velocity towards the outer wall within the transitional regime, a trend which was absent for the non-Newtonian fluid flows.

Gucuyener and Mehmetoglu (1996) applied Hanks' stability criterion (Hanks and Bonner, 1971) to pseudoplastic and yield stress fluids. Using the modified Reynolds number (based on an equivalent diameter and characteristic parameters of the flow) the authors found that, regardless of the fluid rheology, two very distinct critical Reynolds numbers are obtained in a concentric annulus. The inner flow region will always have a lower critical Reynolds number value compared to the outer flow region. Mishra and Mishra (1980), however, predicted only one critical Reynolds number for the transition to turbulence using Mishra and Tripathi's criterion (Mishra and Tripathi, 1971) for power law fluids. This critical Reynolds number is found to be an increasing function of the radius ratio. Transition to turbulence is also predicted to be delayed for the more shear-thinning fluid.

FIGURES

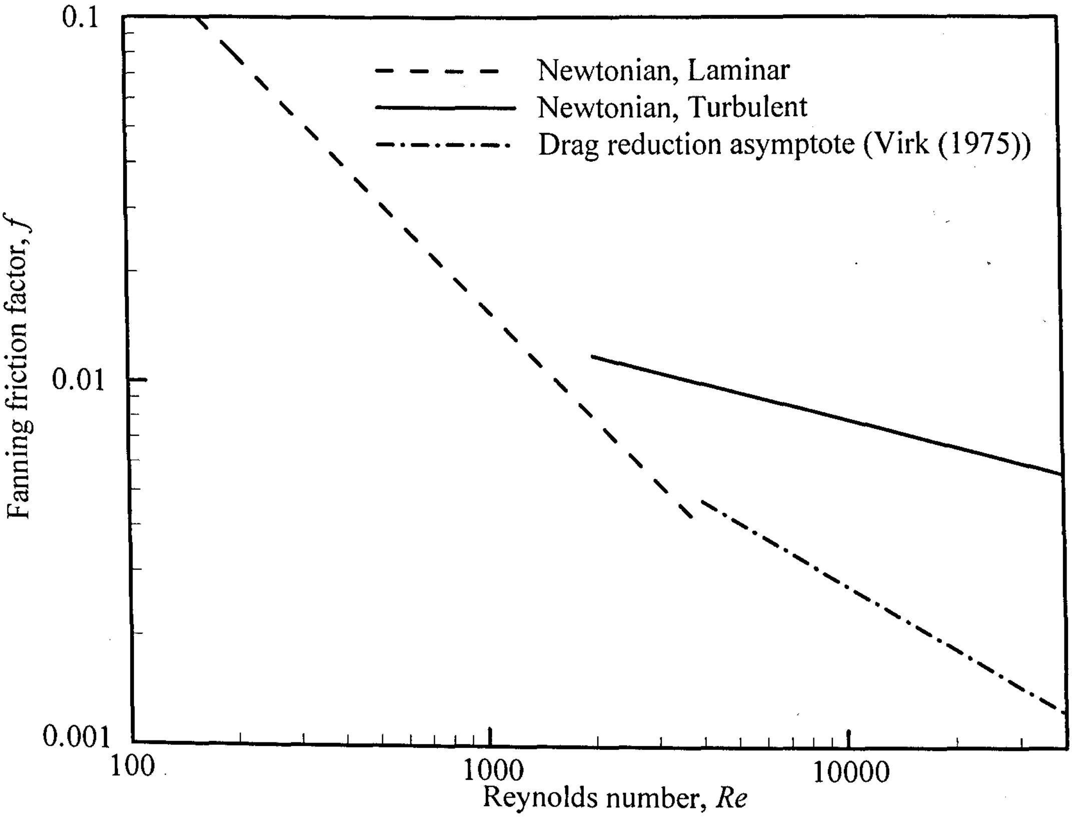

Figure 2.1: Friction factor, *f*, against Reynolds number, *Re*, plot.

3 RHEOLOGY

For non-Newtonian fluid flows the detailed fluid dynamics is dependent on the rheology of the fluid, in addition to other well known factors such as the density and compressibility of the fluids and also the geometry within which the fluid flows. In this chapter, the concept of rheology and how it is related to the definition of non-Newtonian behaviour is discussed. Complete rheological characterizations of different polymer solutions utilized in the pipe and annular-flow studies are also performed and elaborated upon here with the intention that they could be used to partly explain the fluid dynamic behaviour.

3.1 Terminology

Rheology, a terminology used since 1929 when the American Society of Rheology was founded (Barnes et. al., 1989), was conceived by Professor Eugene Bingham of Lafayette College, Indiana to describe "the study of deformation and flow of matter". The field of study extends the classical discipline of elasticity, described by Hooke's law for solids, and Newtonian fluid mechanics, described by Newton's law for fluids, to the flow of materials that behave between these classical extremes, namely, materials categorized as being non-Newtonian.

3.2 Newtonian Fluid

For a Newtonian fluid under a steady simple shear flow as illustrated in **Figure 3.1**,

$$u = \dot{\gamma} y,\ v = w = 0 \qquad [3.1]$$

where $\dot{\gamma}$ is the constant shear rate, the only stress acting on the fluid is the shear stress in the direction of the flow, τ_{xy} or commonly termed only as τ in a one-dimensional flow. The shear stress is a function of shear rate and viscosity, η which is constant with respect to shear rate and time, by

$$\tau = \eta\dot{\gamma}. \qquad [3.2]$$

Upon cessation of shearing, in the absence of inertia, the stress immediately falls to zero (Barnes et. al., 1989). The normal stresses, τ_{xx}, τ_{yy} and τ_{zz} are all equal to the isotropic pressure for an incompressible fluid and hence, will give differences of zero, i.e. $\tau_{xx} - \tau_{yy} = 0, \tau_{xx} - \tau_{zz} = 0$.

The fluid dynamic behaviour of a Newtonian fluid can be described by the full Navier Stokes equations, presented here in Cartesian coordinates as:

Continuity equation

$$\frac{\partial \rho}{\partial t} + \left[\frac{\partial(\rho u)}{\partial x} + \frac{\partial(\rho v)}{\partial y} + \frac{\partial(\rho w)}{\partial z}\right] = 0$$

x - momentum equation

$$\frac{\partial(\rho u)}{\partial t} + \left[\frac{\partial(\rho uu)}{\partial x} + \frac{\partial(\rho uv)}{\partial y} + \frac{\partial(\rho uw)}{\partial z}\right] = -\frac{\partial p}{\partial x} + \eta\left(\frac{\partial^2 u}{\partial x^2} + \frac{\partial^2 u}{\partial y^2} + \frac{\partial^2 u}{\partial z^2}\right) + \rho f_x$$

y - momentum equation

$$\frac{\partial(\rho v)}{\partial t} + \left[\frac{\partial(\rho vu)}{\partial x} + \frac{\partial(\rho vv)}{\partial y} + \frac{\partial(\rho vw)}{\partial z}\right] = -\frac{\partial p}{\partial y} + \eta\left(\frac{\partial^2 v}{\partial x^2} + \frac{\partial^2 v}{\partial y^2} + \frac{\partial^2 v}{\partial z^2}\right) + \rho f_y$$

z - momentum equation

$$\frac{\partial(\rho w)}{\partial t} + \left[\frac{\partial(\rho wu)}{\partial x} + \frac{\partial(\rho wv)}{\partial y} + \frac{\partial(\rho ww)}{\partial z}\right] = -\frac{\partial p}{\partial z} + \eta\left(\frac{\partial^2 w}{\partial x^2} + \frac{\partial^2 w}{\partial y^2} + \frac{\partial^2 w}{\partial z^2}\right) + \rho f_z$$

[3.3]

Another significant characteristic of a Newtonian fluid is that the viscosities measured under different types of deformations are always in simple proportion to one another; e.g. the viscosity measured in uniaxial extensional flow, η_E, is always three times the value measured in simple shear flow, i.e. $\eta_E = 3\eta$ (Barnes et. al, 1989).

3.3 Non-Newtonian Fluid

In principle, any fluid whose behaviour deviates from the classical Newtonian behaviour is known as a non-Newtonian fluid. Non-Newtonian fluids cannot be described on the basis of the Navier-Stokes equations alone. As opposed to constant viscosity, η, observed for a Newtonian fluid at constant temperature and pressure, the viscosity for most non-Newtonian fluids varies with the shear rate. For these types of fluid, the shear viscosity is defined analogously to the viscosity of the Newtonian fluid as

$$\eta(\dot{\gamma}) = \frac{\tau(\dot{\gamma})}{\dot{\gamma}} \tag{3.4}$$

where η is now a function of shear rate, with the exception of the yield stress fluid (below the critical shear stress) and the Boger fluid. A yield stress fluid behaves like an ideal elastic solid at low stresses while beyond a critical stress, known as the yield stress, the fluid flows. A Boger fluid (Boger, 1977) is a highly viscoelastic fluid with the change in viscosity found to be negligible with increasing shear rate. It is a dilute solution of a high-molecular-weight polymer in a normally viscous solvent.

Viscoelastic fluids are fluids which exhibit elastic recovery from deformation as well as viscous material properties. All viscoelastic fluids are non-Newtonian but not all non-Newtonian fluids are viscoelastic (Barnes et. al., 1989). In simple-shear flow, a viscoelastic fluid also gives rise to two additional normal stresses apart from the shear stress. These stresses are commonly presented in the form of stress differences; the first and second normal-stress differences, N_1 and N_2. N_1 is an increasing function of shear rate and can be used to determine elasticity while N_2, which is always much smaller than N_1 (typically $N_2 \sim 0.1N_1$), is of less practical significance (Barnes et al, 1989). For a Boger fluid, N_2 is virtually zero (Bird et. al., 1977). As the normal-stress differences are associated with viscoelastic effects, these stress difference will be zero for a Newtonian fluid and purely viscous non-Newtonian fluid in simple shear flows. When a viscoelastic fluid is sheared some of the energy is stored elastically and not all is dissipated (ultimately) as heat as for purely viscous fluids. When the shearing applied to a viscoelastic fluid is removed, the stored energy is released and the sample will take some time to stop (even in the absence of inertia). The fluid is then said to exhibit stress relaxation. Barnes et. al. (1989) proposed a measure of elasticity in a viscoelastic fluid using recoverable shear, $N_1/2\tau$. A value of 0.5 or greater indicates that the fluid is highly elastic.

Shear thinning, also known as pseudoplasticity, is used to describe fluids which possess a viscosity which decreases with increasing shear rate due to the intermolecular associations and/or entanglement that are broken apart by the shear forces allowing other particles and molecules to move past each other more easily (Apel, 1997). Typical graphs known as flow curves or rheograms for a shear-thinning fluid are shown on log scales in **Figure 3.2**. In the first Newtonian plateau and the second Newtonian plateau, the viscosities are constants with the first Newtonian plateau viscosity known as the zero-shear viscosity and the second known as the infinite-shear viscosity. Within the first Newtonian plateau, the fluid behaves similar to a Newtonian fluid, beyond which, the applied shear stress causes the molecular or particle motion to exceed Brownian motion resulting in the reduction of viscosity (Bird et. al., 1977). In the second Newtonian plateau, optimum orientation of the molecules is reached; hence, the viscosity approaches a constant level again (Apel, 1997). The opposite of shear thinning, termed shear thickening, also known as dilatancy, is when the viscosity increases with shear rate. This behaviour is much less common than shear thinning.

As we have already briefly mentioned, a yield stress fluid is a shear-thinning fluid which possesses a so-called "yield stress". At rest, the fluid has an intermolecular binding force which restricts the molecular motion giving the material a character of a solid with infinitely high viscosity. At this point, only elastic behaviour is observed where if the force applied to the material is less than the binding force, it will elastically deform the shape of the material (Barnes, 2000). Only when the force is greater than the binding force, is the critical shear stress reached causing the molecular network to collapse and flow to occur, showing a "liquid-like" behaviour. The critical shear stress is called the yield stress of the material.

If the viscosity is also time dependent, apart from being shear rate dependent, the fluid is thixotropic. Thixotropy is a phenomenon where the viscosity decreases under constant shear rate followed by a gradual recovery over time when the shear rate is removed. If the viscosity is increasing with time instead, the effect is known as rheopexy or anti thixotropy (Barnes et. al., 1989). Many gels and colloids exhibit thixotropic behaviour where they are solid-like at rest and when agitated, become fluid.

3.3.1 Steady simple shear flow

Under the application of steady simple shear flow the corresponding stress distribution for non-Newtonian fluids is

$$\begin{aligned} \tau &= \eta(\dot{\gamma})\dot{\gamma} \\ N_1(\dot{\gamma}) &= \tau_{xx} - \tau_{yy} = \dot{\gamma}^2 \psi_1 \\ N_2(\dot{\gamma}) &= \tau_{xx} - \tau_{zz} = \dot{\gamma}^2 \psi_2 \end{aligned} \qquad [3.5]$$

with $N_1(\dot{\gamma})$ being the first normal-stress difference, $N_2(\dot{\gamma})$, the second normal-stress difference while ψ_1 and ψ_2 are the normal-stress coefficients.

3.3.2 Oscillatory-shear flow

One popular deformation mode to study the linear viscoelastic behaviour is through oscillatory-shear flow. Under oscillatory-shear flow,

$$\begin{aligned} u &= \alpha\omega y \cos\omega t \\ v &= 0 \\ w &= 0 \end{aligned} \qquad [3.6]$$

with α and ω being the small amplitude and angular frequency, respectively. The broadest view of fluid rheology can be obtained using oscillatory flow at a selected frequency because both elastic and viscous properties are revealed in the form of the storage modulus, G' and the loss modulus, G'' as

$$\begin{aligned} G' &= \frac{\eta\lambda\omega^2}{1+(\lambda\omega)^2} \\ G'' &= \frac{\eta\omega}{1+(\lambda\omega)^2} \end{aligned} \qquad [3.7]$$

where λ is a time constant known as the relaxation time.

For a Newtonian fluid, the storage modulus, G', is equal to zero while the loss modulus, G'' is a linear function of the fluid shear viscosity and the angular frequency. In the linear viscoelastic region, these viscoelastic functions, G' and G'' are independent of the magnitude of stresses and strains applied and are only functions of the frequency. However, the linear viscoelastic region only exists in the limit of small stress and strain rates. Beyond a critical point, the viscoelastic response becomes nonlinear and complex, where G' and G'' are functions of the magnitude of stresses, strains and also the frequency (Barnes, 2000).

The corresponding stress in an oscillatory flow is

$$\tau = \alpha\omega\left[\eta' \cos\omega t + \tfrac{G'}{\omega}\sin\omega t\right] \qquad [3.8]$$

where η' is the dynamic viscosity determined by the equation

$$\eta' = \frac{G''}{\omega}. \qquad [3.9]$$

The dynamic viscosity measured at the zero frequency limit should approach that of the shear viscosity measured in steady shear at low shear rate (Barnes et. al., 1989), i.e.

$$\eta'(\omega)\big|_{\omega\to 0} \approx \eta(\dot{\gamma})\big|_{\dot{\gamma}\to 0}. \qquad [3.10]$$

The three normal stress components, τ_{xx}, τ_{yy} and τ_{zz} are equal to the ambient pressure in the linear viscoelastic region, hence, the normal-stress differences, N_1 and N_2, are zero because the flow is slow enough for the square of the shear rate term $\dot{\gamma}$ to be negligible (Barnes et. al., 1989).

3.3.3 Extensional flow

The first realization of the concept of extensional flow was by Trouton where he introduced the term "coefficient of viscous traction" (Trouton, 1906) which bears the same meaning as the term extensional viscosity, widely used nowadays. There are several modes of extensional deformations; uniaxial extension, biaxial extension and planar extension. For the purpose of rheology characterization, only the uniaxial extension mode will be utilized and discussed here. Further explanations on extensional flow can be found in Barnes et. al. (1989) and Petrie (2006).

For uniaxial extensional flow, upon reaching steady state, the velocity field should obey

$$\begin{aligned} u &= \dot{\varepsilon}x, \\ v &= -\dot{\varepsilon}y/2 \\ w &= -\dot{\varepsilon}z/2 \end{aligned} \qquad [3.11]$$

where $\dot{\varepsilon}$ is the constant strain rate. The corresponding extensional stress distribution for a non-Newtonian elastic liquid is

$$\tau_{xx} - \tau_{yy} = \tau_{xx} - \tau_{zz} = \eta_E(\dot{\varepsilon})\dot{\varepsilon} \qquad [3.12]$$

where η_E is the extensional viscosity, also known as the elongational viscosity.

A fluid for which the extensional viscosity increases with increasing strain rate is said to be tension thickening while the fluid is said to be tension thinning if the extensional viscosity decreases with increasing strain rate. The behaviour of the fluid under extension may be qualitatively different from that under shear where any two polymeric fluids having essentially the same behaviour in shear flow can show a different response in extensional flow (Barnes et. al., 1989). The extensional behaviour for dilute polymer solutions and polymer melts can also be distinguished based on the behaviour of extensional viscosity where in dilute solutions it rises abruptly with strain rate, while for polymer melts it is a weak function of strain rate. In the semidilute region, where the formation of entanglements exists, the solution properties are very similar to those of melts (Barnes et. al., 1989).

The Trouton ratio, as introduced by Trouton in 1906 is given as

$$Tr = \frac{\eta_E(\dot{\varepsilon})}{\eta(\dot{\gamma})}. \qquad [3.13]$$

The ratio, $\eta_E/\eta = 3$, is valid for Newtonian fluid and for viscoelastic fluids under very small strain rates in uniaxial extension. For biaxial extension, the Trouton ratio is $\eta_{EB}/\eta = 6$ and is also valid for Newtonian fluid and viscoelastic fluid under very small strain rates (Petrie, 2006).

The extensional viscosity, η_E and the biaxial extensional viscosity, η_{EB} are not in general connected except that both show Newtonian behaviour in the limiting case of small strain rate. For viscoelastic fluids, rheologists have also used the concept of a Trouton ratio with a slight modification to the equation (Jones and Walters, 1987) to quantify extension effects

$$Tr = \frac{\eta_E\left(\sqrt{3}\dot{\varepsilon}\right)}{\eta(\dot{\gamma})}. \qquad [3.14]$$

3.4 Working fluids

3.4.1 Newtonian fluids

Newtonian fluids were utilized in this research work as a means of validation of the experimental arrangements employed and to provide a control to which the non-Newtonian fluids' data can be compared. Liverpool tap water was used to obtain the data in the fully-turbulent regime at high Reynolds numbers while a vegetable based glycerine-water solution, supplied by Hays Chemical Ltd was used in this study for the laminar, transition and lower Reynolds number turbulent regimes. Glycerine is a viscous Newtonian liquid widely used in the pharmaceutical and food industries as a thickening agent or as a solvent. The glycerine-water mixture (40% w/w) utilized in this study has a density of 1070 kg/m^3 and a shear viscosity, measured at 20°C, of 0.00386 Pa.s.

3.4.2 Polymers

Many polymer solutions exhibit non-Newtonian behaviour. A polymer is a large molecule (macromolecule) composed of many repeating structural units where a structural unit is a building block of a polymer chain. More detailed explanations of polymer properties and dynamics can be found in Bird et. al. (1977). The diameter of a polymer molecule varies with the type of polymer but is always less than its length. Helical polymer molecules are polymers with the largest diameters and hence, tend to be very rigid. The flexibility of the polymer chain is also measured by its persistence length[*] (Lapasin and Pricl, 1995). Polymers whose diameter and persistence length are both a few tenths of nanometres assume the random coil conformation and tend to be flexible. Polymers with diameters of several nanometres and persistence length of greater than 100 nanometres assume “rod-like” conformations. These polymers tend to be rigid and have linear polymer chains (Tracy and Pecora, 1992; Sear, 1997). **Figure 3.3** illustrates the difference between a flexible polymer and a rigid polymer configuration. The rigid-rod conformation has been found to be more responsive to shear than the random coil conformation found in flexible polymers (Kim and Yoo, 2006) since flexible molecules show less anisotropy and shear orientation than rigid helices (Lapasin and Pricl, 1995). Many biological macromolecules, including polysaccharides[†], are rigid or semi-rigid rod-like molecules (Tracy and Pecora, 1992) while all synthetic polymers are flexible polymers (Bird et. al., 1977).

3.4.2 (a) Scleroglucan (SG)

Scleroglucan is a non-ionic polysaccharide produced by the fungi of genus Sclerotium (Bais et. al., 2005). The primary structure consists of a linear chain with its rheological properties known to be independent of culture conditions (Moresi et. al. 2001). About 25% of its mass is located in the side chains giving the polymer high structural rigidity (Stokke et. al. 1992). Its secondary structure has been well established to adopt the triple helix conformation in neutral or slightly alkaline environment and hence it can be assumed to behave like a rigid chain (Farina et. al. 2001).

---

[*] Persistence length is normally used to quantify the stiffness of polymers where shorter persistence length means that the polymer molecule is flexible. A detailed explanation of persistence length is provided by Lapasin and Pricl (1995).

[†] Polysaccharides are polymeric carbohydrate structures or biopolymers.

Studies have shown that since scleroglucan is not a polyelectrolyte, it is stable over a wide range of pH from highly acidic to moderately alkaline (Farina et. al., 2001). However at pH above 13 a significant decrease of viscosity is observed. The thermal history of the solution has also been established to have only a slight effect on the rheological properties up to 100°C (Stokke et. al., 1992; Farina et. al., 2001).

Scleroglucan is known to exhibit shear-thinning behaviour at low concentrations and gel-like behaviour at high concentrations. The critical concentration for the sol-gel transition; i.e. transition from the liquid to solid-like material or gel, is observed to be between 0.25% to 0.4% by weight (Grassi et. al., 1996; Farina et. al., 2001; Moresi et. al., 2001; Bais et. al., 2005). Scleroglucan systems belonging to the weak gel domain show appreciable time-dependent properties, and a delay time of approximately 4-5 minutes is sufficient to substantially remove (~ 95%) shear history and reconfigures the solution to its unperturbed state (Grassi et. al., 1996). The persistence length of scleroglucan has been reported to be approximately 200 nm (Sasaki, 1991; Paschkewitz et. al., 2005) making it one of the most rigid biopolymers. This non-toxic polysaccharide is used as a biomedical drug to treat infections. It is known to have antitumoral effects and has been shown to strengthen the immune system (Farina et. al., 2001). This biopolymer in native form is mainly used in the oil industry, as additives in drilling fluids and spacer fluids[‡], and also in other applications such as in agriculture industries (in sprays) and in the food and pharmaceutical industries. Refined scleroglucan is mainly used for cosmetics (Stokke et. al., 1992; Grassi et. al., 1996; Farina et. al., 2001; Moresi et. al., 2001; Bais et. al., 2005; Palleschi et. al., 2005).

[‡] Spacer fluids are normally used to physically separate one special purpose fluid from another. For example, it is used to separate an oil-based drilling fluid from a water-based drilling fluid during the process of changing drilling fluids (Schlumberger, 2009).

3.4.2 (b) **Xanthan gum (XG)**

Xanthan gum is a natural high-molecular weight polysaccharide produced by a fermentation process using bacterium Xanthomonas campestris found in cabbage plants in a medium containing a carbohydrate source (glucose), a nitrogen source and nutrient salts (Katzbauer, 1998). The rheological properties of xanthan gum vary with fermentation and processing conditions, which subsequently lead to different degrees of acetyl and pyruvic acetal substitutions (Carrington et. al., 1996). A high degree of acetylation and pyruvate contents has been found to result in higher intermolecular association and hence increases the viscosity of the xanthan gum solutions (Casas et. al., 2000).

The primary structure of xanthan gum is based on a linear chain and the secondary structure is a double helix whose stability varies depending on salt concentration and temperature (Rochefort and Middleman, 1987). Xanthan has about 60% of its mass located in the side chains (Stokke et. al., 1992). The persistence length, given by the helical structure of xanthan gum, has been reported to be approximately 255 nm with flexible side groups (Hoyt, 1985; Sasaki, 1991). It is soluble in hot and cold water, stable over a broad range of pH and is reported to be fully biodegradable within two days (Katzbauer, 1998). Aggregations of xanthan gum chains have been found even at low concentrations, at rest or at low shear, which are stabilized by hydrogen bonds (Katzbauer, 1998). Upon shearing, the extent of molecule aggregation in xanthan gum is reduced resulting in a lower viscosity, i.e. the solutions exhibit shear thinning. The thermal history of xanthan has been shown to affect the rheological behaviour since the process removes xanthan aggregation and hence promotes a true molecular dispersion (Stokke et. al., 1992; Rodd et. al., 2000).

Xanthan gum has been observed to suffer from the effects of preshearing where intermolecular entanglement is disturbed. The effect of preshearing increases with the magnitude of pre-shear and a period of up to a day can be necessary if the sample is left to recover (Walters et. al., 1990). The effects of preshearing are reduced, however, as the concentration is increased (Kim and Yoo, 2006). The time scale required for the re-entanglement process, the characteristic time of recovery under rest conditions, differ significantly from the relaxation time which characterizes the stress decay upon cessation of steady shearing flow.

Xanthan gum is mostly used in the food industry as a thickener. It is most often found in salad dressings and sauces and in frozen food and beverages. Apart from that, it is also utilized in the oil industry to thicken drilling fluids at minimal cost. Due to its skin hydrating properties, xanthan gum can also be found in many cosmetics (Stokke et. al., 1992; Katzbauer, 1998; Zirnsak et. al., 1999; Casas et. al., 2000).

3.4.2 (c) Carbopol 980

Carbopol is a polyelectrolyte belonging to a class of resins known as carbomers. It is mostly used as thickening and gelling agents for commercial products in the cosmetic and pharmaceutical industries. This microgel comprises of a collection of highly cross-linked synthetic polymer, polyacrylic-based polymer cross-linked with a polyalkenyl polyether (Roberts and Barnes, 2001; Curran et. al., 2002). It is highly soluble in water and other polar solvents[§]. When hydrated, carbopol solutions have been found to possess a yield stress detected at rest and at low shear, while at higher shear the solutions exhibit shear-thinning behaviour. The rheological behaviour of carbopol solutions are usually best described using the Herschel-Bulkley model (Curran et. al., 2002).

[§] A polar solvent is a compound that is composed of polar molecules, where there is some separation of charge in the chemical bond, which can dissolve ionic compounds or covalent compounds that ionize. Water and liquid ammonia are common examples of polar solvents.

However, the yield stress can usually only be produced when the pH balance of the solution is "neutralized" between 5.0 and 9.0 according to the supplier (Noveon, 2008). Depending on the concentration, unneutralized carbopol solutions have an approximate pH range between 2.5 to 3.5 with low solution viscosity. For the 0.065% and 0.1% carbopol solutions used in this study, pH balance of unneutralized solutions between 3 and 3.5 were observed. As carbopol is a polyelectrolyte addition of salt, such as sodium chloride, to a carbopol solution can reduce the solution viscosity. Viscoelastic effects for carbopol solution, i.e. the elasticity and extensional viscosity, has been reported to be low despite it being a yield stress fluid (Roberts and Barnes, 2001; Curran et. al., 2002) with the solutions found to be thixotropic (Moller et. al., 2006).

3.5 Methods of measurements

3.5.1 Working fluids

Samples of xanthan gum were obtained from the Kelco Co. (Ketrol TF) with the molecular weight of an individual xanthan gum chain reported by the supplier to be in excess of 10^6 g/mol. Samples of scleroglucan (Actigum™ CS) were obtained in powder form from Cargill Incorporated. The scleroglucan sample from Cargill has been reported by the supplier to have an average molecular weight of 5.4×10^5 g/mol and to have a semi-gelled appearance below 10°C which disappears on shaking or heating.

The Carbopol 980 utilized in this study was supplied by Noveon, France in white flocculated powder form with a molecular weight of 4.00×10^6 g/mol. It is a non-toxic version of Carbopol 940 (Roberts and Barnes, 2001; Zhu et. al., 2005) and has been reported to show an apparent yield stress (Roberts and Barnes, 2001) when neutralized. The carbopol solutions prepared in this research work is neutralized using laboratory grade 2N sodium hydroxide supplied by BDH Ltd, UK in the annular rig (the rig will be described in detail in **Chapter 4**) and circulated at

30% of the maximum pump speed for 30 minutes prior to any rheology measurements in an attempt to provide a uniform shear history. Due to the thixotropic behaviour, samples for the rheology measurements were taken straight from the annular rig immediately prior to measurements to better reflect the viscosity behaviour during the LDA measurements.

Apart from carbopol, aqueous solutions of the polymers for the rheology measurements were prepared by addition of the polymer powder to about 500 ml of non-filtered tap water. Mixing of the solutions was achieved using an overhead stirrer in a beaker, which was sealed to avoid water loss by evaporation. The overhead stirrer was operated at a minimum rotational speed (~250 rpm) until the polymer solutions appeared to be visibly homogeneous. All xanthan gum solutions were left to hydrate for at least 8 hours before rheological tests were conducted. The gelation property of the scleroglucan solutions were monitored via the shear viscosity profile as shown in **Figure 3.4** for a 0.2% scleroglucan solution. The variation between the shear viscosities were found to be most significant at low shear rates and to reduce as the shear rate increased. Similar gelation behaviour was also observed for more dilute solutions. The gelation period, however, is reduced as the solution concentration is further increased. On average, a period of 48 hours is required for the solutions to gel, hence, all scleroglucan solutions were left standing for at least 48 hours prior to the rheology measurements. No biocide was added to the xanthan gum solutions. However, since the scleroglucan solutions were left for a longer duration prior to testing, 100 ppm of formaldehyde was added to the solutions to inhibit bacterial growth. All solutions were disposed of once the solutions became cloudy (an obvious sign of bacterial growth). Tests conducted on a 'cloudy' xanthan gum solution, six weeks after it was initially mixed, showed a significant decrease in the viscosity. Therefore, all tests to determine the rheological behaviour of the xanthan gum solutions were conducted within one week of preparation. The scleroglucan solutions (with formaldehyde added) were also monitored for signs of degradation in the form of viscosity decrease and were disposed of once bacterial degradation was detected.

The effects of preshearing when loading into the rheometer were monitored by comparing the rheological results tested immediately after the sample was loaded on the plate of the rheometer and the results obtained by leaving the sample on the plate for 30 minutes prior to the start of the test. Xanthan gum was found to suffer from the effect of preshearing while no significant difference was observed for scleroglucan and carbopol. Hence, all the xanthan gum samples placed were allowed to rest at room temperature for 30 minutes prior to the start of the rheological tests while all scleroglucan and carbopol samples were tested immediately after loading.

The samples tested using the Capillary Break-up Extensional Rheometer, or CaBER, showed no significant differences if the solution was left for 30 minutes prior to testing, or tested immediately after loading due to the nature of the testing in CaBER where a large step strain was applied. Similarly, all solutions were tested using CaBER within one week of preparation.

3.5.2 Rheology measurements

Steady-shear measurements and small-amplitude oscillatory-shear measurements (SAOS) were conducted over a wide range of concentrations for scleroglucan and xanthan gum (0.005%-0.75% w/w for steady shear and 0.025%-0.75% w/w for SAOS). Similar to SAOS, extensional property measurements were only possible for higher concentration of both polymer solutions ($c \geq 0.1\%$ w/w) as it was discovered that dilute solutions broke-up too rapidly during the stretching process. Complete rheological characterization of carbopol solutions was not conducted due to the difficulties such as thixotropy and high degradation rate as outlined by

Presti (2000). Only steady shear measurements were performed on 0.065% and 0.1% carbopol solutions which correspond to the concentrations for the detailed fluid-dynamic measurements.

3.5.2 (a) Shear rheology measurements

A TA Instrument Rheolyst AR 1000N controlled-stress rheometer, shown in **Figure 3.5**, was used for all the shear measurements. Measurements were carried out using the double concentric cylinder for low concentration solutions, while the 4-cm 2° cone-and-plate geometry was used for the higher concentration solutions to achieve a greater shear stress range in order to capture accurately the second Newtonian plateau in the flow curve. Due to wall slip artefacts (Roberts and Barnes, 2001) which exist for thickeners in aqueous phase such as carbopol, a 4-cm stainless steel roughened parallel plate geometry was also used for the rheology measurements of carbopol solutions. **Figure 3.6** shows schematics of the geometries utilized. The first normal-stress difference measured using the cone and plate and parallel plate geometries was found to be below the sensitivity of the equipment, at least for the range of the solution concentrations measured, which indicates that the fluids studied are very weakly elastic. To minimize evaporation effects, a solvent trap was utilized throughout the measurements.

Steady-shear measurements were conducted over a range of torque from as low as 0.5 μ N.m, which is 5 times the achievable minimum torque for the equipment, up to a torque of 100 μ N.m. Higher torques and correspondingly higher stress levels could not be achieved due to instrument overspeed. Moreover, at higher shear stress levels, for dilute solutions especially, secondary flows arose which absorbed extra energy, increased the measurement torque and hence the shear viscosity, resulting in apparent shear thickening (Barnes et. al., 1989; Barnes, 2000). Such data are not included in the shear viscosity plots. Measurements of the shear viscosity were taken every 15 seconds by the controlled-stress rheometer and the steady state value is considered reached when three consecutive measurements were found to be within 2%.

For the steady-shear measurements, the reproducibility of shear viscosity data was better than 2% at least for $\dot{\gamma} > 1\ s^{-1}$. However, in the oscillatory tests, repeatability was relatively more difficult to achieve for lower concentration solutions. Moreover, as will be shown later, the results for G' for the lower concentrations do not lie within the 'believable' region based on the 'limit' data for the equipment. The limit was determined from the oscillation test conducted on water, as for a Newtonian liquid like water, the storage modulus, G' must be equal to zero. However, due to instrument and geometry inertia, a nonzero storage modulus for water was measured which then represent a limit of the instrument. Hence, any data obtained close to the 'limit' data must be viewed with caution.

For all the measurements conducted using the TA Instrument Rheolyst AR 1000N controlled-stress rheometer, the temperature was maintained at 20°C using a Techne TE10A thermostatic bath and temperature control system, which is capable of maintaining the temperature to within 0.1°C.

3.5.2 (b) Extensional rheology measurements

The extensional properties of the solutions were investigated using the Capillary Break-up Extensional Rheometer or CaBER, shown in **Figure 3.7(a)**, supplied by Thermo Electron GmbH. A small sample of about 25 mm^3 was loaded, using a syringe, between the 4-mm plates of the instrument shown schematically in **Figure 3.7(b)**, making sure that the sample was totally homogeneous with no bubbles. The gap between the plates was entirely filled with the sample and the sides of the plates were completely dry to avoid any disagreement with the theory used for the technique where no flow was assumed over the edges of the plates. A uniaxial step strain was then applied where the plates were rapidly pulled apart, resulting in a formation of an elongated filament. McKinley et. al. (2001) discovered that exponential stretching would not lead to a homogeneous fluid elongation due to the no-slip condition, which will consequently lead to reverse squeeze flow**. Hence, a linear stretching deformation was employed as the mode of the step strain. The "stretch" time was set to 50 ms and the temperature was maintained at 20°C throughout the process.

The CaBER utilized a laser micrometer, with a resolution of around 10 μm, to monitor the diameter of the thinning elongated filament, which evolved under the action of viscous, inertia, gravitational and elastocapillary forces. High-speed digital imaging of the process was captured by a Dantec Dynamics Nano Sense MKIII high-speed camera with a Nikon 60mm f/2.8 lens at 2000 frames per second.

Rodd et. al. (2005) made several recommendations in relation to the initial aspect ratio, $\Lambda_i (\equiv h_i / b$ where h and b are the gap distance and diameter of the plate respectively). To minimize the effects of reverse squeeze flow when the plates are first separated at low initial aspect ratio, and sagging at high initial aspect ratio, the initial aspect ratio should be

$$0.5 \leq \Lambda_i \leq 1 \quad . \qquad [3.15]$$

In order to keep the initial configuration close to cylindrical and to maintain maximum stable size, the initial gap between the 4-mm plates, h_i, needs to be smaller than or equal to the capillary length, $l_{cap} \left(\equiv \sqrt{\frac{\sigma}{\rho g}}\right)$.

** Squeeze flow occurs when a fluid is compressed between two parallel plates and the fluid is then squeezed out radially. In the action of reverse squeeze flow, surface tension also plays an important role.

Based on these recommendations, an initial aspect ratio of 0.5 was chosen. The capillary length, l_{cap} was calculated based on the properties of the solvent which, in this study, was water and was found to be 2.74 mm. With the initial aspect ratio set at 0.5, h_i was maintained at 2 mm, which then guaranteed that the loaded sample was stable.

In this study, the final aspect ratio was varied with solution concentration such that filament thinning was still observed between the 4-mm plates. For example, a final aspect ratio of 1.4 was chosen for 0.1% SG in order to observe filament thinning over a timeframe of about 10ms.

Within the filament-thinning region, the decay of the filament diameter data was fitted to an equation of the form

$$D_{CaBER} = D_{o,CaBER} e^{-t/3\lambda} \tag{3.16}$$

as recommended by Stelter and Brenn (2002) for viscoelastic fluids, where $D_{o,CaBER}$ is the midpoint diameter following cessation of the stretch deformation and λ is a characteristic relaxation time which represents the characteristic time scale for viscoelastic stress growth in uniaxial elongational flow (Rodd et. al., 2005).

As the molecular chain of the solution reached the maximum elongation, or in rigid rod molecular configuration complete orientation along the direction of the flow, the filament decayed rapidly in a linear manner towards break-up, within which inertial, viscous and gravitational effects were important (Oliveira et. al. 2006). A linear fitting characteristic of "Newtonian-like" thinning

$$D_{CaBER} = mt + D_{o,CaBER} \tag{3.17}$$

was also fitted to the data where the slope, $m = dD_{CaBER} / dt$.

The empirical relationship suggested by Oliveira et. al. (2006) was also employed to fit the data where

$$D_{CaBER} = \left(D_1 + \frac{k_1}{t + t_1} \right) \exp\left(-\tfrac{t}{3\lambda}\right) - V_2 (t - t_2) . \qquad [3.18]$$

The equation represents the rapid initial necking immediately after the stretching deformation as it approaches a balance between the surface tension and elasticity $(t < t_1)$, the exponential thinning region $(D_{CaBER} \leq D_1 + k_1 / t_1)$ and the region of finite extensibility and linear decay represented by the linear term in the equation with V_2 being the capillary velocity.

The extensional viscosity was calculated based on the filament thinning diameter profile,

$$\eta_E = -\frac{\sigma}{\frac{dD_{CaBER}}{dt}} . \qquad [3.19]$$

The Trouton ratio was obtained using Equation [3.14] discussed in section 3.3.3 with the strain rate calculated from

$$\dot{\varepsilon} = -\frac{4}{D_{o,CaBER}} \frac{dD_{CaBER}}{dt} . \qquad [3.20]$$

3.6 Results and discussion

3.6.1 Steady-shear measurements

The shear viscosity variation against both shear rate and shear stress is shown in **Figures 3.8(a)-(b)** and **3.9** for scleroglucan and **Figures 3.10(a)-(b)** and **3.11** for xanthan gum, respectively. As can be seen from the figures the shear viscosity, η shows an increased dependence on shear rate, $\dot{\gamma}$ and shear stress, τ with increasing concentration i.e. increased shear-thinning. Based on the viscosity versus shear stress data, it can be seen that the stress at which the fluid started to experience shear-thinning behaviour, i.e. the onset of the non-Newtonian behaviour, was also delayed to higher stresses as the solution became more concentrated. These observations indicate higher molecular association as the solution concentration is increased hence requiring greater stress to break the molecular association or entanglement in the first Newtonian plateau to shift to the shear-thinning regime. Bewersdorff and Singh (1988) reported that in the first Newtonian plateau the non-aligned molecules of rigid-rod polymers form associations and the viscosity in this plateau is due to the bonds of these associations. In the second Newtonian plateau, all the associations are broken down by the high shear stresses and the viscosity is due to individual molecules aligned in the direction of the flow.

The Carreau-Yasuda model (Yasuda et. al., 1981) was used to fit the data shown in **Figure 3.8(a)-(b), 3.9, 3.10(a)-(b)** and **3.11**

$$\frac{\eta-\eta_o}{\eta_o-\eta_\infty}=\frac{1}{\left[1+\left(\lambda_{CY}\dot{\gamma}\right)^a\right]^{\frac{n}{a}}} \qquad [3.21]$$

where η_o and η_∞ are the viscosities in the first and second Newtonian plateaus while λ_{CY}, n and a are the constant which represents the onset of shear thinning, the power-law exponent and a parameter introduced by Yasuda et. al., respectively. **Tables 3.1** and **3.2** list the Carreau-Yasuda parameters for the fits. These model parameters were obtained using the methodology of Escudier et. al. (2001), essentially by minimizing the error

$$\sum_N\left(1-\frac{\eta_{data}}{\eta_{model}}\right)^2 . \qquad [3.22]$$

This type of error determination was preferable to a more traditional linear least square fit, i.e. $\sum_{N}(\eta_{data} - \eta_{model})^2$, because it ensures that the high and low shear rate data have the same level of influence on the determination of the fit.

From **Figure 3.12**, a plot of zero-shear viscosity versus concentration, for scleroglucan, the slope within the dilute region was found to be about 0.7 and the slope within the semidilute region was about 4.5. For xanthan gum, the slope within the range of concentration studied was found to be about 1.4 for the dilute region and 5.2 for the semidilute region. These values agree well with values available in the literature (Milas et. al., 1990; Lapasin and Pricl, 1995; Rodd et. al., 2000). The location of the critical overlap concentration, *c**, thought to be the point at which individual polymer molecules began to interact with each other, was found to be about 0.054% and 0.067% for scleroglucan and xanthan gum, respectively. The data for polyacrylamide, a flexible polymer, is also shown for comparison with *c** of about 0.028% (Keegan, 2009). In the dilute regime, the individual molecules are well separated from one another and are free to move independently. When shear is applied, the flow behaviour of each molecule is not affected by the presence of any other molecules and the rheological property of the solution is considered to be the sum of the individual contributions of the molecules. Above a critical concentration, *c**, the independent rotational and translational motions are restricted due to entanglement formation where the molecules begin to physically interact.

Figure 3.13 shows the shear viscosity data against shear stress for 0.065% and 0.1% carbopol solutions measured using the 4 cm 2° cone and plate and also using the 4-cm roughened plate geometries with the solid lines included to guide the reader's eye. The viscosity data shows clearly that slip problems, which are most severe at low shear stresses, exist on the smooth surface of the cone-and-plate geometry which resulted in a lower viscosity being measured. For the data measured using the roughened plate where the slip effect is minimized, a very high first Newtonian plateau is observed at very low shear stresses. Even though a real yield stress may not exist for these solutions, the abrupt viscosity transition from very high values to low values within a narrow range of shear stresses is an indication that the critical shear stress does exist beyond which the fluid exhibits more 'liquid-like' behaviour.

The viscosity data are fitted using the Herschel-Bulkley model

$$\tau = \tau_y + K\dot{\gamma}^n \tag{3.23}$$

where τ_y, K and n are the apparent yield stress, Herschel-Bulkley consistency index and the power law exponent, respectively. These fitting parameters were obtained in a similar manner to that of the Carreau-Yasuda model by using Equation [3.21]. **Table 3.3** lists the Herschel-Bulkley parameters for both solutions.

A complete rheological characterization by Roberts and Barnes (2001) of Carbopol 980 showed that the zero-shear viscosity and also the critical shear stress, i.e. the stress at which the viscosity/shear stress slope is a maximum (Roberts and Barnes, 2001), increase dramatically ($\eta_o \propto c^{16}$ and $\tau_{crit} \propto c^{16}$) up to a concentration of 0.1%. Above this concentration, the rate of increase is reduced with a power law slope close to unity ($\eta_o \propto c$ and $\tau_{crit} \propto c$).

3.6.2 Oscillatory-shear measurements

3.6.2 (a) Stress sweep

Figures 3.14 and **3.15** show data obtained using a stress sweep procedure to determine the linear viscoelastic region. As seen in **Figure 3.14** for lower concentrations scleroglucan (0.075%-0.1%), the loss modulus (*G''*) was greater than the storage modulus (*G'*) and as the concentration was further increased, the storage modulus was greater, indicating that the solutions were becoming more structured with greater viscoelastic properties at these concentrations. The difference between both moduli initially reduced but after the crossover at about 0.2% it increases with concentration. Similar observations can be deduced for xanthan gum in **Figure 3.15** where a crossover occurs between 0.2% and 0.25%.

3.6.2 (b) Frequency sweep

Figure 3.16 shows the storage (*G'*) and loss (*G''*) moduli plotted against frequency for higher solution concentrations of scleroglucan ($c \geq 0.075\%$ w/w) measured in small amplitude oscillatory shear (SAOS). Data for lower concentrations are not included as the *G'* data fell within 50% of the instrument/geometry limit data. The limit data was based on an oscillatory test conducted on water: non-zero values of *G'* obtained in such a test are a consequence of inertia and represent a limit of the instrument. As shown, the loss modulus, *G''* is greater than the elastic modulus *G'* prior to the crossover for the lower concentration solutions. The crossover frequency decreases with concentration indicating viscous dominance at low concentrations compared to that at high concentrations. For the 0.5% solution, the elastic component plays a dominant role, at least for the frequency range tested. The dependence of both moduli on frequency reducing with concentration is indicative of structure build-up as suggested by Rochefort and Middleman (1987) and Lee (2001). At the highest concentration (0.5%) the solution is essentially gel-like.

Based on the data plotted in **Figure 3.17**, for low concentrations xanthan gum (0.025% to 0.1%), *G''* is always greater than *G'* within the range of frequency tested. For more concentrated solutions *G''* is greater than *G'* until the crossover frequency, which decreased as the concentration increased. The overall frequency dependence of the storage and loss moduli, however, decreased with increased concentration indicating structure build-up in a similar manner to scleroglucan. The difference between both moduli becomes larger with concentration over an extended frequency range underlining the elastic dominance of the more concentrated solutions.

For all xanthan gum concentrations, as also found by Walters et. al. (1990), there was a discrepancy between the results of dynamic viscosity obtained in oscillatory shear and the shear viscosity obtained from steady shear measurements. Though not so severe, a similar trend was also found for scleroglucan solutions. Lee (2001) argued that if networking or entanglement is present in the system, the dynamic viscosity will be higher than the shear viscosity since the entanglement or network formed is broken down under steady shear.

Due to the sensitive nature of xanthan gum solutions, different steps were taken to monitor the effect of preshearing for different xanthan gum concentrations. Preshearing was applied at 1 Pa for 60 s to both 0.2% and the 0.25% xanthan gum solutions and the storage and loss moduli were monitored immediately after preshearing. The dynamic viscosities, as given in Equation [3.9], were calculated for the solutions. As can be seen from inspection of **Figures 3.18** and **3.19**, the effect of preshearing at 1 Pa for 60 s reduced the dynamic viscosity to the steady-shear viscosity level for 0.2% xanthan gum. However, a longer or more intense preshearing would be necessary to observe the same effect at the higher concentration of 0.25% xanthan gum.

Figure 3.20 shows the steady-shear and dynamic viscosity versus shear rate and frequency for 0.25% xanthan gum. Samples were left for 30 minutes and overnight prior to testing. The data shows that even after leaving the sample to rest at room temperature overnight, full recovery was not observed since there was still a discrepancy between the steady-shear viscosity for samples left overnight and the dynamic viscosity obtained in the oscillatory-shear measurement. The results indicate that a longer time period is needed for the molecular entanglement to be fully recovered.

The storage and loss moduli plotted against frequency for 0.2% xanthan gum for samples left for both 30 minutes and overnight (approximately 12 hours) at room temperature is shown in **Figure 3.21**. Run 1 and Run 2 represented samples which were left for only 30 minutes while Run 3 was performed for sample which was left overnight. As can be seen, the samples which were left for 30 minutes agreed well with each other, while the sample left overnight showed an increase in G' and G'' indicating slight recovery.

3.6.3 Extensional viscosity measurements

Figures 3.22 to **3.30** show the measured filament diameter data from the CaBER tests, semi-logarithmically plotted, and the high-speed camera images captured for scleroglucan and xanthan gum solutions at various concentrations. Filament thinning was observed immediately after the plates were stretched for most solutions. However, immediately after the stretching process, rapid initial necking of the filament for the first 10 ms was seen for higher concentration xanthan gum solutions (0.5% and 0.75%). Oliveira et. al. (2006) suggested that within the necking process inertial and gravitational effects play important roles. All the filament thinning data were fitted with Equation [3.16] within the region where the filaments are thought to decay exponentially. A linear fit (Equation [3.17]) and an "Oliveira fit" (Equation [3.18]) were included as well throughout the thinning process up until the break-up time, T_B. In all the figures, the filament thinning data are better described using Equation [3.17] where the filaments decay linearly as opposed to exhibiting exponential decay, commonly observed in highly viscoelastic fluids (McKinley et. al., 2001; Rodd et. al., 2005). As can be seen from these figures, the Oliveira et. al. fit essentially resembles the linear fit with the influence of the exponential term in Equation [3.18] found to be small.

Figures 3.31 and **3.32** show the filament diameter data of 0.1% scleroglucan and 0.2% xanthan gum shown in **Figures 3.22** and **3.26** plotted on linear scales. Approximate Newtonian linear thinning was observed over the entire time to breakup with slopes of about 70 mm/s for scleroglucan and 36 mm/s for xanthan gum. Linear fitting the last ten data points prior to breakup, where the sample most closely resembles the uniform cylindrical shape used in deriving Equations [3.16] and [3.17], gave a slope within 10% of the global fit suggesting that the thinning process is governed mainly by the inertial, viscous and gravitational effects rather than a balance between the surface tension and elasticity as suggested by Oliveira et. al. (2006) for flexible polymers. Similar linear thinning behaviour was also observed for higher concentrations. The corresponding relaxation time for the solutions could not be calculated since the filaments decayed linearly like a Newtonian fluid. Composite plots of the filament thinning data for various concentrations of scleroglucan and xanthan gum are shown in **Figure 3.33** and **3.34**, respectively. The filament diameter on the *y*-axis is normalized with the initial diameter while the time is normalized with the filament break-up time on the *x*-axis. Almost complete collapse of the normalized data of scleroglucan is observed showing a linear thinning trend for all the concentrations studied. Although the agreement between the normalized filament diameter data is slightly worse compared with that observed for scleroglucan, all the data for xanthan gum also exhibit a linear thinning trend.

The steady uniaxial extensional viscosity which quantifies the resistance to stretching, η_E, plotted against scleroglucan and xanthan gum concentration in **Figure 3.35** shows almost the same degree of resistance to stretching for both polymers and power-law dependency (linear slope on a log-log plot of 1.2) on concentration. The results obtained are consistent with the fact that as the solution concentration is increased, there are more molecules per unit area within the fluid column. The rotational motion of the molecules results in molecular contact, which subsequently leads to stronger molecular interaction and greater extensional viscosity. However, the extensional viscosities for these rigid and semi-rigid polymers, scleroglucan and xanthan gum, are still low compared to flexible polymers, polyacrylamide for instance, and the dynamics of the filament were nearly indistinguishable from that of Newtonian fluid as seen in the Newtonian linear thinning behaviour. Keegan (2009) studied the filament thinning behaviour of several concentrations of polyacrylamide using CaBER and observed exponential filament diameter thinning with the steady terminal extensional viscosity (Stelter and Brenn, 2002) to be about 70 Pa.s for 0.03%PAA and 340 Pa.s for 0.3%PAA. The Trouton ratio plotted against concentration in **Figure 3.36** confirms the non-Newtonian behaviour of both scleroglucan and xanthan gum as the magnitude for all the concentrations studied was significantly greater than that of a Newtonian fluid, i.e. $Tr >> 3$, despite the apparent Newtonian linear thinning behaviour observed. Although, due to instrument limitations, CaBER data could not be obtained for concentrations at which the fluid-dynamic measurements were carried out, it can be seen that across a wide range of concentration (0.1%-0.3%) for scleroglucan the Trouton ratio remains approximately constant at a value of 340 while for xanthan gum the values at lower concentrations tend to be higher than the values at higher concentrations for $c \leq 0.75\%$. It is also important to note that the Trouton ratio for xanthan gum is lower than that of scleroglucan due to the higher shear viscosity of the solutions in the Trouton ratio calculations (even though η_E is approximately the same). **Tables 3.4** and **3.5** list the extensional viscosity and the Trouton ratio for scleroglucan and xanthan gum.

TABLES

Table 3.1: Carreau-Yasuda parameters for scleroglucan solutions (viscosity data measured at 20°C)

Concentration c (w/w %)	**Zero-shear viscosity** η_o (Pa.s)	**Infinite-shear viscosity** η_∞ (Pa.s)	**Constant which represents onset of shear thinning** λ_{CY} (s)	**Power-law exponent in the Carreau-Yasuda equation** n	**Carreau-Yasuda parameter** a
0.005	1.48×10^{-3}	1.12×10^{-3}	1.70×10^{-1}	0.30	5.82
0.0075	1.56×10^{-3}	1.12×10^{-3}	1.71×10^{-1}	0.31	5.84
0.01	2.14×10^{-3}	1.41×10^{-3}	1.73×10^{-1}	0.31	5.78
0.015	3.33×10^{-3}	1.49×10^{-3}	2.04×10^{-1}	0.42	5.63
0.02	3.45×10^{-3}	1.67×10^{-3}	1.26×10^{-1}	0.50	5.15
0.03	6.59×10^{-3}	1.73×10^{-3}	6.17×10^{-1}	0.55	1.62
0.05	8.48×10^{-3}	1.74×10^{-3}	7.21×10^{-1}	0.47	1.27
0.06	1.52×10^{-2}	1.73×10^{-3}	8.19×10^{-1}	0.59	1.24
0.075	7.42×10^{-2}	2.51×10^{-3}	2.08×10^{0}	0.73	0.90
0.1	2.24×10^{-1}	2.59×10^{-3}	5.01×10^{0}	0.78	0.55
0.2	5.33×10^{0}	3.07×10^{-3}	4.99×10^{1}	0.82	0.45
0.3	3.48×10^{1}	4.22×10^{-3}	1.46×10^{2}	0.86	0.62
0.5	7.70×10^{1}	5.53×10^{-3}	1.37×10^{2}	0.87	1.86

Table 3.2: Carreau-Yasuda parameters for xanthan gum solutions

Concentration c (w/w %)	**Zero-shear viscosity** η_o (Pa.s)	**Infinite-shear viscosity** η_∞ (Pa.s)	**Constant which represents onset of shear thinning** λ_{CY} (s)	**Power-law exponent in the Carreau-Yasuda equation** n	**Carreau-Yasuda parameter** a
0.01	1.73×10^{-3}	1.12×10^{-3}	4.93×10^{-2}	0.21	29.50
0.0124	3.15×10^{-3}	1.12×10^{-3}	9.53×10^{-2}	0.33	10.00
0.025	6.02×10^{-3}	1.12×10^{-3}	1.53×10^{-1}	0.35	4.98
0.0375	9.67×10^{-3}	1.12×10^{-3}	2.52×10^{-1}	0.37	3.35
0.05	1.97×10^{-2}	1.13×10^{-3}	3.88×10^{-1}	0.42	2.10
0.07	5.33×10^{-2}	1.33×10^{-3}	8.34×10^{-1}	0.49	1.12
0.10	2.25×10^{-1}	1.88×10^{-3}	1.77×10^{0}	0.60	0.57
0.15	2.16×10^{0}	2.67×10^{-3}	2.88×10^{0}	0.80	0.31
0.20	3.68×10^{0}	2.24×10^{-3}	2.15×10^{1}	0.66	0.81
0.25	9.83×10^{0}	3.45×10^{-3}	2.34×10^{1}	0.75	0.80
0.375	2.85×10^{2}	4.60×10^{-3}	4.14×10^{2}	0.81	1.47
0.5	8.41×10^{2}	5.25×10^{-3}	7.11×10^{2}	0.84	1.22
0.75	1.55×10^{3}	9.58×10^{-3}	1.04×10^{3}	0.85	0.92

Table 3.3: Herschel-Bulkley parameters for carbopol solutions

Concentration c (w/w %)	**Geometry**	**Yield stress** τ_y (Pa)	**Herschel-Bulkley consistency index** K (Pa.s^n)	**Power-law exponent in the Herschel-Bulkley equation** n
0.065	Roughened plate	3.88×10^{-1}	1.10×10^{-2}	0.98
	Cone and plate	4.64×10^{-2}	3.32×10^{-2}	0.81
0.1	Roughened plate	1.14×10^{0}	6.19×10^{-1}	0.52
	Cone and plate	8.52×10^{-2}	1.03×10^{0}	0.44

Table 3.4: Steady uniaxial extensional viscosity and Trouton ratio from CaBER tests for scleroglucan solutions

Scleroglucan solution concentration (%)	**Steady uniaxial extensional viscosity,** η_E (Pa.s)	**Trouton ratio,** Tr
0.1	1.03	345
0.2	1.92	336
0.3	4.46	319
0.5	6.73	190

Table 3.5: Steady uniaxial extensional viscosity and Trouton ratio from CaBER tests for xanthan gum solutions

Xanthan gum solution concentration (%)	**Steady uniaxial extensional viscosity, η_E** (Pa.s)	**Trouton ratio, *Tr***
0.2	2.08	151
0.25	2.06	122
0.375	6.20	111
0.5	8.74	75.3
0.75	10.40	61.0

FIGURES

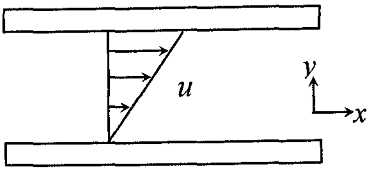

Figure 3.1: Two parallel planes with the intervening space between the planes filled with fluid experiencing steady simple shear flow

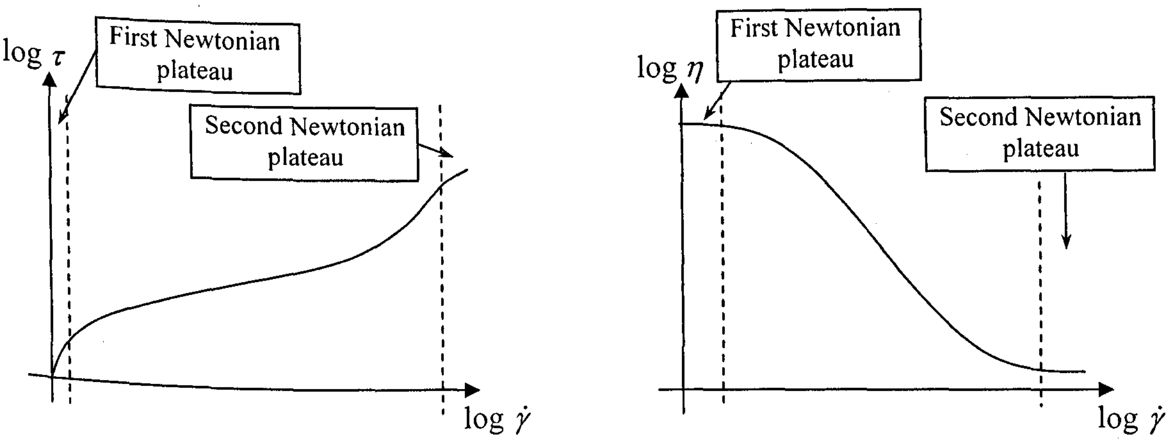

Figure 3.2: Typical graphs for a shear-thinning fluid plotted on log scales

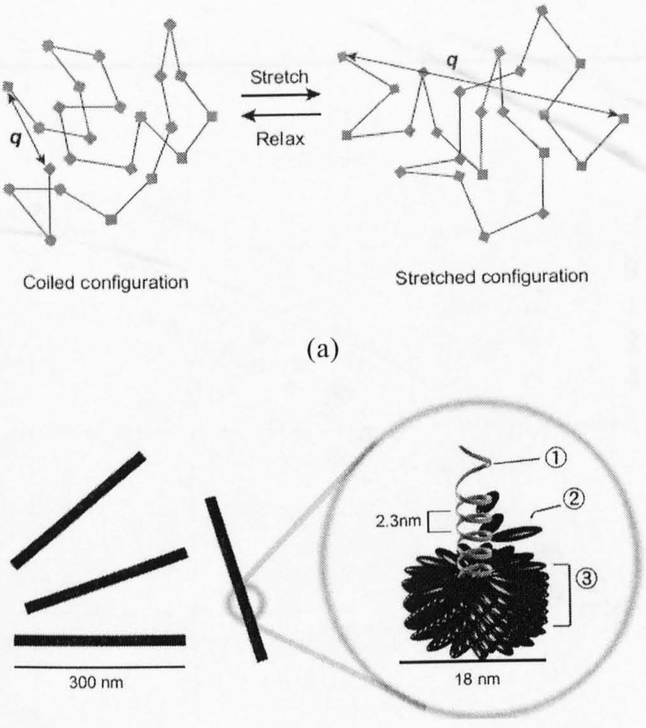

(a)

(b)

Figure 3.3(a): Flexible polymer configuration where polymer stretching is characterized by the change in the end-to-end vector, *q* (Figure from White and Mungal, 2008), **(b)** Tobacco mosaic virus, an example of rigid rod polymer (Figure from Wikipedia, 2005)

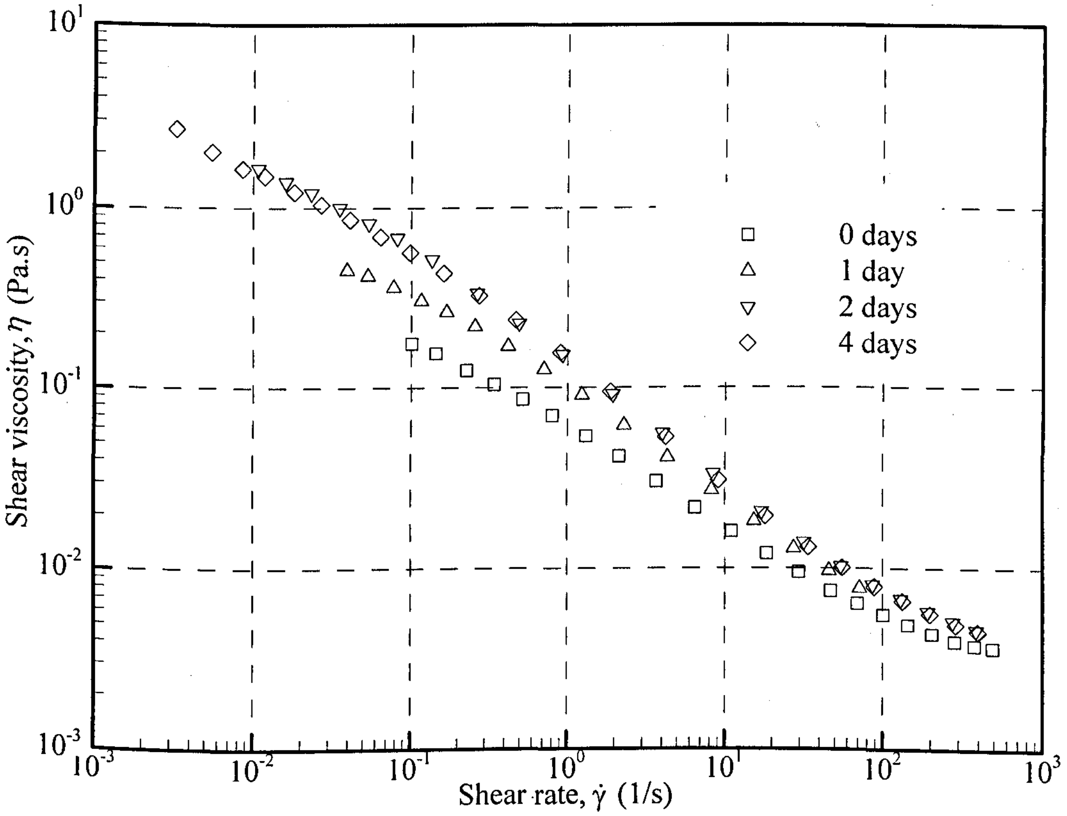

Figure 3.4: Shear viscosity versus shear rate for 0.2% scleroglucan indicating the gelation period of the fluid sample

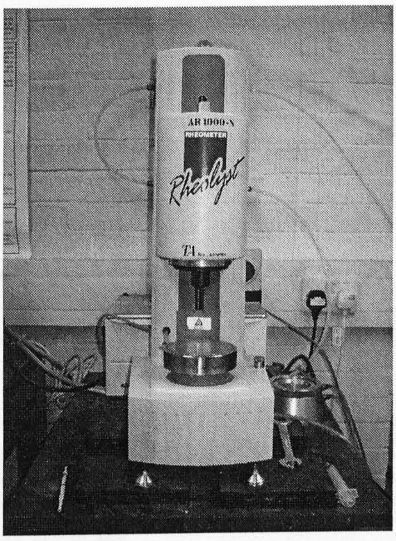

Figure 3.5: Photograph of TA Instrument Rheolyst AR 1000N controlled-stress rheometer

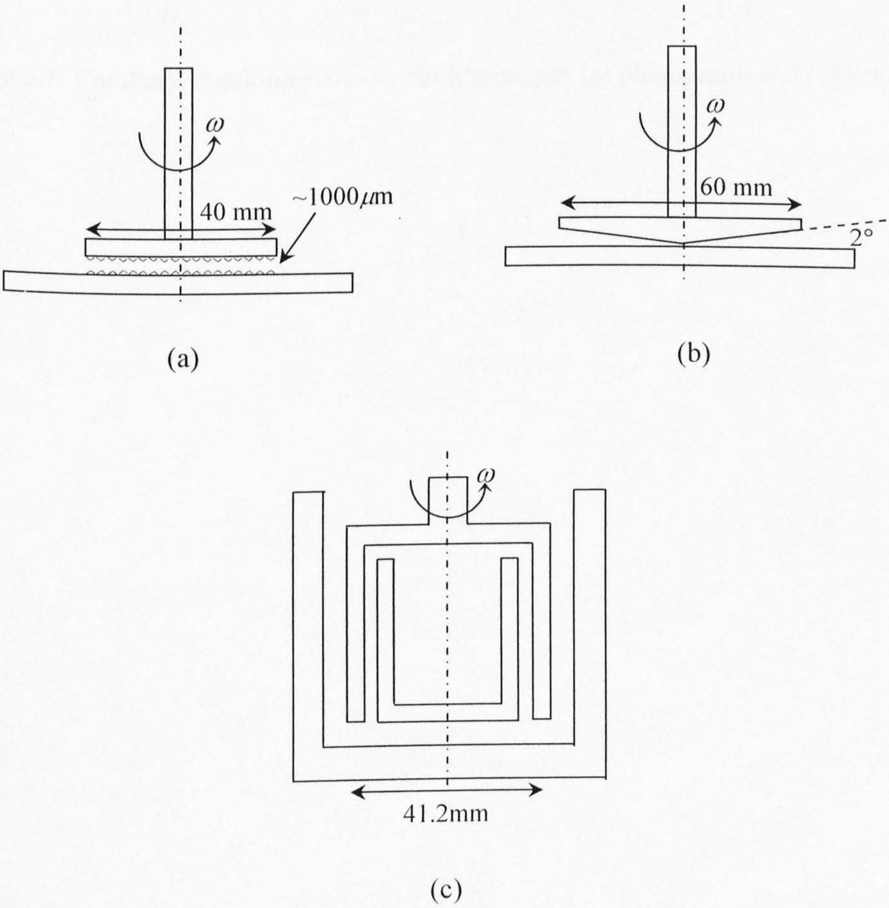

Figure 3.6: Schematic diagrams of (a) roughened parallel plate, (b) cone and plate and (c) double concentric cylinder geometries

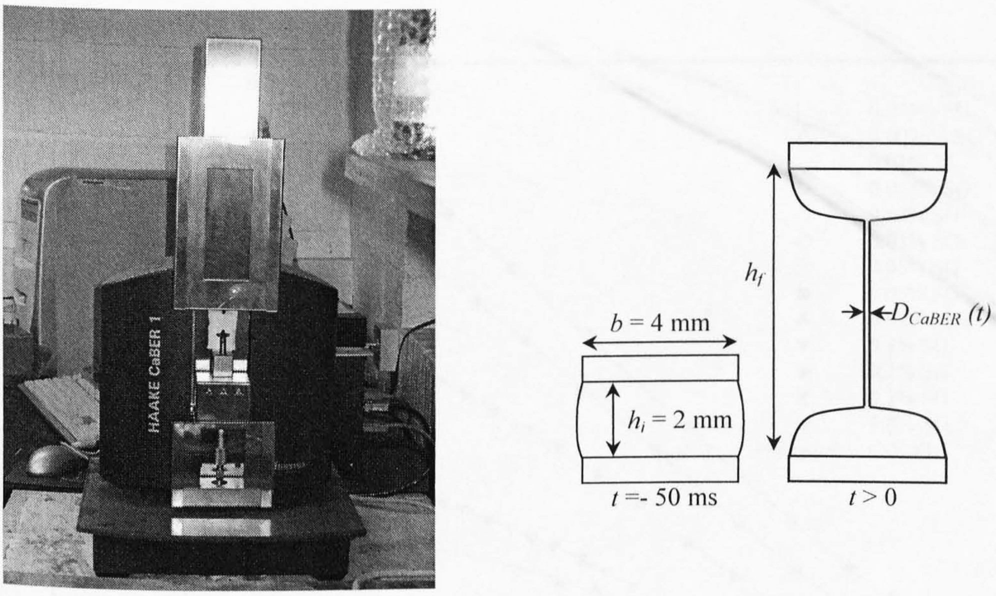

(a) (b)

Figure 3.7: Capillary Break-up Extensional Rheometer (a) photograph and (b) schematic

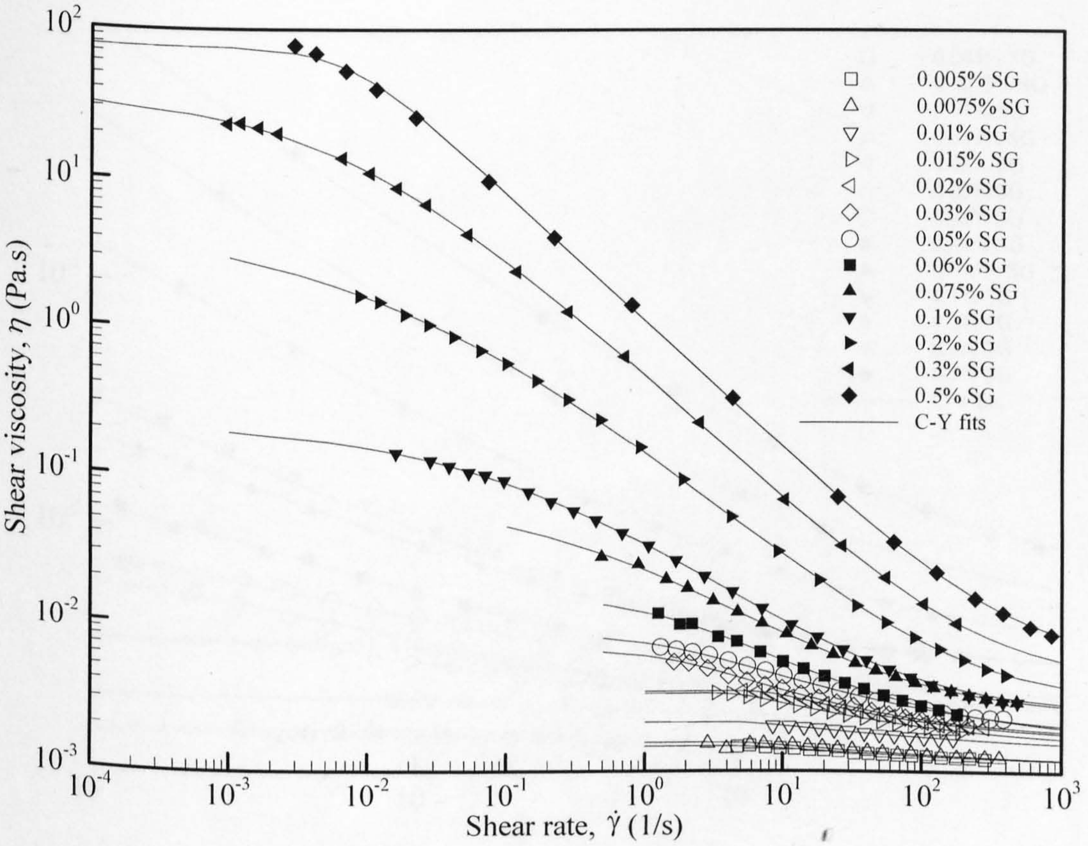

Figure 3.8(a): Viscometric data for various scleroglucan concentrations together with the Carreau-Yasuda fits

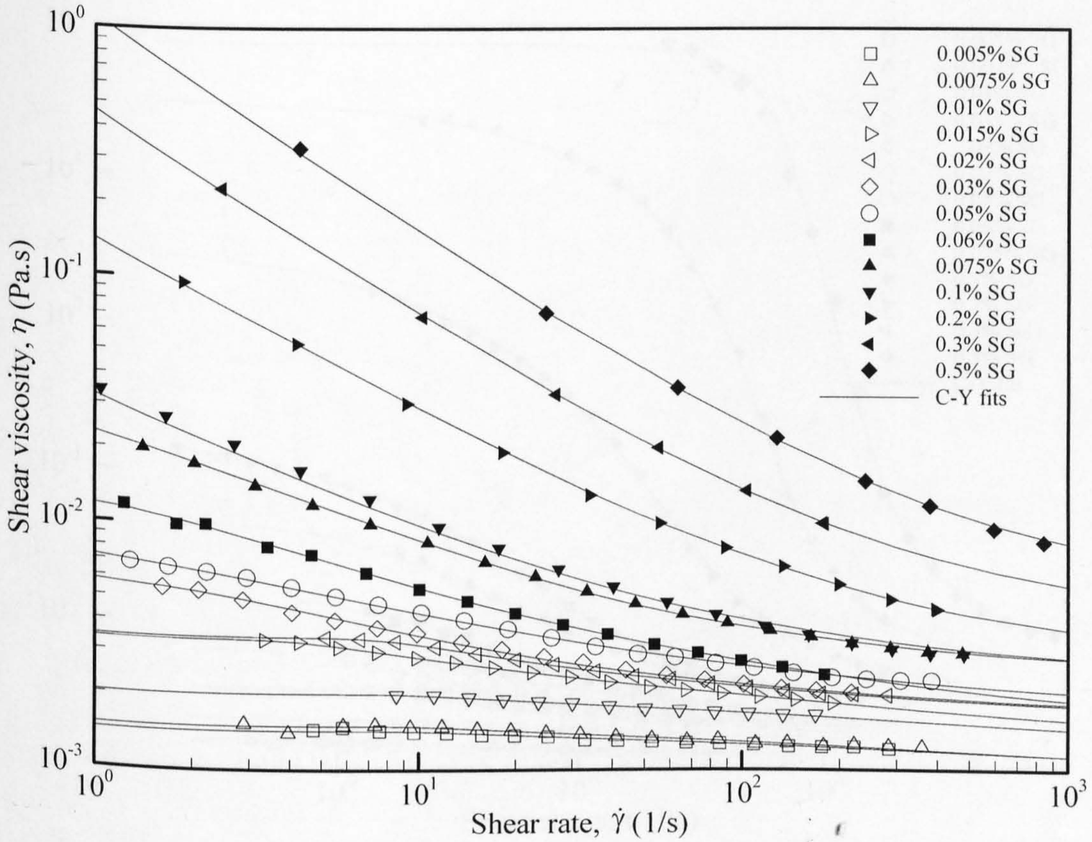

Figure 3.8(b): Viscometric data for various scleroglucan concentrations together with the Carreau-Yasuda fits at higher shear rate range

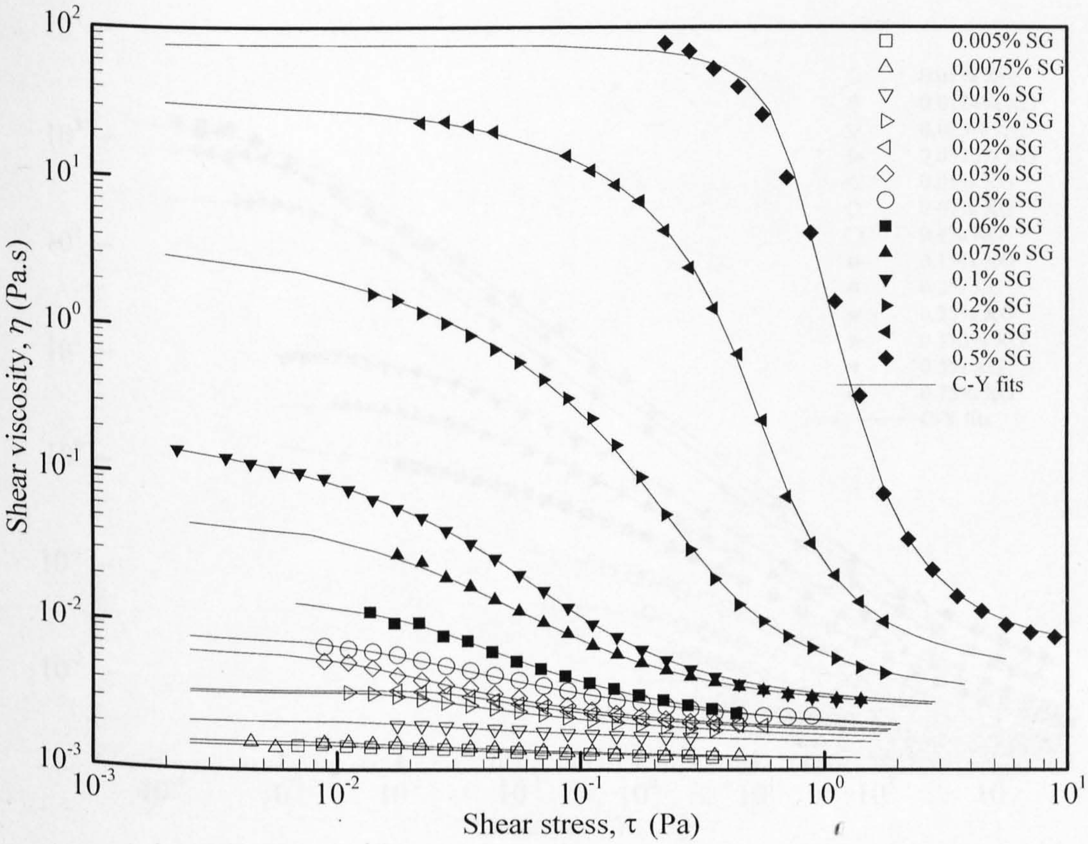

Figure 3.9: Shear viscosity versus shear stress for various scleroglucan concentrations together with the Carreau-Yasuda fits

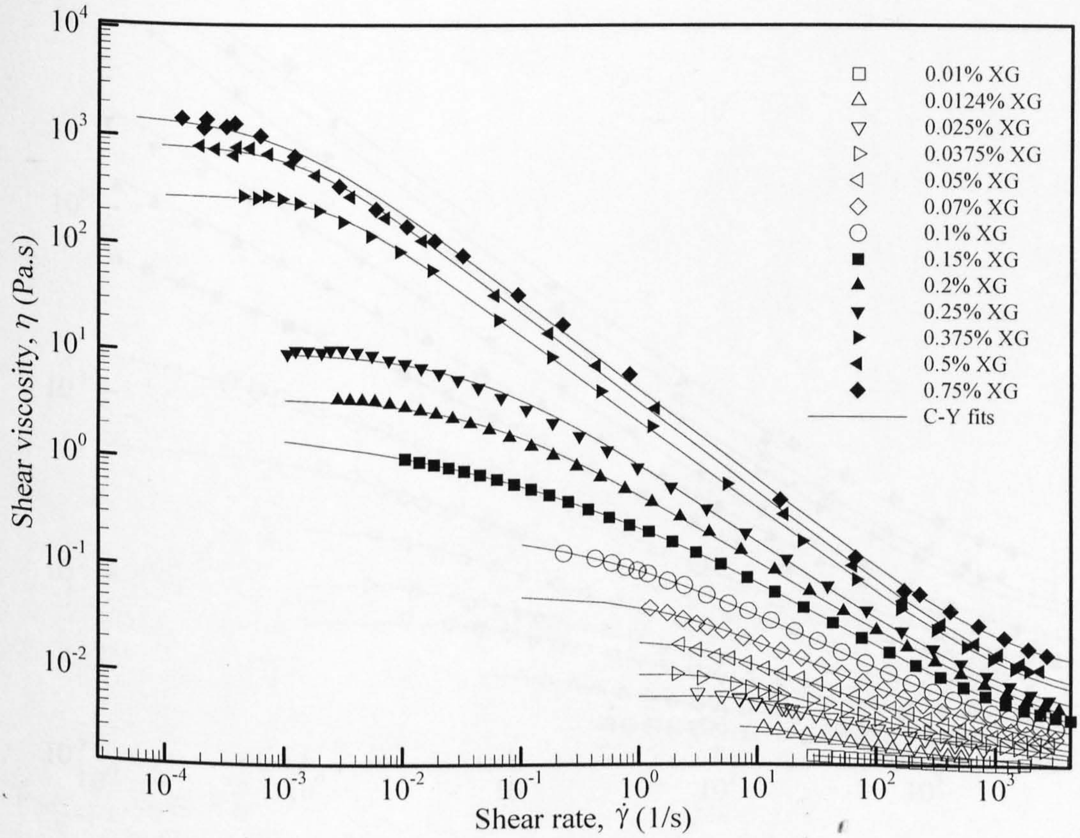

Figure 3.10(a): Viscometric data for various xanthan gum concentrations together with the Carreau-Yasuda fits

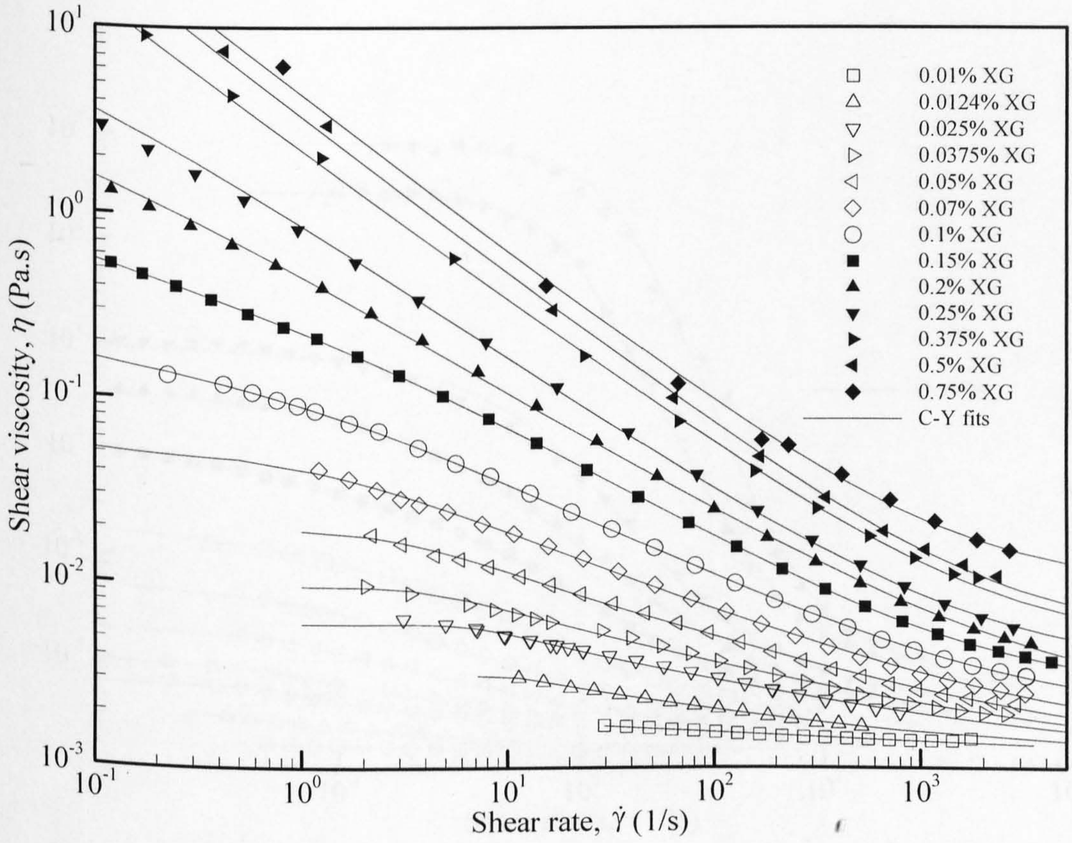

Figure 3.10(b): Viscometric data for various xanthan gum concentrations together with the Carreau-Yasuda fits at higher shear rate range

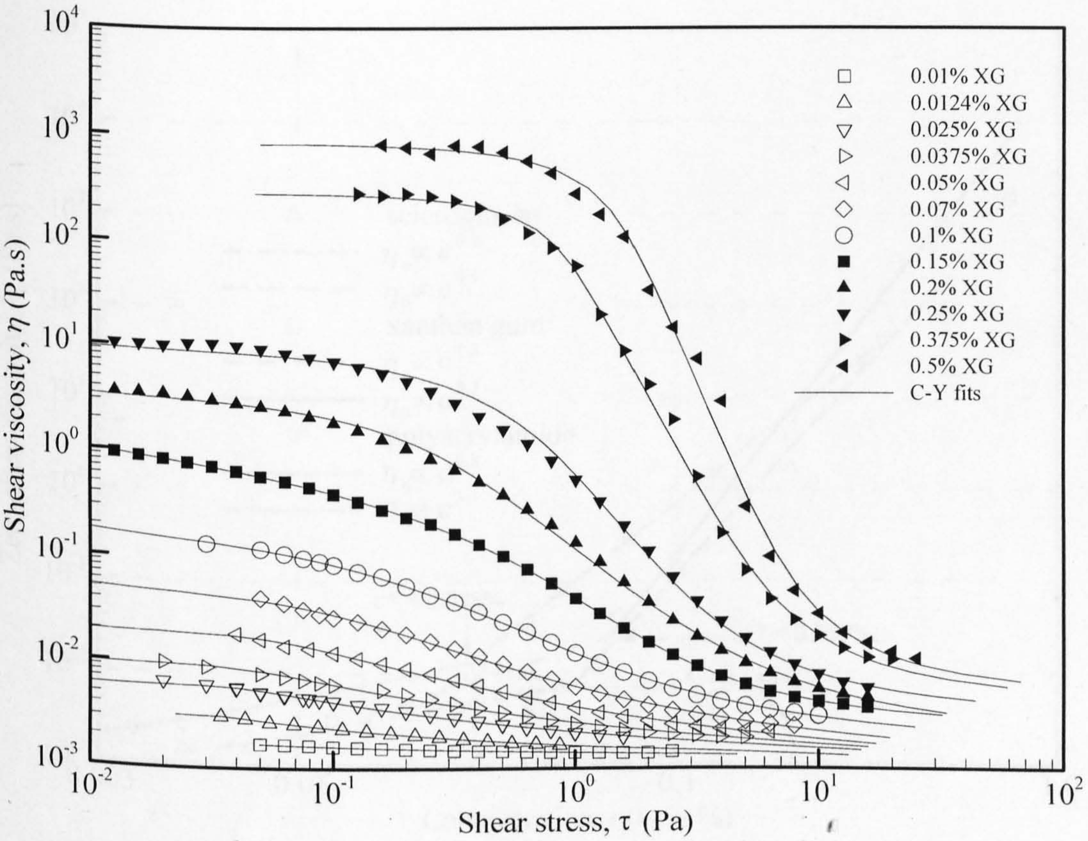

Figure 3.11: Shear viscosity versus shear stress for various xanthan gum concentrations together with the Carreau-Yasuda fits

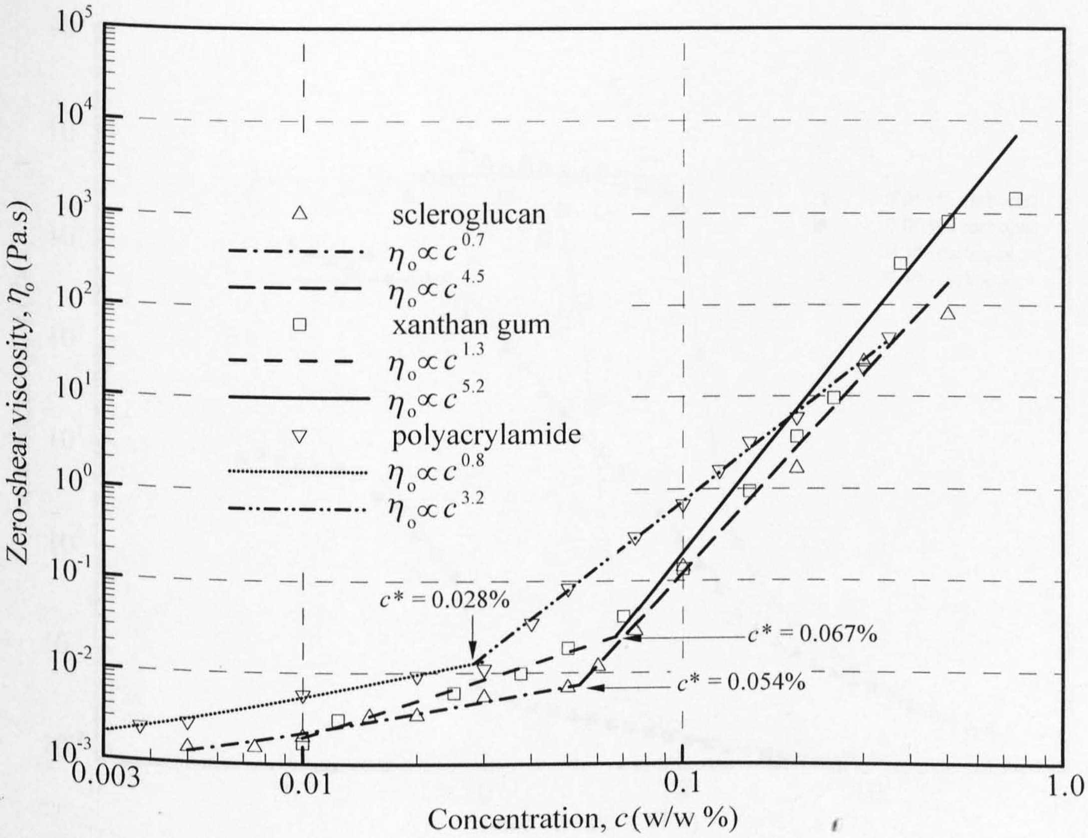

Figure 3.12: Zero-shear viscosity versus scleroglucan, xanthan gum and polyacrylamide concentrations at 20°C

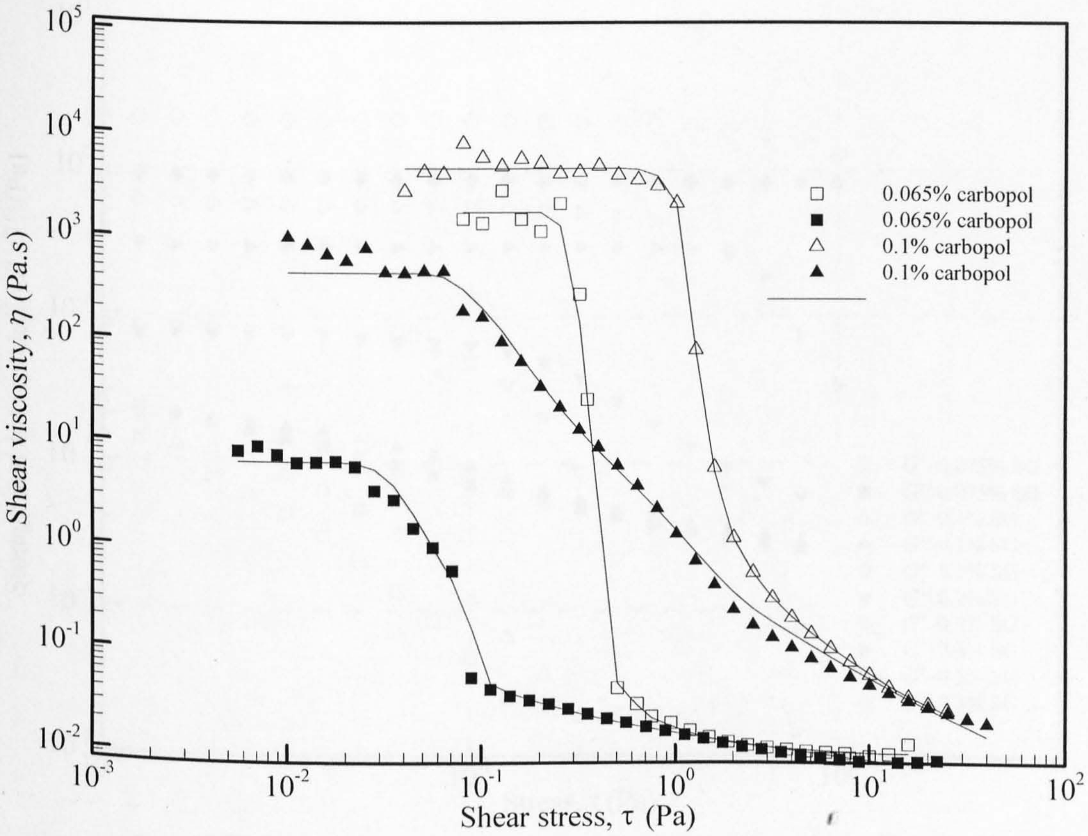

Figure 3.13: Shear viscosity versus shear stress for carbopol solutions. (Hollow symbols: measured using 4-cm roughened plate, filled symbols: measured using 6 cm 2° cone and plate). The solid lines are included to guide the eye.

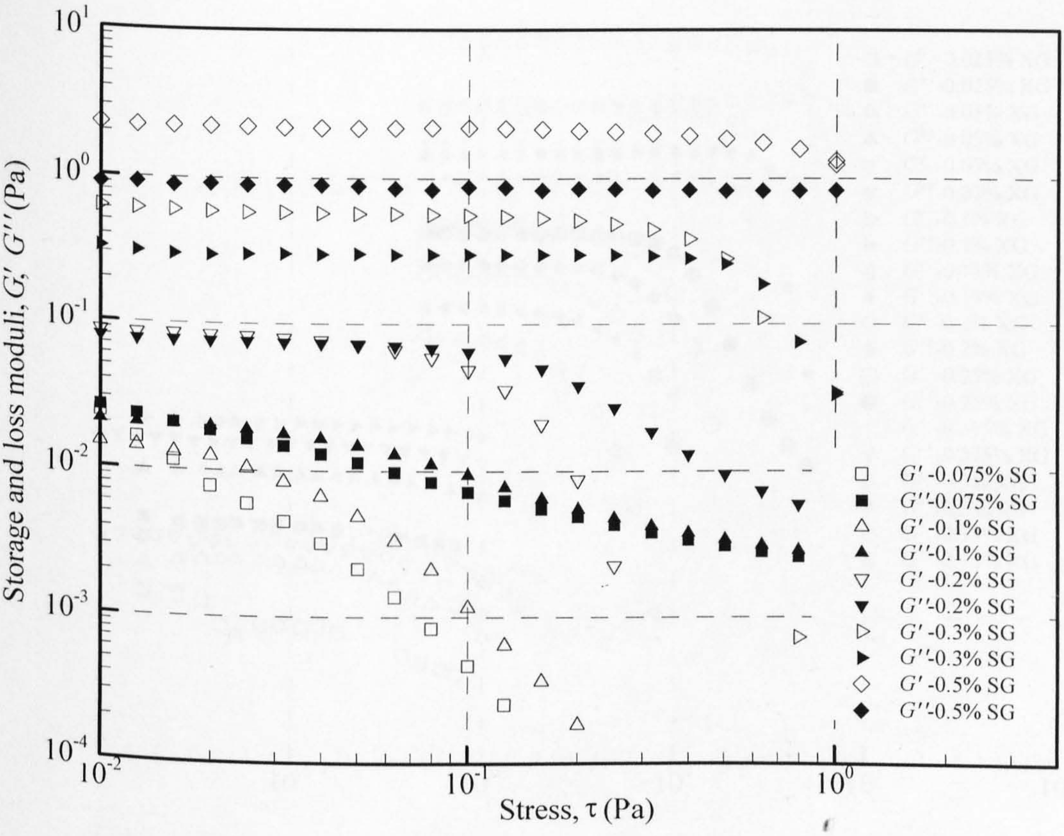

Figure 3.14: Storage and loss moduli versus oscillation stress for various scleroglucan concentrations measured at a constant frequency of 0.1 Hz

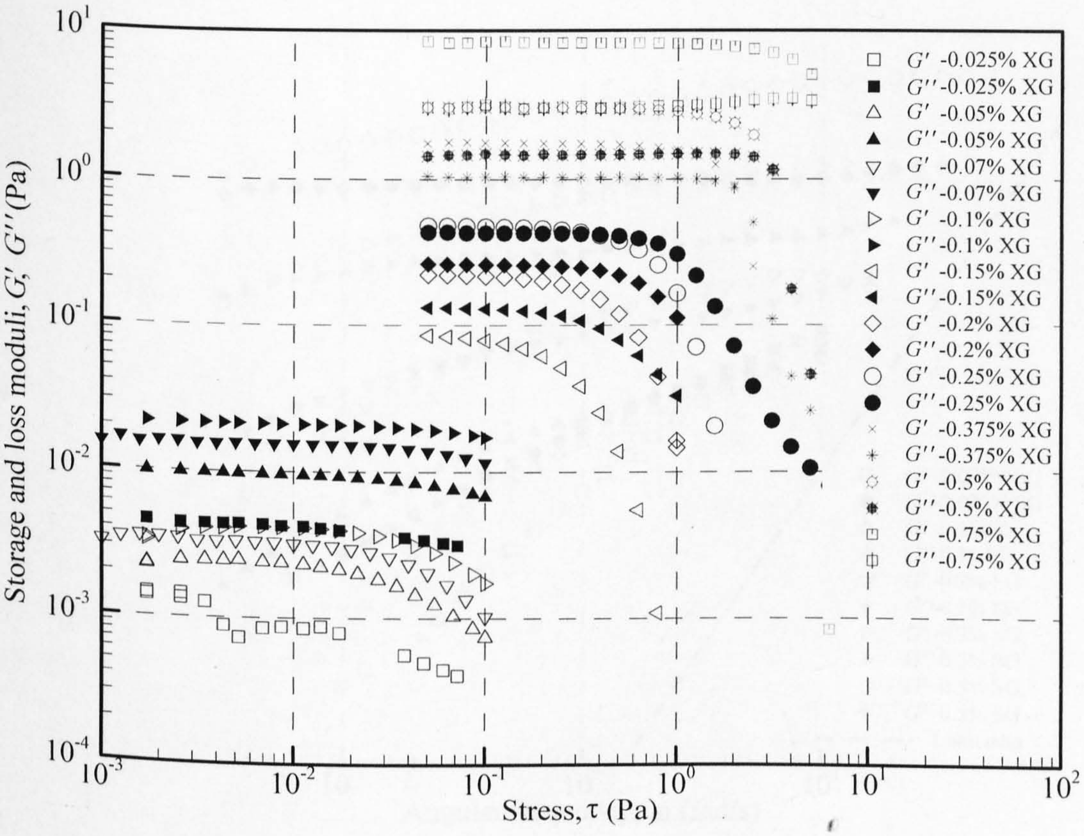

Figure 3.15: Storage and loss moduli versus oscillation stress for various xanthan gum concentrations measured at a constant frequency of 0.1 Hz

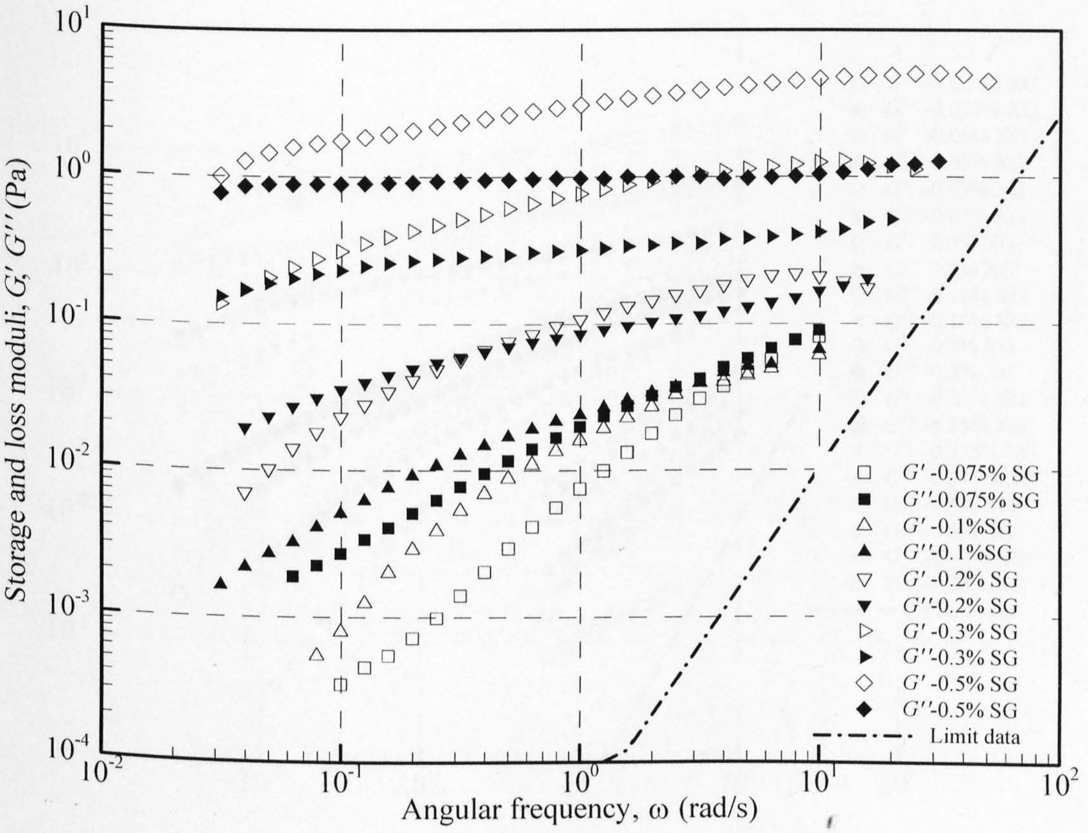

Figure 3.16: Storage and loss moduli versus frequency for various scleroglucan concentrations

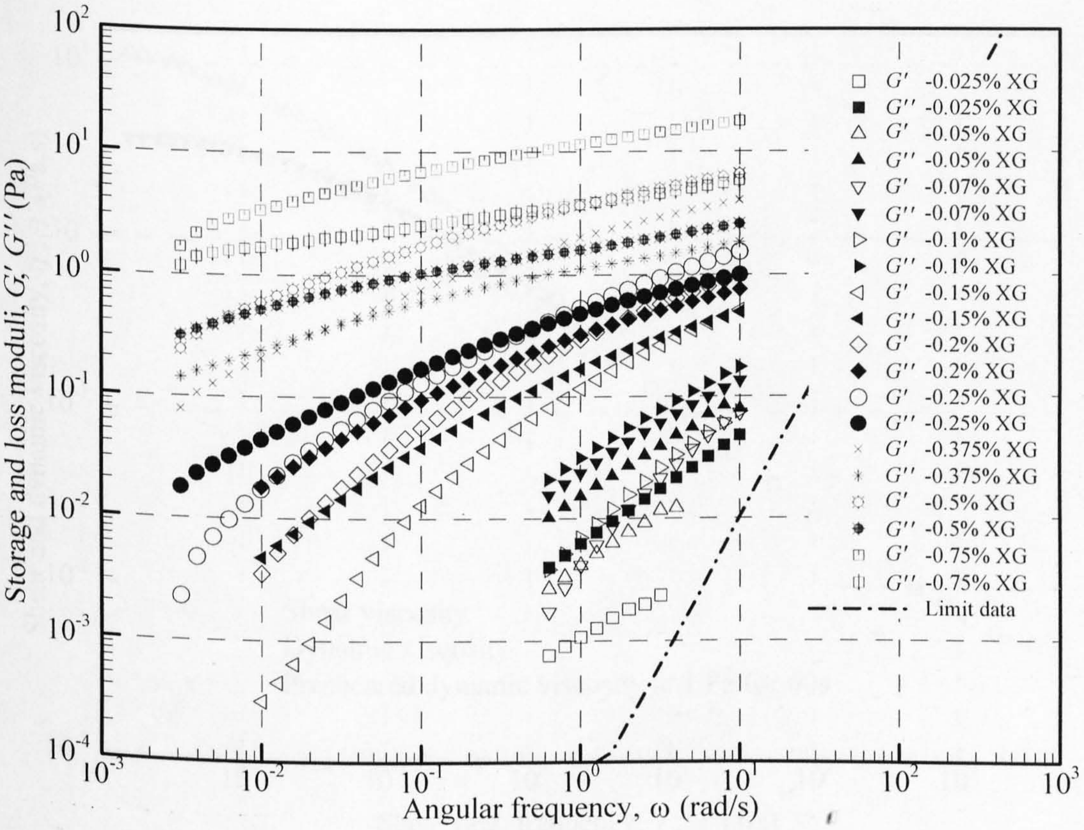

Figure 3.17: Storage and loss moduli versus frequency for various xanthan gum concentrations

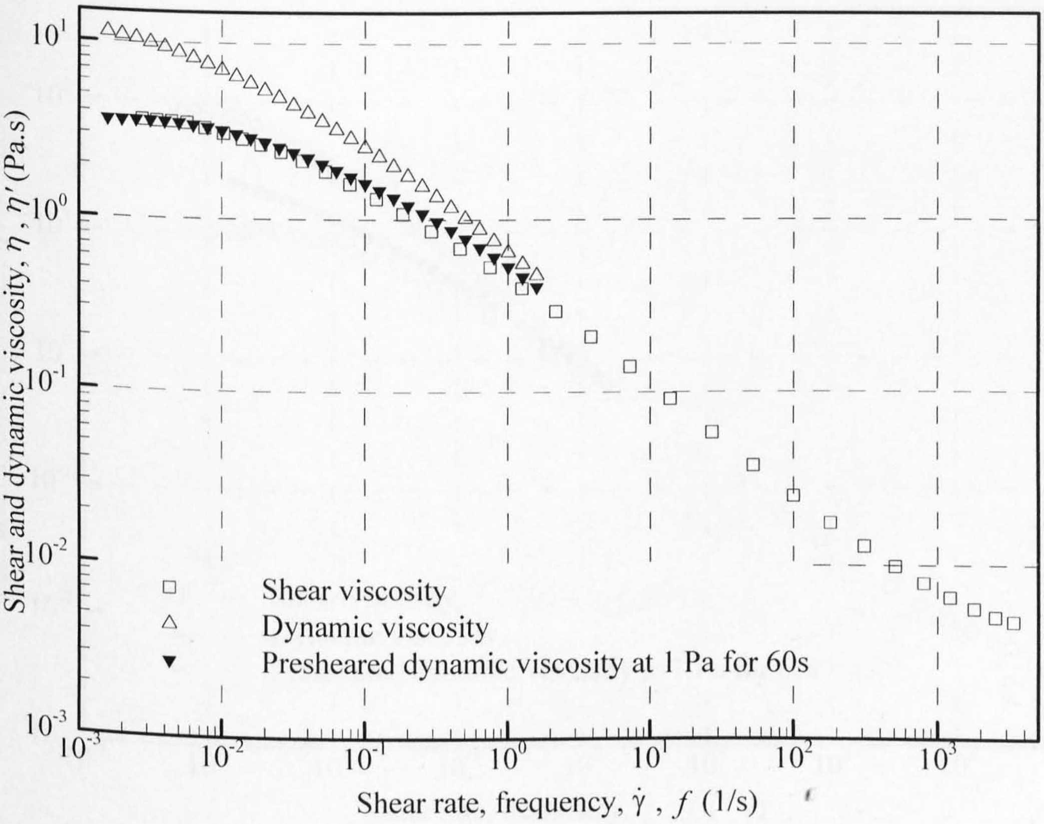

Figure 3.18: Shear and dynamic viscosities versus shear rate/frequency for 0.2% xanthan gum solutions

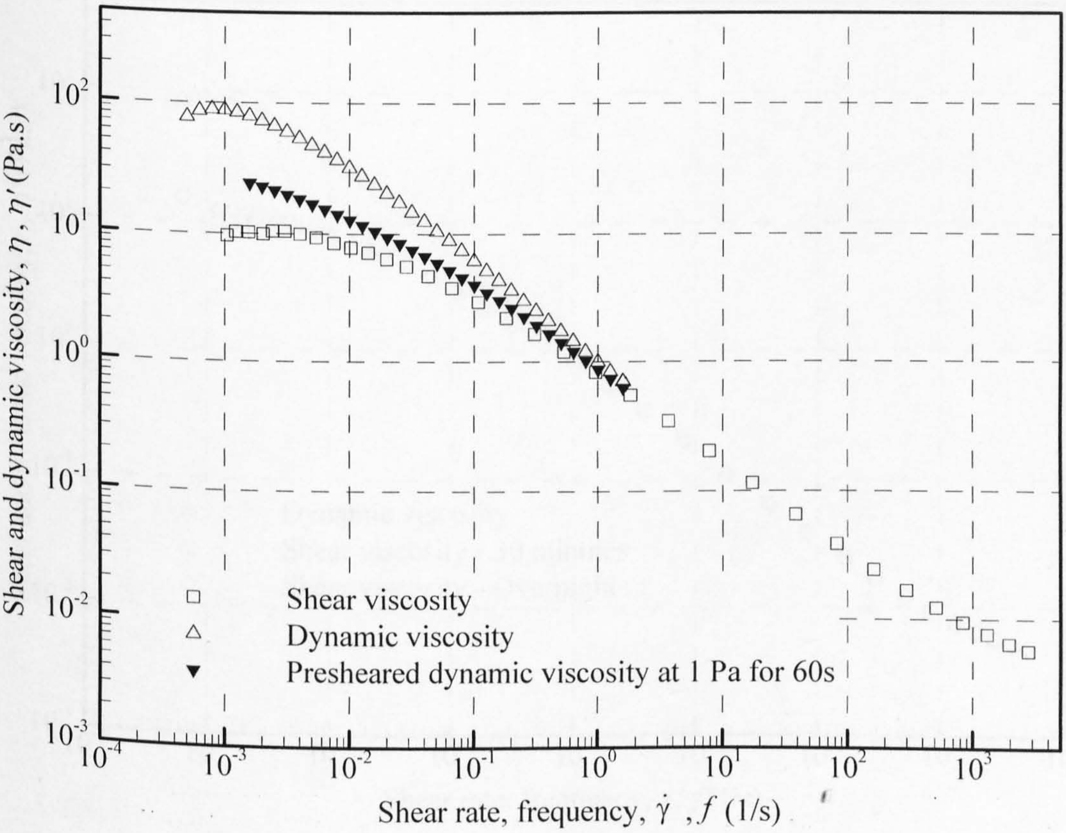

Figure 3.19: Shear and dynamic viscosities versus shear rate/frequency for 0.25% xanthan gum solution

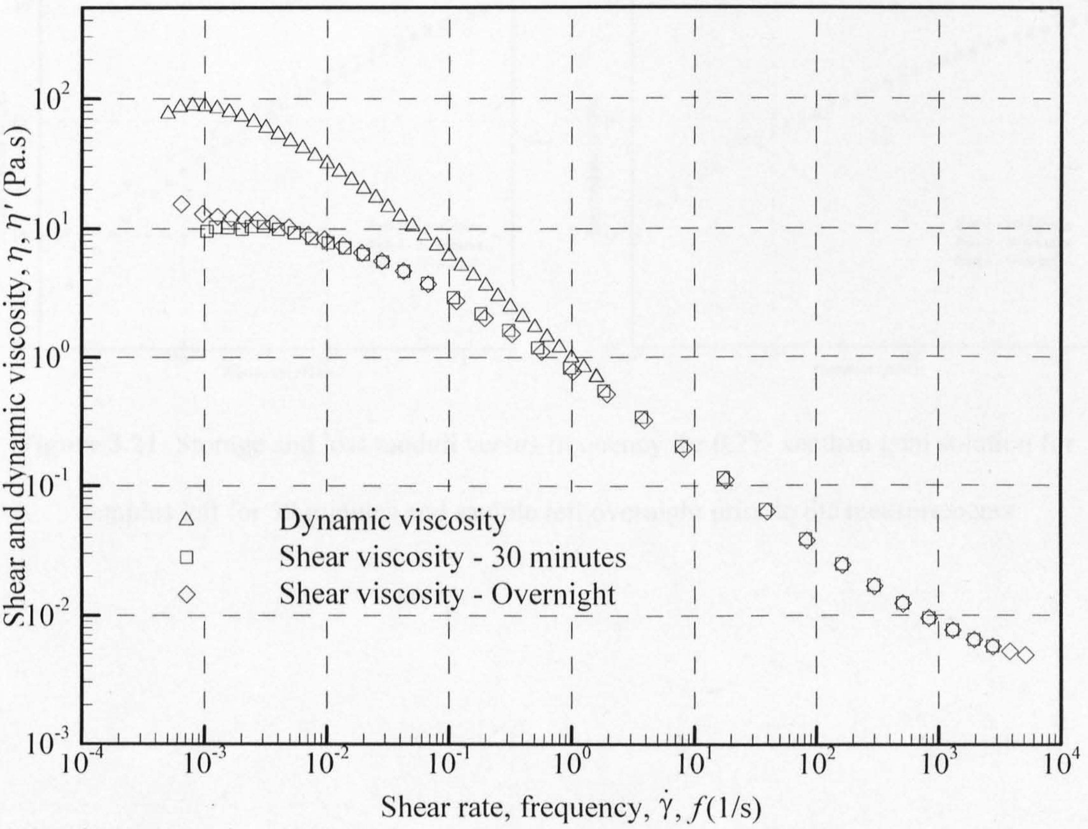

Figure 3.20: Shear and dynamic viscosities versus shear rate/frequency for 0.25% xanthan gum solution for sample left for 30 minutes and sample left overnight prior to the measurements

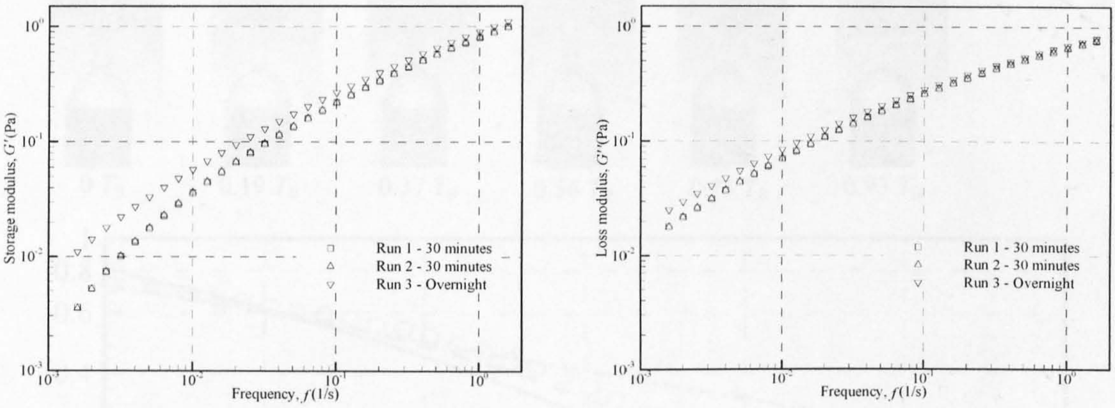

Figure 3.21: Storage and loss moduli versus frequency for 0.2% xanthan gum solution for samples left for 30 minutes and sample left overnight prior to the measurements

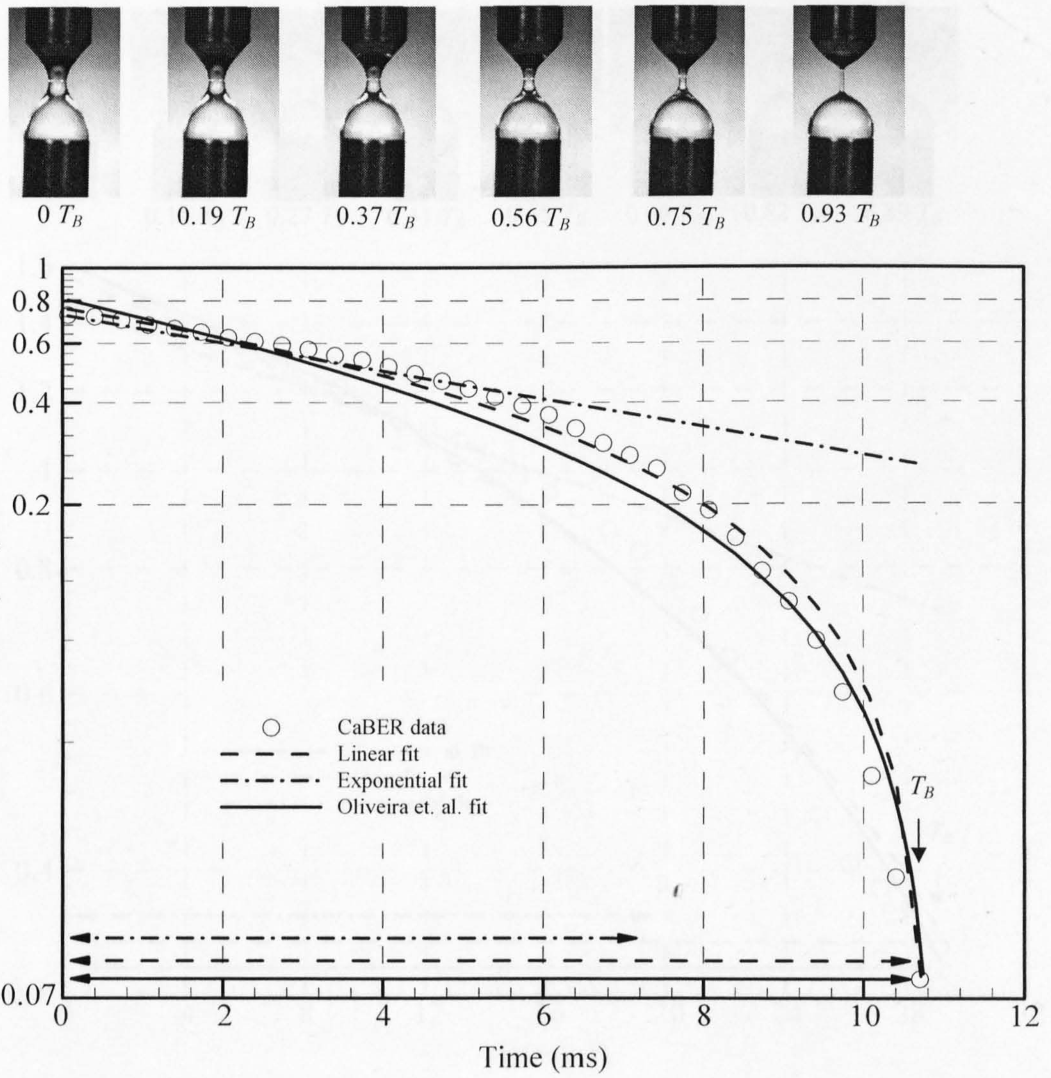

Figure 3.22: Filament diameter thinning as a function of time for 0.1% SG at 20°C ($\Lambda_{i,f}$=0.5, 1.4) (Arrow lines represent the time period for exponential fit (–·–), linear fit (––) and Oliveira et. al. fit (—))

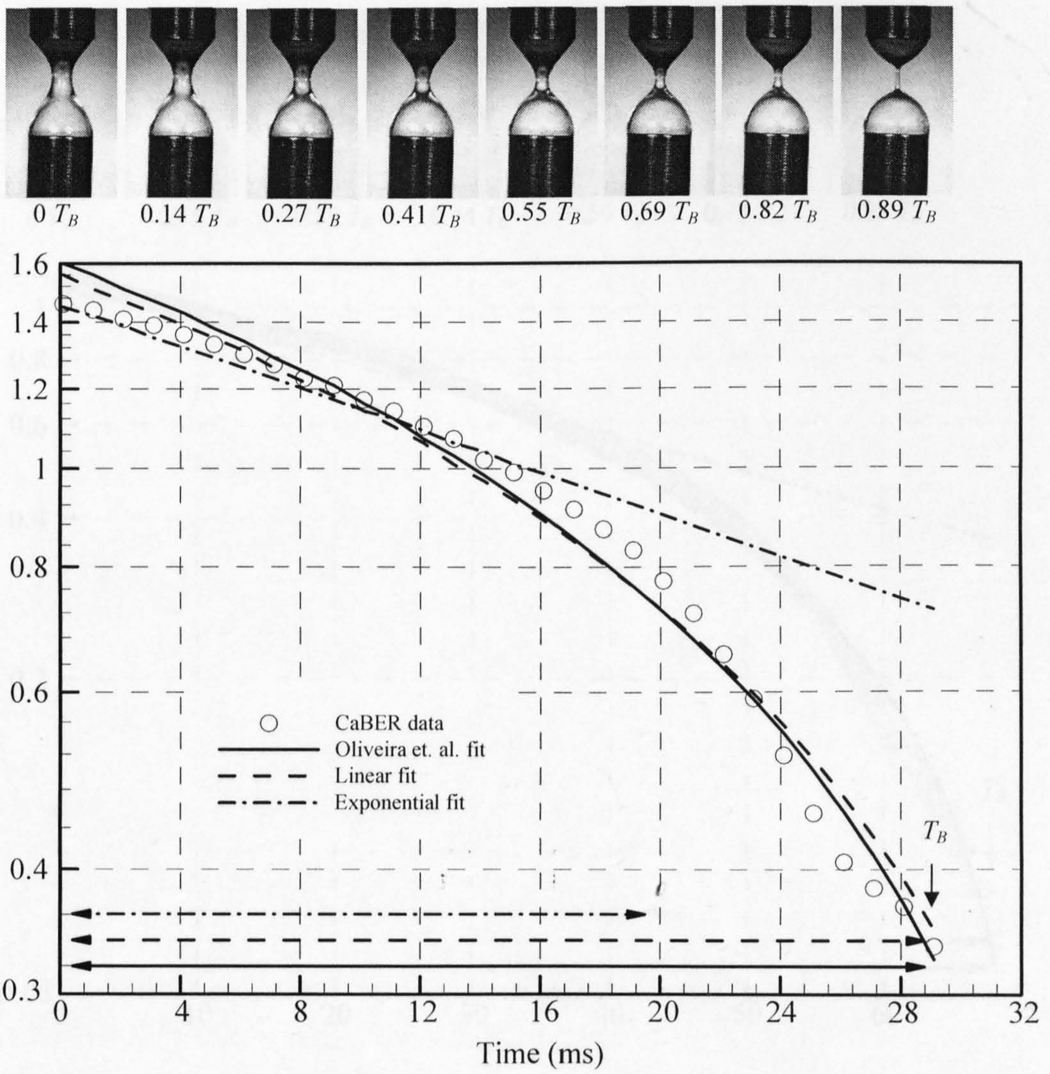

Figure 3.23: Filament diameter thinning as a function of time for 0.2% SG at 20°C ($\Lambda_{i,f}$=0.5, 1.4)

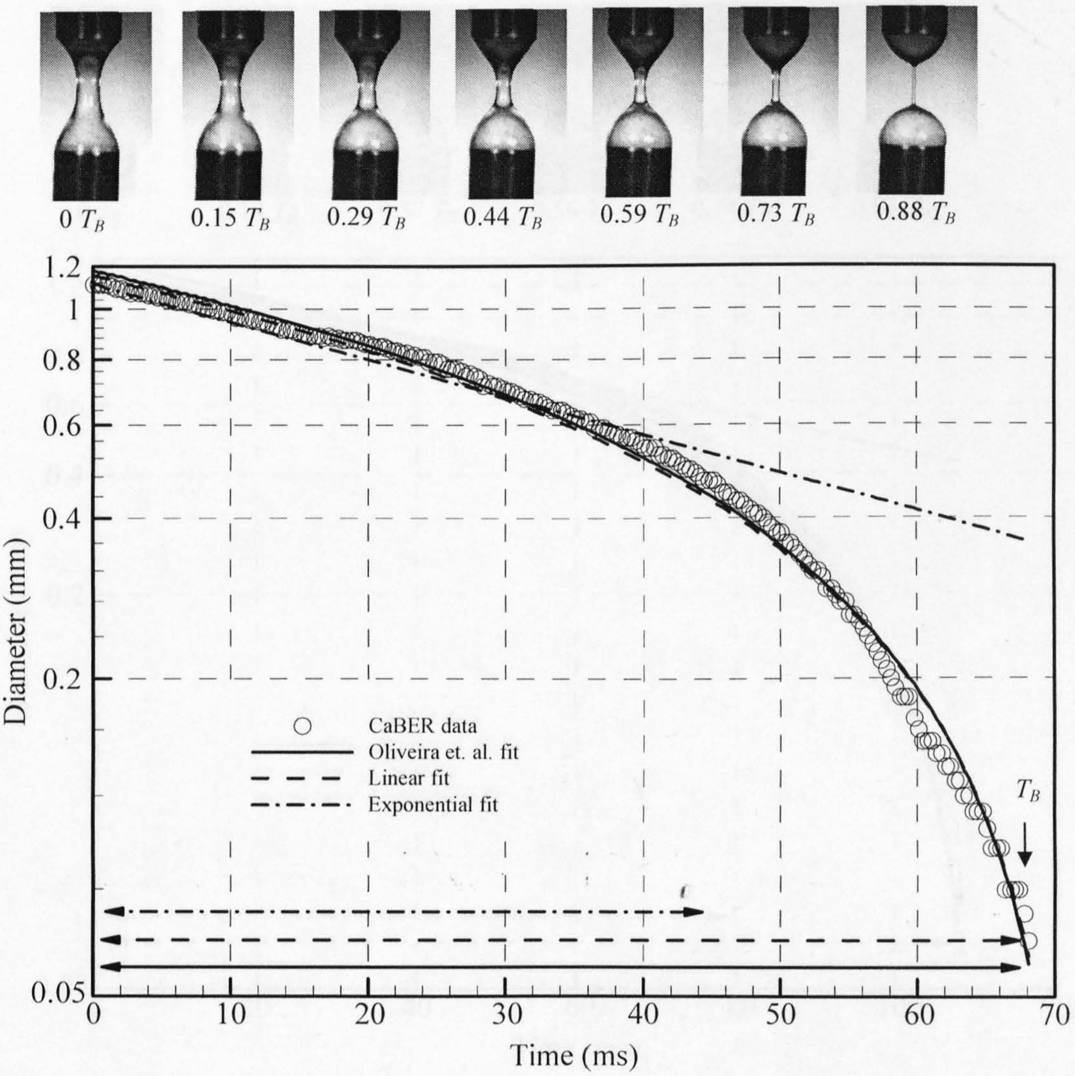

Figure 3.24: Filament diameter thinning as a function of time for 0.3% SG at 20°C ($\Lambda_{i,f}$=0.5, 1.6)

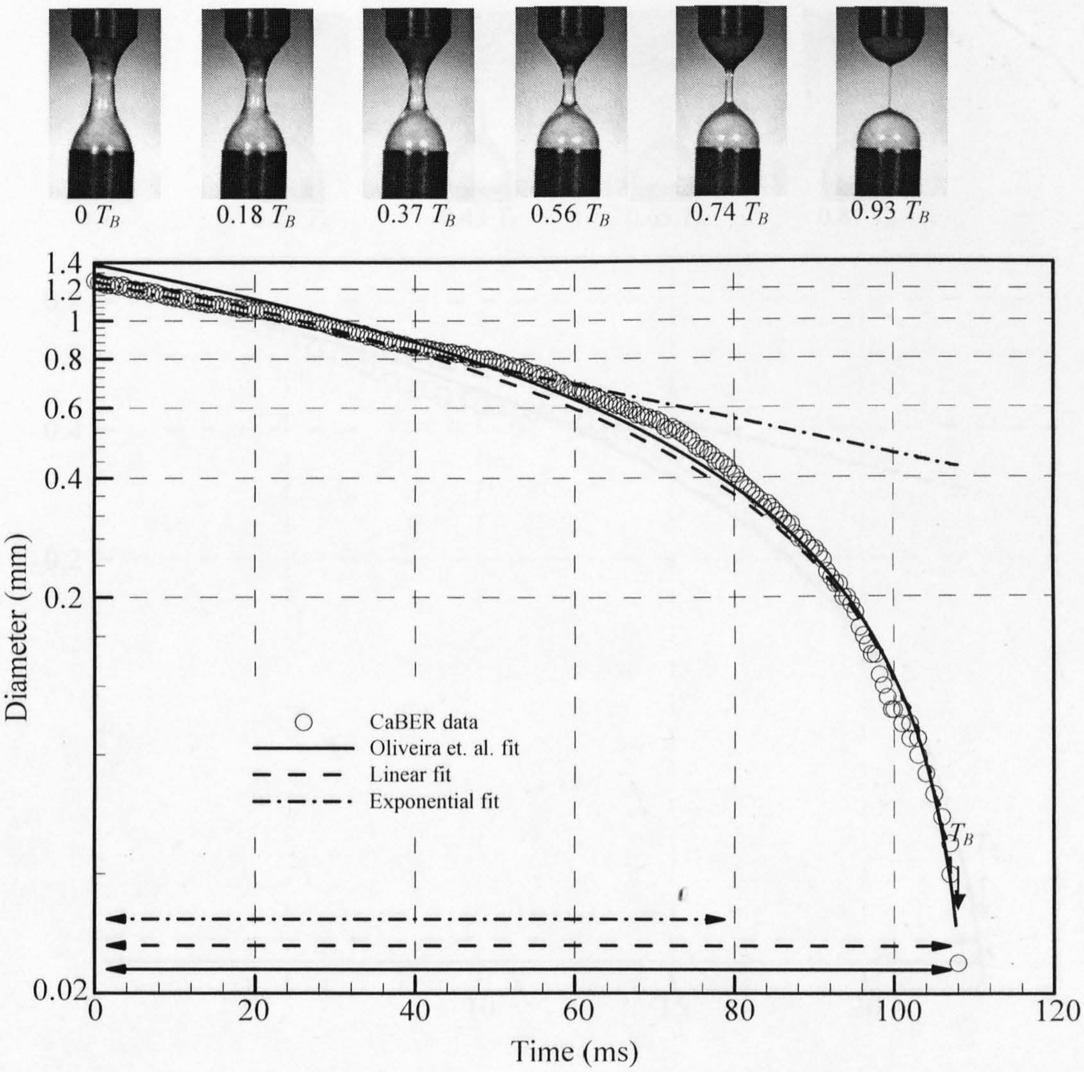

Figure 3.25: Filament diameter thinning as a function of time for 0.5% SG at 20°C ($\Lambda_{i,f}$=0.5, 1.6)

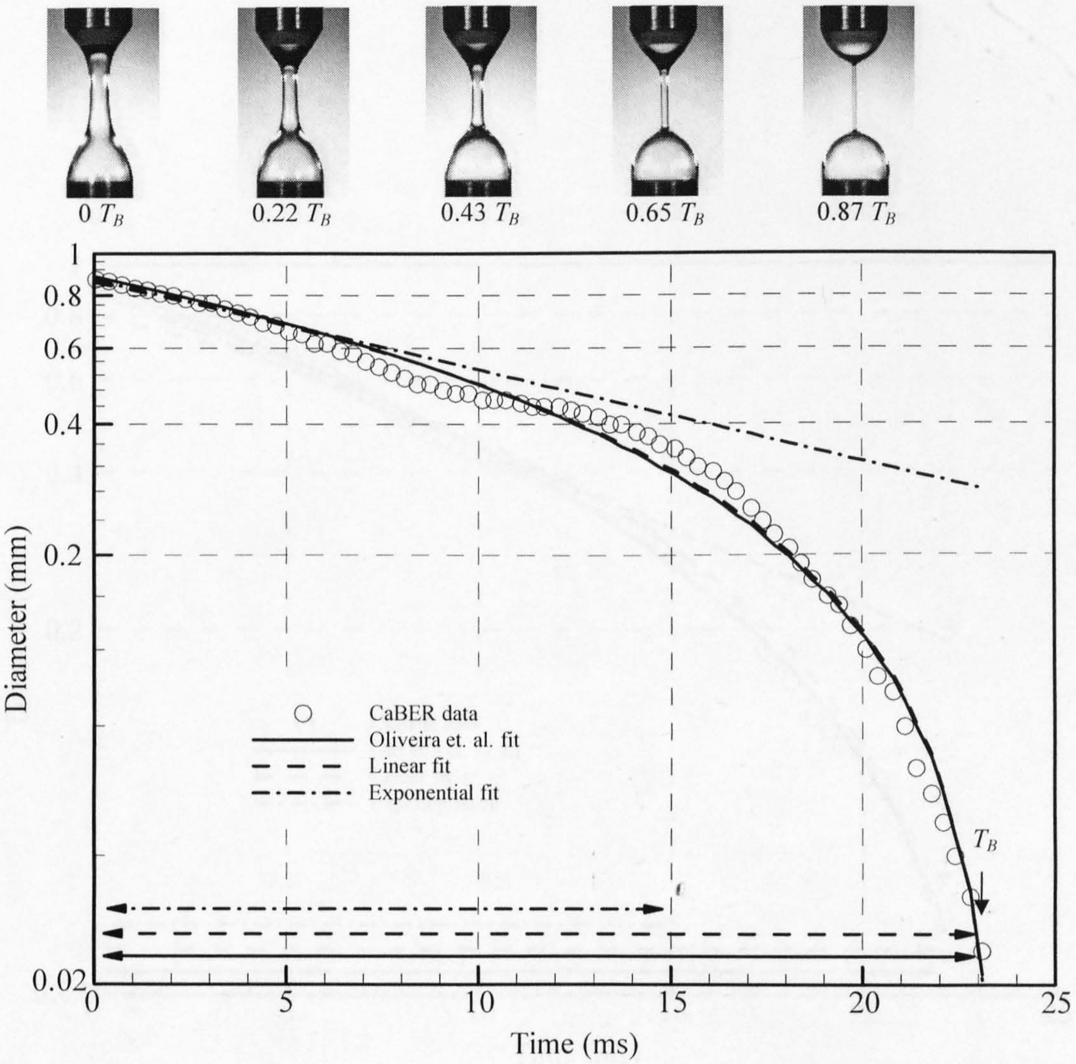

Figure 3.26: Filament diameter thinning as a function of time for 0.2% XG at 20°C ($\Lambda_{i,f}$=0.5, 1.8)

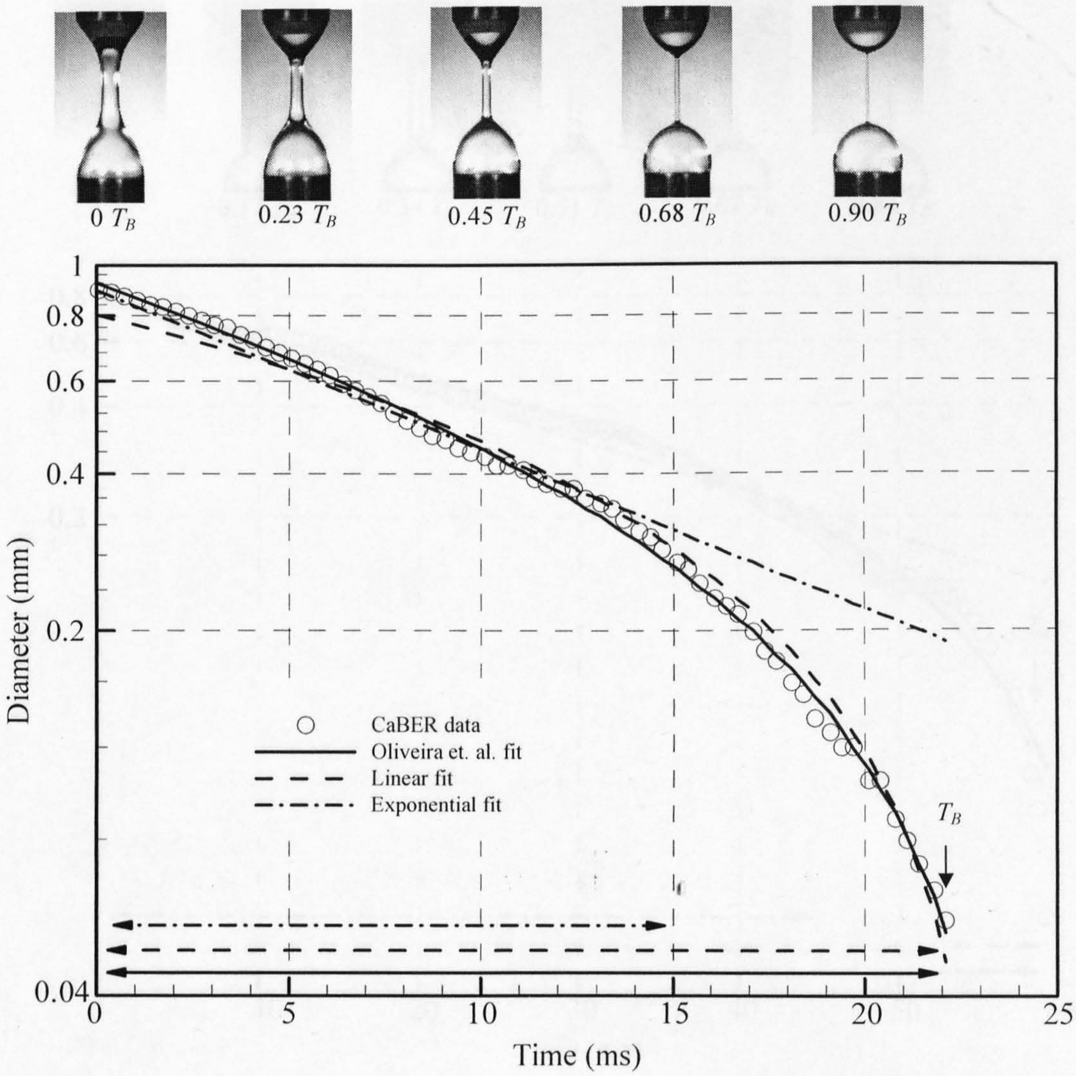

Figure 3.27: Filament diameter thinning as a function of time for 0.25% XG at 20°C ($\Lambda_{i,f}$=0.5, 1.8)

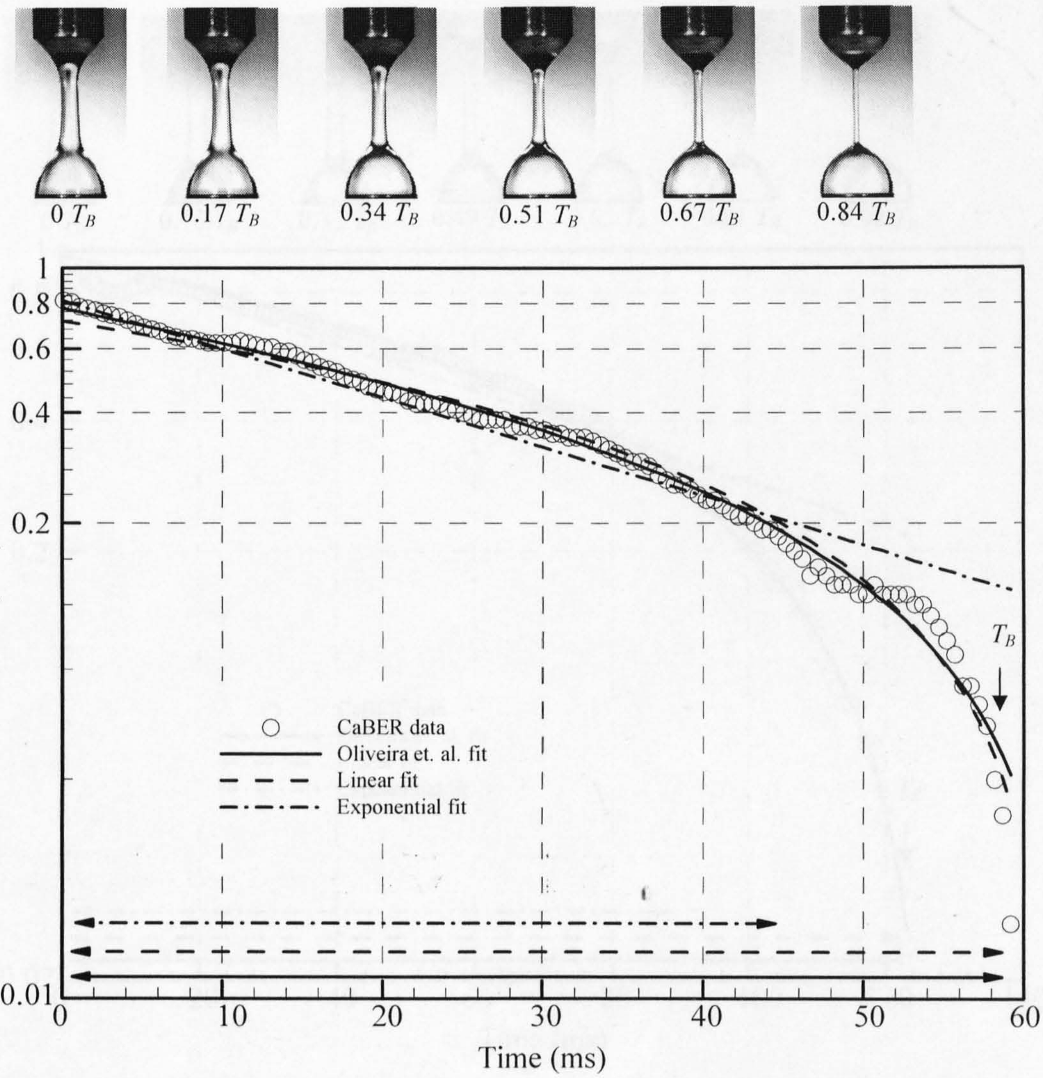

Figure 3.28: Filament diameter thinning as a function of time for 0.375% XG at 20°C ($\Lambda_{i,f}$=0.5, 2.0)

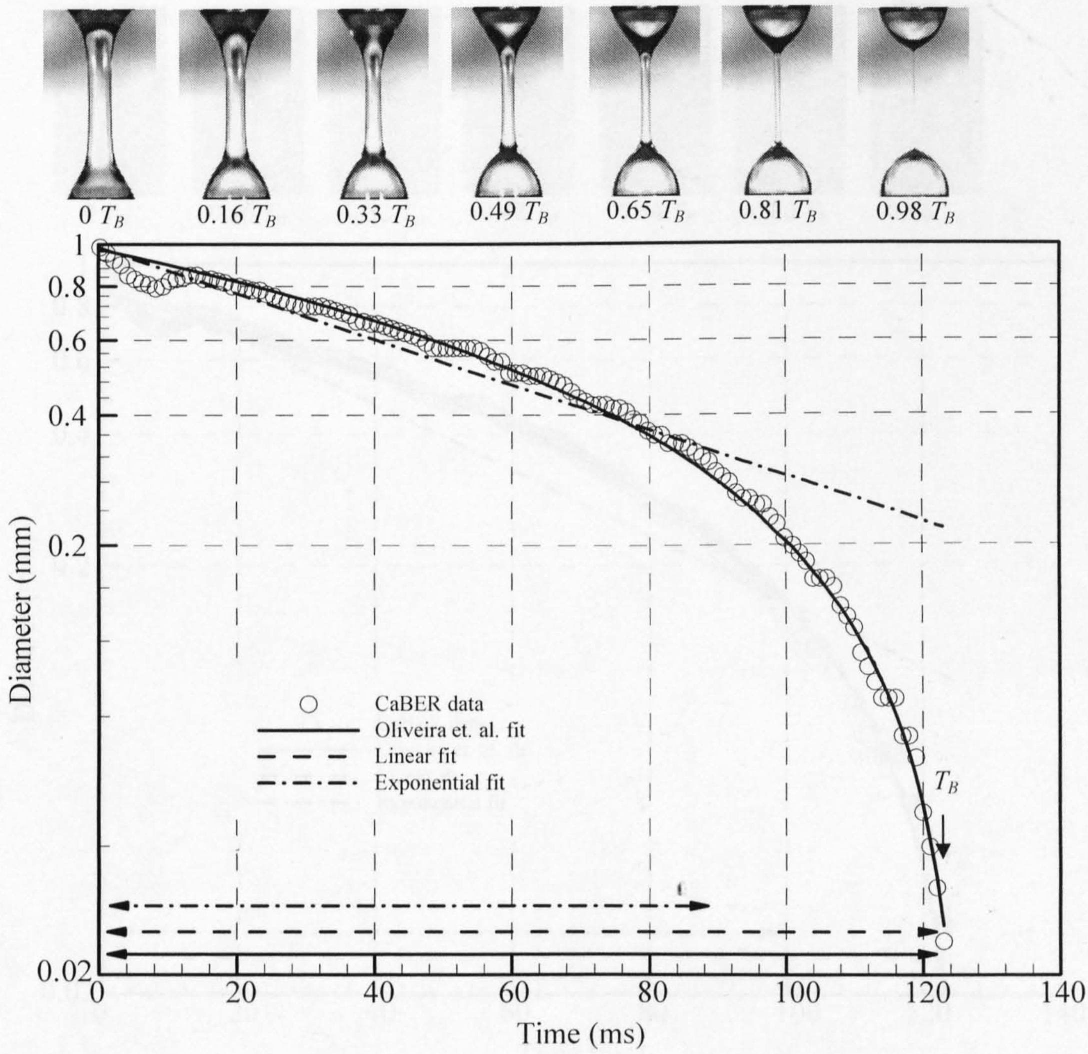

Figure 3.29: Filament diameter thinning as a function of time for 0.5% XG at 20°C ($\Lambda_{i,f}$=0.5, 2.2)

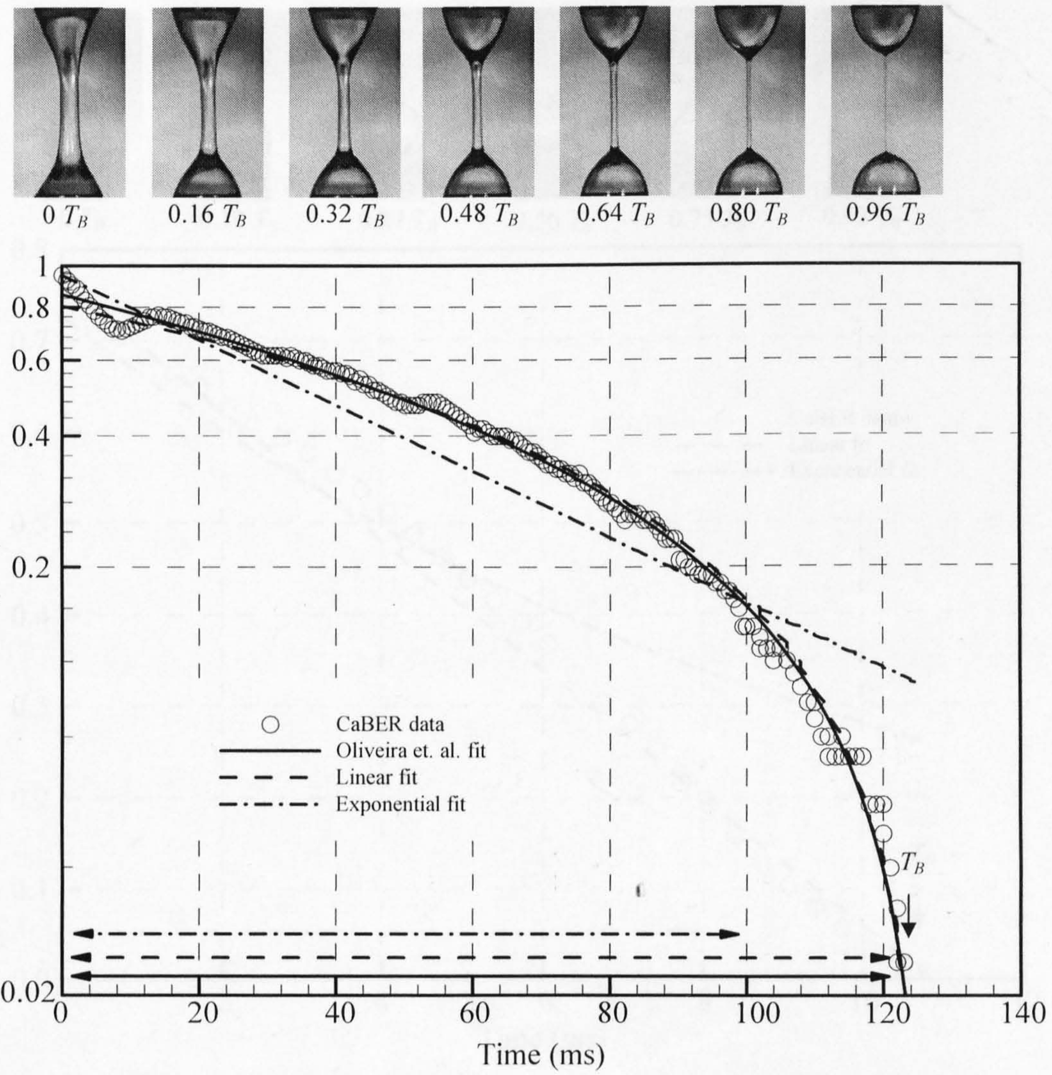

Figure 3.30: Filament diameter thinning as a function of time for 0.75% XG at 20°C ($\Lambda_{i,f}$=0.5, 2.2)

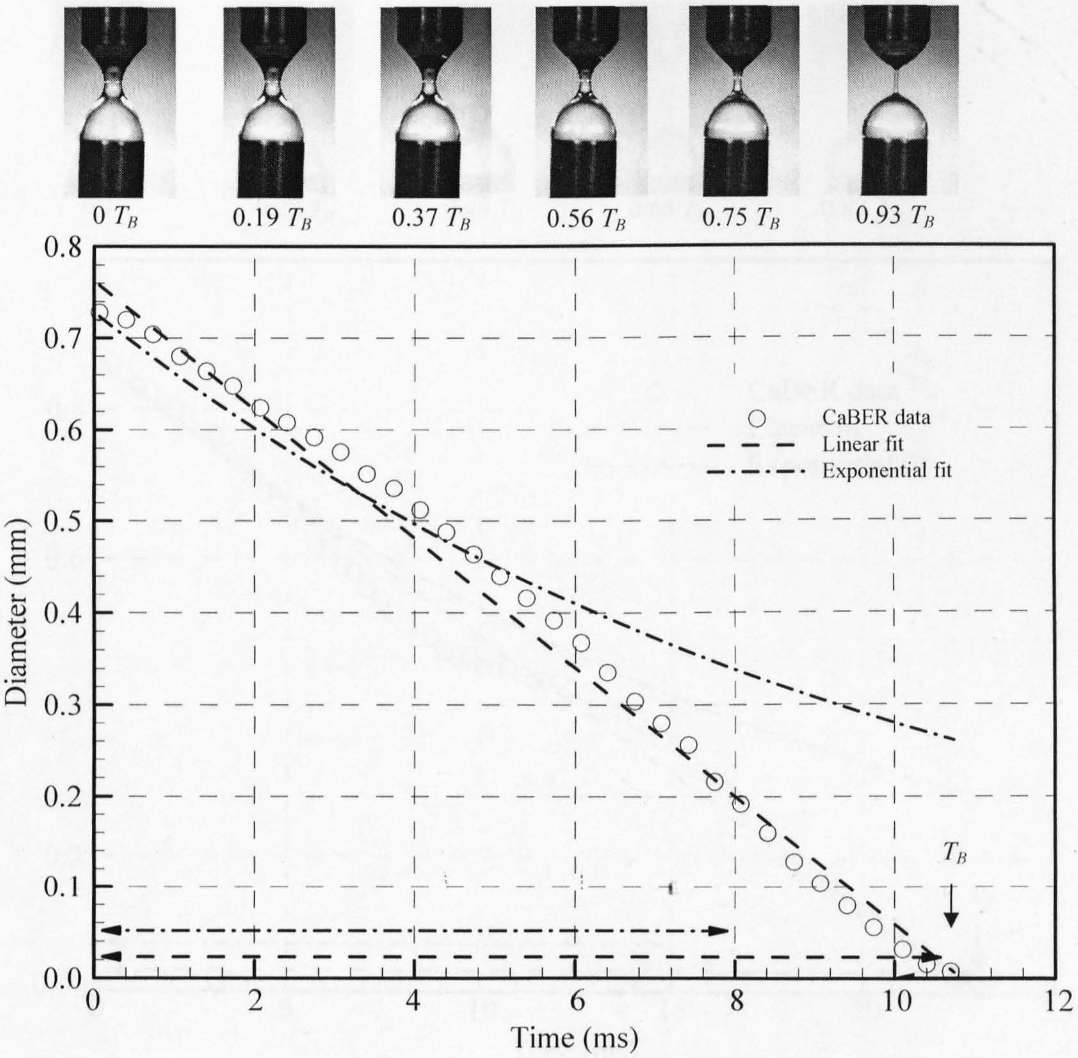

Figure 3.31: Filament diameter thinning as a function of time for 0.1% SG at 20°C – Linear plot

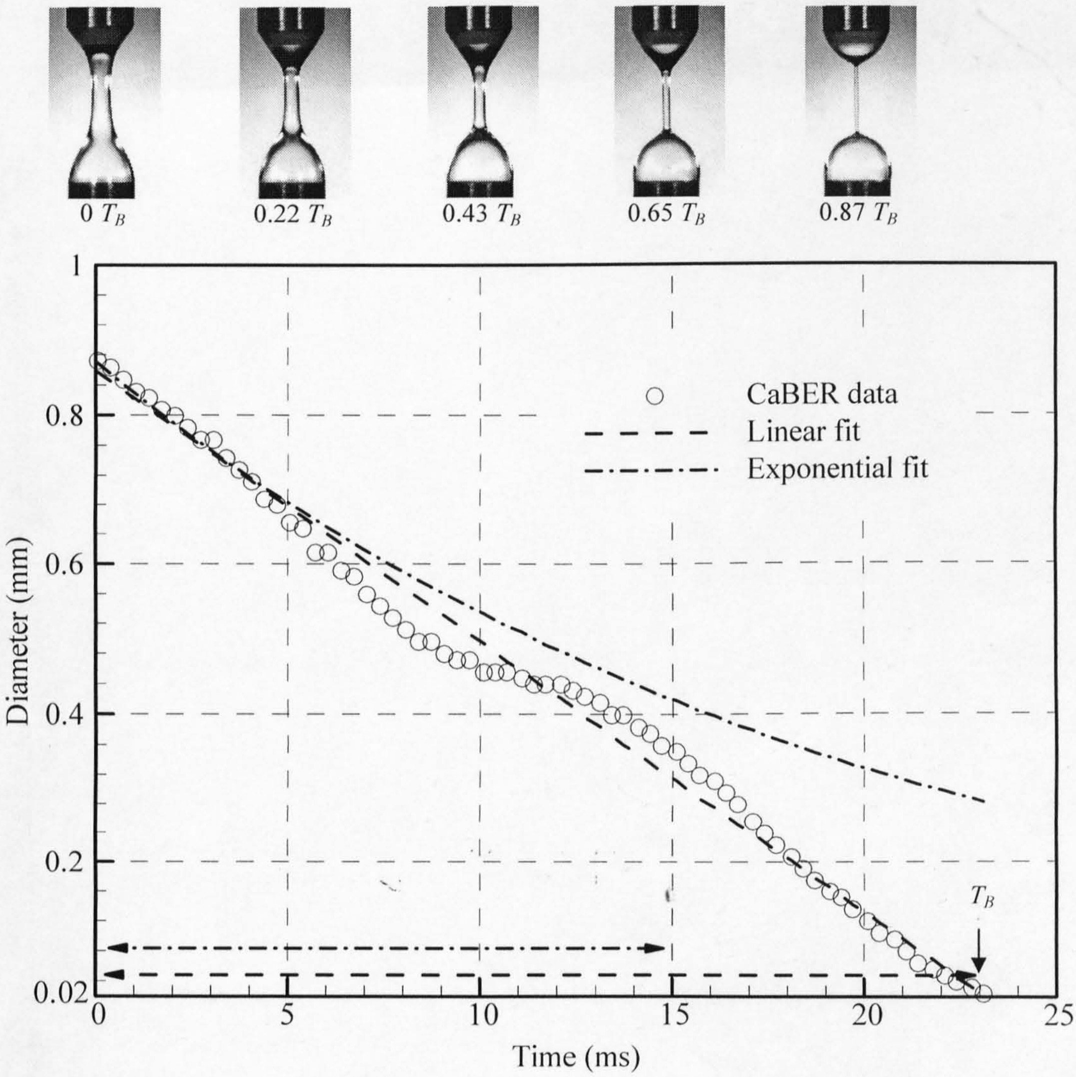

Figure 3.32: Filament diameter thinning as a function of time for 0.2% XG at 20°C – Linear plot

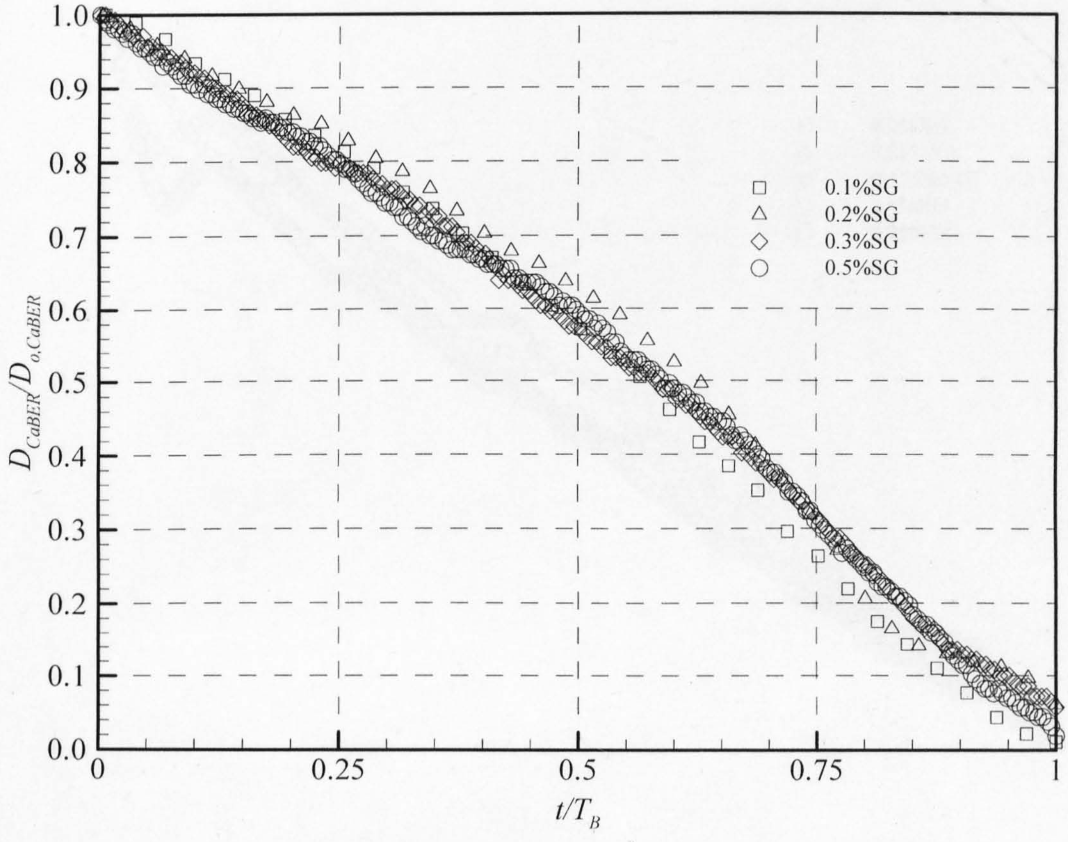

Figure 3.33: Normalized filament diameter thinning as a function of normalized time for scleroglucan at 20°C

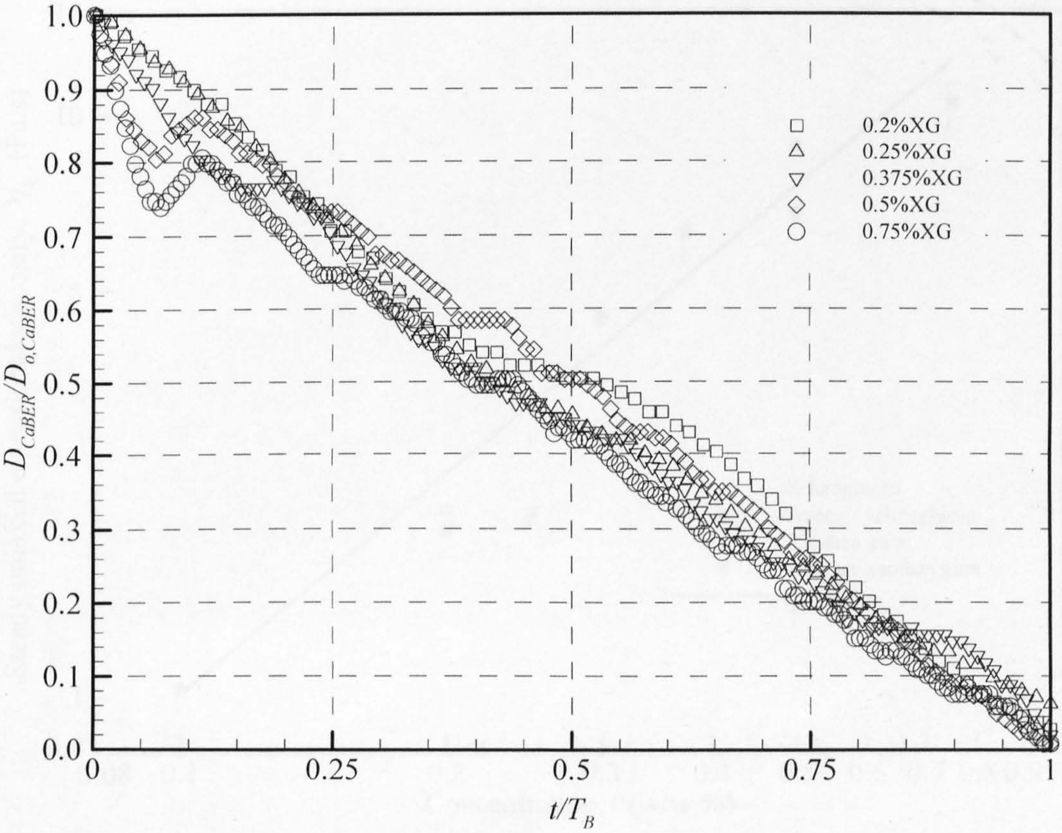

Figure 3.34: Normalized filament diameter thinning as a function of normalized time for xanthan gum at 20°C

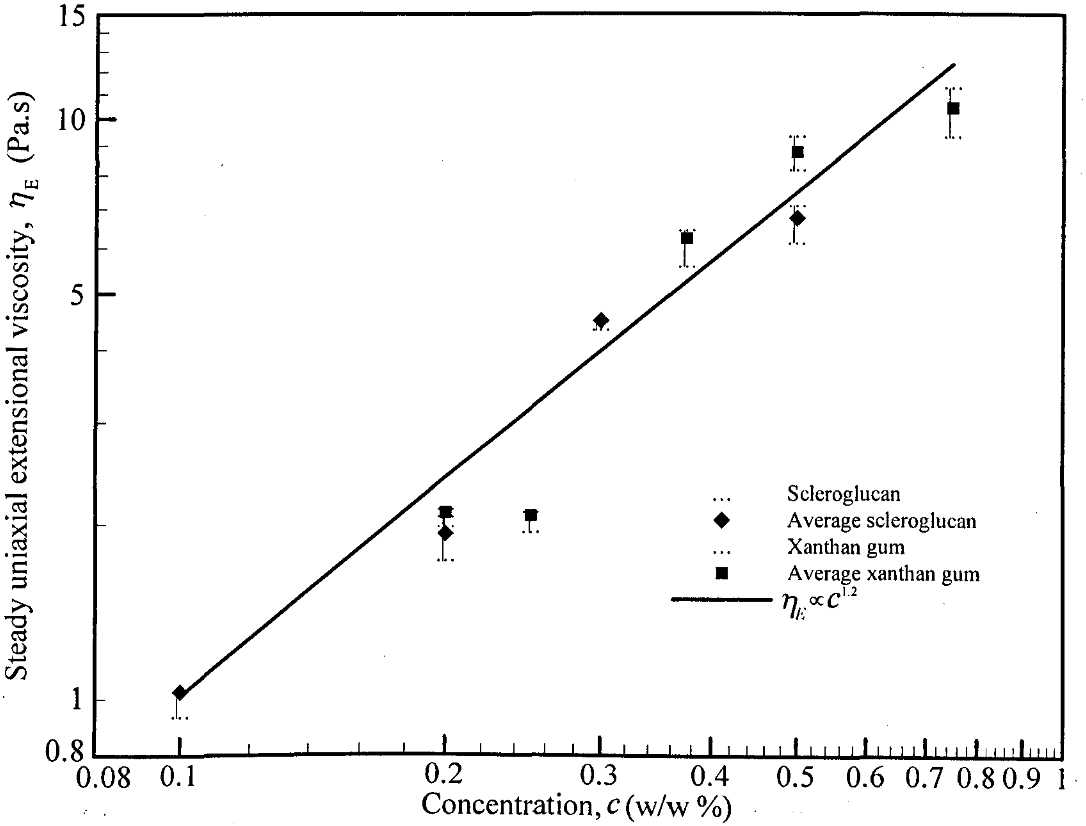

Figure 3.35: Steady uniaxial extensional viscosity versus concentration. The error bars represent data variations calculated from at least four measurements.

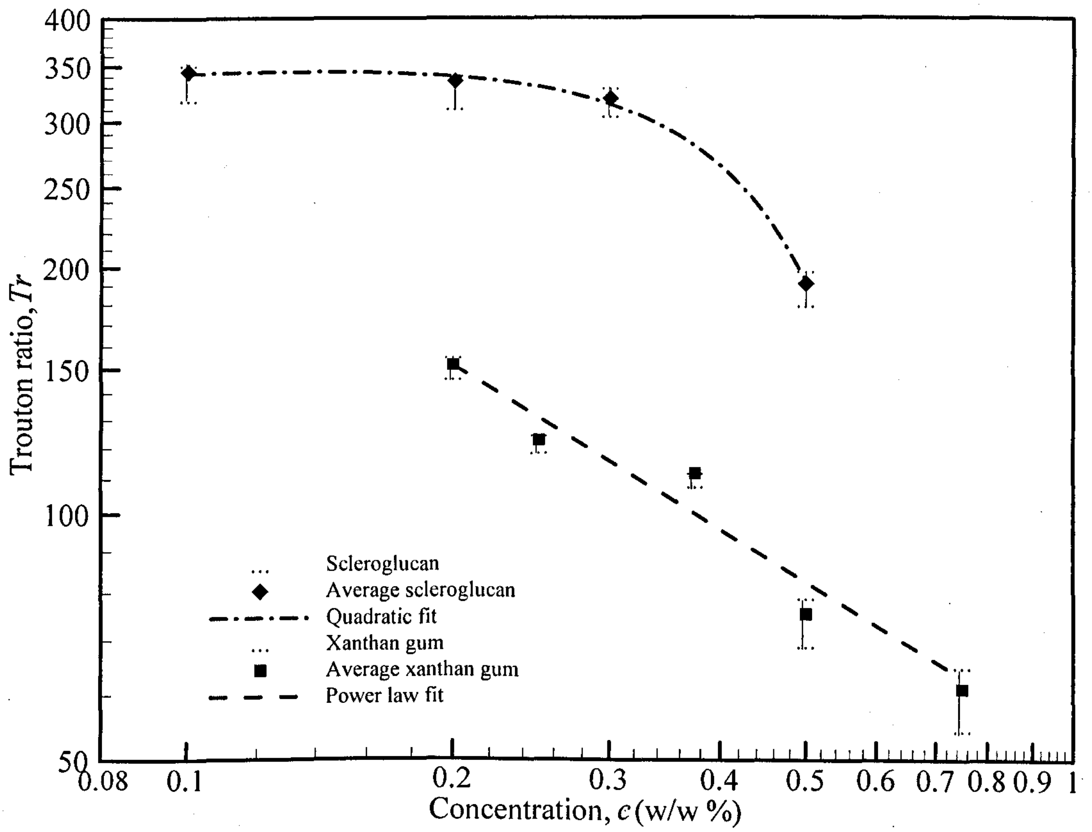

Figure 3.36: Trouton ratio versus SG and XG concentration (fit is provided to guide the eye). The error bars represent data variations calculated from at least four measurements.

4 EXPERIMENTAL ARRANGEMENT AND PROCEDURE

Flow velocity and turbulent measurements were conducted in a pipe facility described by Rosa (2008) and in an extended version of an annular pipe facility described by Gouldson (1997). Described in this chapter are the details of the flow facilities together with their associated instrumentation enabling the flow measurements.

4.1 Pipe rig configuration

Figure 4.1 shows a schematic of the 23.28 m long pipe-flow facility. The test pipe [1] consisted of 22 precision bore borosilicate glass tubes (21 tubes of 1027 mm lengths and one 656 mm long tube) and one plastic pipe at the entrance with a length of 1060 mm. The average internal diameter of the glass tube was 100.4±0.1 mm. Transparent borosilicate glass tubes were chosen due to the smooth surface of the glass and also to permit velocity measurements using a laser Doppler anemometer (LDA). The pipes were assembled with male/female stainless-steel flanges at alternate ends. The flanges, which were separated from the tube by a PTFE ring and bonded together using Devcon urethane rubber, were assembled with the tube in a jig. The PTFE ring and the Devcon urethane rubber provided a small amount of flexibility to compensate for the expansion and compression of the glass tubes and the stainless-steel flanges. The linear alignment of the glass tube assemblies was achieved through a laser target arrangement as discussed in Rosa (2008). A laser device was centrally positioned at the upstream extremity of the test section within the pipe and the target was manually placed at the other extremity. The position of the glass pipe was adjusted until the target was centred on the laser. This procedure produced a linear alignment, of the centreline of each pipe, to within ±0.1 mm of the first pipe.

The fluid was driven from a 500-*l* capacity stainless steel tank [2] by a positive displacement progressive cavity pump [3] (Mono-type, E101 with a maximum flowrate of 0.025 m^3/s). The pump was operated by a 15 kW electric motor controlled by a frequency regulator enabling constant pump speed control. Three pulsation dampers [4] located immediately after the pump outlet acted to remove pulsations resulting from the rotation of the mono pump. Fluid was filled to about three-quarter of the height of each damper leaving pressurized air pockets above the fluid, which acted as a damper. A cylindrical plenum-chamber [5] upstream of the pipe test section minimized swirl and suppressed disturbances with the intention of providing a smooth uniform inflow into the pipe. A detailed description of the plenum chamber can also be found in Rosa (2008). A Coriolis mass flowmeter [6] (Promass 63, manufactured by Endress + Hauser) was incorporated in the experimental facility giving the bulk flowrate and temperature of the fluid. Pressure-drop measurements were conducted at a location of 140*D* downstream of the inlet over a distance of 72*D*, while mean velocity profiles and turbulent fluctuation levels were measured at 22m (220*D*) downstream of the inlet of the pipe test section. These measurement locations are sufficient for the Newtonian and non-Newtonian flows to reach fully-developed conditions as they are longer than that of the laminar development length proposed by Durst et. al. (2005) for Newtonian fluid and by Poole and Ridley (2007) for power-law non-Newtonian fluids. The development length is defined as the axial distance required for the centreline velocity to reach 99% of its fully-developed value. For example, a development length of 112*D* is required for a laminar, Newtonian fluid flow at Re=2000 while the same length is required for a laminar, non-Newtonian fluid flow with a power law index n of 0.4 at the same Reynolds number based on Metzner and Reed (1955) ($Re_{MR} \equiv 8\left(\rho U_B^{2-n}/k\right)\left(n/(6n+2)\right)^n$), to be fully developed. The development length required for laminar flow has been established to be greater than the development length required for turbulent flow at the same Reynolds number (White, 2005, Munson et. al., 2002).

4.2 Annular rig configuration

A 5.81 m long annular-flow facility, essentially a modified version of the facility described in detail in Escudier, Gouldson and Jones (1995a), was utilized as shown in **Figure 4.2**. The test pipe [1] comprised of four 1041 mm long, one 625 mm long and one 718 mm long precision-bore borosilicate glass tubes, with an average internal diameter of 100.4±0.1 mm and wall thickness of 5±0.1 mm.

The pipes were assembled in a similar manner as for the pipe-flow facility described in section 4.1. The inner centrebody [2] was made of stainless-steel thin-walled tube with an outside diameter of 50.8 mm giving a radius ratio κ=0.506 and a length-to-hydraulic diameter ratio of 117 (the hydraulic diameter is defined later in Equation [4.2]). The thin wall thickness of the centrebody gave a near neutral buoyancy in water based solutions, minimizing hog and sag: i.e. the possibility of the centrebody to arch upwards or downwards is reduced. The centrebody was held in position by a thrust bearing located in the upstream end and a hydraulic jack [3] tensioned to 3 tonnes axial load on the downstream end of the annulus.

To measure the two-component velocity using LDA for the calculations of Reynolds shear stress ($\rho\overline{u'v'}$), it is important that the two laser beam pairs measuring the axial and radial components coincide at the measuring volume. The presence of a curved pipe wall changes the optical path of the beams, which are of different wavelengths, resulting in the measuring volumes of the beam pairs occupying different spatial locations, making the determination of the stress component impossible. Hence a device is required which is simple to construct and requires only simple refraction corrections to allow accurate measurements of the two-component velocity, specifically close to the pipe wall. At the test region, located 96.6 D_H downstream of the pipe entrance, a "slit module" [4] of 303 mm long, adapted from the idea by Poggi et. al.

(2002), which consisted of an open cross slit on the outer pipe of the annulus, was positioned. The open cross slit allows the laser beams to have the same optical path without any refraction. The section of the outer pipe of the annulus which contains the cross slit could be rotated to enable measurements at different points in the annular gap. A flat-faced box was constructed around the outer pipe with the cross slit to hold the fluid stationary in the outer region of the slit and also to minimize refraction of the beams giving a guarantee that the measuring volumes of the beam pairs coincide with each other. The openings of the cross slit had been constructed to be as small as possible - just sufficient to permit the laser beams to go through - with the intention of reducing the possibility of disturbing the flow field near the wall. Photographs of the test section are shown in **Figure 4.3(a)-(b)**. **Figure 4.3(a)** shows the view from the downstream end with the slit module well visible while **Figure 4.3(b)** is a close-up of the slit module with the schematic of the slit module provided in the inset.

The fluid was driven from a 500-*l* capacity stainless-steel tank [5] by a positive displacement progressive cavity pump [6] (Mono-type, E101 with a maximum flowrate of 0.025 m^3/s) with three pulsation dampers [7] to reduce pulsations. No flow conditioner was required as it has been previously determined by Escudier et. al. (1995a) that fully-developed flow is reached prior to the test region without any flow conditioner. Gouldson (1997) found that placing flow conditioners within the loop could be more detrimental to the flow quality within the rig due to the build up of debris and could further increase the disturbances at the inlet of the test section.

A Fischer and Porter MAG-SM Series 1000 electromagnetic flowmeter (model 10D1) with a maximum capacity of 0.0333 m^3/s [8] was also incorporated in the experimental facility. The temperature of the fluid was monitored using a platinum resistance thermometer, with an accuracy of ± 0.1°C, positioned inside the tank.

Pressure-drop measurements were conducted at a location of $75.8D_H$ downstream of the inlet to the pipe test section over a distance of $41.3D_H$. Mean velocity profiles and Reynolds stress measurements, i.e. $\overline{u'^2}$, $\overline{v'^2}$ and $\overline{u'v'}$ were performed at the slit module located $96.6D_H$ downstream of the inlet. Measurements were also conducted using only a flat-faced optical box [9], filled with water, without the cross-slit at a location $104.7D_H$ downstream to compare and study the effects of the presence of the cross slit. The tangential velocity fluctuation component w' was measured using only the flat-faced optical box. Poole (2009) has established that for radius ratios $\kappa \geq 0.5$ the required development length for laminar Newtonian flow is equal to that of the equivalent channel flow; e.g. a development length of $88D_H$ is required for Re=2000. As the development length for turbulent flow is known to be significantly lower than that of laminar flow at the same Reynolds number (White, 2005; Munson et. al., 2002) it is considered that the distance from the inlet to the location of measurements in the annular-flow study was more than sufficient for the flow to reach fully-developed conditions.

As mentioned in Escudier et. al. (1995a), the utilization of a stainless-steel centrebody results in back reflections of the Doppler signal close to the wall of the centrebody. To reduce this effect, the traverse was operated vertically to obtain complete profiles of both axial and radial velocity components.

4.3 Test fluid

The glycerine-water solution was prepared by first adding the 60% (weight) glycerine into the tank. Water was then added until the total volume of fluid was sufficient to fully fill the rig (~500 litre) during pump operation. The solution was circulated around the whole flow loop until homogeneity was achieved. Homogeneity was confirmed by measurements of the shear viscosity of the fluid collected from the flow loop every 30 minutes.

A quantity of approximately 700 litres of tap water was used as a solvent for the test fluid. Prior to the addition of polymer, water was circulated within the facility to remove any dissolved air. Removal of air bubbles present in the fluid was necessary as they can act as light scatterers, interfering with the LDA measurements (Naqwi and Durst, 1991; Warholic, 1997). Mixing of part of the solvent with the polymer powder was achieved by circulating the polymer solution within the mixing loop at a low pump speed for at least 5 hours before the mixing loop was opened and the solution was circulated in the flow loop, allowing further mixing with the rest of the solvent in the pipe for at least another 5 hours, until the solutions appeared to be visibly homogeneous. The homogeneity of the solution was confirmed by comparing the viscometric data with a small sample (~500 ml) solution of the same concentration prepared separately. To retard bacteriological degradation of the solution, 37% (w/w) formaldehyde was added to the polymer solution at a concentration of 100ppm. Seeding particles (Timiron MP-1005, mean dia. $\approx 5\mu m$ supplied by S. Blanck Ltd) were also added at a concentration of 1ppm in order to increase the signal to noise ratio and the data rate for the LDA measurements. The polymer solution was then left to hydrate in the rig for at least 24 hours prior to the LDA measurements. All polymer solutions in the pipe and annular-flow facility were mixed in the same manner. Measurements of fluid rheology for all the solutions were conducted prior to and after each LDA profile to check for signs of mechanical and bacteriological degradation; a decrease of the shear viscosity by more than 5% from the initial state was taken as a sign of degradation.

Special treatments were required for the carbopol solution where, apart from the procedure listed above, the solution was also neutralized using laboratory grade 2N sodium hydroxide during mixing prior to the LDA measurements. Moreover, due to the thixotropic nature of carbopol, the solution within the flow loop was circulated at 30% of the maximum pump speed for 30 minutes prior to any measurements. This pre-shear was necessary to ensure reproducibility of the results by standardization of the solution shear history.

Mechanical and bacteriological degradation in polymer solutions results in a decrease of the drag-reduction effectiveness (Hoyt, 1985). Mechanical degradation is due to the high deformation experienced, especially when the fluid goes through the pump or any contraction section, resulting in molecular breakage. The mechanical degradation has been reported to be in inverse proportion to concentration (Nakano and Minoura, 1975; Moussa and Tiu, 1994) and also a function of structural chain rigidity. Rigid polymer solutions have been discovered to exhibit better degradation resistance compared to flexible polymer solutions (Paschkewitz et. al., 2005; Hoyt, 1985). Bacteriological degradation, on the other hand, occurs due to the organic nature of the polymer solutions but can be minimized by addition of a suitable amount of biocide. As the fluids utilized throughout this study were circulated for long periods of time, it was critical for the chosen fluid to have a good degree of resistance to mechanical degradation. To obtain accurate and repeatable results, only a minimal temperature difference (within ±1°C) was allowed during the measurements.

4.4 Pressure-drop measurement

The pressure drop was measured by means of a differential pressure transducer, GE Druck (LPX9381), capable of measuring up to 5000 Pa. The transducer was connected to a computer via a LabJack data logger. The readings from the transducer were periodically checked for accuracy with a high accuracy differential pressure transducer, MKS Baratron by MKS Instruments Inc., USA. The 1-mm diameter pressure taps in the pipe flanges were surface polished to avoid disturbing the flow, which could generate further uncertainties in the readings. The pressure taps were connected to the transducer via clear vinyl tubing filled with deionised water. Deionised water was utilized to eliminate corrections due to different specific gravities. Readings of the transducer under no-flow conditions were made at the beginning and end of each measurement to account for any drift where the zero flowrate readings were monitored and subsequent readings were corrected accordingly. The wall shear stress can then be calculated using the pressure gradient via

$$\tau_W = \frac{\Delta p}{L}\frac{D}{4} \qquad [4.1]$$

where $\Delta p/L$ is the pressure gradient over the length, L of the pipe section with internal diameter, D. For the annular pipe, the diameter is replaced by the hydraulic diameter, D_H given by

$$D_H = \frac{4A}{P} = \frac{4\frac{\pi}{4}\left(D_o^2 - D_i^2\right)}{\pi\left(D_o + D_i\right)} = D_o - D_i \qquad [4.2]$$

4.5 Laser Doppler Anemometer (LDA)

4.5.1 Specifications

Velocity profiles and the Reynolds stress measurements were conducted using a Dantec Fibreflow laser Doppler anemometer system supplied by Dantec Electronic Ltd, UK, comprising of 60×10 probe and a Dantec 55×12 beam expander, used to obtain a small measuring volume and improved signal to noise ratio, together with Dantec Burst Spectrum Analyzer signal processors (model 57N10 and 57N20). The laser source used (Model Stellar-Pro-CE) was manufactured by Modu-Laser, LLC and supplied by Laser Physics, UK. The maximum power of the laser was nominally 150 mW. The Argon ion laser provided three wavelengths of light of which one was used for the pipe-flow measurements; the green beam with a wavelength of 514.5 nm; and two were used to allow two-component measurements to be made for the annular-flow study; the green and the blue (wavelength of 488 nm).

The lens focal length was 160 mm and the measured half angle between the laser beams was 8.4° which produced a measuring volume with a diameter of 40 μm and a length of 0.27 mm in air, calculated using the procedure of Buchhave et. al. (1979). For the annular-flow measurements a different probe head lens with a focal length of 160 mm and measured half angle of 9.14° was utilized. The measuring volume produced was 36 μm in diameter and 0.22 mm in length. A manual traverse in conjunction with digital vernier scales was utilized to move the probe head in the radial and vertical directions, with an accuracy of ±0.001mm and ±0.01mm respectively.

Measurements were conducted in forward-scatter mode while off-axis scattering mode was utilized in measuring the tangential component for annular flow. Off-axis scattering can reduce the effective size of the measuring volume and hence reduces problems with reflections especially near the inner centrebody (Jensen, 2004). However the data rate was also reduced in off-axis scattering mode. At each location across the test section, 10000 to 30000 data samples were collected. BURSTware 3.23 (Burst spectrum analyzer) software supplied by Dantec Measurement Technology was used to process the raw velocity data.

The velocity profiles taken from both the circular and annular pipe flows were integrated and compared to the flowrate values given by the flowmeters as a consistency check. Flowrates indicated by the flowmeters were found to be within 2% of the values estimated from the velocity profiles for all runs.

4.5.2 Probe reference location

Prior to the LDA measurements, a reference point at the inner wall of the outer glass tube was established. This point was determined by monitoring the photomultiplier voltage of the LDA system where a maximum signal was achieved at the wall because the wall acts as a stationary scatterer of light resulting in a high amount of reflections. This location is then assumed to be the location of the interface between the glass tube and the fluid within the pipe. The probe volume was then moved to the opposite wall position to further verify the reference point. To further precisely obtain the location of the LDA measurement control volume, linear interpolation of the last two or three points in the velocity profile close to the wall was performed to give the zero velocity location. This point, taken as the position of the wall, allowed further adjustments to the wall location in the velocity profiles to be made, typically of the order of 0.2mm.

4.5.3 Axial, tangential and radial LDA measurements

Figure 4.4 shows the laser beam orientations and traversing directions when measuring the axial, radial and tangential velocity components. The axial velocity component - which is parallel to the direction of the fluid flow - was measured by placing the beams in the *y*-plane and traversing the probe in the *z*-direction. The axial component could also be measured by traversing the *y*-plane beams vertically in the *y*-direction. The tangential component was measured by rotating the beams to the *x*-plane. The same horizontal traverse action was applied for the tangential measurement. Traversing the probe-head in the *y*-direction with the beams in the *x*-plane allows the measurement of the radial component to be made.

For the calculations of the Reynolds shear stress, the axial and radial components were measured simultaneously with the arrival time of the particles monitored for the cross-moment $\overline{u'v'}$ to be measured. The magnitude of the time coincidence window required in determining the cross moment was selected such that it is greater than the measurement volume diameter, d_{vol} divided by the highest velocity present in the flow, U_{max} (Brown, 1989). The determination of the required coincidence window time involves gradually increasing the time from a minimum value equal to d_{vol}/U_{max} and monitoring the corresponding calculated cross moment, $\overline{u'v'}$ until it is no longer changing with further increase in coincidence window time. However the time window should also be small enough so that the measurements from one particle and the next are not mistakenly taken as from the same scatterer i.e. the arrival time between two "consecutive" particles should be greater than the coincidence time (Brown, 1989). Hence, further increasing of the time window can result in the calculated cross moment value diverging again.

The perpendicularity between the pipe axis and the laser beam planes was determined using the method proposed by den Toonder and Nieuwstadt (1997) where the probe was rotated about its optical axis and subsequent measurements at several rotation angles were taken. The probe was then fixed in a position where the measured mean velocity using the vertical laser beams (i.e. mean radial and tangential velocity) in the centre of the pipe, or the centre of the gap for the annulus, was zero.

4.5.4 Refraction of beams

The change in the refractive index as the laser beams travel into the test section results in refraction of the beams. In the pipe facility, i.e. without the slit module, the axial and tangential velocities and their respective locations were corrected according to Bicen (1982). Only one component of velocity could be obtained at any one time due to the refraction of two beam pairs of different wavelengths, in this case the green and the blue beams, at the curved surface of the pipe wall resulting in the measuring volumes of the beam pairs occupying different spatial locations. The radial velocity measurements were conducted with a light box in place to minimize the amount of refraction of the beams and to obtain data closer to the wall. The radial velocities and locations were corrected using the ray-tracing method outlined by Presti (2000). The method provides corrections for the small tangential component within the measured radial velocity.

The velocity measurements in the annular-flow facility were conducted within the cross-slit module or using the flat-faced optical box without the cross slit. With the optical box measurements, all three components were corrected using the method of Presti (2000) while for the measurements with the cross slit, only a simple correction to the position was required as the beams only travelled through a flat-faced wall. **Table 4.1** lists the refractive indices of the fluid and the solid components used in the refraction correction calculations.

4.5.5 Errors and uncertainties

The uncertainties which will be considered in this study are the positional error of the measuring volume and the velocity measurements by the LDA system. The positional error is due to the method used to find the probe reference location and also the accuracy of the traverse system. The positional error can be minimized by plotting the mean axial velocity profiles and shifted accordingly such that a linear profile was obtained near the wall as described in section 4.5.2. The uncertainty involved in this method is about half of the measuring volume length, which is ± 0.1mm.

There are several uncertainties involved in the velocity measurements by any LDA system. The assumption of uniform density and concentration of the scattering particles allows these uncertainties to be narrowed to three main sources which are related to the velocity data obtained; velocity bias, statistical uncertainty and velocity gradient broadening. A more detailed discussion on the uncertainties in the LDA measurements is provided by Buchhave et. al. (1979) and Durst et. al. (1981).

As the measurements conducted within a volume are not continuous, LDA approximates the overall flow statistics in the volume by the sample statistics of the measured particles. The measurements on these particles which are passing through the measuring volume over a limited time frame results in high dependency on the particle arrival rate. Ensemble averaging these measured data to obtain the sample statistics could, in turn, result in a biased velocity distribution towards higher particle velocities due to the more frequent arrival of the faster particles, a problem known as the velocity biasing effect (Buchhave et. al., 1979; Durao et. al., 1980). This effect is particularly significant in turbulent flows.

The velocity biasing effect can be compensated by using a time-averaged velocity bias correction or the transit-time weighting method (Dimotakis, 1976),

$$u = \frac{\sum u_i t_i}{\sum t_i},\ u' = \frac{\sum (u_i - u)^2 t_i}{\sum t_i}, \overline{u'v'} = \frac{\sum (u_i - u)(v_i - v) t_i}{\sum t_i} \qquad [4.3]$$

where u_i is the individual velocity while t_i is the corresponding transit time. This method is already incorporated into the BURSTware software utilized for the LDA system.

Assuming a Gaussian velocity distribution, the relative statistical error of both mean velocity (u) and turbulence intensity (u') can be estimated (Yanta and Smith, 1973) by:

$$Error_u = Z_C \frac{\frac{\sigma}{\mu_s}}{\sqrt{N_s}} \qquad [4.4]$$

$$Error_{u'} = Z_C \frac{1}{\sqrt{2N_s}} \qquad [4.5]$$

where N_S is the sample size, μ_s and σ are the average and standard deviation, respectively. For 95% confidence level with a sample size bigger than 50, Z_C = 1.98. With an average of 20000 velocity samples collected per point in this study and assuming $\mu_s = U_B$ and $\sigma = u'_{max}$, a maximum statistical error, for a 95% confidence interval, was less than 0.5% in mean velocity and less than 1.0% in the turbulence intensity.

Velocity gradient broadening is produced when there is a mean gradient across the measurement volume resulting in the arithmetical average of the velocities not equal to the average velocity within the measuring volume. However, due to the small measuring volume size utilized in this study gradient corrections to the measured velocities were unnecessary (Gouldson, 1997; Presti, 2000).

The sensitivity of the polymers, scleroglucan and carbopol to shear history effects as discussed in **Chapter 3** could also introduce uncertainties in the data. Care has been taken to provide uniform shear history prior to any LDA measurements for the polymer solutions. This experimental protocol has managed to slightly reduce the thixotropic effect where repeatability checks on the polymer flow, scleroglucan, a few days apart showed overall variations of less than 0.5% in the mean and less than 4% in the turbulence components. A replication test conducted with nominally identical conditions but with a different hydration period was also performed. The solution was left for more than two days instead of just for 24 hours prior to testing to allow more complete gelation. Overall variations of less than 2% and 8% for the mean and turbulence components respectively were observed. As the carbopol solutions become increasingly turbid beyond four days of preparation, repeatability measurements were conducted only a day apart and showed variations of less than 2% in the mean and 6% in the turbulence components at a location close to the inner wall in the annular pipe.

Given the uncertainty estimates and the repeatability analysis, the maximum experimental uncertainty in the mean velocity was then estimated to be less than 4% and less than 10% for the turbulence intensities.

TABLES

Table 4.1: Refractive indices of the measuring test section

Medium	**Air**	**Wall of slit module**	**Glass tube**	**Water**	**Glycerine**	**Polymer solutions**
Refractive index, *n*	1.000	1.478	1.478	1.333	1.382	1.333

The refractive indices of all the non-Newtonian fluid tested in this research work, determined using an ABBE 60/ED high accuracy refractometer (type degree scale, ± 0.001%), have almost the same value as the solvent.

FIGURES

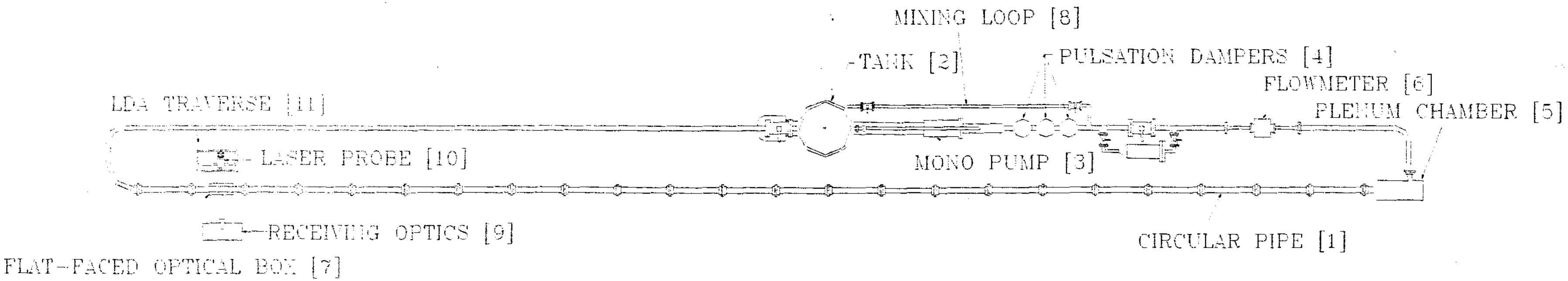

Figure 4.1: Schematic diagram of the pipe-flow loop

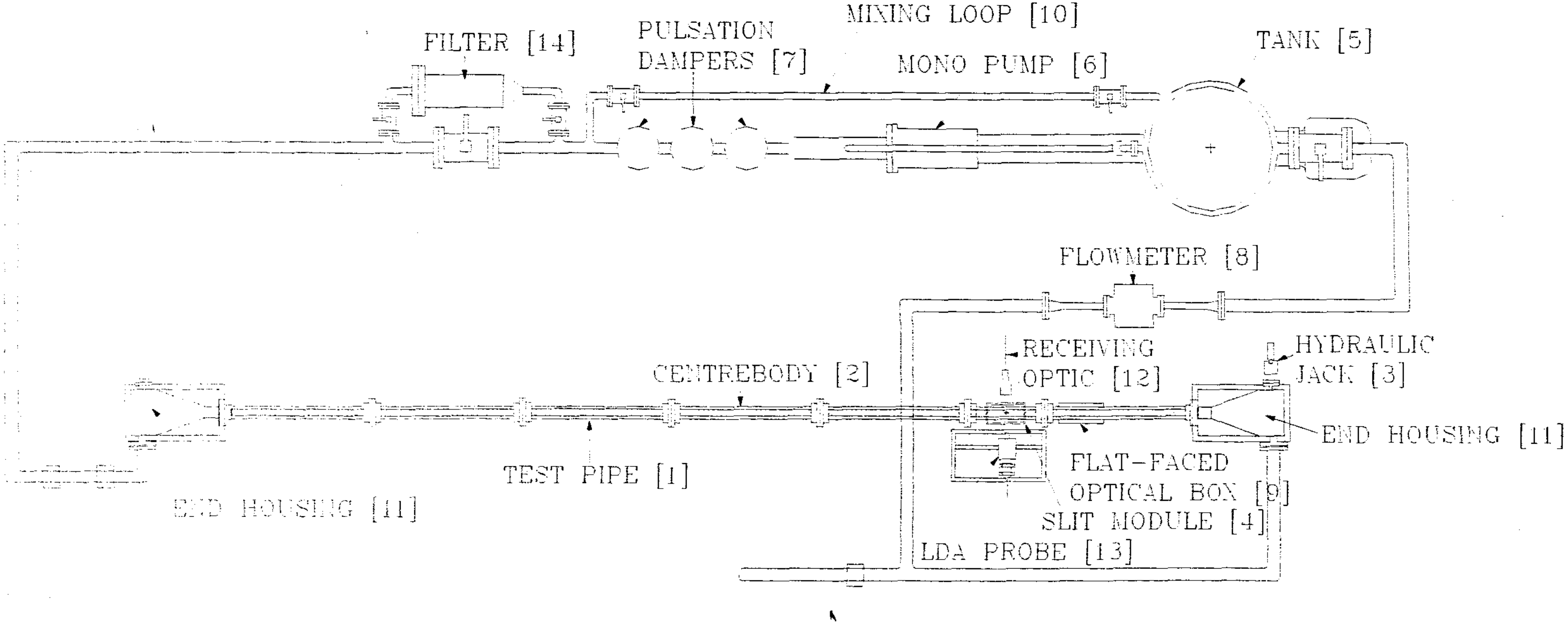

Figure 4.2: Schematic diagram of the annular-flow loop

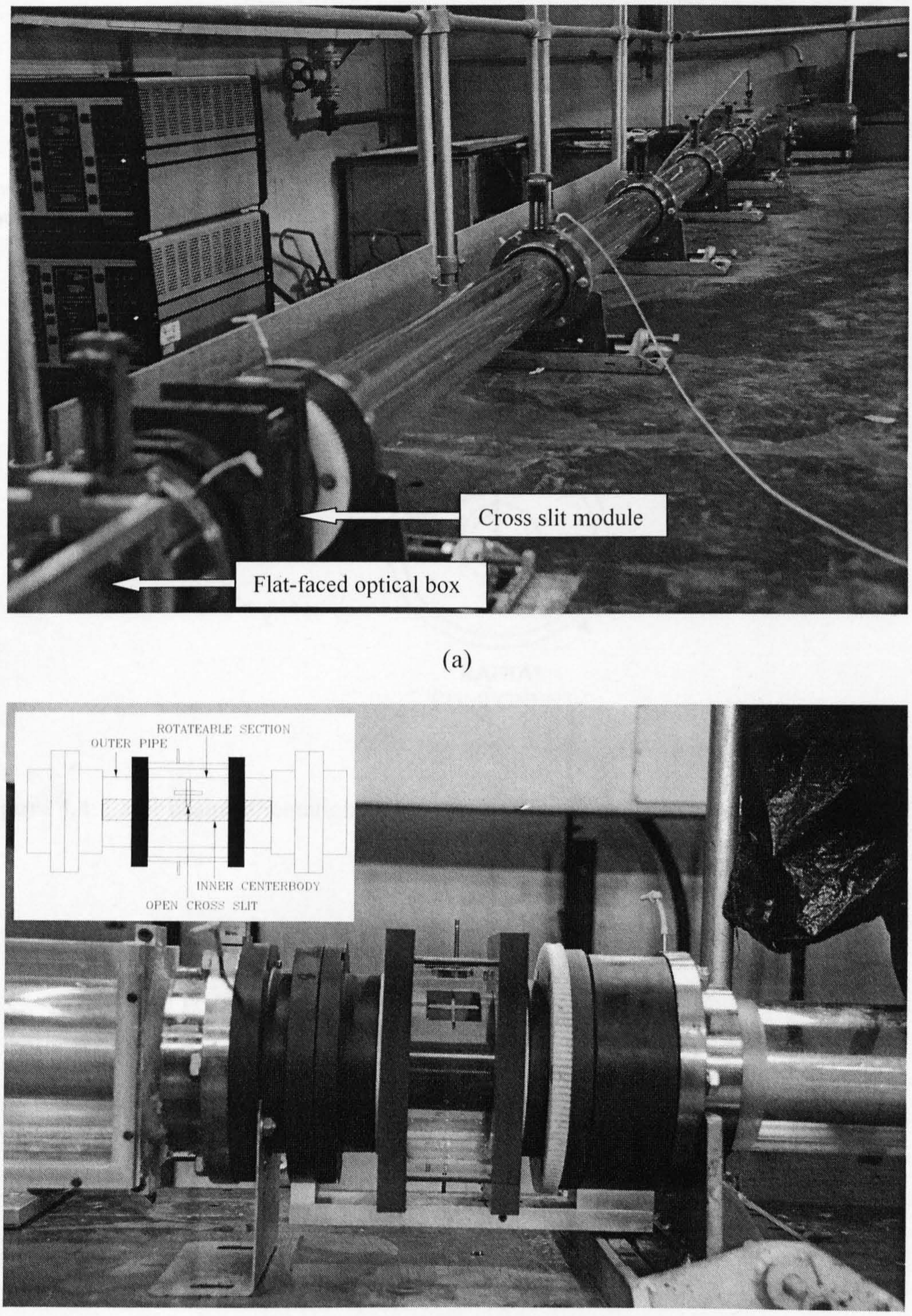

(a)

(b)

Figure 4.3(a-b): Photographs of the annular-flow facility with closeup of the slit module

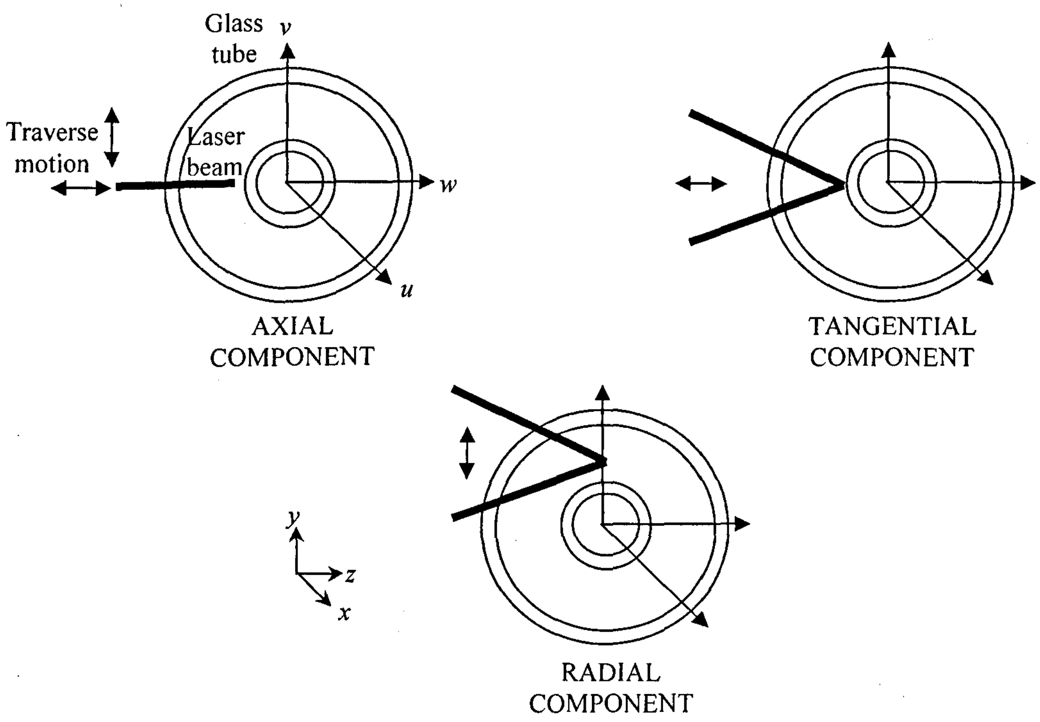

Figure 4.4: Laser beams orientation and traversing directions for axial, radial and tangential measurements

5 PIPE FLOW

In this chapter the results of experiments carried out on water and aqueous solutions of scleroglucan at several concentrations (0.005% - 0.075% w/w) within the turbulent regime in the pipe-flow facility are discussed. The background of the work together with the definitions of the parameters used to analyze the results are also presented.

5.1 Background

5.1.1 Newtonian laminar and turbulent pipe flow

Analytical and empirical solutions for Newtonian pipe flows are well-established and readily available in the literature. Knudsen and Katz (1958) and Bird et. al. (1977), for example, have provided extensive derivations for fully-developed, Newtonian, isothermal laminar flow in a pipe. For a Newtonian fluid the Fanning friction factor, f and the Reynolds number, Re $(\equiv \rho U_B D/\eta)$ relationship is given by Poiseuille's law (Schlichting, 1987) as

$$f.Re = 16. \qquad [5.1]$$

The Fanning friction factor, which represents the non-dimensional wall shear stress, can be calculated from the wall shear stress, τ_W via

$$f = 2\tau_W / \rho U_B^2 . \qquad [5.2]$$

The theoretical axial velocity profile for a laminar flow, known as the Hagen-Poiseuille profile, (see e.g. Munson et. al., 2002) is

$$u = U_{max}\left(1-\left(\frac{r}{R}\right)^2\right) \qquad [5.3]$$

where U_{max} is the maximum velocity given by

$$U_{max} = \frac{\Delta p}{4\eta L} R^2 . \qquad [5.4]$$

The maximum velocity, which has been established to be located at the centreline of the pipe is equal to twice the bulk velocity within the laminar flow regime, i.e. $U_{max} = 2U_B$.

The *f-Re* empirical relationship for the turbulent pipe flow of Newtonian fluid, known as the Blasius approximation, is

$$f = 0.0791 Re^{-\frac{1}{4}} . \qquad [5.5]$$

This equation is valid up to a Reynolds number of 100,000 (Knudsen and Katz, 1958).

In contrast to laminar flow there is no single equation that can describe the velocity profile over the entire pipe in a turbulent flow. A turbulent flow near a wall can be divided into three layers; the viscous sublayer (or laminar sublayer), the buffer layer and the Newtonian core region (or inertial sublayer). Ludwig Prandtl (White, 2005) proposed the use of "wall coordinates" to describe these layers where u^+, the dimensionless velocity and y^+, the dimensionless wall distance are utilized:

$$u^+ = \frac{u}{u_\tau}, \; y^+ = \frac{\rho y u_\tau}{\eta} . \qquad [5.6]$$

The term u_τ, the so called "friction velocity" as it has the dimensions of velocity, is given by

$$u_\tau = \sqrt{\frac{\tau_W}{\rho}} . \qquad [5.7]$$

In the viscous sublayer, where the effect of turbulence is reduced (Tennekes and Lumley, 1972), the shear stress is essentially constant and is equal to the shear stress at the wall which can be calculated from Newton's law given in Equation [3.2]. The viscosity dominates in this region and the Reynolds shear stress contribution, $\rho\overline{u'v'}$ is negligible. Within this region, in wall coordinates,

$$u^+ = y^+ \ . \tag{5.8}$$

In the inertial sublayer, where the viscosity effects vanish and the Reynolds stress dominates, the well-known log law (see e.g. Tennekes and Lumley, 1972) applies where

$$u^+ = 2.5 ln y^+ + 5.5 \ . \tag{5.9}$$

The empirical constant of 5.5 was adopted from Nikuradse's experimental data (Schlichting, 1987) for turbulent flow of water in pipe. However, the exact value of the constant is still a matter of dispute due to the scatter of data from various studies (see den Toonder and Niewstadt, 1997; Zagarola and Smits, 1998 and Afzal, 2001, for further discussion of this issue). Between these two layers lies the buffer region where both the viscous and turbulent shear stresses are important. The location of maximum turbulent production is usually within this region (Pope, 2000). It is important to note that the y^+ limit to classify the various layers or zones varies from one source to another. However, here we follow Tennekes and Lumley (1972) and Pope (2000) and take the following values to apply; for the viscous sublayer, $0 \le y^+ \le 10$, for the buffer layer, $10 < y^+ \le 30$ and for the Newtonian core region, $y^+ > 30$.

5.1.2 Non-Newtonian laminar and turbulent pipe flow

The friction factor relationship given by Equation [5.1] is also valid for fully-developed laminar non-Newtonian flow in circular pipes provided that the Reynolds number defined by Metzner and Reed (1955) for a power-law fluid is utilized. This generalized Reynolds number is

$$Re_{MR} = \frac{\rho U_B^{2-n}}{k} \cdot 8\left(\frac{n}{6n+2}\right)^n . \tag{5.10}$$

An analytical solution for the velocity profile of a power-law fluid in the laminar regime is given as (Bird et. al., 1977; Barnes et. al., 1989)

$$u = U_{max}\left(1-\left(\frac{r}{R}\right)^{\frac{n+1}{n}}\right) \qquad [5.11]$$

where n is the power law index while U_{max} is related to the power-law index and the bulk velocity, U_B via

$$U_{max} = \frac{Q(3n+1)}{\pi R^2(n+1)} = U_B\left(\frac{3n+1}{n+1}\right). \qquad [5.12]$$

The expression above shows that the flow within the centre region of the pipe becomes more uniform as the fluid becomes more shear thinning.

In non-Newtonian turbulent flow the friction factor is bound between two asymptotes (refer to **Figure 2.1**); the Blasius approximation as given in Equation [5.5], and the empirical relation proposed by Virk (1975), also known as Virk's maximum drag reduction asymptote,

$$f = 0.58\,Re^{-0.58}. \qquad [5.13]$$

The Reynolds number for a non-Newtonian fluid utilized for this equation is defined based on the bulk velocity, pipe diameter and the shear viscosity at the wall ($Re \equiv \rho U_B D/\eta_W$). This Reynolds number definition, used by Pinho and Whitelaw (1990), Ptasinski et. al. (2001) and Escudier et. al. (2009a), amongst others, is suitable to describe the fully-developed flow field as it is physically based on a fluid quantity in the flow, i.e. the fluid viscosity at the wall, and hence will be employed throughout this study (in preference to the Metzner and Reed Reynolds number defined in Equation [5.10]). The wall viscosity, η_W was obtained from the Carreau-Yasuda model (Yasuda et. al., 1981) fitted to the steady-shear viscosity data using the wall shear stress determined from the pressure-drop measurements. The degree of deviation of the friction factor for non-Newtonian turbulent flow from the Blasius approximation depends on many parameters such as the type of polymer, polymer concentration and geometry of the pipe, amongst other factors (Seyer and Metzner, 1969; Berman, 1980 and Gasljevic et. al., 2001). The maximum drag reduction asymptote, however, is independent of pipe diameter, type of polymer, molecular weight and concentration (Virk, 1975).

As discussed in detail in **Chapter 2** the review by Virk (1975) on the subject of drag reduction provided a very extensive phenomenological understanding of the effects on polymer addition on fluid flow. He proposed a three layer model for drag-reducing polymer flow as illustrated in **Figure 5.1**; close to the wall is the viscous sublayer where $u^+ = y^+$, near the pipe axis is the Newtonian core region and between these layers is the buffer layer. The velocity profile within the Newtonian core region is also bound by two asymptotes; the Newtonian log law as given by Equation [5.9] and the maximum drag reduction asymptote (Virk et. al., 1970; Virk, 1975) given as

$$u^+ = 11.7 \ln y^+ - 17.0 \ . \qquad [5.14]$$

5.2 Results and discussions

5.2.1 Pressure-drop measurements

The Fanning friction factor, *f* is plotted against Reynolds number, *Re* for water and a wide range of scleroglucan concentrations (0.005% - 0.075% w/w) in **Figure 5.2** with the lines included in the figure to guide the reader's eye. Due to the low viscosity of most of the solutions, especially those for which $c < c^*$, laminar flow conditions were not attainable within the operating range of the flow loop. The majority of pressure-drop measurements taken were therefore limited to the turbulent regime and little information could be gleaned regarding transitional Reynolds numbers, etc.

The behaviour of water, which was the solvent for the polymer solutions, in the turbulent regime follows the empirical relationship given by Equation [5.5]. The friction factors of scleroglucan solutions show increased deviation with increasing concentration from those of the Newtonian solvent (water) towards Virk's maximum drag reduction asymptote. These data exhibit 'ladder' characteristics typical of "Type B" drag reduction as discussed by Virk et. al. (1997), where the friction factor variation with Reynolds number (plotted in log-log coordinates) is almost parallel to that of the Newtonian flow as the Reynolds number is increased. According to Virk et. al. (1997), who initially proposed the idea of a distinction between flexible and rigid polymer drag reduction, Type A drag reduction, which is typical for flexible polymer molecules requires a certain level of shear stress before the onset of drag reduction, while Type B, which is typical of extended and rigid polymer molecules, exhibits drag reduction immediately after transition from laminar to turbulent flow. For Type A the drag reduction beyond the onset increases with increase of the Reynolds number while Type B shows a constant level of drag reduction. "Retro-onset" (Virk et. al., 1997) from the maximum drag reduction asymptote can also be observed for Type B beyond which the friction factor is almost parallel to that of the Newtonian fluid data on a log-log plot. The 'ladder' characteristic was also observed by Amarouchene et. al. (2008) for xanthan gum solutions. In **Figure 5.2** no onset is observed for low concentration solutions within the Reynolds number range, however, the *f-Re* data for 0.075% scleroglucan solution showed retro-onset from Virk's maximum drag reduction asymptote beyond which the friction factor increased and remained almost parallel to that of the Newtonian flow. The increase in friction factor is not a sign of degradation as the retro-onset is repeatable and within the experimental uncertainty. The shear viscosity of the 0.075% scleroglucan solution was also measured before and after the pressure-drop measurements and showed no reduction suggesting that the retro-onset is not related to fluid degradation. Gasljevic et. al. (2001) suggested that the departure from Virk's maximum drag reduction asymptote at higher Reynolds number implies that the drag-reducing effectiveness of the fluid has probably reached a maximum beyond which the polymer molecules can no longer cope with increase in the fluid velocity and turbulence dynamics.

The drag-reduction values quoted in **Table 5.1** at several Reynolds numbers are calculated based on the friction factor of the polymer solution and the friction factor for water calculated at the same wall Reynolds number based on the Blasius approximation i.e.

$$DR(\%)=\left[\frac{f_n-f_p}{f_n}\right]\times 100 \qquad [5.15]$$

where the subscripts n and p refer to the Newtonian fluid and the polymer solution respectively. It is already discussed in **Chapter 2** that other methods of quantifying the degree of drag reduction are also available, such as at the same Reynolds number based on the friction velocity (e.g. Escudier et. al., 2009a) or based on the maximum Reynolds shear stress (e.g. Paschkewitz et. al., 2005) and to a certain extent quantification of the "degree" of drag reduction is somewhat arbitrary. However, regardless of definition, the differences are small. For example, in this study, the drag reduction calculated using the wall Reynolds number differs by ~2% from the drag reduction calculated based on the friction Reynolds number, Re_τ, for 0.01% xanthan gum at the wall Reynolds number of 97000.

The degree of drag reduction for all concentrations studied, as seen from **Figure 5.2** and documented in **Table 5.1,** is a strong function of concentration but only weakly dependent on the Reynolds number, at least in the range measured here, in marked contrast to the data for flexible polymers (Virk, 1975; Ptasinski et. al., 2001; Escudier et. al., 1999).

From these results we can see that the mechanism of drag reduction for rigid polymer solutions is somewhat different from that of flexible polymer solutions. Flexible polymer molecules need to be stretched and aligned along the flow for drag reduction so local flow dynamics are important. As a consequence the magnitude of drag reduction for flexible polymers is also dependent upon the Reynolds number (Seyer and Metzner, 1969; Berman, 1980 and Gasljevic et. al., 2001) and the extensional behaviour of the molecules (Tabor and de Gennes, 1986; den Toonder et. al., 1995; White and Mungal, 2008). As rigid polymer molecules are already in a stretched conformation no minimal amount of shear stress is required for the drag-reduction effect to take place resulting in immediate drag reduction once transition to turbulence has occurred.

Microscopically, rigid polymer molecules only need to be aligned with the flow for drag reduction (Sasaki, 1991). Due to the high shear rates in turbulent flow, especially near the wall, the rigid molecules will orient in the flow direction. As the shear rate is reduced within the Newtonian core region there is a possibility that the number of oriented molecules is reduced. The process of randomization of the molecule orientation must then start within the buffer layer. Higher polymer concentration means a larger number of molecules to be randomized and hence a greater possibility of drag reduction. The dependency on Reynolds number also depends on the amount of aligned molecules. If all the molecules are aligned further increasing the Reynolds number would not have any significant effect of the drag-reducing ability, hence the 'ladder' characteristic seen in the *f-Re* plot of **Figure 5.2**.

5.2.2 Mean flow and turbulence statistics

Mean axial velocity and complete Reynolds normal stress data, i.e. u', v' and w', were measured at three different Reynolds numbers, all in the turbulent-flow regime for both 0.005% and 0.01% scleroglucan. Only one component of velocity could be obtained at any one time due to the refraction of two beam pairs of different wavelengths at the curved surface of the pipe wall resulting in the measuring volumes of the beam pairs occupying different spatial locations, as discussed in **Chapter 4**. As a consequence it was not possible to measure the Reynolds shear stress component, $\rho \overline{u'v'}$. LDA measurements for higher concentrations of scleroglucan were not possible due to the higher opacity of the solutions. Control runs with a Newtonian fluid, water, also within the turbulent-flow regime at approximately identical Reynolds numbers were also performed as a basis for comparison.

5.2.2 (a) Mean flow

Prior to any LDA measurements on polymer solutions velocity profiles for water at several Reynolds numbers were measured as shown in **Figure 5.3**. A slight decrease in the normalized maximum velocity is observed resulting in a slightly flatter profile for higher Reynolds number flows. The ratio of the maximum to the bulk velocities at these Reynolds numbers (*Re*=34000, 67000 and 101000), which are significantly lower than that of laminar flow given in Equation [5.3] and [5.4], are 1.23, 1.21 and 1.20 respectively. The velocity profiles were integrated across the pipe to obtain the volumetric flowrate and found to differ by less than 1% from the flowmeter readings. This comparison provides a direct check on the accuracy of the velocity measurements.

Axial velocity measurements were conducted for the scleroglucan solutions at several different Reynolds numbers all within the turbulent flow regime. The normalized velocities are shown in **Figures 5.4(a)-(b)** with the reflected data included to confirm symmetry. It was observed that all profiles show good symmetry within the turbulent regime with the Reynolds number having a lesser effect on the normalized maximum velocity compared to that of the Newtonian profiles with the ratio of the maximum to bulk velocities found to be practically constant between 1.19 and 1.20. The slight decrease of the velocity ratio compared to that of Newtonian profiles is due to the low degree of shear thinning ($n \approx 0.7$) for 0.005% and 0.01% scleroglucan, similar to the behaviour predicted for laminar non-Newtonian flow in Equation [5.12].

The mean flow data is shown in wall coordinates (i.e. u^+ against y^+) in **Figure 5.5**. The abscissa is plotted in log coordinates to expand the velocity profile closer to the wall region. For the Newtonian fluid good agreement is observed with the well-known log law. The data close to the wall are also in good agreement with that expected for the viscous sub layer (i.e. $(y^+ \leq 10)$ $u^+ = y^+$). More detailed measurements within the viscous sublayer region were not possible for these high Reynolds number flows as a very thin sublayer is created at these Reynolds numbers ($\approx$0.2mm). The scleroglucan data in the viscous sublayer also follow $u^+ = y^+$ while in the Newtonian core region the data are shifted upward from but remain essentially parallel to the Newtonian data as expected for low drag-reducing flows (Warholic et. al., 1999; Escudier et. al., 1999) discussed in **Chapter 2**. The onsets of the shifts of the scleroglucan data were found to be independent of Reynolds number and drag reduction, occurring at a constant y^+ location of about 15, i.e. within the buffer layer, similar to that of the flexible polymer solution observed by Virk (1975). In physical units this implies that the distance of onset location from the wall decreases with increasing Reynolds number. Sasaki (1991) proposed that polymer turbulence interaction responsible for drag reduction commences within this vicinity $(y^+ \approx 15)$. Hence, the process of randomization of aligned molecules discussed in section 5.2.1 might also interfere with the process of turbulent bursting. From the figure the magnitude of the shifts is also seen to be a function of drag reduction but is only mildly dependent on Reynolds number.

5.2.2 (b) Turbulence structure

The rms fluctuation levels of the axial velocity, u', again plotted in wall coordinates, u'^{+}, and shown in **Figure 5.6** show that closer to the wall (y^{+}<30) the water data collapse and are independent of the Reynolds number, in agreement with the observations of den Toonder and Nieuwstadt (1997). Closer to the pipe centreline there are clear Reynolds-number trends, again in agreement with previous results (den Toonder and Nieuwstadt, 1997). Compared to the data for a Newtonian fluid at the same Reynolds number both concentrations of scleroglucan showed increased values of u'^{+} close to the wall with the location of the peaks found to be within the region of the onset of the shifts in the mean velocity profiles ($y^{+}\approx15$), i.e. in the buffer layer. Close to the pipe centre the fluctuation levels are essentially identical to the water data at comparable Reynolds numbers.

Figure 5.7 and **5.8** show that the rms radial and tangential turbulent fluctuations for the Newtonian solvent are globally much lower than for the axial component but both exhibit increases with Reynolds number. The scleroglucan results show increased suppression of the tangential and radial fluctuation levels with drag reduction with the exception of the peak of the radial fluctuation level at the highest Reynolds number measured for 0.005% scleroglucan. The peaks were situated slightly further away from the wall compared to that of the Newtonian data, consistent with the increasing buffer layer thickness with drag reduction of drag-reduced flow. Greater peak suppressions of the tangential component (between 9% to 17%) compared to the radial component (between 6% to 10%) are observed. Similar trends were also observed by den Toonder et. al. (1997) using direct numerical simulations and experiments carried out on 20 ppm hydrolyzed polyacrylamide (DR=24.2%) in a 40-mm diameter pipe where the tangential component was found to be 20% higher than that of the radial component.

The experimental data in the literature with regards to the shifts of the peak positions in pipe flow are not conclusive. For low drag-reducing flows (DR<40%) Warholic et. al. (1999) and Presti (2000) found that the peak locations remained unchanged, within the experimental uncertainty, compared with that of the Newtonian flow while den Toonder et. al. (1997) and Ptasinski (2002) observed shifts of the peak locations towards the pipe centre. Regardless, the results obtained in this study suggest that the turbulence structure has been changed with strong anisotropy, i.e. increase in axial component while radial and tangential components are reduced, at these Reynolds number and concentration to produce drag reduction.

The turbulent structure data as shown in **Figures 5.6-5.8** are in agreement with that of the low drag-reducing flexible polymer solution as observed by Pinho and Whitelaw (1990) and Warholic et. al. (1999), amongst others. The axial turbulence intensity is increased near the wall relative to the Newtonian solvent while the tangential and radial components are suppressed but these effects are only significant near the wall compared to overall suppression for highly effective drag reducers. The increase of axial and decrease of radial and tangential components are thought to be associated with the preferential orientation of the polymer molecules as suggested by Pinho and Whitelaw (1990). It is important to note that this behaviour could only be apparent when the Reynolds number is defined using the shear viscosity at the wall. If the solvent viscosity is used in the definition of the Reynolds number instead, comparing the rms data to that of the Newtonian flow at the same Reynolds number might not show an apparent increase in the axial component. A decrease in this component might be detected instead and the suppression in radial and tangential components will be further magnified.

In these figures data close to the wall in the region $y^+ < 10$, especially those of the tangential and radial velocity components, are excluded from the results. Very close to the wall sources of measurement error, which manifest in the form of enhanced scatter in the data, are present due to reflections of the laser beams from the pipe wall picked up by the receiving optics; the vertical laser beam pair measuring the tangential and radial velocity components being the most sensitive. Further detailed assessments of the data for the radial and tangential turbulence components, such as the exact peak location trends with concentration and Reynolds number, were also difficult due to the large degree of data scatter associated with low data rates and low quality of LDA signals particularly when making measurements close to the wall.

In **Figure 5.9** the peak values of the turbulent fluctuation components, normalized with the bulk velocity, have been plotted against drag reduction together with selected data from the literature for comparison (Presti, 2000; Ptasinski et. al., 2001; McComb and Chan, 1985; Allan et. al., 1984; Chung and Graebel, 1971; Mizushina and Usui, 1977; Schummer and Thielen, 1980; McComb and Rabie, 1982 and den Toonder et. al., 1997). It can be seen that the data for the rigid rod-like polymer from the current study agree well with the trend of decreasing normalized peaks with increasing drag reduction similar to what is observed for two-dimensional channel flow (Escudier et. al., 2009a). In **Figure 5.10** the same data are plotted with the peak values normalized with the friction velocity, u_τ, and the trend is for a decrease in the radial and tangential peak levels but an increasing trend of axial peak level below 40% drag reduction with more complex behaviour at higher drag reduction. The lines in the figures are included to guide the eye where clear trends are apparent. A dotted vertical line is also included within the figures to demarcate these two regions.

TABLES

Table 5.1: Flow parameters and drag reduction of scleroglucan solutions

Scleroglucan concentration c (w/w %)	**Reynolds number** $\frac{\rho U_B D}{\eta_W}$	U_B (m/s)	u_τ $\left(\equiv\sqrt{\tau_W/\rho}\right)$ (m/s)	**Drag reduction** (%) $\left[\frac{f_n-f_p}{f_n}\right]\times 100$
0.005%	31000	0.38	0.019	13
	65000	0.76	0.035	15
	109000	1.26	0.053	17
0.01%	36000	0.50	0.024	24
	67000	0.88	0.038	25
	97000	1.01	0.043	27
0.02%	35000	0.05	0.023	37
	67000	1.01	0.040	39
	75000	1.14	0.044	40
0.05%	33000	0.63	0.026	40
	69000	1.14	0.042	43
	78000	1.26	0.047	42
0.075%	31000	0.76	0.030	47
	60000	1.26	0.042	55

Table 5.2: Maximum velocity fluctuations data of scleroglucan solutions and water

Fluid concentration	**Reynolds No.**	Axial $\left(u'^{+}\right)$	Radial $\left(v'^{+}\right)$	Tangential $\left(w'^{+}\right)$
Water	34000	2.71	1.25	1.50
	67000	2.87	1.38	1.80
	101000	3.11	1.39	1.86
0.005% SG	65000	3.42	1.30	1.63
	109000	3.62	1.43	1.69
0.01% SG	36000	3.16	1.18	1.37
	67000	3.51	1.24	1.49
	97000	3.63	1.30	1.54

FIGURES

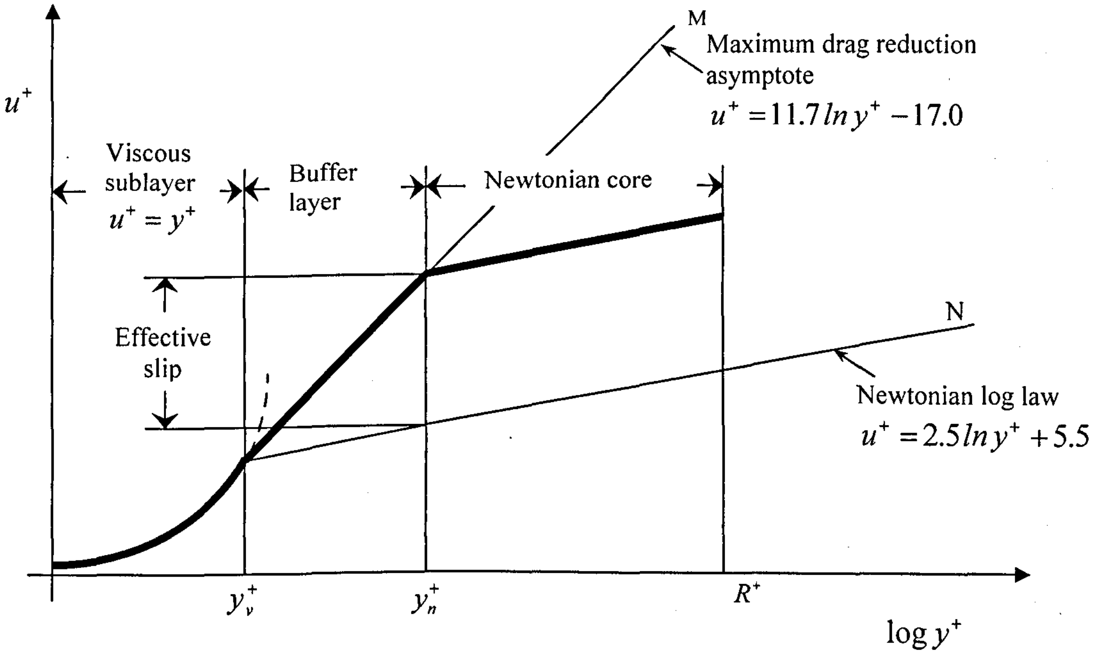

Figure 5.1: Three-zone mean flow model (Virk, 1970, 1975)

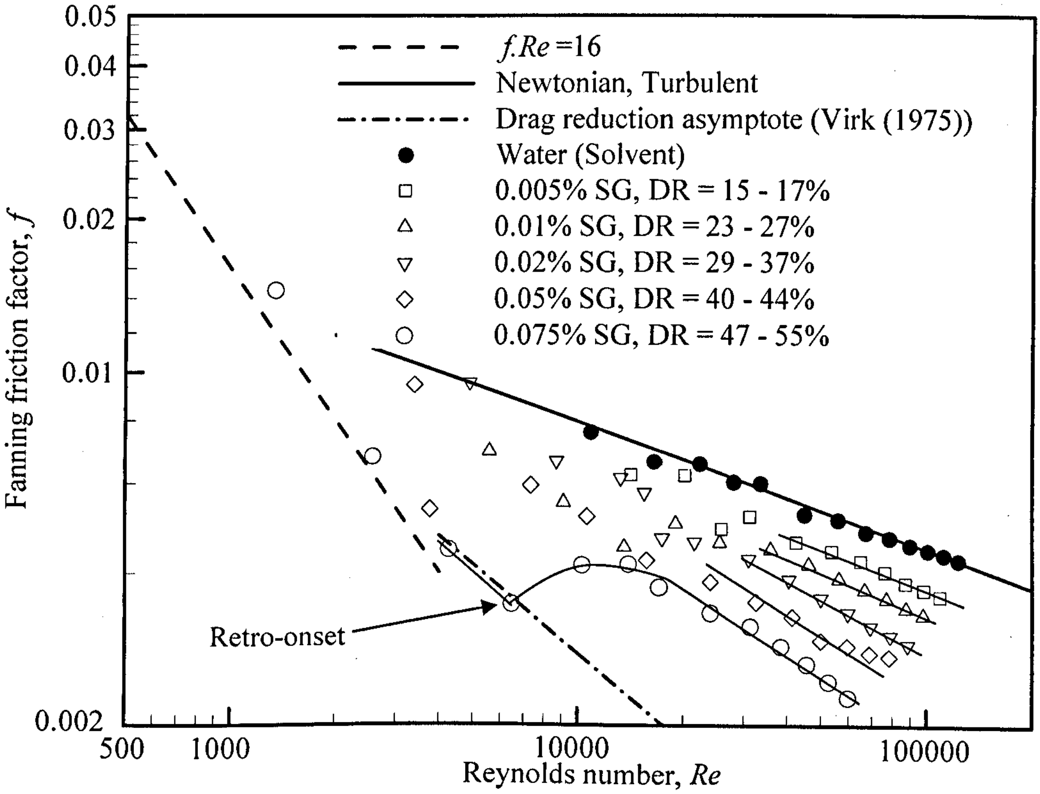

Figure 5.2: *f-Re* data for various SG concentrations (lines through the SG data are to guide the eye and highlight the "ladder" effect).

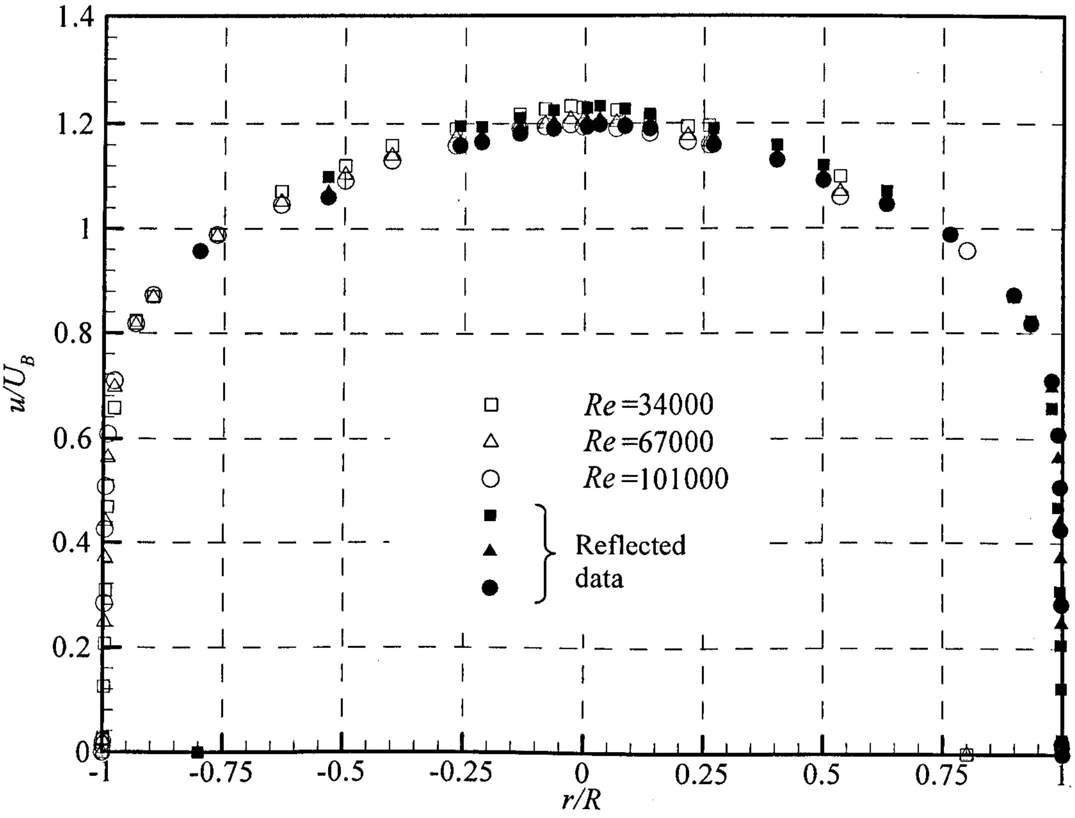

Figure 5.3: Normalized mean velocity distribution of water in circular pipe

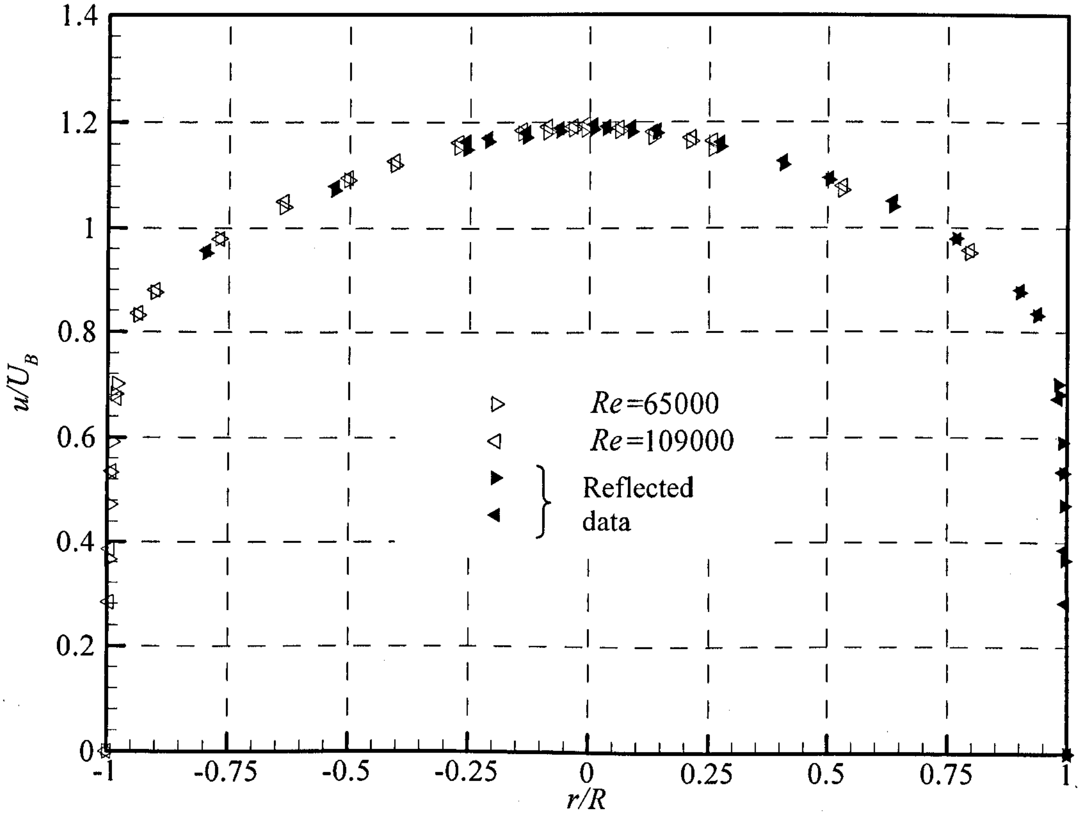

Figure 5.4(a): Normalized mean velocity distribution of 0.005%SG in circular pipe

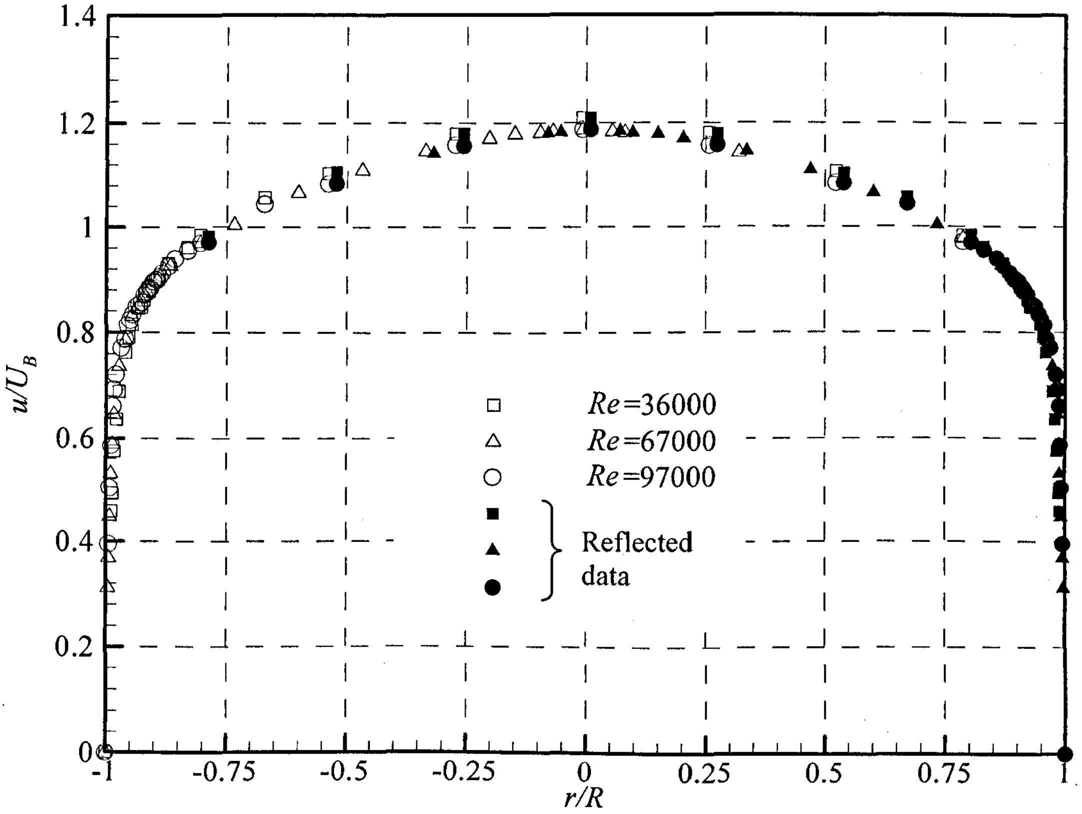

(b)

Figure 5.4(b): Normalized mean velocity distribution of 0.01%SG in circular pipe

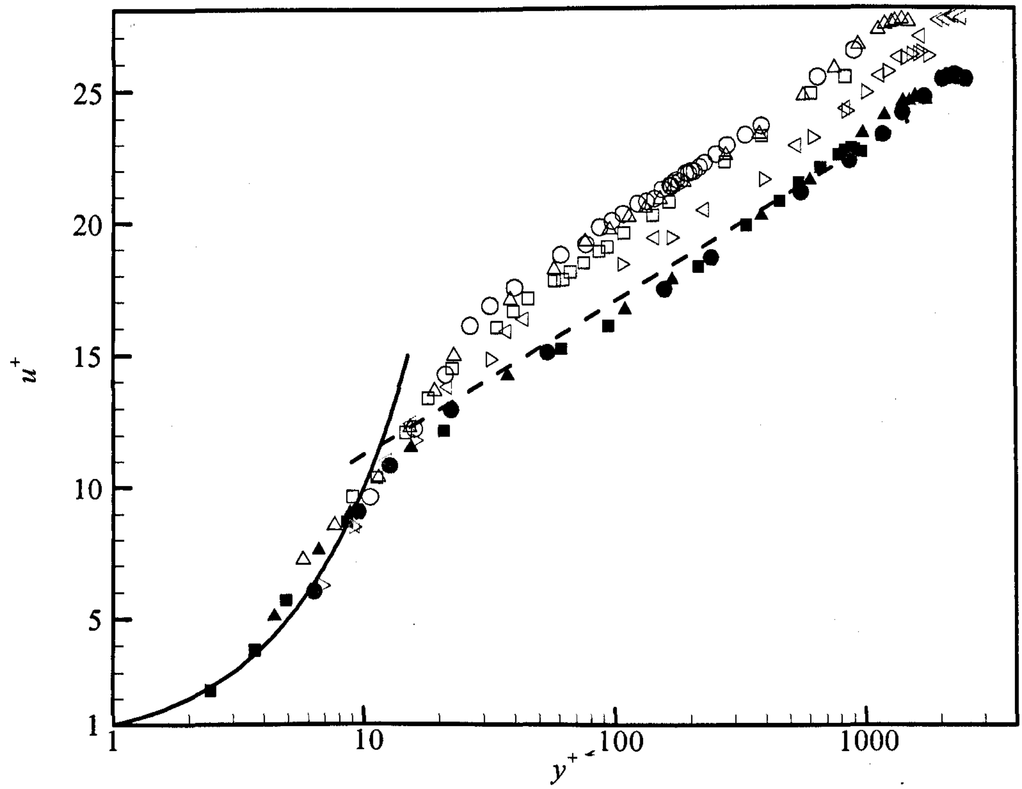

Figure 5.5: Universal mean velocity distribution for water, 0.005% SG and 0.01% SG. —: $u^+=y^+$; - - -: $u^+=2.5\ ln\, y^+ +5.5$; ■: Water, *Re*=34000; ▲: Water, *Re*=67000; ●: Water, *Re*=101000; ▷: 0.005%SG, *Re*=65000, DR=15%; ◁: 0.005%SG, *Re*=109000, DR=17%; □: 0.01%SG, *Re*=36000, DR=24%; Δ: 0.01%SG, *Re*=67000, DR=25%; ○: 0.01%SG, *Re*=97000, DR=27%.

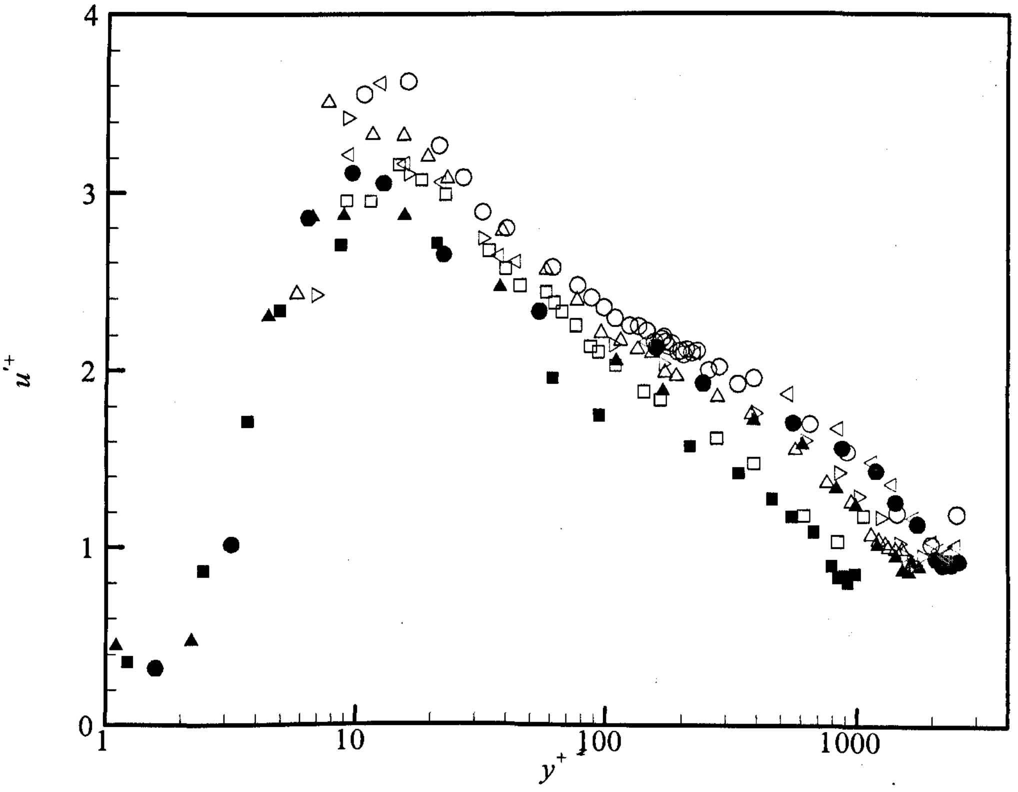

Figure 5.6: Axial rms fluctuation levels in wall coordinates for water, 0.005% SG and 0.01% SG. ■: Water, *Re*=34000, u'^+_{max}=2.71; ▲: Water, *Re*=67000, u'^+_{max}=2.87; ●: Water, *Re*=101000, u'^+_{max}=3.11; ▷: 0.005%SG, *Re*=65000, u'^+_{max}=3.42; ◁: 0.005%SG, *Re*=109000, u'^+_{max}=3.62; □: 0.01%SG, *Re*=36000, u'^+_{max}=3.16; Δ: 0.01%SG, *Re*=67000, u'^+_{max}=3.51; ○: 0.01%SG, *Re*=97000, u'^+_{max}=3.63.

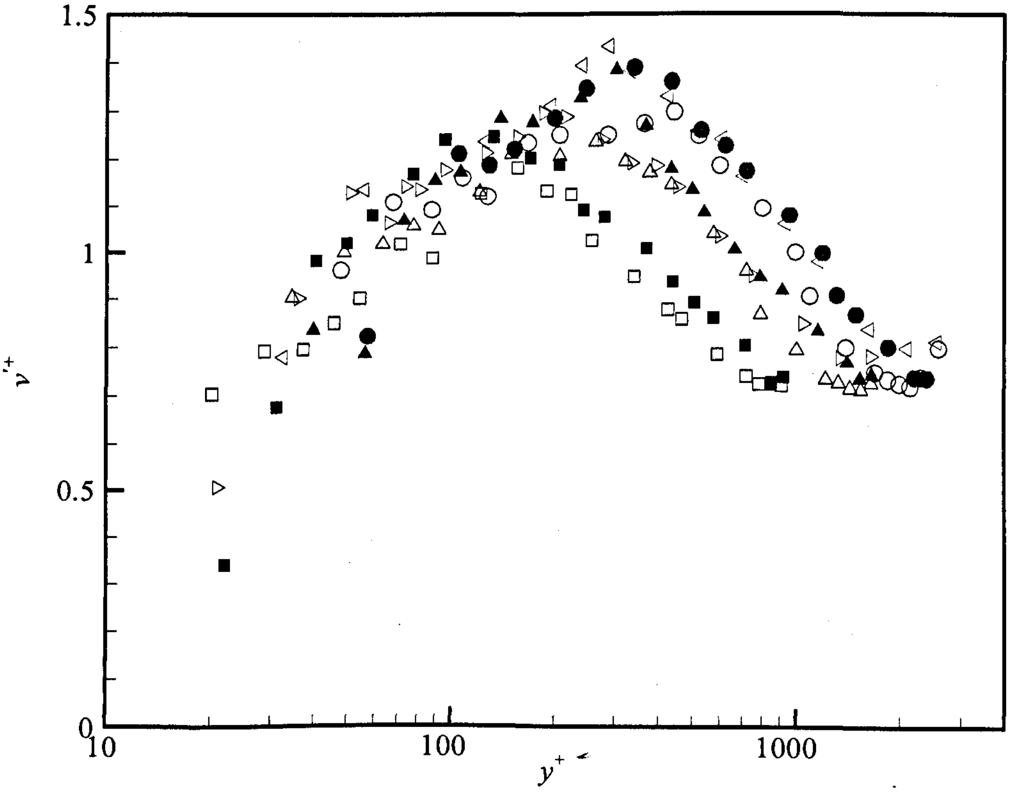

Figure 5.7: Radial rms fluctuation levels in wall coordinates for water, 0.005% SG and 0.01% SG. ■: Water, *Re*=34000, v'^+_{max}=1.25; ▲: Water, *Re*=67000, v'^+_{max}=1.38; ●: Water, *Re*=101000, v'^+_{max}=1.39; ▷: 0.005%SG, *Re*=65000, v'^+_{max}=1.30; ◁: 0.005%SG, *Re*=109000, v'^+_{max}=1.43; □: 0.01%SG, *Re*=36000, v'^+_{max}=1.18; Δ: 0.01%SG, *Re*=67000, v'^+_{max}=1.24; ○: 0.01%SG, *Re*=97000, v'^+_{max}=1.30.

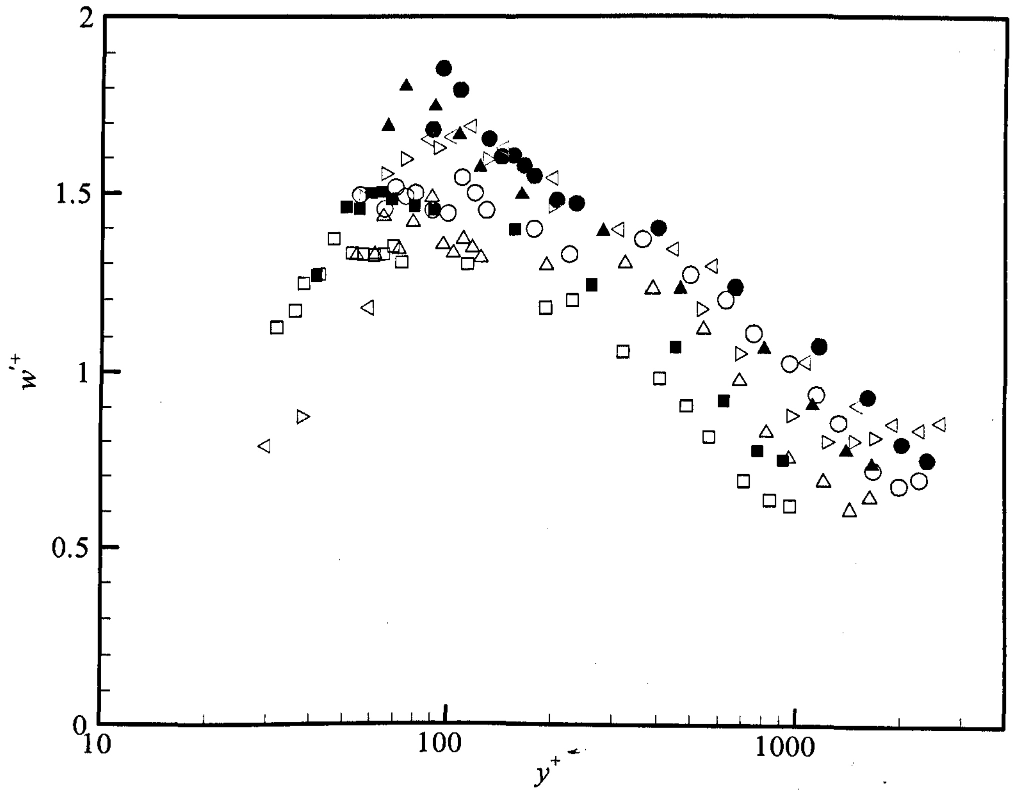

Figure 5.8: Tangential rms fluctuation levels in wall coordinates for water, 0.005% SG and 0.01% SG. ■: Water, *Re*=34000, w'^+_{max} =1.50; ▲: Water, *Re*=67000, w'^+_{max} =1.80; ●: Water, *Re*=101000, w'^+_{max} =1.86; ▷: 0.005%SG, *Re*=65000, w'^+_{max} =1.63; ◁: 0.005%SG, *Re*=109000, w'^+_{max} =1.69; □: 0.01%SG, *Re*=36000, w'^+_{max} =1.37; Δ: 0.01%SG, *Re*=67000, w'^+_{max} =1.49; ○: 0.01%SG, *Re*=97000, w'^+_{max} =1.54.

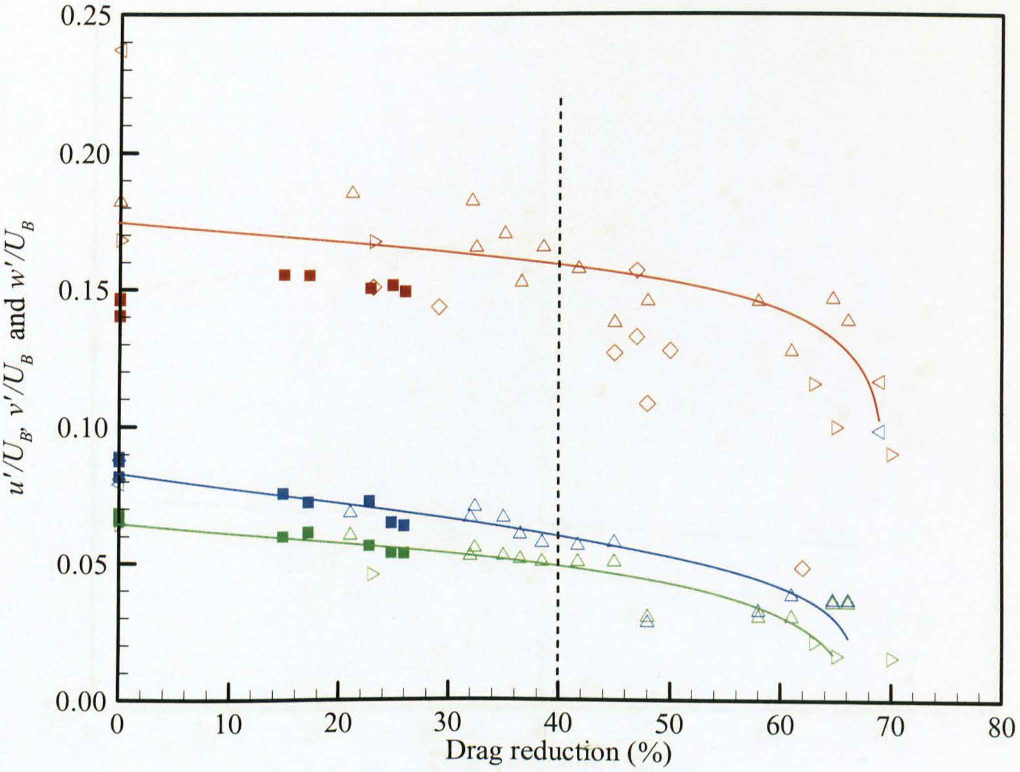

Figure 5.9: Peaks of axial, radial and tangential fluctuation components normalized with the bulk velocity, U_B, against drag reduction (■:current study, Δ: PAA, XG, CMC (Presti, 2000), ▷: HPAM (Ptasinski et. al., 2001), ◁: Macro Fibres (McComb and Chan, 1985), ◇: PEO, PAA (Allan et. al., 1984), Red: u'/U_B , Green: v'/U_B , Blue: w'/U_B)

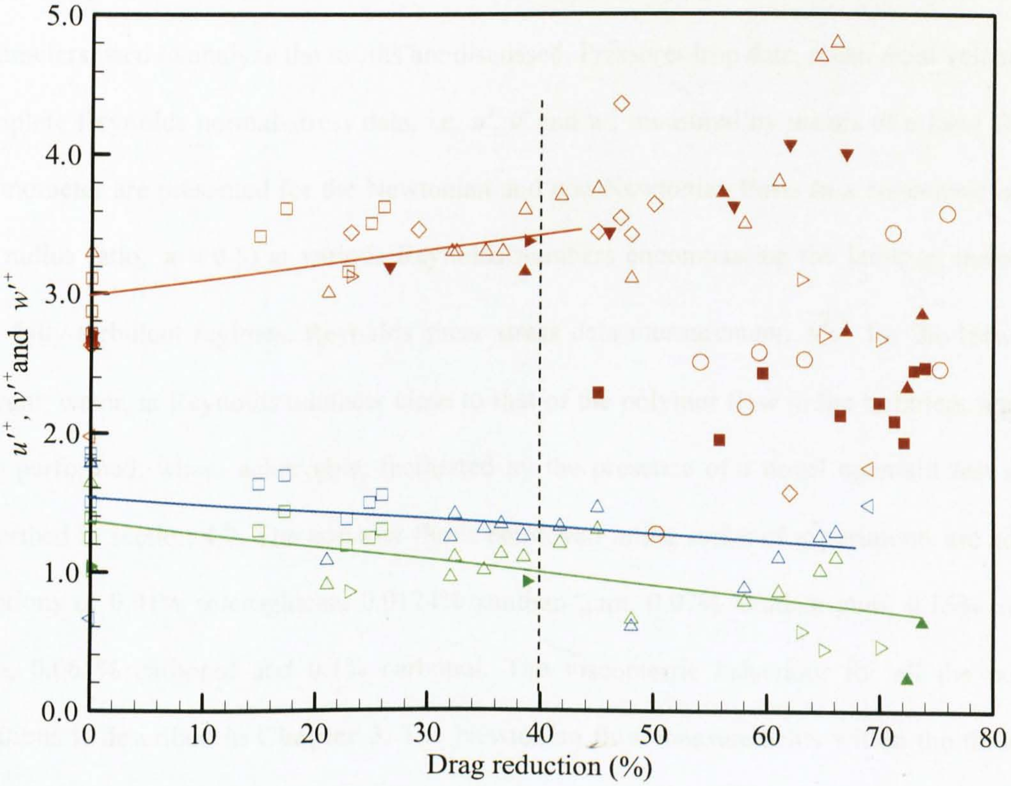

Figure 5.10: Peaks of axial, radial and tangential fluctuation components in wall coordinates against drag reduction (□:current study, Δ: PAA, XG, CMC (Presti, 2000), ▷: HPAM (Ptasinski et. al., 2001), ◁: Macro Fibres (McComb and Chan, 1985), ◇: PEO, PAA (Allan et. al., 1984), ○: PEO, PAA (Chung and Graebel, 1971), ■: PEO (Mizushina and Usui, 1977), ▲: PAA (Schummer and Thielen, 1980), ▼: PEO (McComb and Rabie, 1982), ►: PAA (den Toonder et. al., 1997), Red: u'^+, Green: v'^+, Blue: w'^+)

6 ANNULAR FLOW

In this chapter the background of the work on annular flow together with the definitions of the parameters used to analyze the results are discussed. Pressure-drop data, mean axial velocity and complete Reynolds normal-stress data, i.e. u', v' and w', measured by means of a laser Doppler anemometer are presented for the Newtonian and non-Newtonian flows in a concentric annulus (of radius ratio, $\kappa = 0.5$) at various Reynolds numbers encompassing the laminar, transitional and fully-turbulent regimes. Reynolds shear stress data measurement, $\overline{u'v'}$ for the Newtonian solvent, water, at Reynolds numbers close to that of the polymer flow in the turbulent regime is also performed, where achievable, facilitated by the presence of a novel open-slit test section described in section 4.2. The polymer fluids employed in the series of experiments are aqueous solutions of 0.01% scleroglucan, 0.0124% xanthan gum, 0.07% xanthan gum, 0.15% xanthan gum, 0.065% carbopol and 0.1% carbopol. The viscometric behaviour for all the polymer solutions is described in **Chapter 3**. The Newtonian flow measurements within the three flow regimes, laminar, transition and low Reynolds number fully turbulent, were achieved using a glycerine-water mixture while measurements at even higher Reynolds numbers within the turbulent regime were conducted using water.

6.1 Background

Fluid flow in a concentric annular pipe is of great importance due to its extensive engineering applications such as in heat exchangers and drilling pipes (Azouz and Shirazi, 1997; Escudier et. al., 2002a). As confirmed in **Chapter 5** Newtonian and non-Newtonian fluid flow in a circular pipe is symmetrical in the fully-turbulent regime. Seyer and Metzner (1969), Pinho and Whitelaw (1990) and Escudier et. al. (2009b), amongst others, also discovered similar symmetrical profiles for Newtonian and non-Newtonian pipe flow in the laminar regime. However, fully-developed annular flow involves a combination of two boundary layers extending from the pipe walls to a point of maximum velocity which does not lie in the centre of the annular gap. The boundary layers emanating from the inner and outer pipes are of different sizes and possibly of different regimes due to different degrees of curvature of the inner and outer pipe walls (Hanks and Bonner, 1971). As a result of the interaction of these two layers the flow is then asymmetric. Hence, in this type of flow, the position of zero shear stress might not be coincident with the position of maximum velocity and the turbulent transport phenomena are also expected to differ from those of symmetric flows in circular pipes (Lawn and Elliot, 1972; Rehme, 1974; Nouri et. al., 1993; Chung et. al., 2002).

6.1.1 Annular Newtonian fluid flow

For a fully-developed laminar flow of Newtonian fluid the Fanning friction factor, f ($\equiv 2\tau_A / \rho U_B^2$ where τ_A is the average wall shear stress as defined in Equation [6.3]) and the Reynolds number, Re ($\equiv \rho U_B D_H / \eta$ where $D_H(\equiv D_o - D_i)$ is the hydraulic diameter) relationship is given by (Knudsen and Katz, 1958)

$$f = \frac{16}{Re}\left(\frac{\left(1-{D_i}/{D_o}\right)^2}{1+\left({D_i}/{D_o}\right)^2+\left\{\frac{\left[1-\left({D_i}/{D_o}\right)^2\right]}{ln\left({D_i}/{D_o}\right)}\right\}}\right) \qquad [6.1]$$

where D_i and D_o are the inner and outer pipe diameters respectively. Given a radius ratio, κ=0.5 as utilized in this study, the above equation reduces to

$$f = \frac{23.82}{Re}. \qquad [6.2]$$

The average wall shear stress, τ_A, utilized in the calculation of the friction factor is given by

$$\tau_A = \frac{1}{4}(D_o - D_i)\frac{\Delta p}{L} \qquad [6.3]$$

where Δp is the pressure drop measured over an axial distance, L. Knudsen and Katz (1958) presented the mean axial velocity for fully-developed, Newtonian, isothermal laminar flow in an annulus as

$$u = \frac{\Delta p}{4\eta L}\left(R_o{}^2 - r^2 + 2r_{max}^2 \, ln\frac{r}{R_o}\right) \qquad [6.4]$$

with

$$r_{max} = \sqrt{\frac{R_o^2 - R_i^2}{2ln\left(R_o/R_i\right)}} \qquad [6.5]$$

where R_i ($\equiv D_i/2$) and R_o ($\equiv D_o/2$) are the inner and outer pipe radii respectively. Rothfus et. al. (1955) and Knudsen and Katz (1958) proposed that Equation [6.5] above also holds for fully-turbulent flow. The shear stress for Newtonian laminar flow in an annulus is given by

$$\tau = -\frac{r}{2}\frac{\Delta p}{L} + \frac{1}{r}\left(\frac{R_o^2 - R_i^2}{4ln\left(R_o/R_i\right)}\right)\frac{\Delta p}{L}. \qquad [6.6]$$

For the geometry utilized in this research work the radius of maximum velocity, r_{max}, as calculated using Equation [6.5] is 74.2 mm, which coincides with the position of zero shear stress as calculated from Equation [6.6], giving a non-dimensional radial location, $\xi \left(\equiv (r - R_i)/(R_o - R_i)\right)$ of 0.472.

Unlike laminar annular flow, the predictions for fully-developed turbulent flow are empirical in nature. The experimental work of Nouri et. al. (1993) showed that the friction factor can be represented by

$$f = 0.36\,Re^{-0.39} \qquad [6.7]$$

where the Reynolds number is calculated using the hydraulic diameter, D_H, of the annulus. However, Jones and Leung (1981) argued that the hydraulic diameter is insufficient to correlate the friction factor in geometries other than circular pipes and proposed the use of a "laminar equivalent diameter" instead. The laminar equivalent diameter, d_L is a function of the hydraulic diameter and the shape factor, $\phi^*(\kappa)$ via

$$d_L = D_H \phi^*(\kappa) \qquad [6.8]$$

where the shape factor is

$$\phi^*(\kappa) = \frac{1}{(1-\kappa)^2}\left[1+\kappa^2 - \frac{1-\kappa^2}{ln\frac{1}{\kappa}}\right]. \qquad [6.9]$$

For fully-developed turbulent flow, using the laminar equivalent diameter, Jones and Leung (1981) provided the empirical *f-Re* relationship for a radius ratio of 0.5 as

$$\frac{1}{\sqrt{f}} = 4\,log(1.343\,Re\,f^{1/2}) - 1.6\ . \qquad [6.10]$$

Kays and Leung (1963) discovered through a series of experiments that the radius of maximum velocity for turbulent flow is dependent on the radius ratio and is independent of the Reynolds number via

$$\frac{r_{max} - R_i}{R_o - r_{max}} = \left(\frac{R_i}{R_o}\right)^{0.343} \ . \qquad [6.11]$$

Their findings were further verified by Brighton and Jones (1964), who were also the first to measure turbulence intensities and shear stress distributions in an annulus. Using Equation [6.11] for the geometry utilized in this study the location of maximum velocity is r_{max} =72.7 mm giving a non-dimensional radial location, ξ, of 0.442.

Lawn and Elliot (1972) determined that the average shear stress calculated from the pressure drop measurement as shown in Equation [6.3] is a combination of the inner and outer wall shear stresses via

$$(R_o - R_i)\tau_A = (R_o\tau_o + R_i\tau_i)\,. \qquad [6.12]$$

The inner and outer walls shear stresses can be calculated provided the location of zero shear stress is known. Using the location of zero shear stress, $r_{\tau=0}$, in the equations derived from the momentum equation for fully-developed, steady and incompressible flow in an annulus, the wall shear stresses are given as (Knudsen and Katz, 1958; Lawn and Elliot, 1972; Nouri et. al., 1993)

$$\begin{aligned} \tau_o &= -\left(\frac{\Delta p}{L}\right)\left[\frac{R_o^2 - r_{\tau=0}^2}{2R_o}\right] \\ \tau_i &= -\left(\frac{\Delta p}{L}\right)\left[\frac{r_{\tau=0}^2 - R_i^2}{2R_i}\right] \end{aligned}\,. \qquad [6.13]$$

The equation above holds for both laminar and turbulent flow in an annulus.

In wall coordinates, Clauser (1956) gave the law of the wall for the Newtonian core region for wall bounded flows as

$$u^+ = 2.44\,ln\,y^+ + 4.9\,. \qquad [6.14]$$

Within the viscous sublayer $u^+ = y^+$ applies. In order to present the velocity profiles in wall coordinates, it is necessary to know the location of zero shear stress to calculate the shear stresses on the inner and outer walls. These shear stresses are then utilized to calculate the friction velocity, u_τ $\left(\equiv \sqrt{\tau_W / \rho}\right)$. In the absence of direct measurements of the shear stress inside the annular gap, τ_i, τ_o or $\rho\overline{u'v'}$, one would resort to the velocity gradient method where the velocity data close to the wall are utilized to calculate the shear stress ($\tau_W = \eta\, dU/dy$ in a fully-developed pure shear flow). However, this method would only be sufficiently reliable if accurate velocity measurements are available within the viscous sublayer (Poggi et. al., 2002).

6.1.2 Annular non-Newtonian fluid flow

The laminar friction factor relationship for a non-Newtonian fluid can be deduced from the equation given by Escudier et. al. (1995a) who provided a close approximation to the theoretical analysis of Fredrickson and Bird (1958) for a laminar, power law fluid flow. For a radius ratio $\kappa = 0.5$ the relationship is given as

$$f.Re = 23.8\left(\frac{2n+1}{3n}\right) . \qquad [6.15]$$

For turbulent non-Newtonian fluid flow in an annular pipe the friction factor is bound between two asymptotes; the empirical relationship for turbulent Newtonian flow as given in section 6.1.1 and a drag-reduction asymptote analogous to that originally proposed by Virk (1975) for turbulent pipe flow. By assuming that the velocity profile for maximum drag reduction in wall coordinates for a circular pipe is also applicable to an annulus Escudier et. al. (1995a) suggested a modified ultimate drag reduction asymptote which for a radius ratio of 0.5 is

$$\frac{1}{\sqrt{f}} = 8.27\, ln(Re\, f^{\frac{1}{2}}) - 34.6 . \qquad [6.16]$$

The three layer model proposed by Virk (1975) for the velocity profile of a drag-reducing polymer flow in a pipe as discussed in section 5.1.2 is also assumed to be applicable to annular flow of non-Newtonian fluids.

6.2 Numerical procedure

A commercial computational fluid dynamics (CFD) software, Fluent v6.1.22, was utilized, together with Gambit v2.1.6 for geometric modelling, to numerically simulate the velocity distribution in a concentric annulus in the laminar regime for both Newtonian and non-Newtonian fluids. The simulations were carried out using second order differencing schemes together with the well known semi-implicit method for pressure link equations (SIMPLE) with double precision used for the calculations. For the non-Newtonian fluids both the power-law model and the Herschel-Bulkley model were utilized depending upon the fluid in question. The numerical simulations, however, did not take into account viscoelastic effects from either the normal stress or the elongational viscosity. This simplification is valid for laminar fully-developed shear flow, as in this study, where the normal stresses and extensional viscosity play no role.

The geometry, modelled and meshed using Gambit, was centred at the cylinder axis with the front and rear boundaries set to be periodic boundaries as shown in **Figure 6.1(a)**. Due to the fully-developed nature of the flow, only one row of cells with the length of the hydraulic diameter is needed in the direction of the flow (x-direction) as recommended by Escudier et. al. (2002b). **Figure 6.1(b-c)** shows the computational grid for 1000 cells (100×10) and 10000 cells (100×100). For the numerical simulations, the total number of cells used is 10000, 100×100 in the radial and tangential directions. This grid was chosen after a grid dependency study was conducted by systematically assessing the accuracy of the simulations using several progressively finer grids. The numerical accuracy was estimated by comparing with the available analytical solution for Newtonian fluids and with the values determined from using Richardson's extrapolation-to-the-limit technique, as outlined in Ferziger and Peric (2002), when analytical solutions are not available in the case of power-law and Herschel-Bulkley fluids. Using this method, the relative error, $e_r \left(\equiv \frac{\left| X_{an,\,ext} - X_{MX} \right|}{X_{an,\,ext}} \% \right)$ for the chosen mesh is maintained below 0.05%. **Table 6.1** and **6.2** list the maximum velocities determined by varying the cell size (and subsequently, the total number of cells) and the relative error, e_r.

The isothermal, laminar, fully-developed numerical simulations were carried out by setting the mass flow rate calculated from the power law Reynolds number,

$$Re_{PL} = \frac{\rho U_B^{2-n} D_H^n}{k} \qquad [6.17]$$

as recommended by Escudier et. al. (2002b), at the periodic boundaries where n and k are the power-law index and the power-law consistency index respectively. For the Herschel-Bulkley fluid the power-law index and the consistency index obtained via a Herschel-Bulkley fit to the viscosity data are used instead as suggested by Escudier et. al. (2002b). The experimental data by Nouri and Whitelaw (1994) for 0.2% CMC at Reynolds number of 664, calculated using the equation proposed by Escudier et. al. (2002b) for a power-law fluid, is shown and compared to the numerical simulation data in **Figure 6.1(d)**. The agreement between the experimental data and the FLUENT data (M4: 100×100 cells) are clearly satisfactory and represent a validation of the methods used in the numerical simulations.

6.3 Validation of data measured with and without cross slit

As discussed in **Chapter 4**, at the test region, 96.6 D_H downstream of the pipe entrance, a "slit module" is incorporated which consisted of a narrow cross slit on the outer pipe of the annulus to allow two-component laser measurements. This section discusses the effectiveness of the cross slit and compares the experimental data with the data available from the literature in order to "validate" the experimental arrangement and instrumentation utilized in the study of annular flow. The main concern here is to investigate if the cross-slit has an effect on the flow.

Figure 6.2(a) shows three velocity profiles normalized with the bulk velocity measured in two different planes, located 90° from each other, at a Reynolds number of 9900 together with that of the direct numerical simulation (DNS) results of Chung et. al. (2002) conducted at a Reynolds number of 8900. As discussed in section 4.5.3, Plane A is the measurement plane when the traverse is moved horizontally in the *z*-direction while Plane B measurements were obtained by moving the traverse vertically in the *y*-direction. Run 1 was conducted in Plane A, Run 2 in Plane B without the cross slit, i.e. using a flat-faced optical box discussed in section 4.2, while Run 3 was conducted in Plane B with the cross slit in place. The non-dimensional radial location, ξ is utilized with the cylinder inner wall corresponding to $\xi = 0$ (i.e. $r = R_i$) and the outer wall to $\xi = 1$ (i.e. $r = R_o$). All three velocity profiles agree well with each other and the DNS data suggesting that the annular pipe assembly is approximately concentric and the effect of slight eccentricity, if present, is minimal (this issue is discussed in further detail in the following section). The circumferential variation in the velocity profiles, obtained by integration of profiles measured in Run 1 (Plane A) and Run 2 (Plane B) were less than 2.2%; therefore, detailed axial measurements hereafter were only made in Plane B as reduced back reflection of the Doppler signal close to the wall of the centrebody and better data rate could be obtained. The average percentage difference between Run 2 (without "cross" slit) and Run 3 (with "cross" slit) data is about 1.2% in the mean and 4.5% in the axial turbulence fluctuation levels for points between $0.04 \leq \xi \leq 0.96$. The effect of the cross slit on the axial velocity was found to be negligible starting from 4% of total distance from the outer wall onwards ($\xi \leq 0.96$). The flowrates obtained from integration of the LDA mean velocity profiles were found to be within 1.5% of the value provided by the flowmeter. Good agreement of the mean flow with the data of Chung et. al. (2002) was also observed with the percentage difference by integration of the profiles found to be less than 1.5%. The non-dimensional radial location of maximum velocity, $\xi_{U_{max}}$, was found to be 0.44, which is closer to the inner wall, in agreement with that predicted using the equation proposed by Kays and Leung (1963). Relatively good agreement, with percentage difference of less than 10% for points between $0.04 \le \xi \le 0.096$, were also observed for the axial rms fluctuation component for all three runs as shown in **Figure 6.2(b)** with a slightly higher peak found on the outer wall for the measurements with the cross slit. However, overall results indicate that the effect of the cross slit on the axial component, u and u', is small.

The radial rms fluctuation component, which could only be measured in Plane B due to the orientation of the flow and limited optical access for the laser probe head, however, highlighted a major problem of the cross-slit technique at a Reynolds number of 9900, as shown in **Figure 6.3**. The rms velocity data measured at this Reynolds number with the cross slit showed a large amount of scatter especially towards the outer wall (i.e. where the slit is located). These data are not in agreement and are significantly lower than the values measured without the cross slit which indicates a possible non-zero radial component, measured with the slit module, into the stationary fluid within the module box. Subsequently the Reynolds shear stress data, which could only be measured with the presence of the slit, showed much lower values when compared to the numerical data of Chung et. al. (2002) as shown in **Figure 6.4**. However, at higher Reynolds numbers ($Re \ge 30{,}000$) the radial rms fluctuation component measured with and without cross slit are in agreement as shown in **Figure 6.5(a)** indicating a threshold limit for which the radial component could be measured accurately with the presence of the cross slit. At these Reynolds numbers the Reynolds shear stress data, as shown in **Figure 6.5(b)** can be utilized with greater confidence. The data by Nouri et. al. (1993) measured at Re=26600 is also included for comparison and shows fair agreement with the data measured in this study.

After the location of zero shear stress was estimated all the wall coordinate data were calculated and plotted using weighted shear stresses as in Equation [6.13]: this issue is discussed further in the following section. In wall coordinates, the axial rms fluctuation component in **Figure 6.6** also shows good agreement with that of Chung et. al. with the data for the outer profile found to be higher than the inner profile values. The inner and outer profiles were found to peak at a similar location relative to the walls ($y^+ \approx 15$). However, as shown in **Figure 6.7**, the profiles of the radial, measured without the slit, and the tangential rms components in **Figure 6.8** were discovered to be higher (~9%) than that predicted by the DNS results away from the walls. The experimental data for radial and tangential components also exhibited smaller differences between the inner and outer walls data compared to that of the DNS data. The higher Reynolds number at which the experimental data were obtained could be a possible reason for these differences. With the exception of the slight disagreement between the radial and tangential components and the DNS data, overall good agreement of the experimental results with the DNS data provided by Chung et. al. (2002) and experimental data by Nouri et. al. (1993) are obtained so "validating" the experimental setup and the instrumentation utilized in this study.

Detailed inspection, by shifting the mean velocity profiles plotted in wall coordinates to locate the wall locations, showed that the inner pipe is slightly "off-centred" in the horizontal and vertical planes with differences from ideal concentric location of 8% in Plane A and 1% in Plane B. However, this eccentricity does not affect the profiles significantly and could only be noticed through such close inspection. Reflections of the laser beams from the steel centrebody close to inner wall were significant and this resulted in difficulty in obtaining complete data across the annular gap when the traverse was moved in the z-direction i.e. in Plane A. As a consequence of this issue, the closest measurement to the inner wall that could be made was only up until $\xi \approx 0.1$.

As observed in **Chapter 5**, there is an increased suppression of the radial rms fluctuation levels with drag reduction when compared to that of Newtonian flow. This presents further complications for the measurements of $\overline{u'v'}$ in the annular pipe with the cross slit module; as has already been seen with the Newtonian fluid that there is a threshold limit for which the cross slit measurements could be accepted with confidence. Even though the mean axial and rms component measured at two Reynolds numbers for 0.0124% xanthan gum seemed to agree well with and without the cross slit as shown in **Figure 6.9(a)-(b)**, the radial component in **Figure 6.10(a)** measured with the presence of the cross slit are below the data measured without the cross slit and again contain an unacceptably large degree of scatter. Disagreement between the data measured with and without the cross slit could also be observed for a more viscous solution, 0.15% xanthan gum, as shown in **Figure 6.10(b).** Due to the higher drag-reduction level at this Reynolds number, low values of the radial component could be observed for the data measured without the cross slit, as expected of drag-reduced flow. However, the data measured using the cross slit show significant scatter throughout the annular gap. The maximum mean radial velocity, v, (not shown) measured with the cross slit never exceeded 5% of U_B but was generally less than 3% while the mean radial velocity measured without the cross slit was always less than 2% of U_B suggesting the presence of the slit does alter the radial velocity distribution. Therefore, all the data measured for the Newtonian fluid, glycerine and non-Newtonian fluid will be measured using only the flat-faced optical box at a location 104.7D_H downstream of the inlet. It is also concluded that the cross-slit module has an unacceptably large effect on the turbulent velocity field, at least in this set up, and cannot be used.

6.4 Results

6.4.1 Pressure-drop measurements

Pressure drop against pipe length measurements were taken to check the fully-developed location. Starting at about $50D_H$ downstream of the inlet, minimal changes in the pressure drop per unit length was observed indicating fully-developed flow beyond this point, as was also established by Gouldson (1997). As described in **Chapter 4**, subsequent pressure-drop measurements were conducted over a distance of $41.3D_H$ starting at $75.8D_H$ downstream of the inlet, a location which is well over the required length for fully-developed conditions.

In **Figure 6.11**, a plot of the Fanning friction factor, *f*, against Reynolds number, *Re*, for water and glycerine, good agreement is observed with the theoretical prediction (Equation [6.2]) within the laminar regime and the empirical predictions by Jones and Leung (1981) in Equation [6.10] within the high Reynolds number turbulent flow regime. It is also interesting to note that within the low Reynolds number turbulent regime, i.e. $6000 < Re < 15000$, the data lies between Nouri et. al. (1993) empirical prediction in Equation [6.7] and the prediction by Jones and Leung (1981). The friction factor data within the turbulent regime is on average 14% higher than the data measured in the circular pipe at the same Reynolds number in **Chapter 5**. Of the results for friction factor reported in the literature Brighton and Jones (1964) observed differences up to 10% above the pipe correlation while Lawn and Elliot (1972) reported a minimum of 5% increase depending on the radius ratio. However, the data of Jonsson and Sparrow (1966) and Quarmby (1967) lie much closer to the pipe values. Due to the low viscosity of the Newtonian fluid, water, laminar flow conditions were not attainable within the operating range of the flow loop. However, the data for glycerine encompasses all three flow regimes, laminar, transition and turbulent. Reasonably good repeatability was observed for the measurements with an average percentage difference of 3.7%.

A method initially suggested by Zakin et. al. (1977) and subsequently by Park et. al. (1989) was utilized in an attempt to detect transition from laminar to turbulent flow by plotting turbulent intensities measured at fixed radial locations against the Reynolds number. This method is especially useful for non-Newtonian fluid where transition is not always apparent in the *f-Re* plot. Escudier and Presti (1996) proposed for circular pipe flows that the near wall ($r/R = 0.8$) axial rms fluctuation level is a reliable indicator of flow regime. For this study, the axial rms fluctuation component is monitored at ξ values of 0.1 and 0.9 with the non-dimensional radial position $\xi = 0.1$ being closer to the inner wall while 0.9 is closer to the outer wall. In **Figure 6.11**, a plot of the axial rms fluctuation component normalized with the local mean velocity against the Reynolds number is shown for glycerine, a clear demarcation from the laminar regime can be detected using this method where abrupt increases in the values are observed from 2% up to 22% of the local velocities. Normalization by the local velocity is chosen as opposed to the conventional bulk velocity normalization due to the asymmetrical nature of the velocity profile within the annular pipe. Two limits of transition could be observed, Re_1 and Re_2, with the first Reynolds number limit, Re_1, identifies the onset of transition seen as a noticeable change in the turbulent activity while the second Reynolds number limit, Re_2, represents the limit where the maximum value of turbulent intensity is reached. However, as it is not possible to accurately determine the intermittency of the flow (this issue will be discussed further in the following section), it is difficult to confirm the intermittency to which Re_2 corresponds. However Re_2 does give the indication of the degree to which transition has been completed. For this study Re_1 is taken as the Reynolds number where the axial rms levels are within the laminar value (<3%) beyond which increases above the laminar limit are seen. For glycerine the first limit is detected at the same Reynolds number of 2100 for the inner and outer walls while the second limit is reached earlier for the inner wall at $Re \sim 2900$ while for the outer wall Re_2 is about 3100. Note that the transition to turbulence for the flows within this research work was allowed to occur naturally by intrinsic imperfections of the flow loop (rather than using a "tripping" mechanism e.g. Wygnanski and Champagne, 1973; Draad, 1996). The small axial rms fluctuations (u'/U_{local}<3%) detected within the laminar regime - which should of course be zero in a laminar flow - are a consequence of noise in the LDA system.

Figure 6.12 shows the friction factor data for 0.0124% xanthan gum where within the flow loop operating range laminar flow was barely observed, as can also be seen in the relatively higher axial turbulence intensity values ($u'/U_{local} \approx 3\%$ at $\xi = 0.1$ for the lowest measureable Reynolds number). However at higher concentrations, 0.07% and 0.15% xanthan gum, all three flow regimes, laminar, transition and turbulent, were clearly encountered, as observed in **Figure 6.13** and **Figure 6.14**. It is also clear that the *f-Re* relationship for power-law fluids as given in Equation [6.15] slightly under-predicts the friction factor for both 0.07% and 0.15% xanthan gum solutions. The *f-Re* and u'/U_{local}*-Re* data for 0.065% carbopol shown in **Figure 6.15** also comprises all three flow regimes while for 0.1% carbopol as shown in **Figure 6.16** the data only spans the laminar flow regime. Similar to Newtonian fluid flow at the inner and outer walls, Re_1 occurs at the same Reynolds number for 0.07% xanthan gum, 0.15% xanthan gum and 0.065% carbopol at $Re \approx 3700$, 2400 and 2000, respectively. The second Reynolds number limit, Re_2, seen as the maximum axial rms value, was also observed at the same Reynolds number for the inner and outer walls with the exception of 0.15% xanthan gum. For 0.07% xanthan gum Re_2=7700 while for 0.065% carbopol Re_2=3800. In **Figures 6.13-6.15**, Re_2 values were found to be higher for the more shear-thinning fluid indicating a larger transitional regime on the Reynolds number scale. **Table 6.3** lists all the Reynolds number limits as seen from the turbulent intensity activities and also the peak values for the fluids studied. It is interesting to note that these peak values decrease with increasing shear-thinning ability.

The *f-Re* data for 0.01% scleroglucan is shown in **Figure 6.17.** The data clearly shows negligible amount of drag reduction where the friction factor values lie within the acceptable error of the Newtonian friction factor. The pressure-drop measurements conducted on scleroglucan showed reasonably good repeatability (<3%) and the fluid rheology of the solution, which was measured prior to and after each pressure drop measurements, confirmed that the fluid was of the correct concentration and the lack of drag reduction was not due to fluid degradation. The friction factor data in the figure shows lower drag-reducing ability of scleroglucan in the annular pipe compared to what is observed in the circular pipe. Further inspection of the average wall shear stress for the circular and annular pipe flows indicate that the lower drag reduction ability is not solely due to the higher shear stress within the annular pipe. As indicated in **Table 6.4**, there are overlapping shear stress values within the circular and annular pipes, where drag reduction is observed in the pipe flow and is absent in the annular flow for almost the same magnitude of shear stress. Also shown in **Figure 6.17**, within the low Reynolds number turbulent regime, $6000 < Re < 15000$, the friction factor data lie between Nouri et. al. (1993) and Jones and Leung (1981) empirical lines, similar to that observed for the Newtonian data.

6.4.2 Time trace measurements

Time traces of the axial velocity at ξ of 0.1 and 0.9 for various Reynolds numbers spanning the three flow regimes were also monitored for the Newtonian and polymer flows. These time traces enable further understanding of the transition to turbulence detection for the fluid flow in question. Wygnanski and Champagne (1973) and Rubin et. al. (1979) found that transition can be detected through the presence of puffs in the time traces which subsequently develop into slugs at even higher Reynolds number. For flow in a circular pipe, velocity fluctuations in a puff are small close to the walls and strongest at the centre of the pipe while for a slug, the fluctuations are present across the entire cross section of the pipe. By monitoring the time traces at the centre of the pipe, the authors observed puffs for a Newtonian fluid within the Reynolds number region of $2000 \leq Re \leq 2700$ for a pipe flow under natural transition mechanism. The puffs were found to grow and split into new puffs between $2300 \leq Re \leq 2600$. Further Reynolds number increase results in the number of puffs to be reduced and a single turbulent region resembling a slug to be observed. **Figure 6.18** shows the typical characteristic shape of a puff and a turbulent slug from time-trace plots. The difference between puffs and slugs could also be detected from the velocity histogram. A puff can be seen as an asymmetry in the histogram while two peaks will appear for flows with turbulent slugs. Further discussions of puffs and slugs can be found in Wygnanski and Champagne (1973), Wygnanski et. al. (1975) and Rubin et. al. (1979), amongst others.

The time traces in this study were recorded for 30 seconds up to a maximum of 90 seconds at the two locations, $\xi = 0.1$ and $\xi = 0.9$. Note that the time traces at these two locations were not measured simultaneously. **Figure 6.19** shows the time traces of the axial velocity for the Newtonian fluid, glycerine. The plots show that the flow is completely laminar for *Re*=2000 and at *Re*=2300 spikes are detected at both positions closer to the inner and outer walls. The velocity spikes seen from the time traces are not typical of puffs or slugs seen at the centre of the pipe by Wygnanski and Champagne (1973) and Rubin et. al. (1979) as discussed earlier and consist of a more complex nature with combinations of high and low velocity spikes. The number of spikes increases as the Reynolds number is further increased and at *Re*=2600, the whole time traces looks like an intermediate between initial transition to fully-turbulent flow. Further *Re* increase results in a more complex behaviour resembling that normally observed in turbulent flow.

To quantify the degree of turbulence at the onset of the transition regime a method known as the $\bar{u}$ method (Zhang et. al., 1996) is utilized where a time ratio is defined such that:

$$\beta = \frac{\Delta t_{turbulent}}{\Delta t_{total}} \% \qquad [6.18]$$

where $\Delta t_{turbulent}$ is taken as the total time for the spikes. A spike is considered to have occurred within the time traces if the peak velocity is different by more than 15% of the local mean velocity, U_{local}. Within the laminar regime, e.g. *Re*=2000, the velocity varies within ± 15% of the U_{local} and no obvious spikes are observed.

At the onset of transition for glycerine at *Re*=2300, the time ratio for the inner wall was found to be $\beta = 26\%$ which is higher than that of the outer wall (β=11%). As the time ratio takes into account the intermittency within the flow, it can be regarded as a measure of how transitional the flow is. Hence, for the Newtonian fluid, glycerine, measured in this study the inner wall flow has a higher degree of turbulence than the outer wall at the start of transition. This observation is in agreement with the behaviour predicted by the theoretical stability analysis by Hanks and Bonner (1971). At higher Reynolds numbers, the occurrence of the spikes are more frequent with higher velocity fluctuations and hence the assessment of the time ratio is subject to a high degree of uncertainty. Therefore, only a qualitative assessment of the time traces has been conducted for higher Reynolds number flows.

More advanced methods of intermittency estimation - such as the square of first derivative method and the second derivative method - which have been used to quantify intermittency for hot-wire anemometry data by Keller and Wang (1995) have also been attempted. However, these methods were found not to be suitable for low sampling rates achieved here (~100 to 500 Hz). The low sampling rate and also the non-uniform arrival time interval of our LDA data results in the actual spikes to be undetected as these spikes occur at large time intervals. As demonstrated by Wang and co-workers (Keller and Wang, 1995; Wang and Zhou, 1998), these methods produced intermittency calculations fairly well for a sampling rate of 2kHz.

Figure 6.20 shows the time traces for 0.07% xanthan gum at various Reynolds numbers. The velocity data at *Re*=4300 is essentially steady indicating laminar flow. At *Re*=6000, the flow close to the inner wall is clearly unsteady with no distinct spikes, however, high amplitude (>50% of local mean velocity) spikes could only be observed for the flow closer to the outer wall. The β values are 15% and 35% for the inner and the outer walls respectively indicating higher turbulent activity near the outer wall. This observation suggests that the flow closer to the outer wall moves to transition earlier than the flow closer to the inner wall. The number of high amplitude spikes increases with Reynolds number and at *Re*=28700 fully-turbulent flow is observed. At the higher concentration of 0.15% xanthan gum in **Figure 6.21** similar characteristics are observed with the first trace of turbulence found at *Re*=6500 with β values of 23% and 31% for the inner and outer walls respectively. As the Reynolds number is further increased to 8100, qualitative assessment of the time traces shows higher amount of turbulence on the outer wall confirming our conclusions.

The transitional flow study of the yield stress fluid, carbopol at a concentration of 0.065% shown in **Figure 6.22**, shows unsteady flow at *Re*=2800 with time ratio of 8% for the inner wall and 15% for the outer wall. The greater number of high amplitude spikes on the outer wall when the Reynolds number is further increased suggests that, similar to the shear-thinning fluid xanthan gum, Re_{crit} for the outer wall is lower than that of the inner wall. For 0.1% carbopol however turbulent flow conditions were not attainable within the operating range of the flow loop.

The observations described above indicate that the higher shear stress on the inner wall compared to that on the outer wall does not lead to earlier transition for shear thinning and yield stress fluids as is observed for the Newtonian fluid, glycerine. Though there are velocity variations detected within the time traces for the flow closer to the inner wall, this effect could be a consequence of the high amplitude spikes occurring for the flow closer to the outer wall, i.e. mass conservation enforcing changes in velocity near the inner wall.

Table 6.5 lists the critical Reynolds number obtained from the time traces and the time ratios of the flow close to the inner and outer walls at the critical Reynolds number.

6.4.3 Mean flow and turbulence statistics for transitional flow

6.4.3 (a) Newtonian fluid

Figure 6.23 shows the mean axial velocity profile for glycerine at several Reynolds numbers spanning the three flow regimes; laminar, transition and turbulent. The velocity profile within the laminar regime at *Re*=2000 is in good agreement with the theoretical profile given by Equations [6.4] and [6.5]. Even though spikes were detected in the time traces at *Re*=2300, the mean velocity profile remained essentially unchanged and agrees well with the theoretical profile. At both Reynolds numbers, the velocity ratios of the maximum velocity to the bulk velocity are within the experimental uncertainty with the theoretical value of 1.51. Deviations from the theoretical laminar profile are observed at *Re*=2600 where a slight shift towards the outer wall in the location of maximum velocity is also observed. As the Reynolds number is further increased, the shape of the velocity profiles agrees with what would be expected of a turbulent flow: a progressively flatter central region is observed with increasing Reynolds number together with an increase of the velocity gradient near the walls. The ratios of the maximum velocity to the bulk velocity at these Reynolds numbers are 1.28, 1.24 and 1.15 respectively. The axial rms turbulent fluctuation component normalized with the bulk velocity is plotted in **Figure 6.24(a)-(b)**. The data measured within the laminar region is a consequence of the noise in the LDA system which is <3%. The axial rms data became scattered with values slightly higher than the noise level ($\approx 5\%$) at *Re*=2300 when spikes where first detected. At *Re*=2600, scatter in the data distribution is still detected, but at even higher values when normalized with U_B. Note that care has been taken to maximize the time to collect the velocity data within the transitional regime in order to obtain an average value representative of the actual flow characteristics. Relatively smooth distributions of axial rms fluctuations became pronounced when the Reynolds number is further increased. The location of the maximum axial rms fluctuation component shifts towards the wall with increasing Reynolds number. The minimum value, which occurs at the location of the maximum axial velocity decreases with Reynolds number. Escudier et. al. (1999), Presti (2000) and Rosa (2008) found that for Newtonian fluid in a circular pipe the maximum value of u'/U_B, which peaks within the transition regime, decreases as the flow moves towards fully-turbulent flow while the location of maximum u'/U_B moves towards the wall with the magnitude of minimum u'/U_B reduces with Reynolds number (Rosa, 2008), similar to that observed in the annular pipe in the current study. **Table 6.6** lists the ratio of maximum velocity to the bulk velocity for each Reynolds number measured together with the non-dimensional location of the maximum velocity.

6.4.3 (b) Non-Newtonian fluids

Two concentrations of xanthan gum, a shear-thinning fluid, and two concentrations of a yield-stress fluid, carbopol, were utilized in the transitional flow study. For 0.07% xanthan gum solution the mean axial velocity profile within the laminar, transition and turbulent regimes is represented in **Figure 6.25**. The numerical solutions for fully-developed laminar annular flow for a power law fluid with *n*=0.61 are also included for comparison. As expected of a shear-thinning fluid, the ratio of maximum velocity to the bulk velocity within the laminar regime

($U_{max}/U_B \leq 1.46$) is lower than the theoretical value for a Newtonian fluid ($U_{max}/U_B = 1.51$). Fairly good agreement within the laminar regime is obtained with the numerical results even at *Re*=6700 where spikes are present in the time trace plot (**Figure 6.20**). However, due to the flat nature of the velocity profiles within the three flow regimes, it is difficult to determine the exact location of the maximum velocity and was therefore assumed to be equal to that in laminar and turbulent Newtonian flows. The corresponding axial rms fluctuation components normalized with the bulk velocity are represented in **Figure 6.26(a)-(b)**. Within the laminar regime, the data is scattered at low values typical of that normally observed in laminar flow due to the noise in the LDA system. At *Re*=6700, above the Reynolds number where spikes in the time traces are first detected, the data showed peaks of greater than 7.5%U_B at $\xi < 0.15$ and $\xi > 0.85$ with minimum values located close to the region of maximum axial velocity. An increase in the peak magnitude is observed with further increase in Reynolds number with the peak locations found to be shifted closer to the walls.

At higher concentration of 0.15% xanthan gum, as plotted in **Figure 6.27**, the mean velocity profiles coincide with that of the numerical data with *n*=0.45 even up to *Re*=8100 when spikes are present in the time traces. At *Re*=15100 where individual spikes could no longer be distinguished, the laminar numerical result failed to predict accurately the profile confirming that turbulent flow is reached. The lower value of *n* indicates greater shear thinning of the higher concentration solution which results in flatter profiles, i.e. slightly smaller ratio of maximum velocity to bulk velocity, when compared to 0.07% xanthan gum. In the axial rms fluctuation component plot in **Figure 6.28**, the data for *Re*=8100, which is above the critical Reynolds number where spikes were first detected in the time traces, show peak values of greater than 3% closer to the wall and a minimum value located close to the region of low shear rates, i.e. maximum axial velocity. At the highest measureable Reynolds number, *Re*=15000, the locations of the maximum values, which are higher in magnitude, were found to be closer to the walls similar to what has been observed for 0.07% xanthan gum. However, it is difficult to say that fully-turbulent flow has been reached at this Reynolds number as the time traces (**Figure 6.21**) observed is not typical of what would be expected of fully-turbulent flow.

As the yield strength is low for 0.065% carbopol, no plug region typical of a yield stress fluid is observed for the laminar profile as shown in **Figure 6.29**. The numerical data was plotted for a Herschel-Bulkley fluid with the parameters obtained from the data measured in the rheometer using the cone and plate geometry, as discussed in **Chapter 3**. If the parameters from the data measured using the roughened plate are used in the numerical simulations, a poorer agreement is observed with the experimental data. These results would seem to indicate that within the annular rig, wall depletion of the carbopol solution does indeed take place. The low yield stress has no significant effect on the transition to turbulence as the behaviour is similar to that of the shear-thinning fluid, xanthan gum. It can also be deduced that U_{max} / U_B, which is lower than the theoretical Newtonian value, decreases with further increase of the Reynolds number towards the fully-turbulent regime. The location of maximum velocity within the laminar and transitional flow regimes was found to be approximately $\xi = 0.44$. However, as the Reynolds number is increasing towards the fully-turbulent regime, the velocity profile becomes progressively flatter meaning it is harder to determine if the location of maximum velocity has in fact shifted. In the axial rms fluctuation component plot in **Figure 6.30(a)-(b)**, again, data scatter is observed within the transitional regime at *Re*=3100 above 5% of the bulk velocity. A relatively smooth distribution of the data is observed as the Reynolds number approaches that of turbulent flow at *Re*=3500. The differences in the peak values as the Reynolds number is further increased are small and because they are within the uncertainty, it is difficult to draw any solid conclusions. However, the minimum axial rms values, which are located close to the position of maximum velocity clearly reduces with Reynolds number within the turbulent regime. For 0.1% carbopol, the turbulent flow regime is not attainable within the operating range of the flow loop as discussed in section 6.4.1. The laminar profiles as shown in **Figure 6.31** agree with the numerical results of Herschel-Bulkley fluid data using the cone and plate, again, suggesting that wall depletion occurs in the flow. If the parameters from the data measured using the roughened plate are utilized the plug region would be significantly over-predicted. From the figure, the existence of the plug zone is more pronounced for this solution when compared to 0.065% carbopol within the laminar regime as expected (τ_y is higher for 0.1%). The axial velocity profiles clearly show a plug region around the axis of the gap. As the Reynolds number is further increased within the laminar regime, the extent of the plug region reduces due to the higher viscous shear stresses (Peixinho et. al., 2005), where the profiles are becoming less flat with the ratio of maximum velocity to the bulk velocity found to be increasing with Reynolds number. Similarly, the Herschel-Bulkley number, as listed in **Table 6.6**, which is the ratio of the yield stress to the viscous stress also shows a decreasing trend with Reynolds number.

From the transitional flow study, the measured mean axial velocity component indicates a slightly different behaviour for the Newtonian and polymer flow in relation to the location of maximum velocity. A shift towards the outer wall from a location of ξ=0.44 could be seen within the transitional flow regime for the glycerine-water mixture. This shift is a consequence of the flow adjusting to the change in momentum transport as suggested by Hanks and Bonner (1971). The shift in the location of maximum velocity is not detected and, if any, it is not significant for the polymer flows due to the shear-thinning behaviour. The axial rms component showed similar trend for both the Newtonian and polymer flows where the peak values, which are located closer to the walls, increases once the Reynolds number increases higher than a critical Reynolds number, Re_{crit} where spikes were first detected. Below this critical value, the axial rms component data are scattered below 5% of the bulk velocity with the maximum values, if any, found to be located at the centre of the annular gap. Once Re_2 is reached the peak location started to shift closer to the walls as the Reynolds number is further increased into fully-turbulent flow.

6.4.4 Mean flow and turbulence statistics for fully-turbulent flow

6.4.4 (a) Newtonian fluid

Axial velocity profiles of water together with the Reynolds stress components have been measured for three different Reynolds numbers using the slit module, 96.6 D_H downstream of the pipe entrance. This location has been established to be sufficient for fully-developed flow. The use of the slit module at these Reynolds numbers has also been shown to be successful as discussed in section 6.3. The mean axial velocity profiles normalized with the bulk velocity for the three Reynolds number are plotted in **Figure 6.32**, together with the measurement at *Re*=9900 where no reliable measurements of Reynolds shear stresses could be made. Flatter profiles are observed with increasing Reynolds number with the location of maximum velocity found to be located closer to the inner pipe wall at a non-dimensional location of $\xi = 0.44$ for all Reynolds numbers. This location is only displaced by less than 1%, which is within the experimental uncertainty, from the location of the zero shear stress as determined from the Reynolds shear stress data plotted in **Figure 6.5(b)**. Since the location of maximum velocity could hardly be distinguished from the location of zero shear stress r_{max} is taken as both the location of maximum velocity and zero shear stress for Newtonian and non-Newtonian fluids studied where measurements of Reynolds shear stresses were not possible (essentially all of the non-Newtonian fluids). In **Figure 6.32**, the ratio of the maximum velocity to the bulk velocity was found to decrease only slightly with increasing Reynolds number. At *Re*=9900, a ratio of 1.16 is observed while at *Re*=76700, the ratio reduces to 1.14. Data obtained by Nouri et. al.

(1993) conducted within a concentric annulus with radius ratio of 0.5 for a Newtonian fluid at *Re*=26600, are also shown for comparison. Note that the data by Nouri et. al. (1993) has been rescaled by 6% to match the bulk velocity from the flowrate obtained through the process of integration of the velocity profiles as done in Chung et. al. (2002). After this rescaling procedure, good agreement with the experimental results obtained from this study are observed. The rms fluctuation components normalized with U_B are shown in **Figure 6.33**, **6.34** and **6.35**. The magnitudes for the fluctuation components decrease from axial to tangential and finally to the radial component. The peak values of the axial rms fluctuation component decrease with increasing Reynolds number especially on the inner wall with the locations found to be shifted closer to both walls. The minimum values, which occurred at the location of maximum velocity remain essentially unchanged for this high Reynolds number turbulent flow regime. The peak values of the radial rms components are all within the experimental uncertainties, as shown in **Figure 6.34**, with the locations found to be shifted towards both walls as the Reynolds number is increased. Increasing peak values were observed in **Figure 6.35** for the tangential component closer to the outer wall. As discussed in section 4.2, only limited measurements could be made close to the inner wall as the presence of a stainless steel centrebody resulted in back reflections of the Doppler signal.

Figure 6.36 shows the mean flow data of water in wall coordinates (i.e. $u^+ \left(\equiv u/u_\tau\right)$ against $y^+ \left(\equiv \rho y u_\tau / \eta_W\right)$) for all Reynolds numbers. The friction velocity, u_τ is calculated using the wall shear stresses at the inner and outer walls. These wall shear stresses were calculated using the pressure-drop measurements and the zero shear stress location, in this case r_{max}, via Equation [6.13]. As shown in the figure the data close to the walls are in good agreement with that expected for the viscous sublayer (i.e. $\left(y^+ < 10\right)$, $u^+ = y^+$). In the Newtonian core region, the data for the inner and the outer walls collapse, in agreement with the empirical equation with the constant proposed by Clauser (1956) as in Equation [6.14], as opposed to the well known log law constant (Tennekes and Lumley, 1972) which is applicable to circular pipe flows. Using the same assumption of maximum velocity location being coincident with the zero shear stress location as used here, Brighton and Jones (1964) found that the outer layer velocity profile agreed with the well-known log law for radius ratios of 0.0625 and 0.562. The inner layer profile agreed with the line for the log law equation with the constant proposed by Clauser only for the higher radius ratio (κ=0.562).

The rms fluctuation component of the axial velocity plotted in wall coordinates is shown in **Figure 6.37**. Data closer to the wall $\left(y^{+} < 10\right)$ is not available especially for the higher Reynolds number flows as the viscous sublayer thickness reduces with Reynolds number and hence less can be said regarding the location of maximum rms values due to the limited data and also due to scatter. Beyond the viscous sublayer, the u'^{+} data on the outer wall is higher than that of the inner wall for all Reynolds numbers measured. A clear Reynolds number trend can be observed with increasing peak values of the inner and outer walls. A similar Reynolds number trend could also be seen for the radial and tangential rms fluctuation levels plotted in wall coordinates as shown in **Figure 6.38** and **6.39**. Only limited data could be obtained close to the outer wall for the radial component due to the curved pipe wall surface while for the tangential component reflections close to the inner centrebody limited the region over which reliable data could be obtained. **Figure 6.40** shows the distribution of the Reynolds shear stress component, normalized by the friction velocity. The data distribution is asymmetric in a similar manner to what is observed for the mean axial velocity with the location of the zero shear stress found to be closer to the inner wall and at essentially the same location as the maximum axial velocity. The distribution is also slightly curvilinear due to the unequal distribution of shear stresses. A very minimal Reynolds number trend could be observed for $0.2 \leq \xi \leq 0.8$. Beyond ξ=0.8 the large data scatter is probably a consequence of the cross slit. On the inner wall, the shear stress maxima increase with Reynolds number within the location of $\xi \approx 0.05$.

6.4.4 (b) Non-Newtonian fluid

Measurements were conducted for turbulent flows of 0.0124% and 0.07% xanthan gum. As discussed in section 6.4.1, 0.01% scleroglucan, the polymer which was initially chosen to match the polymer utilized in the pipe-flow studies, did not show appreciable drag reduction in the annular pipe geometry and hence 0.0124% xanthan gum, which has the same concentration ratio c/c^* as that of 0.01% scleroglucan, has been selected instead. As has been established in **Chapter 5**, and also in many previous studies (Warholic et. al., 1999; Escudier et. al., 1999 and Presti, 2000, amongst others), the effects of drag reduction could mainly be seen in the regions close to the walls where changes in peak magnitudes and locations of the fluctuation components in relation to the Newtonian fluid are observed. As a consequence in what follows wall coordinates are used to highlight this importance.

Figure 6.41 shows the mean flow data in wall coordinates for 0.0124% xanthan gum. The xanthan gum data in the viscous sublayer follows $u^+ = y^+$ as expected. In the Newtonian core region, the data are shifted upward from but remained parallel to the Newtonian data. The higher values of u^+ are clear evidence of drag reduction. At the lowest measured Reynolds number, where the drag reduction is only about 3.2%, the outer wall data lie close to the Newtonian line and is only progressively upshifted with higher Reynolds number. Complete collapse of the inner and outer walls data only occurs at DR$\approx$12%. These observations suggest that the initial contribution of drag reduction comes from the inner wall. At even higher levels of drag reduction, seen in **Figure 6.42** for 0.07% xanthan gum measured at *Re*=28700 where DR=42.3%, both the inner and outer walls data are no longer parallel shifted from the

Newtonian line, as expected for high drag-reducing flows (Warholic et. al., 1999). The outer wall profile is lower than the inner wall data indicating that the inner wall flow contributes more to the overall drag-reduction effect.

Normalizing the axial rms fluctuation component with the friction velocity, as shown in **Figure 6.43**, highlights an interesting effect. Suppressions could be observed for 0.0124% xanthan gum at all Reynolds numbers measured on the outer wall while a slight increase is seen on the inner wall peak values. For the inner wall peak values the differences are small and essentially within the experimental uncertainty although the trend is consistent across all the Reynolds numbers. At even higher levels of drag reduction (DR=42.3% for 0.07% xanthan gum in **Figure 6.44**), an increase in the peak levels are observed at both walls. The radial rms fluctuation levels for 0.0124% xanthan gum, shown in **Figure 6.45**, are globally much lower than that for water, however, in **Figure 6.46** peak increases are observed for the tangential component except for the peak value at the inner wall for *Re*=57600. For higher levels of drag reduction, as in the case for 0.07% xanthan gum, increased suppression could be seen for both the radial and tangential rms fluctuation levels when plotted in wall coordinates as shown in **Figure 6.47** and **6.48**. These results indicate that different turbulent structure behaviour between the "low" and "high" drag-reducing annular flow can be seen than what is observed in pipe and channel flows. Instead of an increase in the peak value of normalized axial velocity fluctuation (u'^{+}) for low drag-reducing flows, suppression of the peak is observed for the outer wall of the annulus only while the inner wall values remain within the experimental uncertainty for DR$\leq$12%. As a consequence, the difference between the inner and outer walls profiles is reduced for these non-Newtonian fluids when compared to that of the Newtonian solvent. An increase in the tangential peak values are observed in the annulus in contrast to the suppression which is typically observed for low drag-reducing flows in channels (Warholic et. al., 1999) and pipes (Presti, 2000). At higher level of drag reduction (DR=42%), the axial velocity fluctuation levels are increased on both walls with a further decrease of the radial and tangential components.

In **Figure 6.49** the peak values of the turbulent fluctuation components close to the inner and outer walls, normalized with the bulk velocity, have been plotted against drag reduction together with the available data from the literature for the same annulus radius ratio of κ=0.5 (Nouri et. al., 1993; Escudier et. al., 1995a). The lines in the figure are included to guide the reader's eye where clear trends are apparent. The limited data for the semi-rigid polymer, xanthan gum, from the current study and the data obtained from the literature shows a decreasing trend below 40% drag reduction of the normalized axial peak level above which a slightly more complex but generally increasing trend is observed. A vertical dotted line is also included in the figure to demarcate these two regions. Apart from a slight increase of the normalized tangential component for DR$\leq$12%, decreasing normalized radial and tangential components with drag reduction can also be seen from the data plotted. Due to limited information provided in the literature qualitative analysis of the wall data, i.e. peak values normalized with the friction velocity, u_τ, is not possible as was conducted for the pipe-flow studies in **Chapter 5**.

TABLES

Table 6.1: Mesh characteristics and maximum velocity for Newtonian flow within a concentric annulus at *Re*=106

MESH	$\frac{\Delta r}{R_o - R_i}$	No. of cells	$\frac{U_{max}}{U_B}$	e_r (%)
Analytical	-	-	1.5078	-
M4	0.01	10000	1.5085	0.046
M5	0.005	40000	1.5080	0.013

Table 6.2: Mesh characteristics and maximum velocity for power law fluid (*n*=0.75) within a concentric annulus at *Re*=664

MESH	$\frac{\Delta r}{R_o - R_i}$	No. of cells	$\frac{U_{max}}{U_B}$	e_r (%)
M1	0.083	1000	1.4056	2.235
M2	0.045	2000	1.4289	0.612
M3	0.02	2500	1.4368	0.063
M4	0.010	10000	1.4374	0.021
M5	0.005	40000	1.4376	0.007
Richardson Extrapolation	0		1.4377	
Nouri and Whitelaw (1994) - Experimental	-	-	1.4271	

Table 6.3: Reynolds number limits and maximum axial rms fluctuation level

Fluid	Re_1		Re_2		u'_{max}/U_{local}	
ξ	**0.1**	**0.9**	**0.1**	**0.9**	**0.1**	**0.9**
Glycerine	2100	2100	2900	3100	0.20	0.22
0.07%XG (n=0.61)	3700	3700	7700	7700	0.15	0.20
0.15%XG (n=0.45)	2400	2400	14000	11600	0.13	0.18
0.065%CARB (n=0.81)	2000	2000	3800	3800	0.19	0.26

Table 6.4: Average wall shear stresses in circular and annular pipe flows (the numbers in bold highlight the overlapping shear stress range)

Re	**τ_W in annular pipe flow** (Pa)	**τ_W in circular pipe flow** (Pa)
10000	**0.31**	0.10
20000	**0.93**	0.25
25000	**1.21**	**0.33**
45000	3.14	**0.83**
57000	5.28	**1.11**
65000	6.60	**1.45**

Table 6.5: Critical Reynolds number from time trace plots together with the values of the time ratios

Fluid	Re_{crit}	β **(%)**	
ξ		**0.1**	**0.9**
Glycerine	2300	26	11
0.07%XG	6000	15	35
0.15%XG	6500	23	31
0.065%CARB	2800	8	15

Table 6.6: Flow characteristics of Newtonian and non-Newtonian fluid

Fluid	***Re***	ξ_{max}	U_{max}/U_B	**HB number** $\left(\equiv \frac{\tau_y}{K(2U_B/D_H)^n}\right)$
Glycerine	2000	0.44	1.51	N/A
	2300	0.44	1.51	N/A
	2600	0.46	1.40	N/A
	2900	0.402	1.28	N/A
	3700	0.460	1.24	N/A
	9600	0.44	1.15	N/A
0.07%XG	900	0.44	1.46	N/A
	2800	N/A	1.40	N/A
	4200	N/A	1.38	N/A
	6700	N/A	1.35	N/A
	10000	N/A	1.26	N/A

	28700	N/A	1.16	N/A
0.15%XG	800	N/A	1.35	N/A
	3700	N/A	1.34	N/A
	8100	N/A	1.34	N/A
	15000	N/A	1.26	N/A
0.065%CARBOPOL	800	0.44	1.48	N/A
	2000	0.44	1.46	N/A
	3100	0.44	1.43	N/A
	3500	N/A	1.29	N/A
	4400	N/A	1.24	N/A
	7600	N/A	1.17	N/A
0.1%CARBOPOL	10	N/A	1.28	0.066
	100	N/A	1.32	0.032
	4200	N/A	1.38	0.013

FIGURES

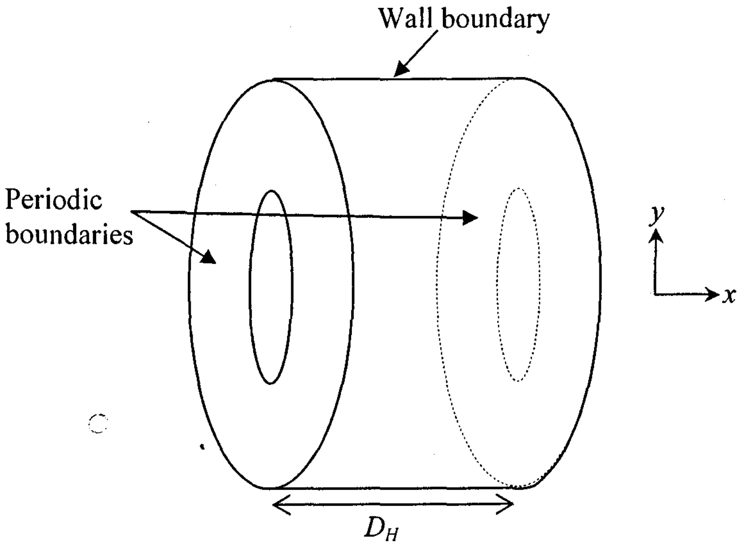

Figure 6.1(a): Annulus geometry

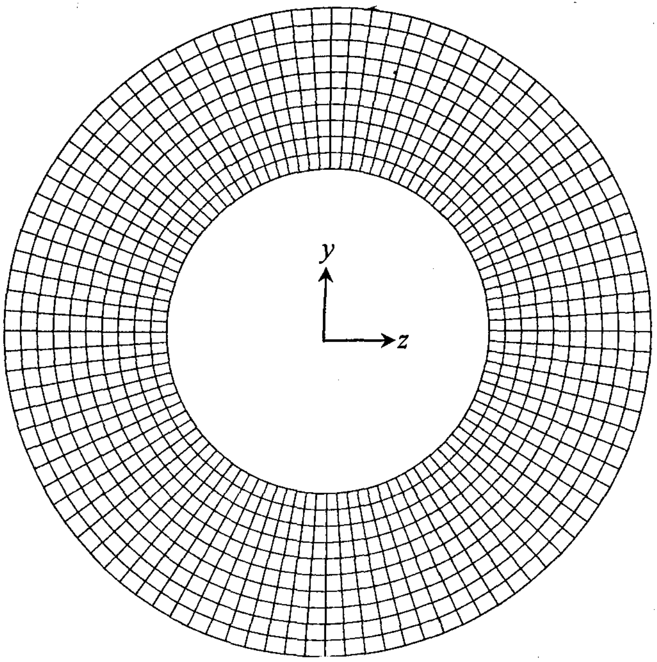

Figure 6.1(b): Computational grid (M1: 100×10 cells)

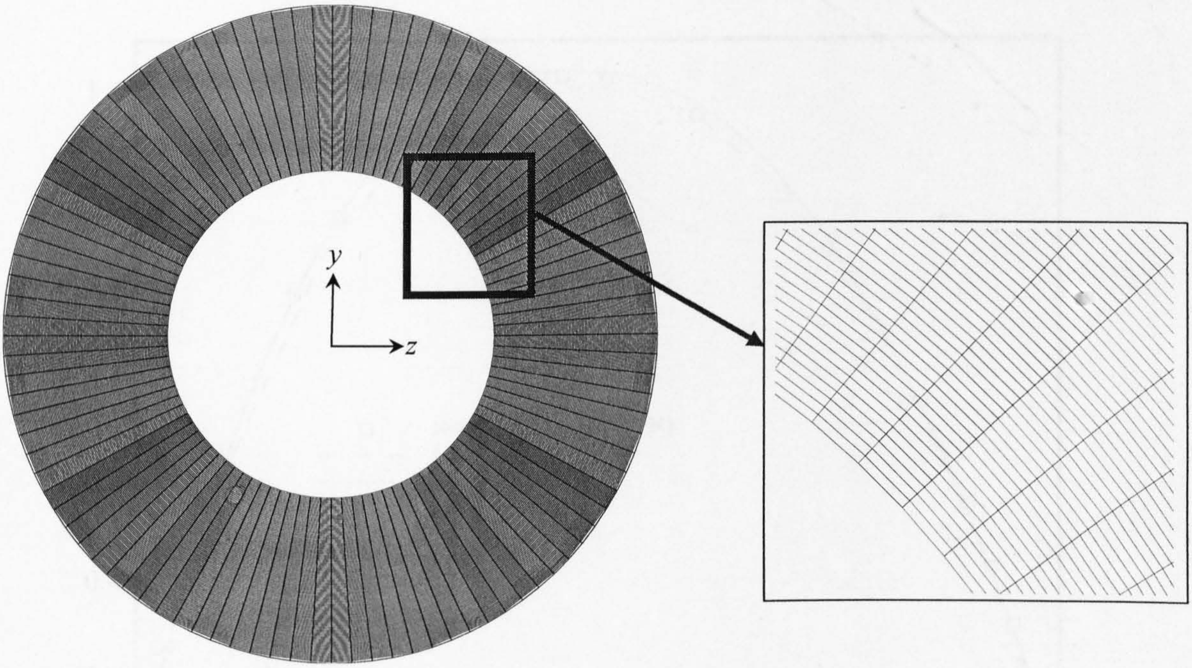

Figure 6.1(c): Computational grid (M4: 100×100 cells)

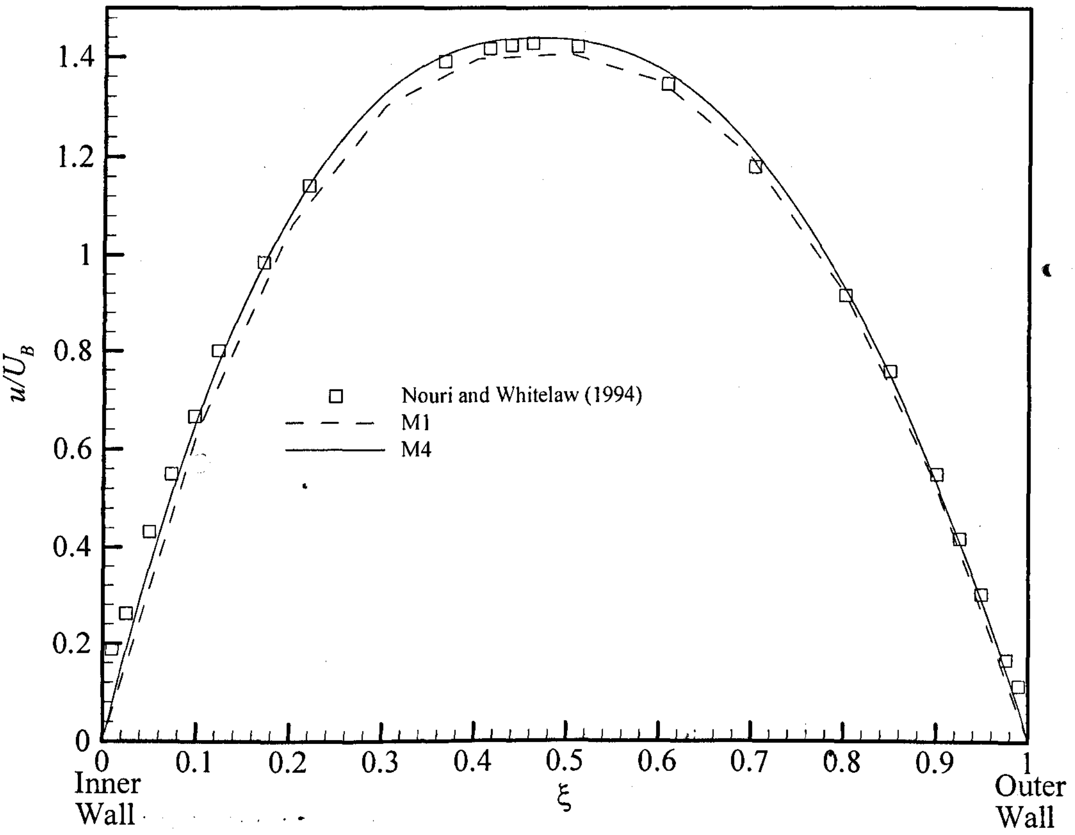

Figure 6.1(d): Comparison between FLUENT normalized velocity data and Nouri and Whitelaw (1994) normalized velocity data at *Re*=664

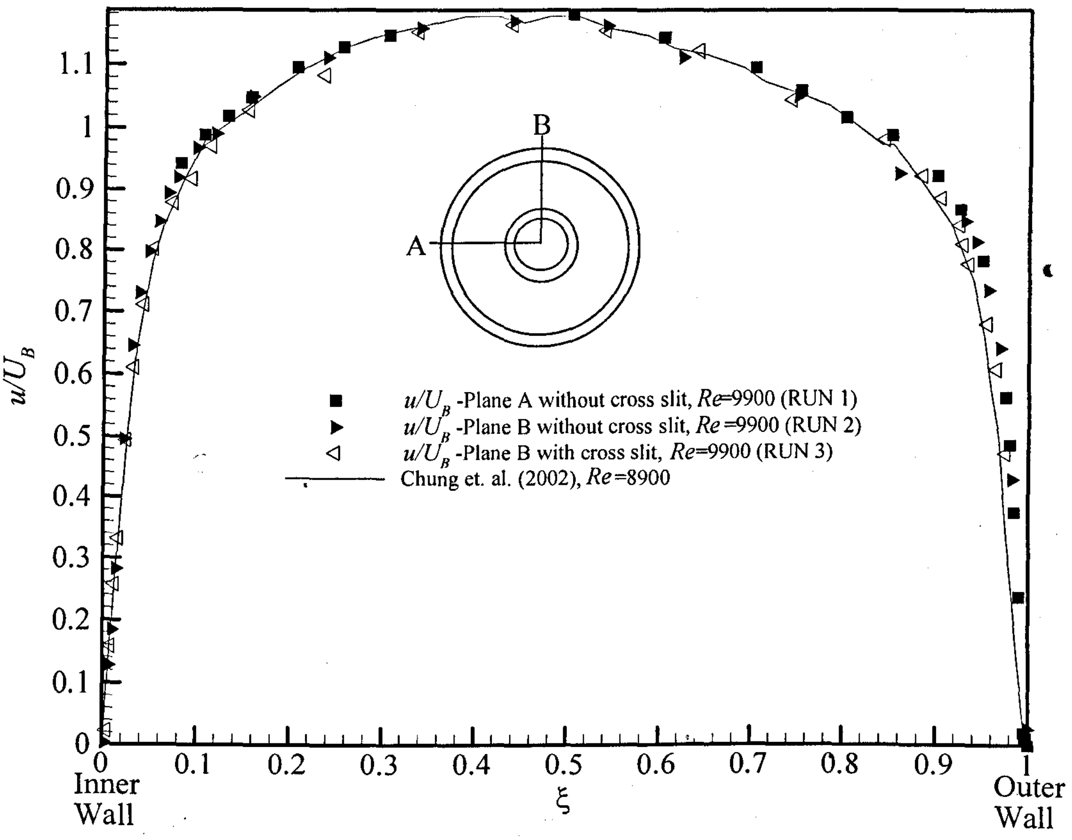

Figure 6.2(a): Normalized mean velocity distribution of water measured in various planes at *Re*=9900

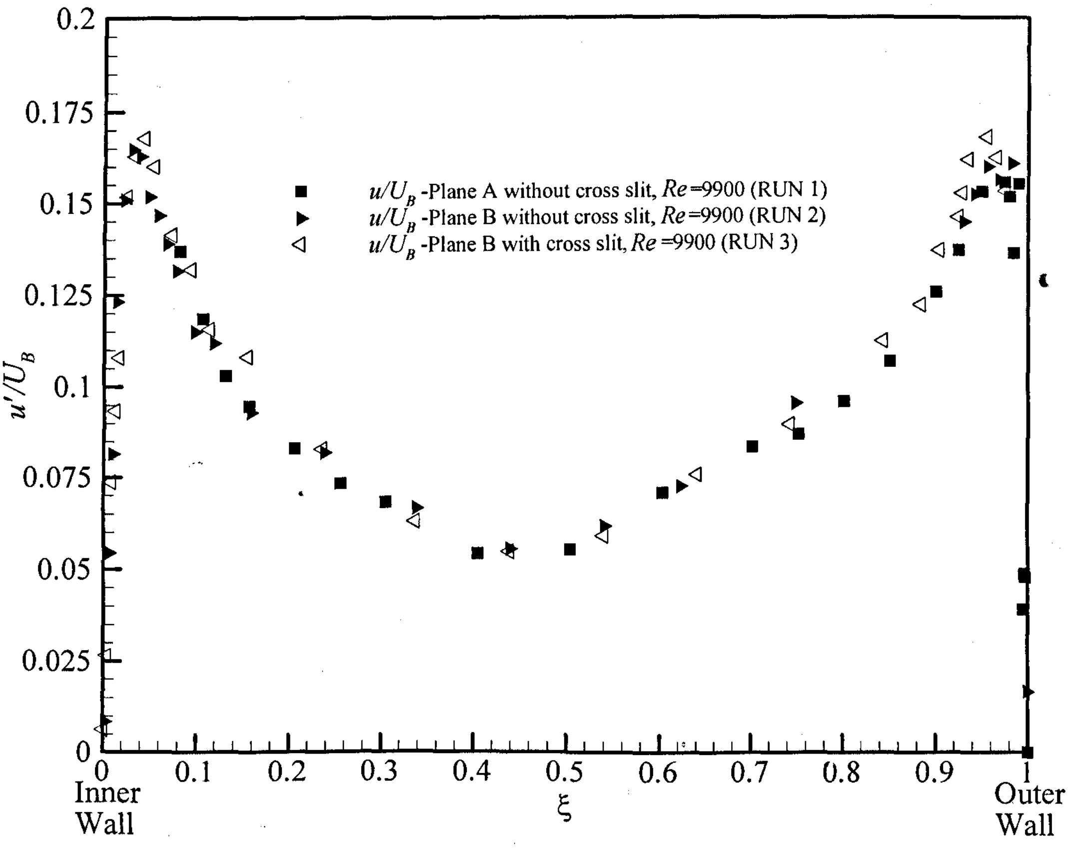

Figure 6.2(b): Normalized axial rms fluctuation level of water measured in various planes at Re=9900

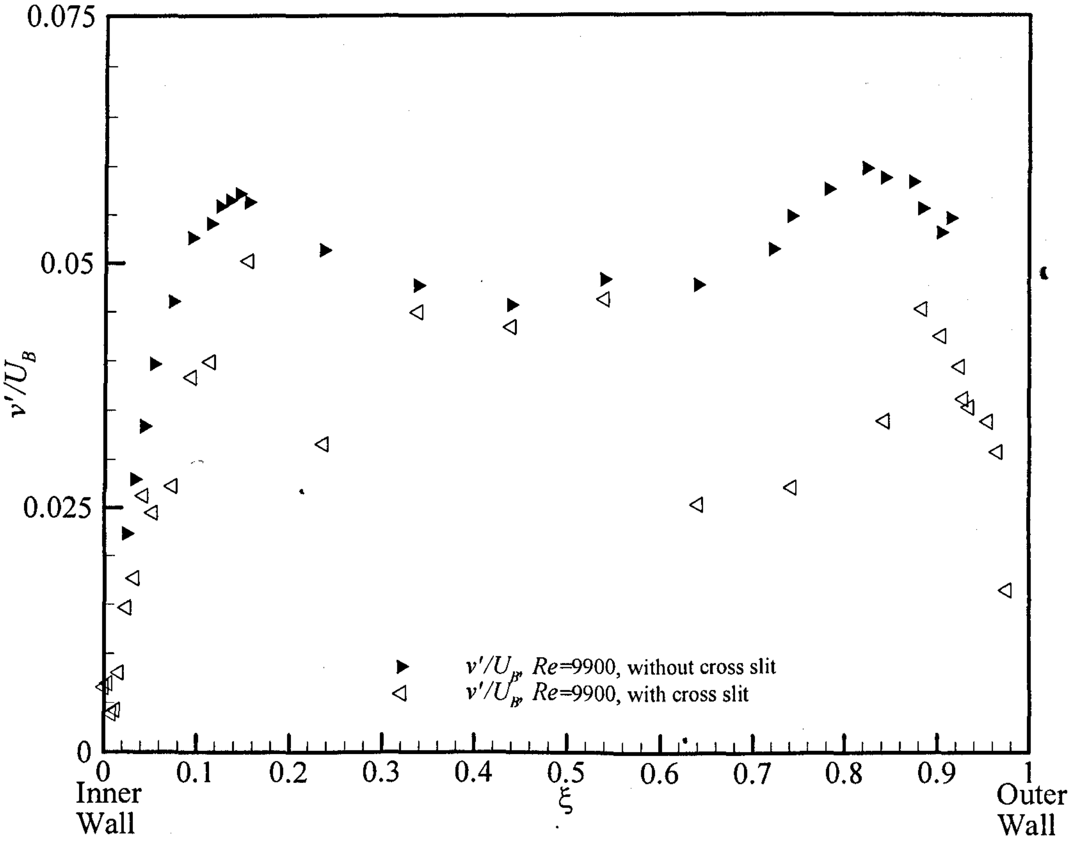

Figure 6.3: Normalized radial rms fluctuation level for water measured in Plane B at *Re*=9900

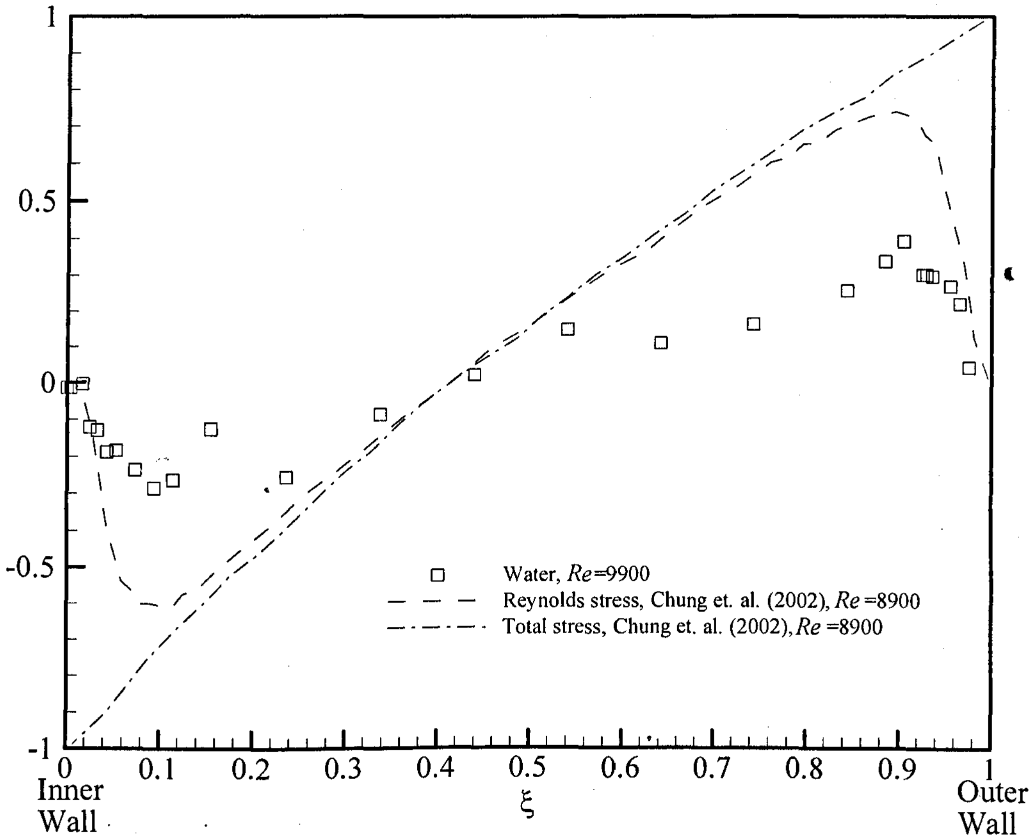

Figure 6.4: Reynolds shear stress values normalized with the friction velocity for water at *Re*=9900

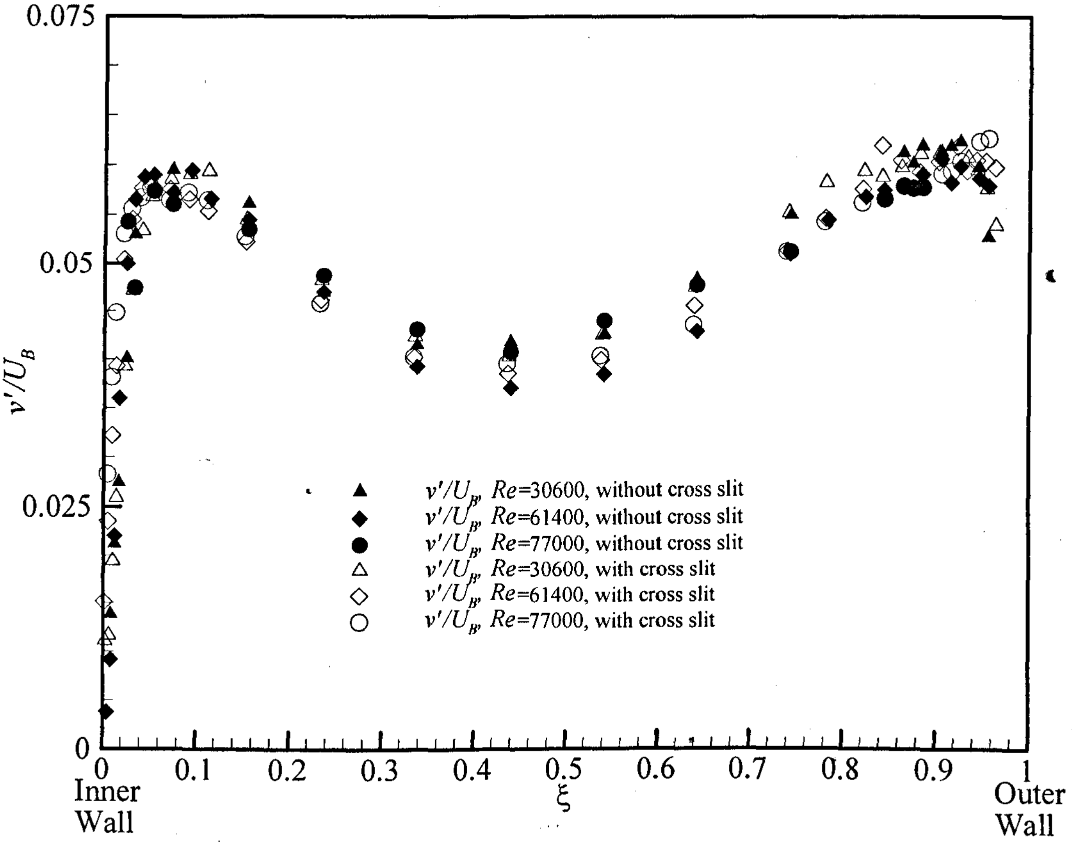

Figure 6.5(a): Normalized radial rms fluctuation level for water measured in Plane B at various Reynolds numbers

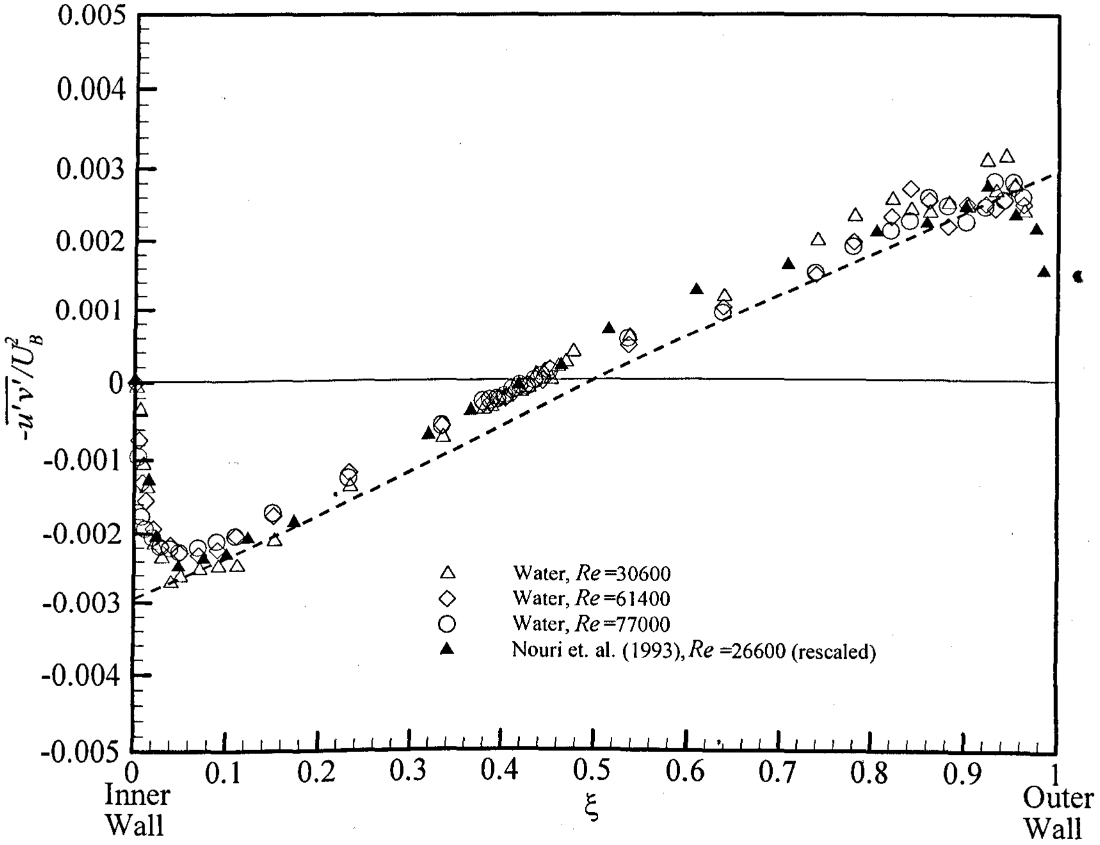

Figure 6.5(b): Reynolds shear stress values normalized with the bulk velocity for water at various Reynolds numbers. A dotted line is included to show the approximate total shear stress assuming linear and equal shear stress distribution.

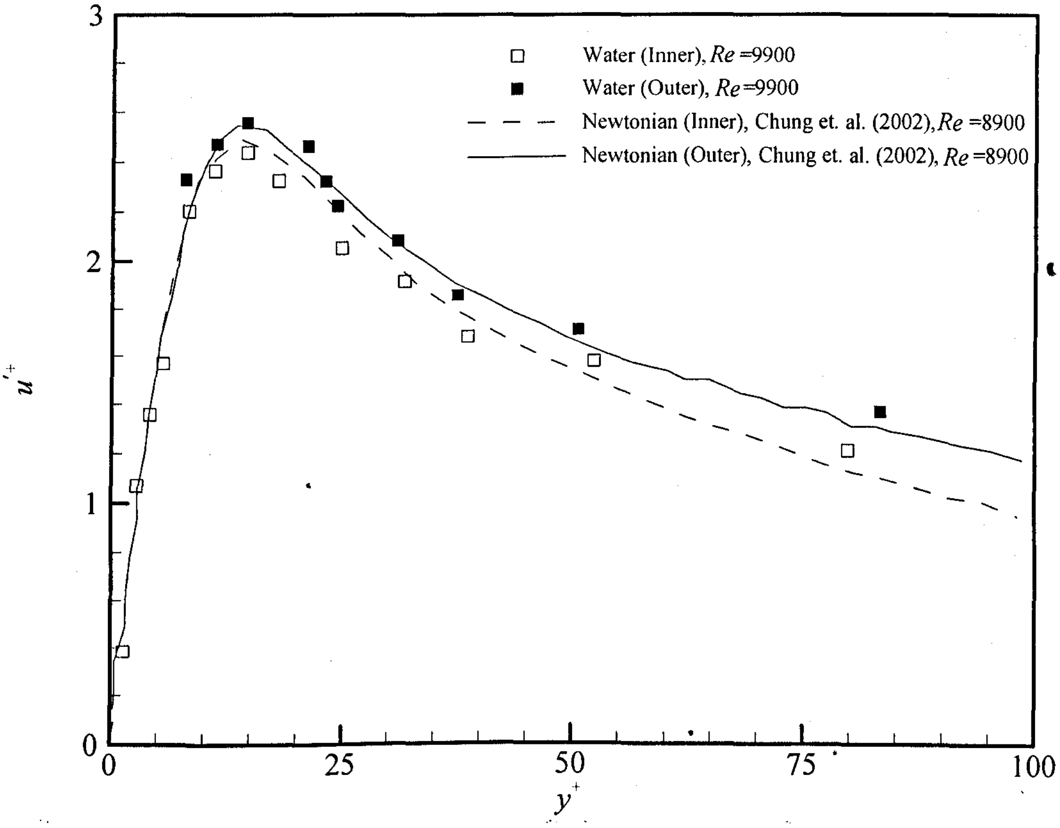

Figure 6.6: Axial rms fluctuation level in wall coordinates for water measured in Plane B without the cross slit at *Re*=9900

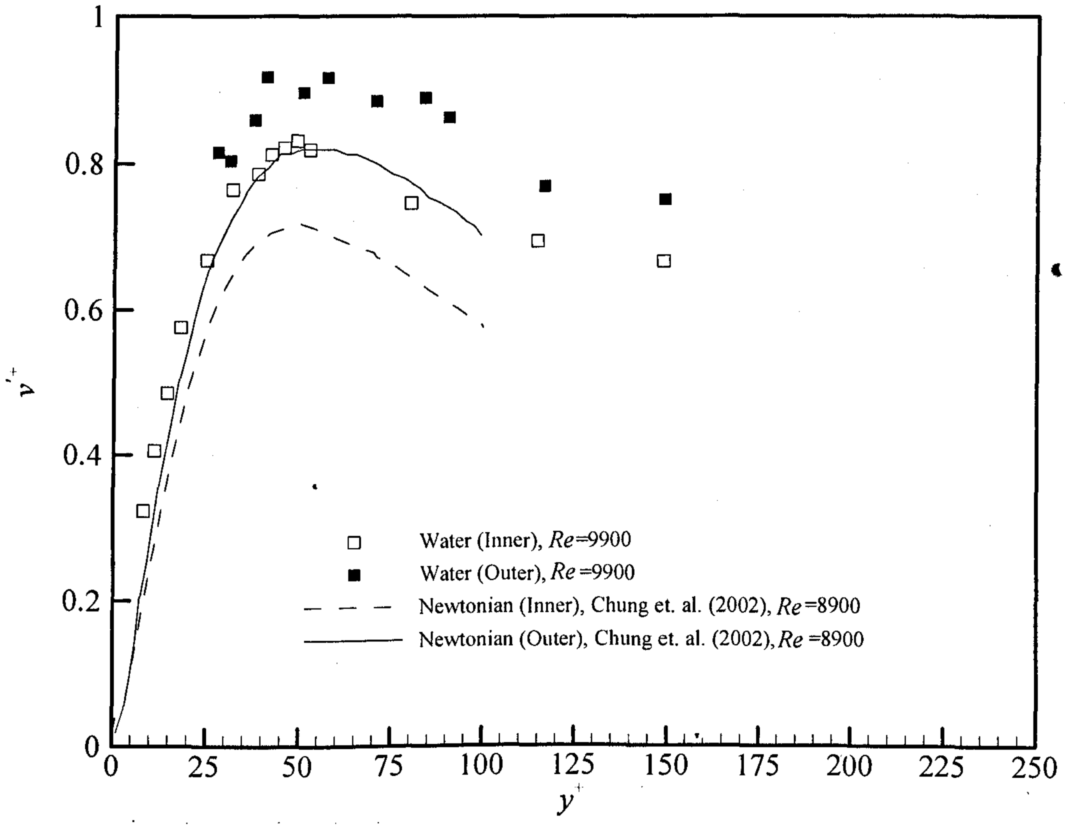

Figure 6.7: Radial rms fluctuation levels in wall coordinates for water measured in Plane B without the cross slit at *Re*=9900

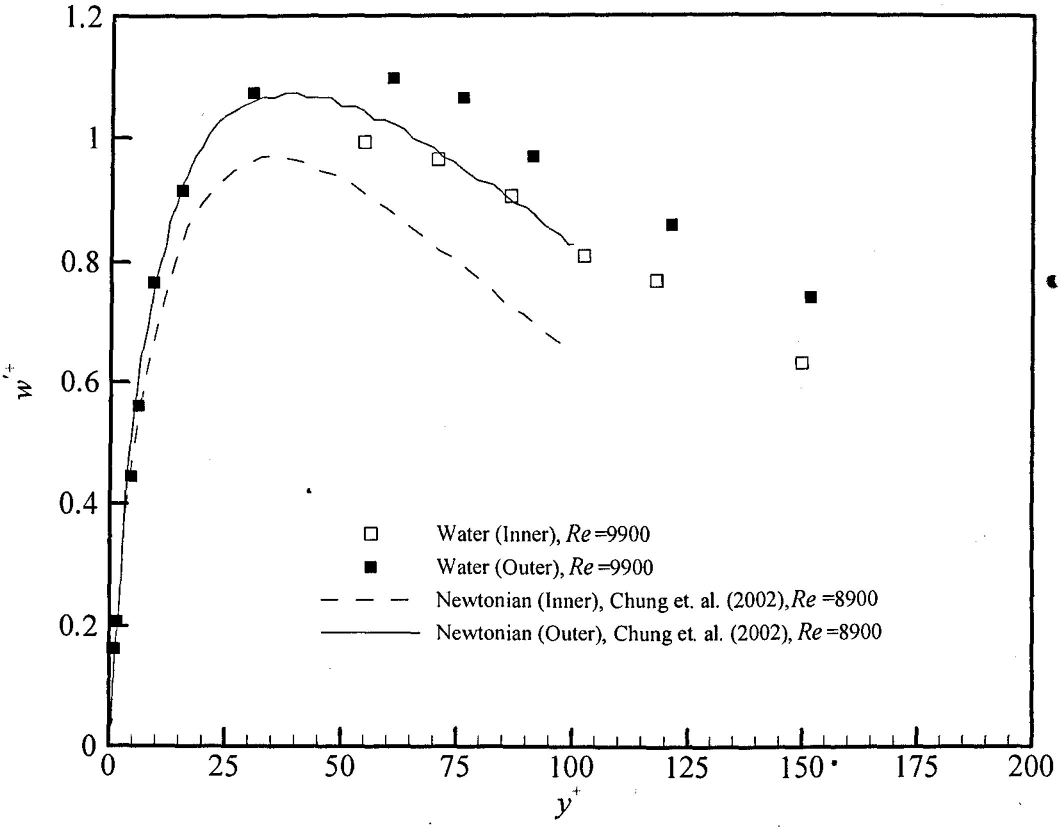

Figure 6.8: Tangential rms fluctuation levels in wall coordinates for water at *Re*=9900

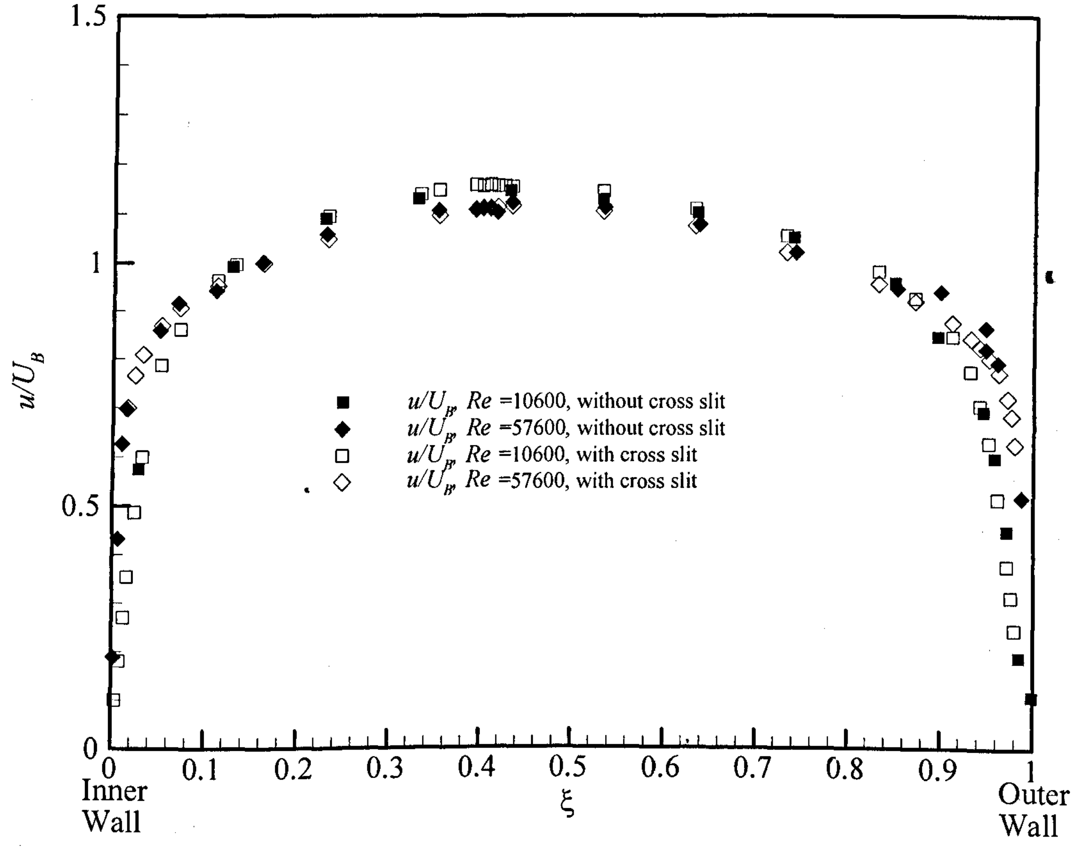

Figure 6.9 (a): Normalized mean velocity distribution of 0.0124%XG measured in Plane B with and without the cross slit module

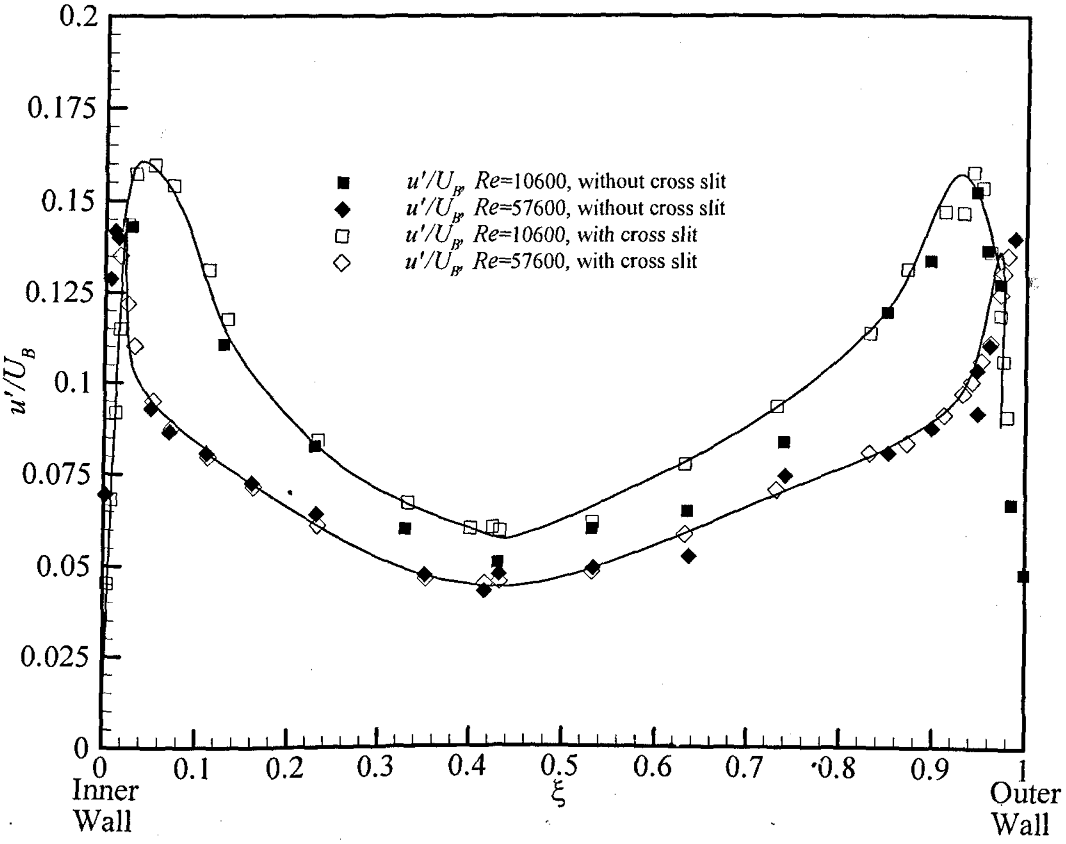

(b)

Figure 6.9 (b): Normalized axial rms fluctuation level for 0.0124%XG measured in Plane B with and without the cross slit module (lines are included to guide the eye)

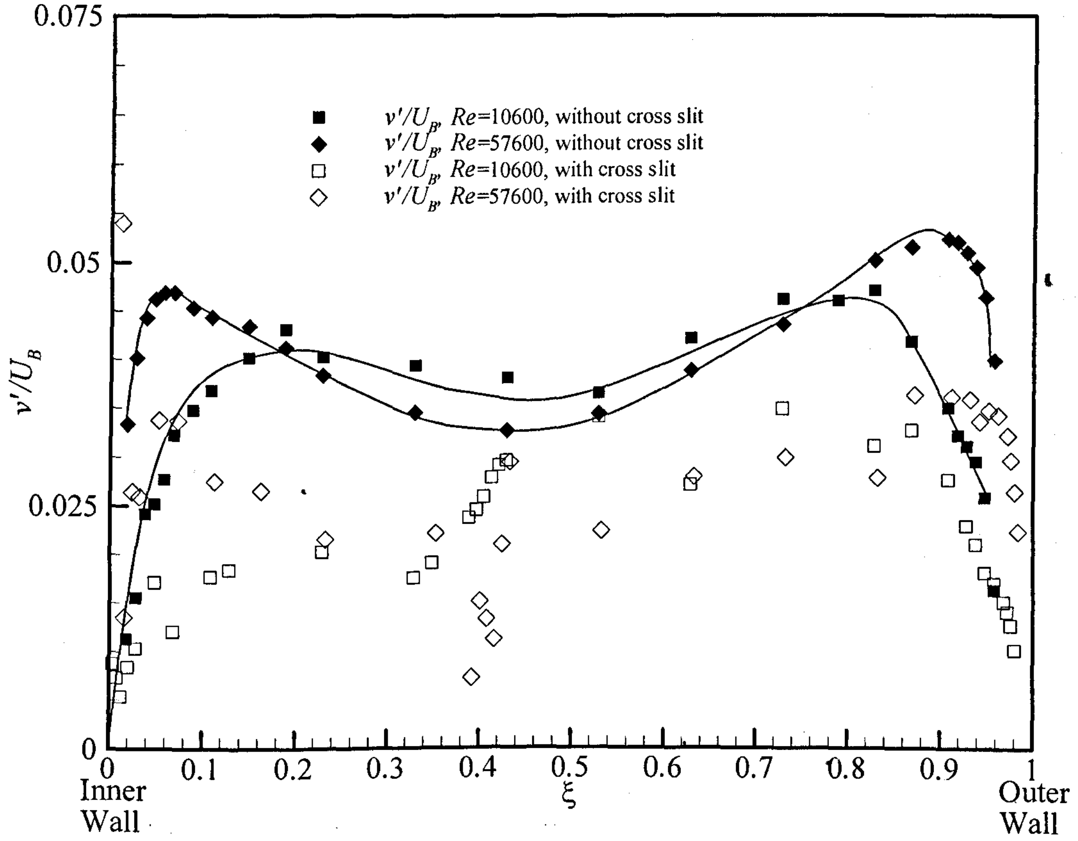

Figure 6.10(a): Normalized radial rms fluctuation level for 0.0124%XG measured in Plane B with and without the cross slit module (lines are included to guide the eye where clear trends are apparent)

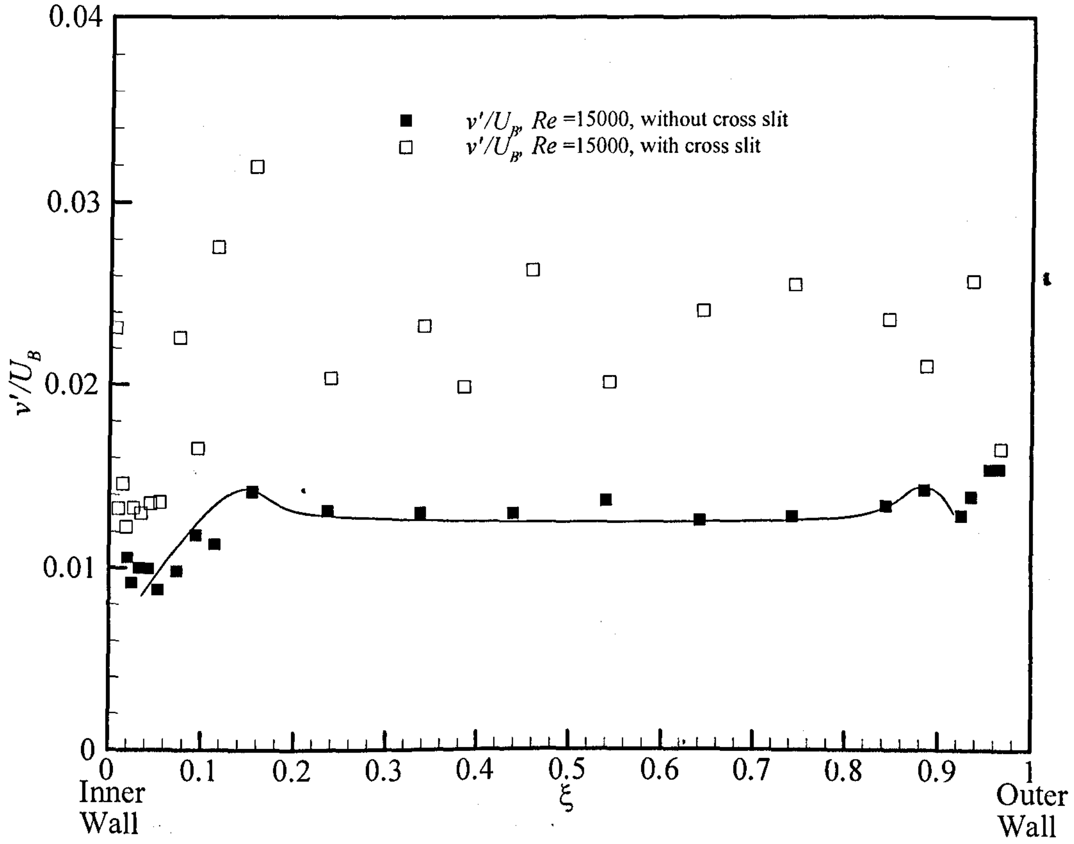

Figure 6.10(b): Normalized radial rms fluctuation level for 0.15%XG measured in Plane B with and without the cross slit module (line is included to guide the eye where clear trends are apparent)

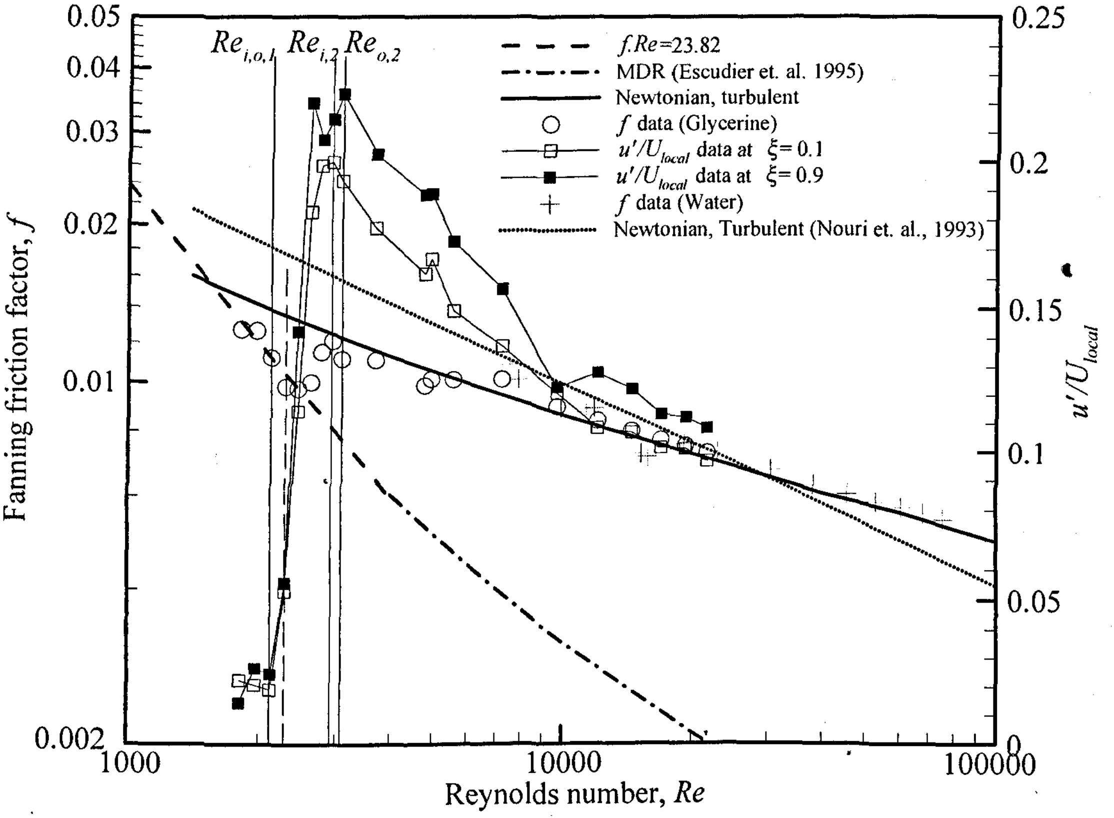

Figure 6.11: *f-Re* data for water and glycerine with u'/U_{local} levels to monitor transition for glycerine ($Re_{a,b}$ is the critical Reynolds number where *a* refers to the positions closer to the inner (*i*) or outer (*o*) walls while *b* refers to the transition stages with 1 refers to the onset of transition and 2 refers to the limit where the maximum value of turbulent intensity is reached).

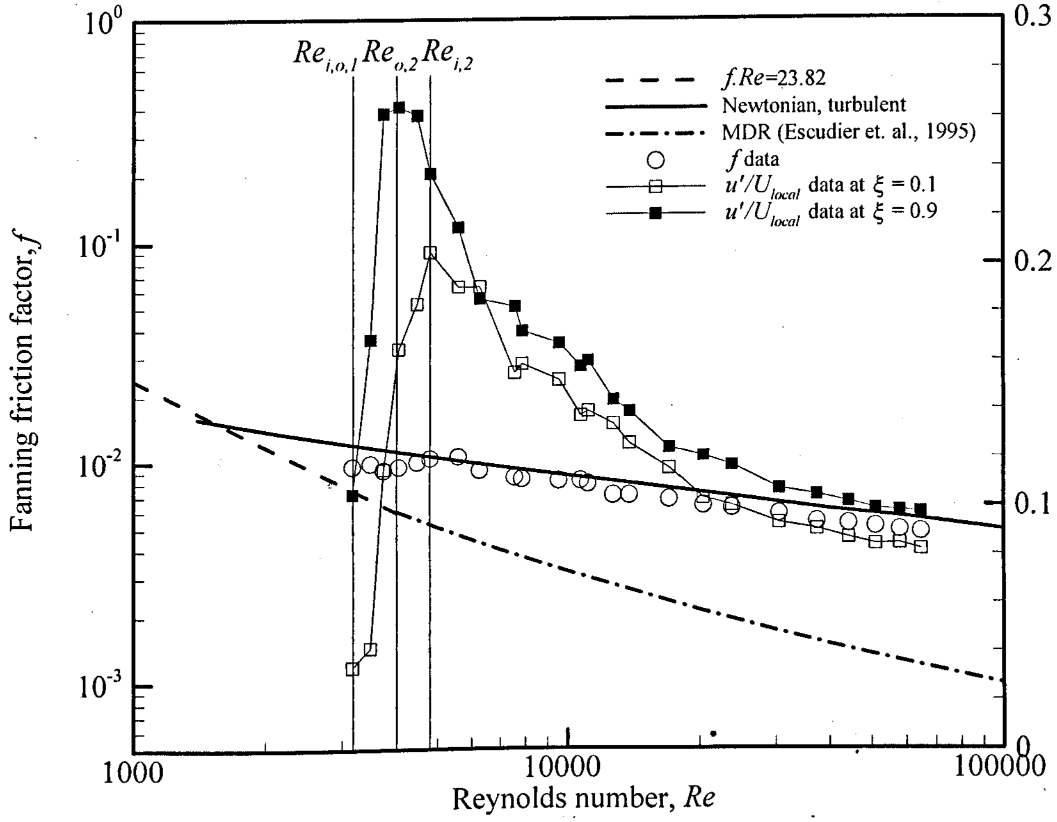

Figure 6.12: *f-Re* and u'/U_{local}-*Re* data for 0.0124%XG

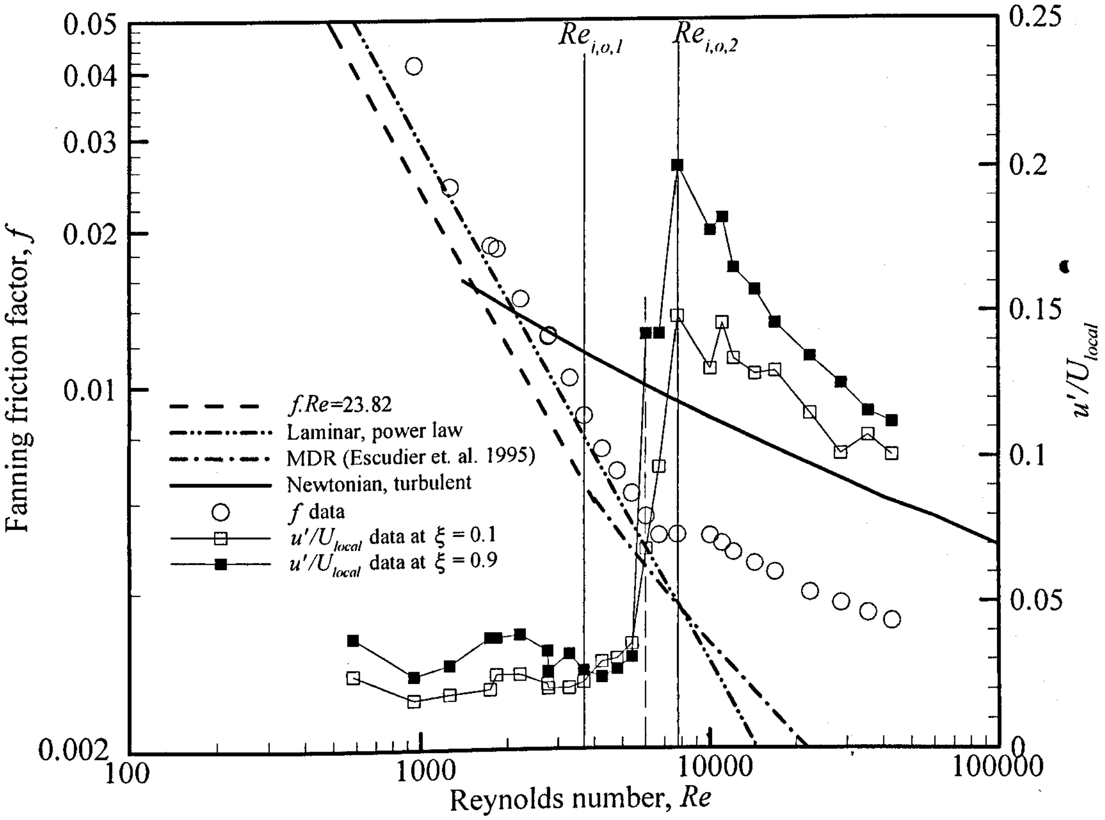

Figure 6.13: *f-Re* and u'/U_{local}-*Re* data for 0.07%XG

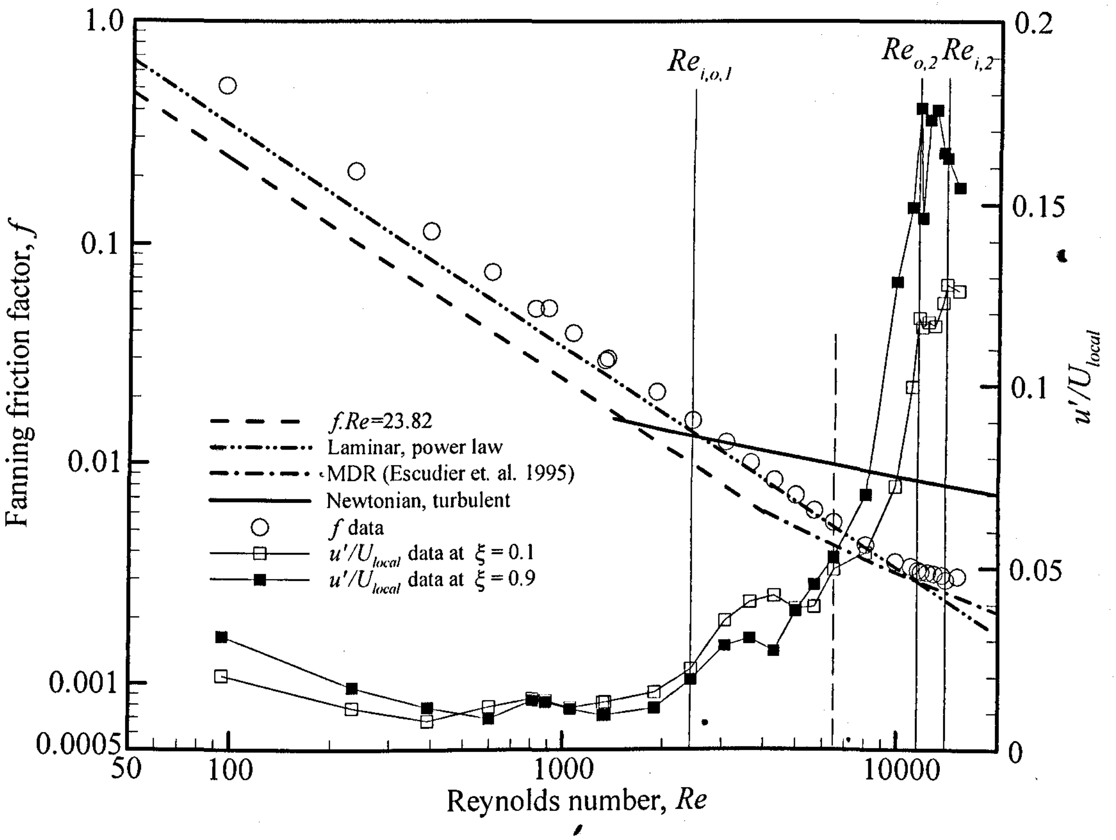

Figure 6.14: *f-Re* and u'/U_{local}-*Re* data for 0.15%XG

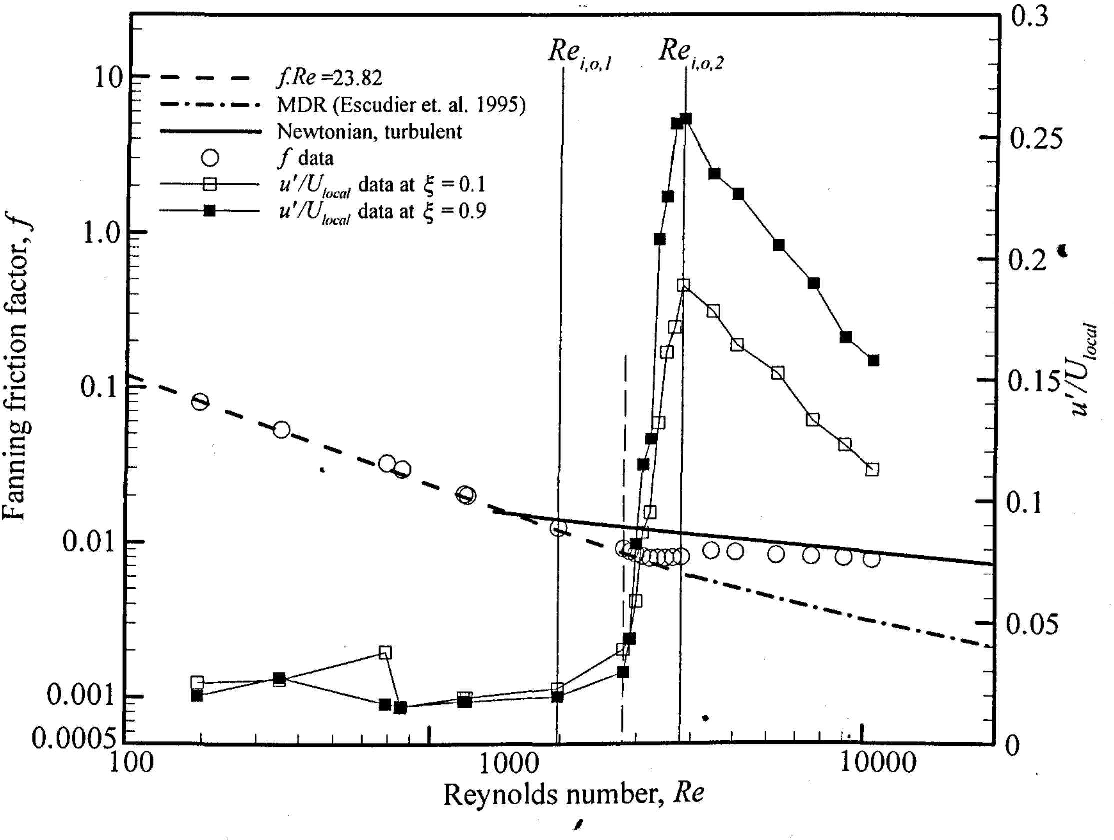

Figure 6.15: f-Re and u'/U_{local}-Re data for 0.065%CARBOPOL

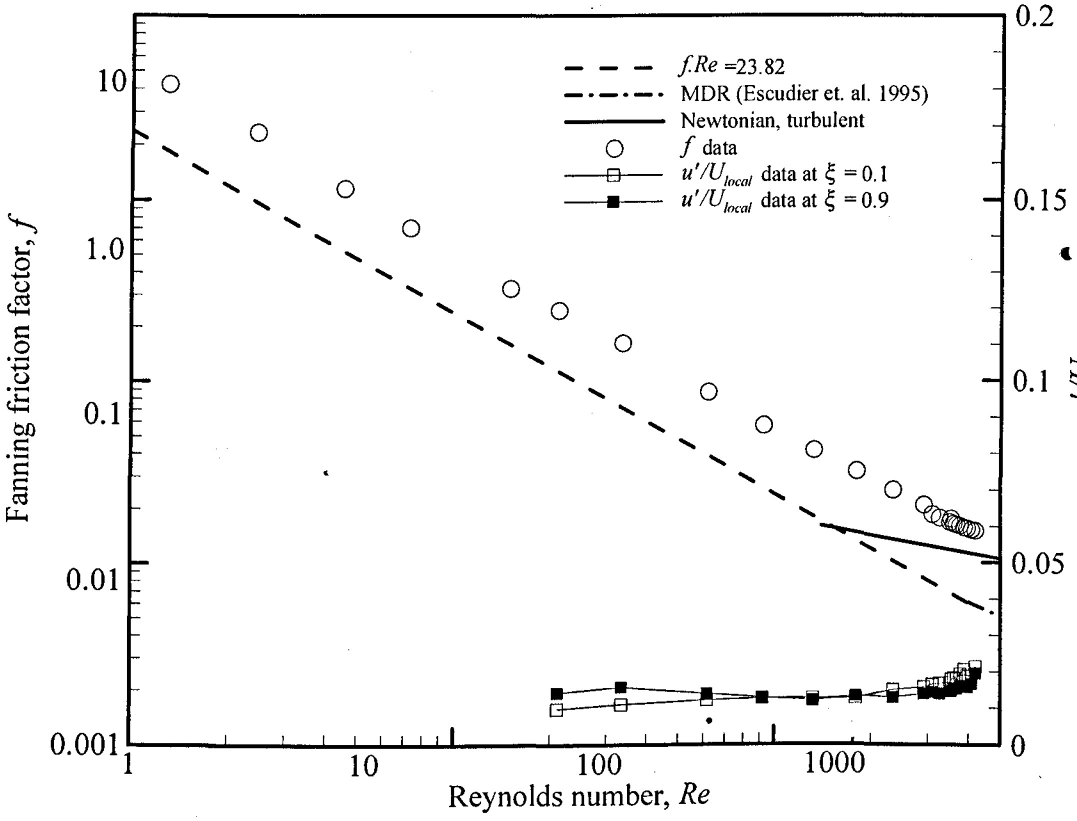

Figure 6.16: *f*-*Re* and u'/U_{local}-*Re* data for 0.1%CARBOPOL

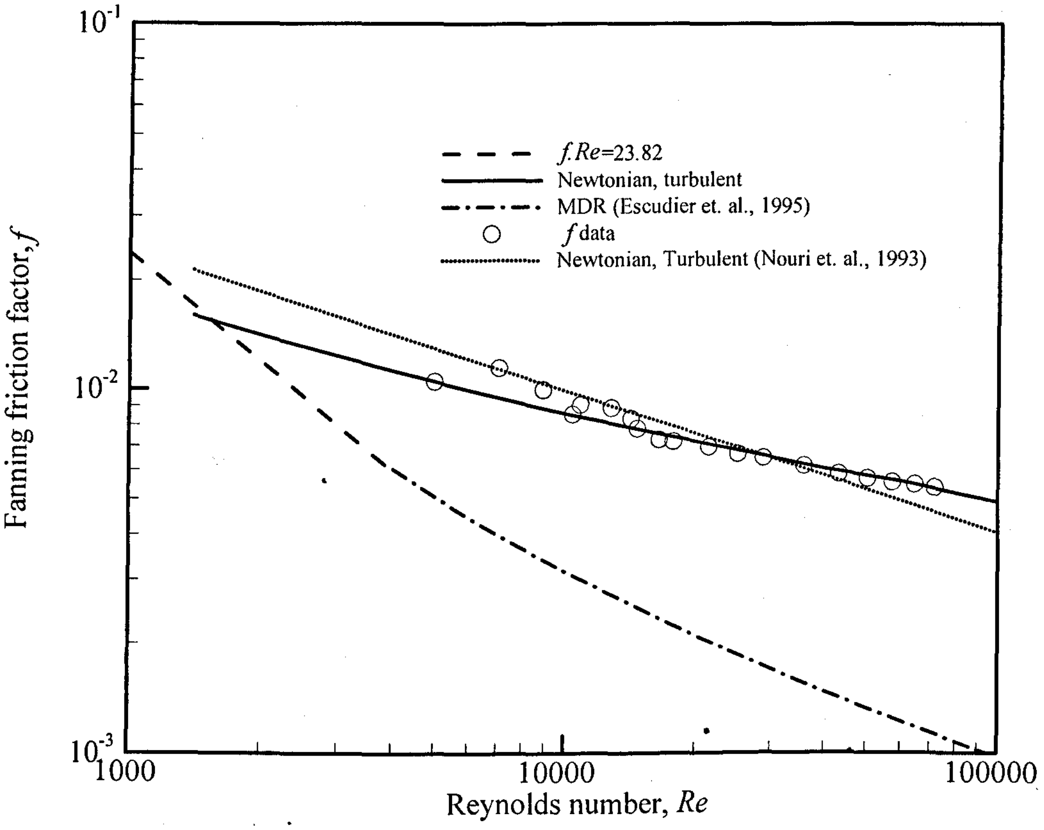

Figure 6.17: *f-Re* data for 0.01%SG

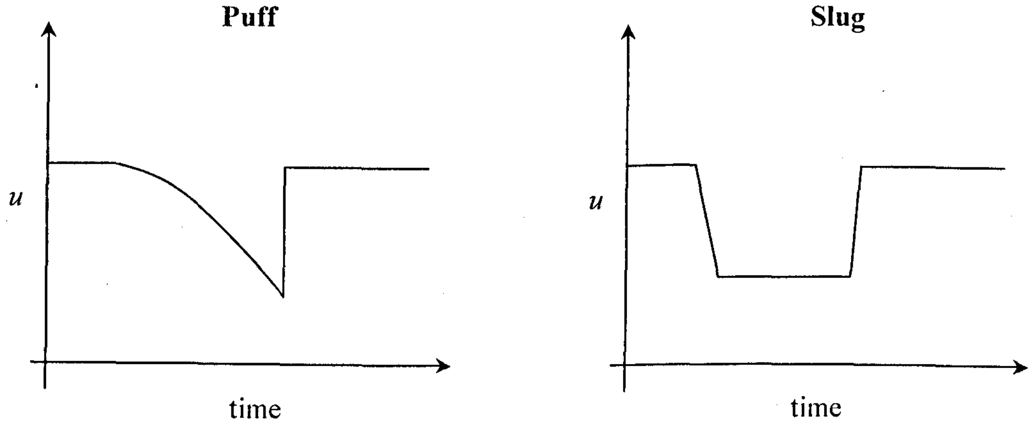

Figure 6.18: Sketch of velocity time trace of a puff and a turbulent slug

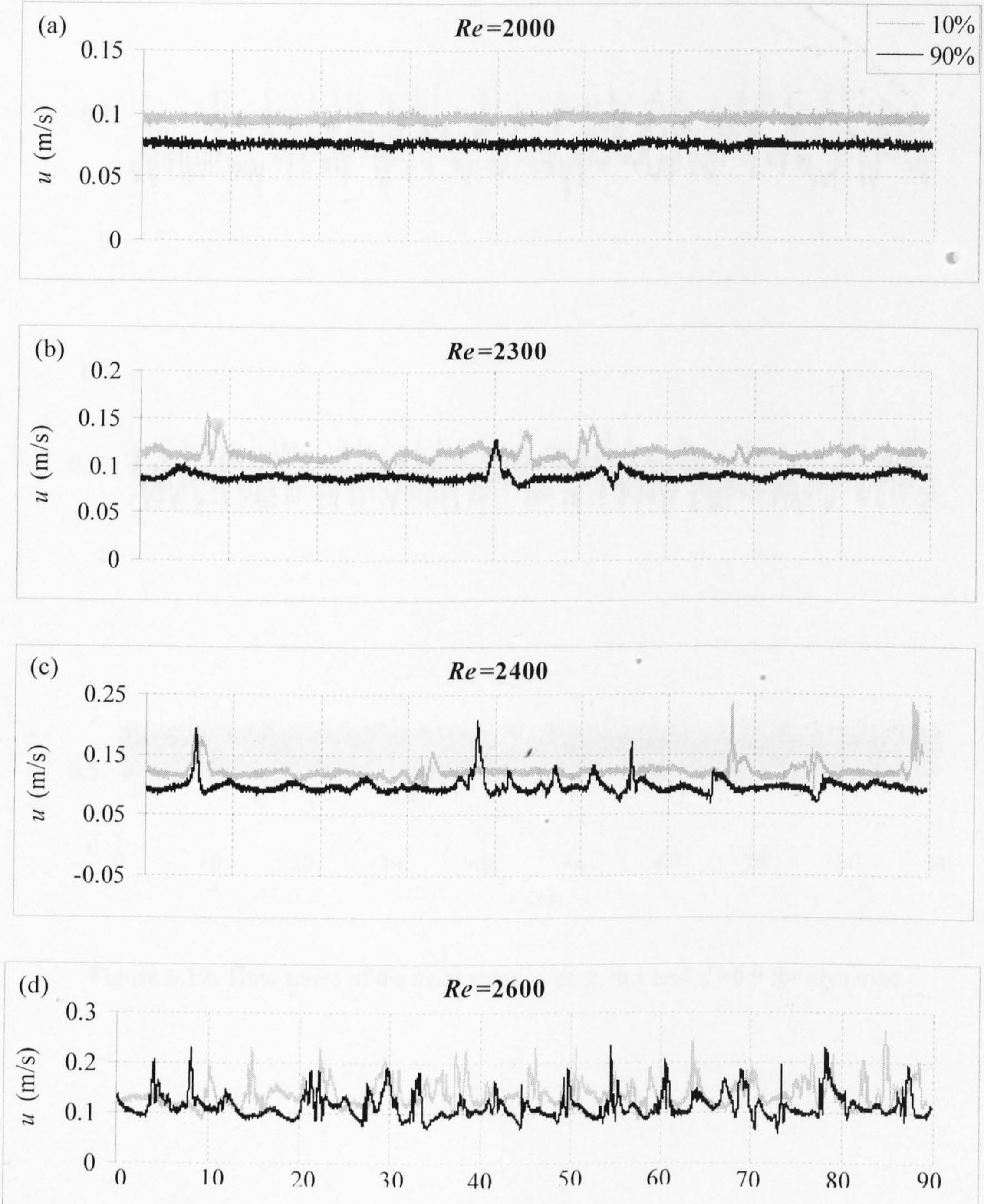

Figure 6.19: Time series of the axial velocity at ξ=0.1 and ξ=0.9 for glycerine

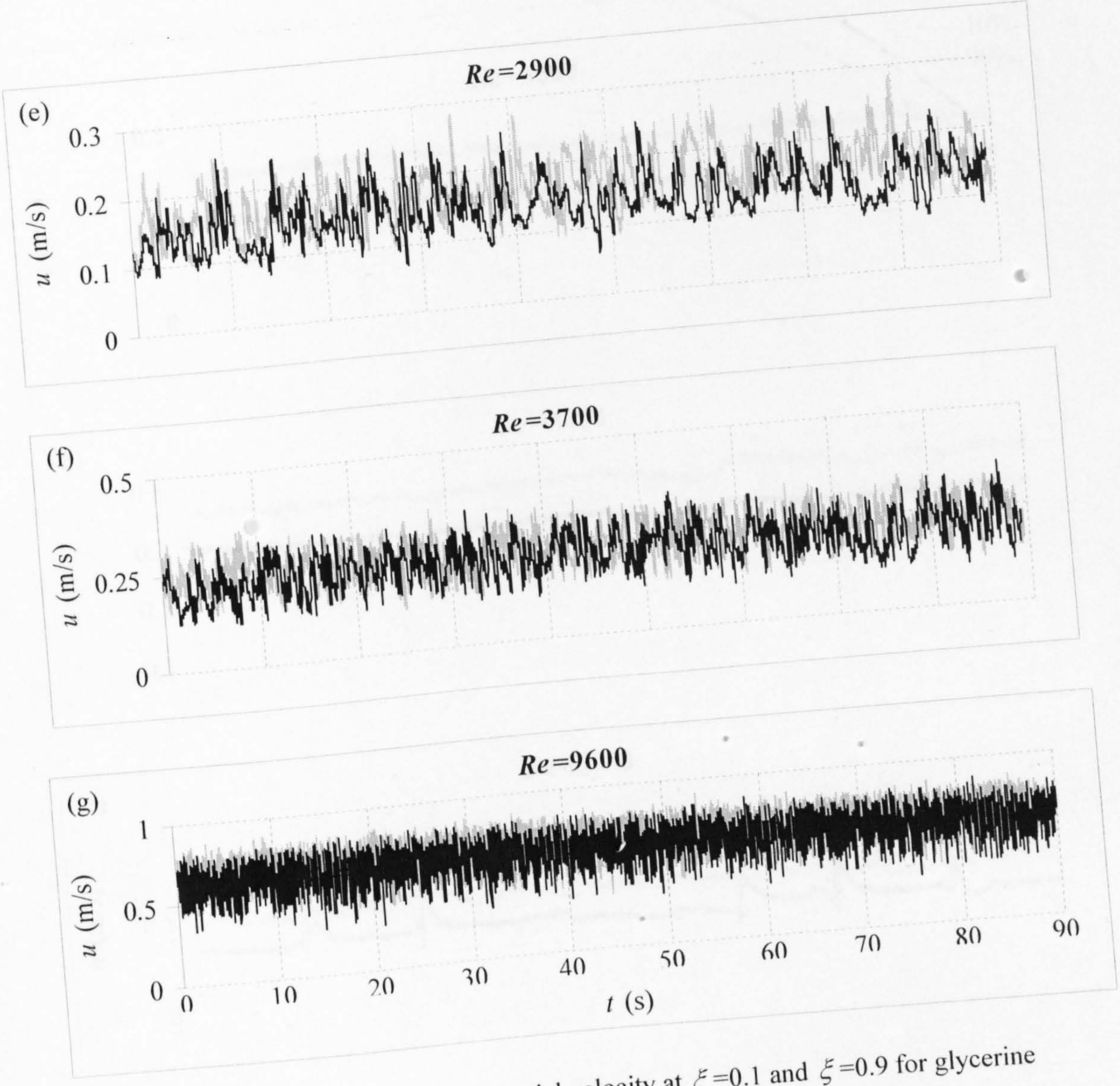

Figure 6.19: Time series of the axial velocity at $\xi=0.1$ and $\xi=0.9$ for glycerine

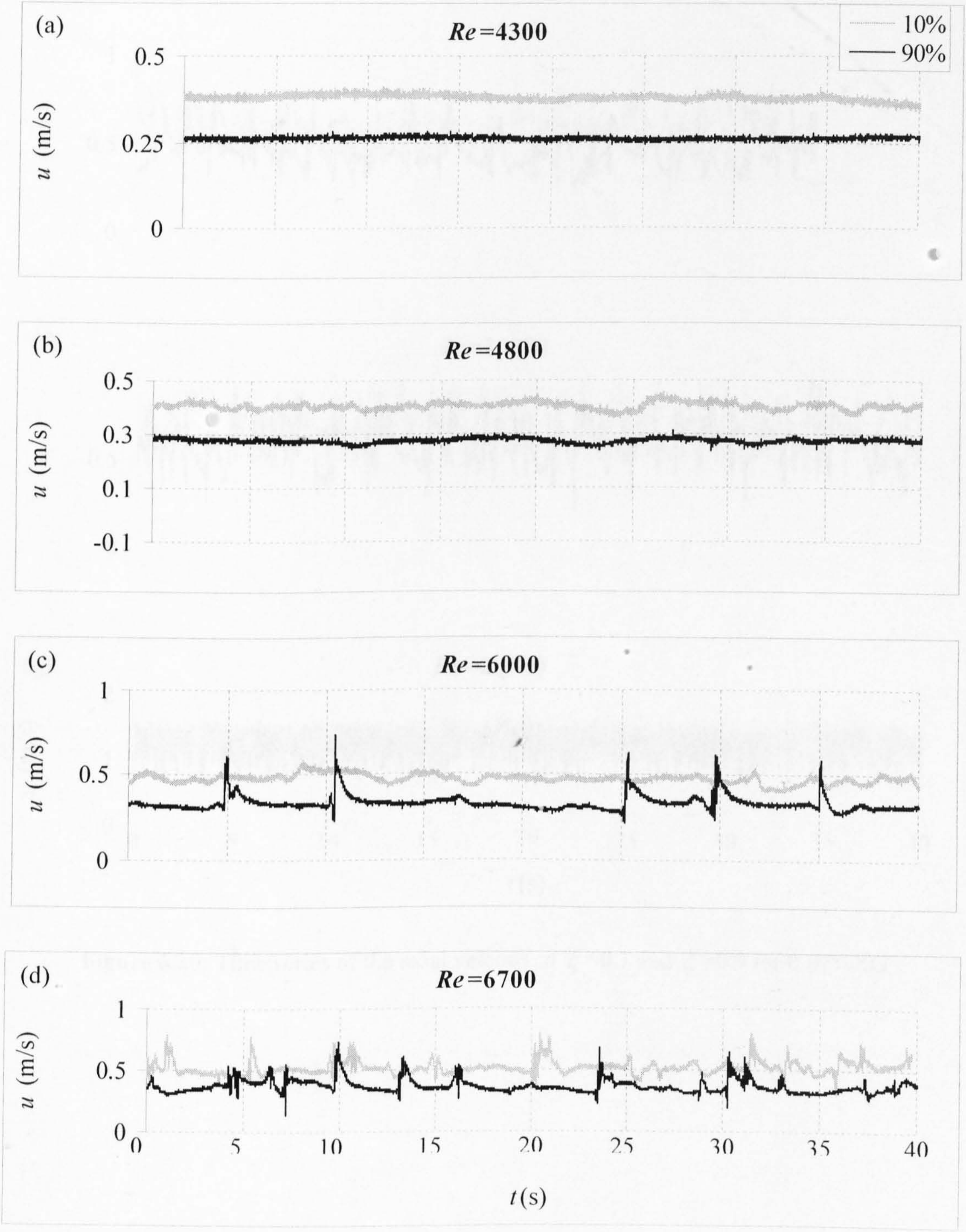

Figure 6.20: Time series of the axial velocity at $\xi=0.1$ and $\xi=0.9$ for 0.07%XG

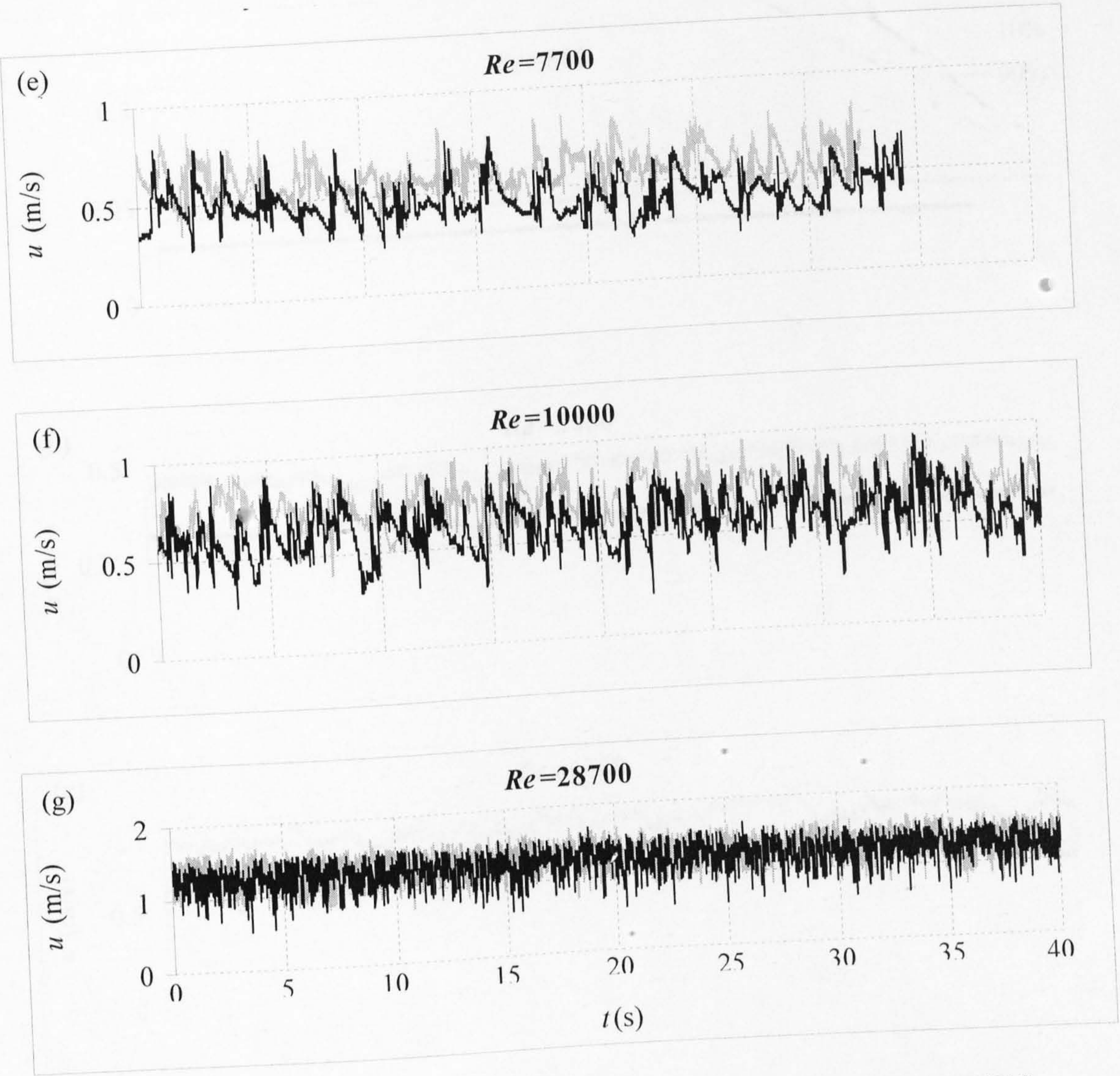

Figure 6.20: Time series of the axial velocity at ξ=0.1 and ξ=0.9 for 0.07%XG

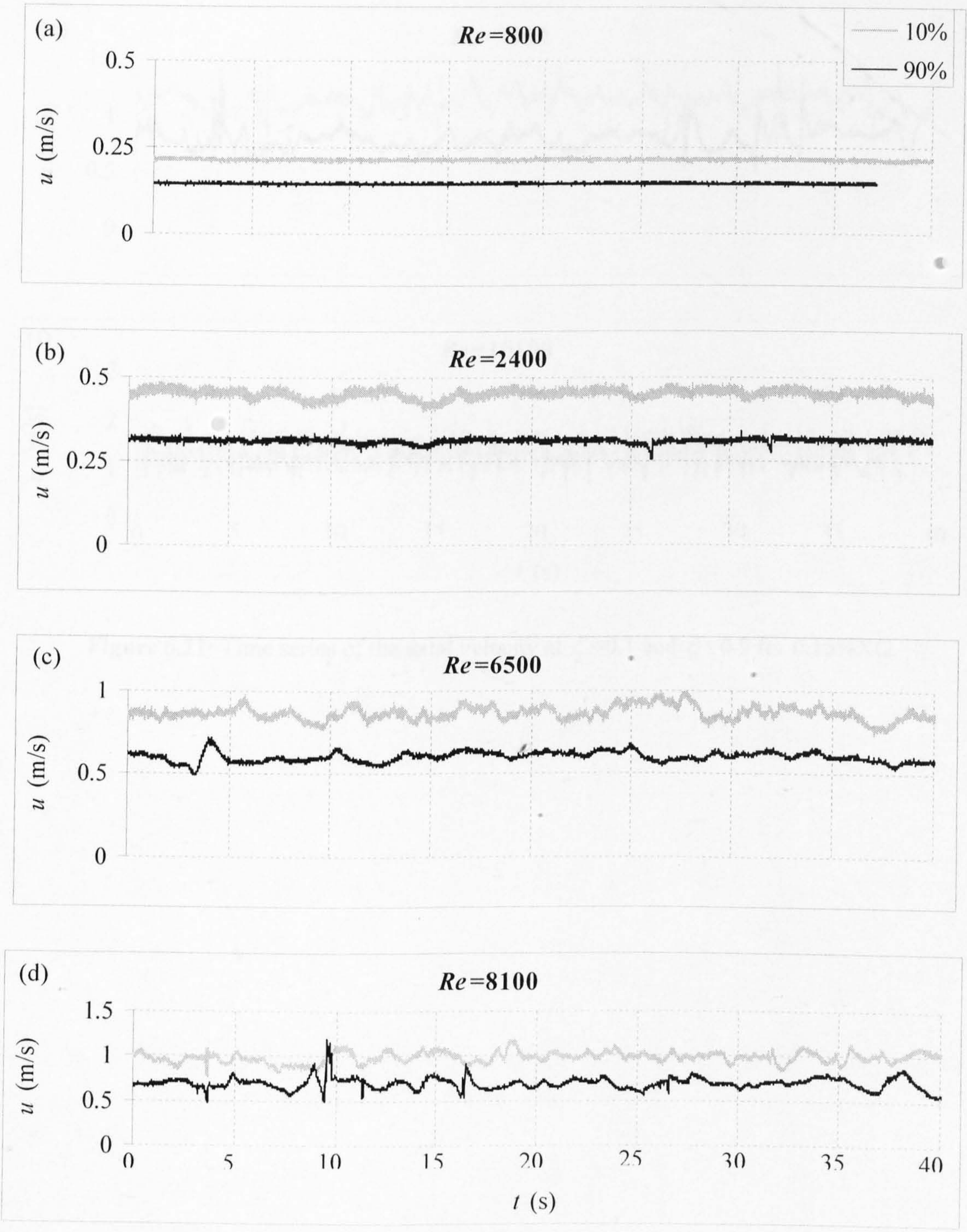

Figure 6.21: Time series of the axial velocity at ξ=0.1 and ξ=0.9 for 0.15%XG

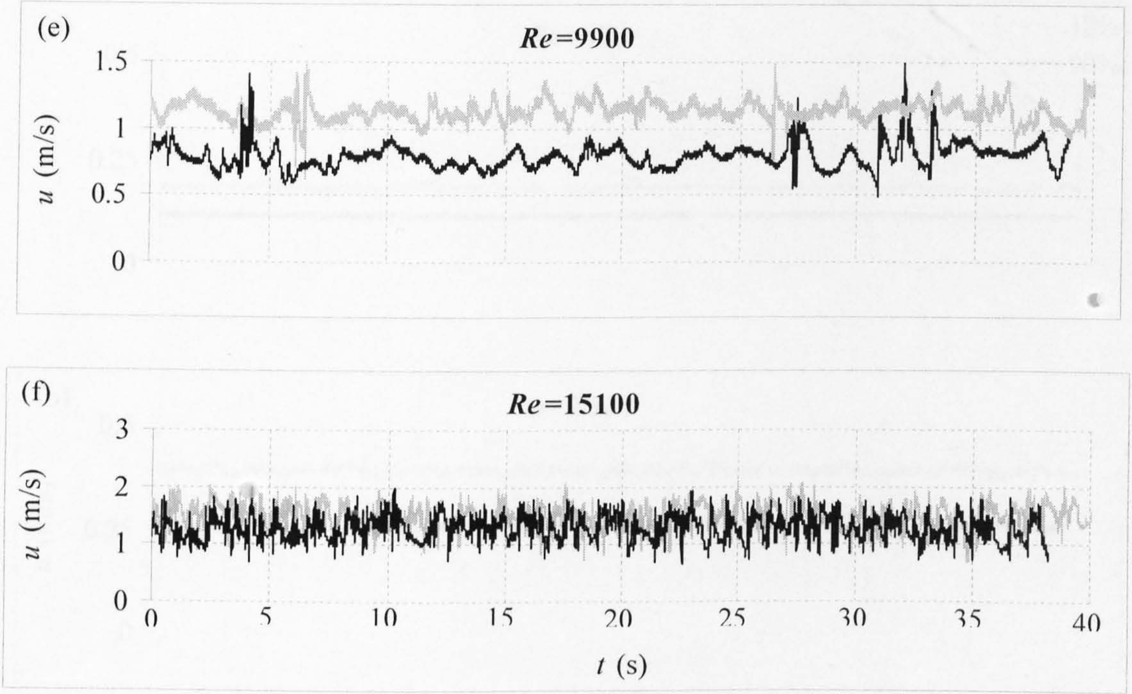

Figure 6.21: Time series of the axial velocity at ξ=0.1 and ξ=0.9 for 0.15%XG

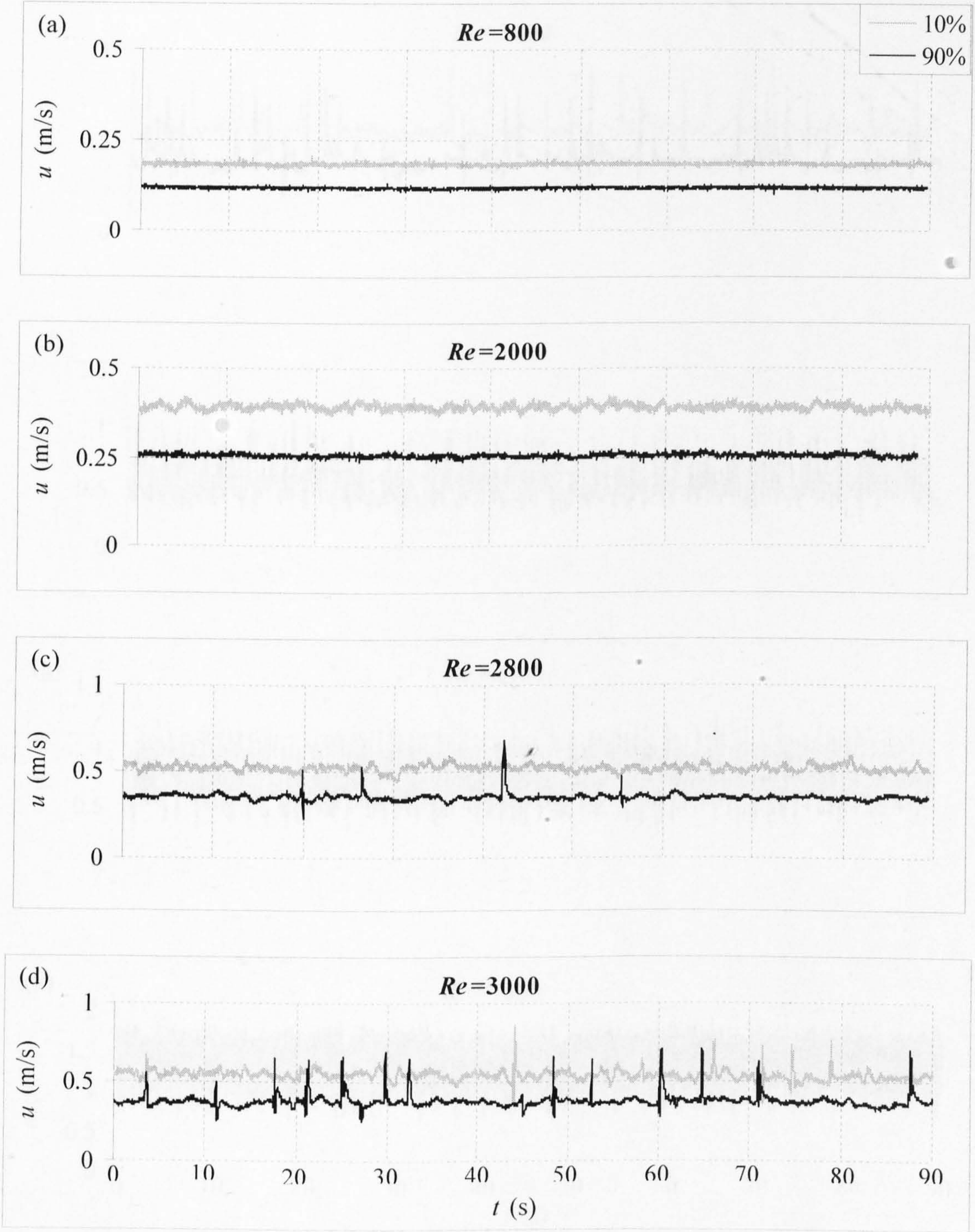

Figure 6.22: Time series of the axial velocity at $\xi=0.1$ and $\xi=0.9$ for 0.065%CARBOPOL

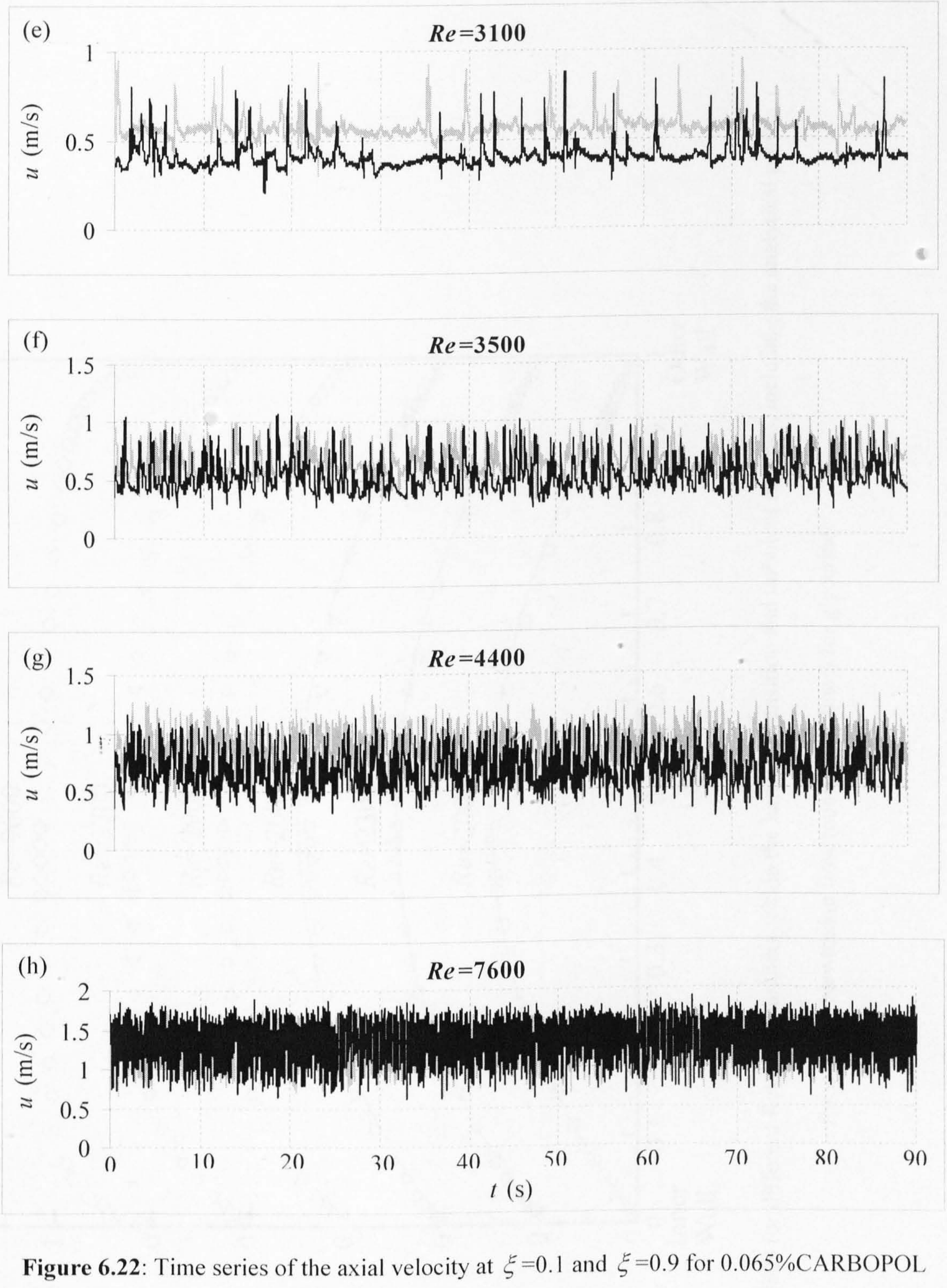

Figure 6.22: Time series of the axial velocity at ξ=0.1 and ξ=0.9 for 0.065%CARBOPOL

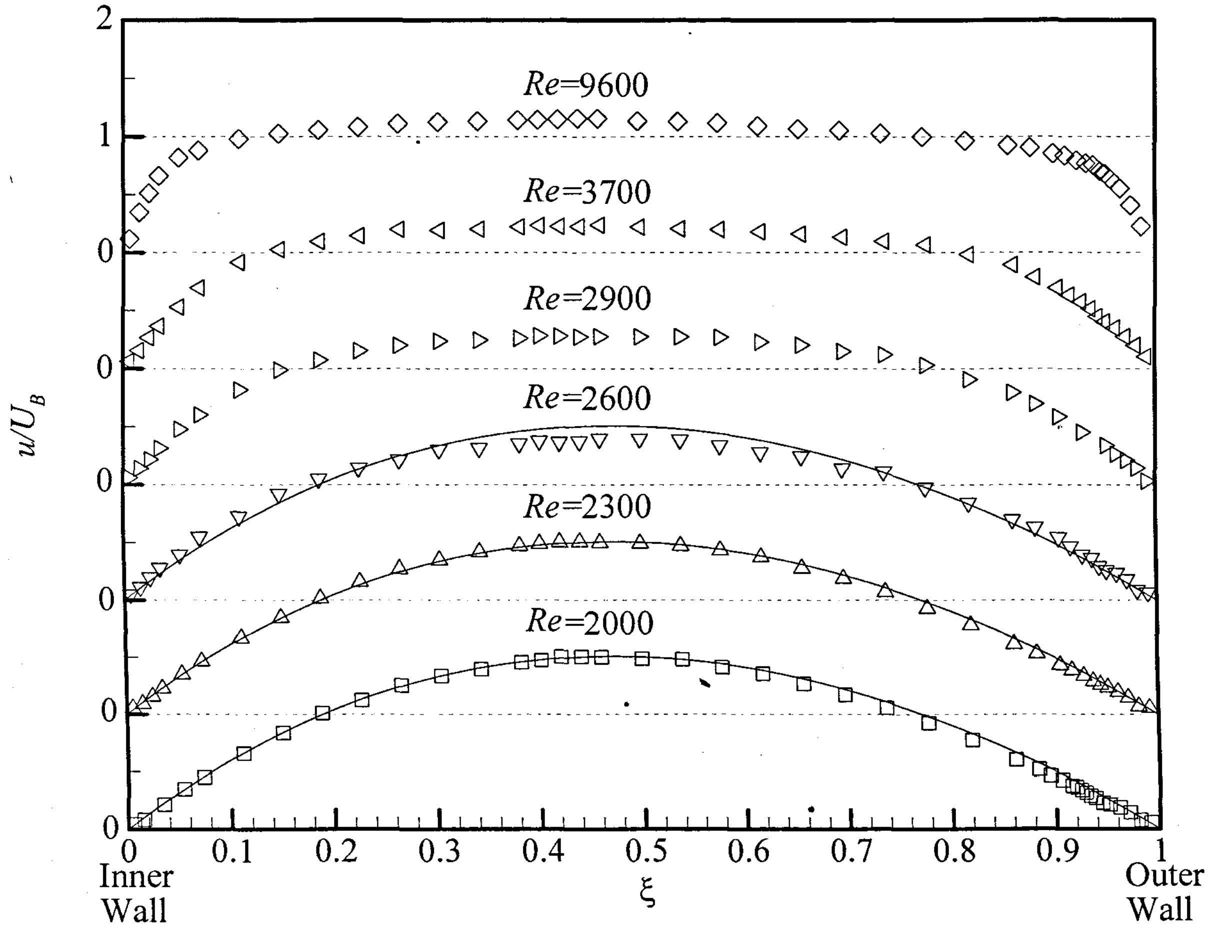

Figure 6.23: Velocity profiles for different Reynolds numbers within the laminar, transition and turbulent regimes, including the analytical profile for laminar, Newtonian flow (continuous lines) for glycerine

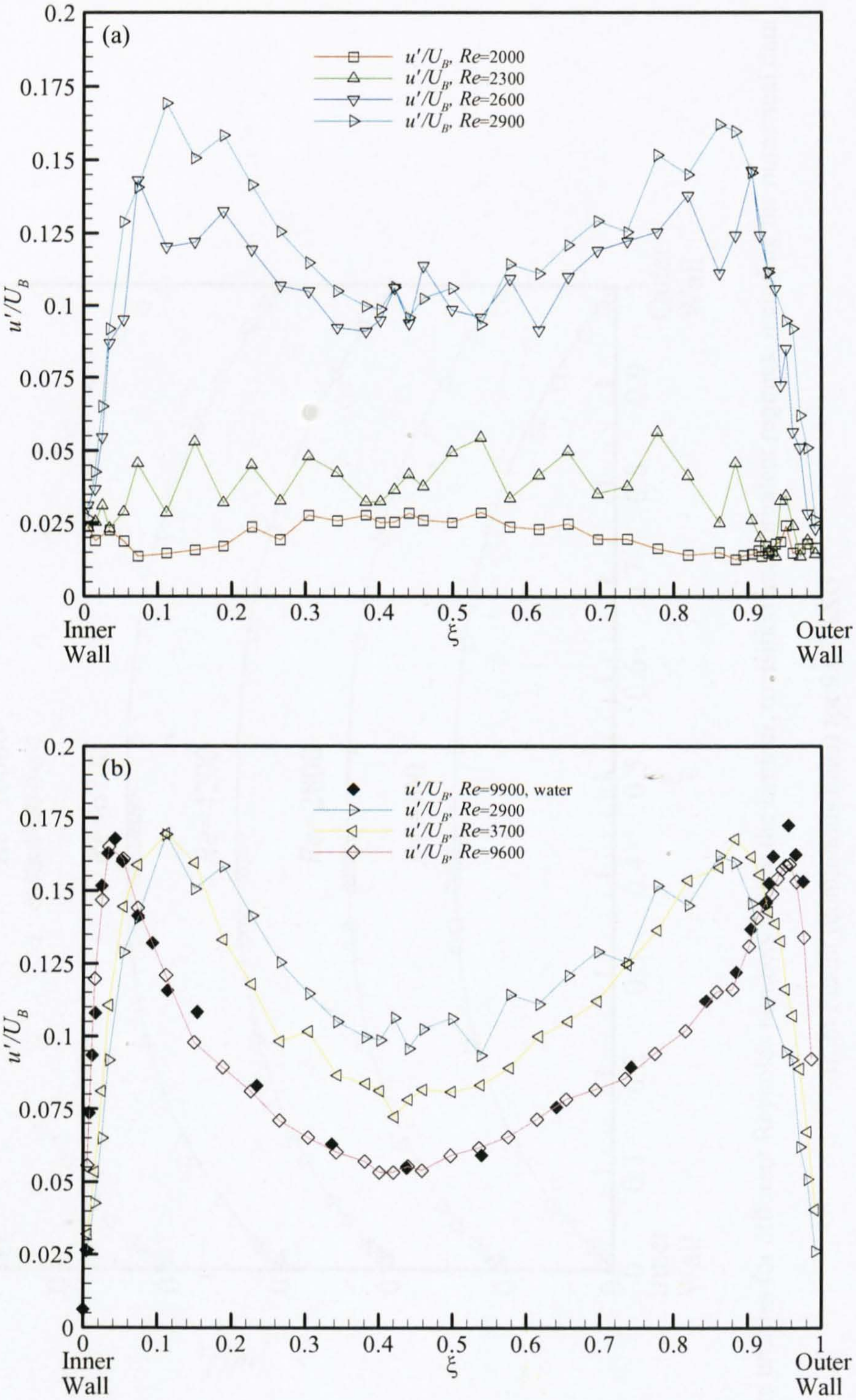

Figure 6.24(a-b): Axial velocity fluctuation component (u'/U_B) for different Reynolds numbers within the laminar, transition and turbulent regimes for glycerine

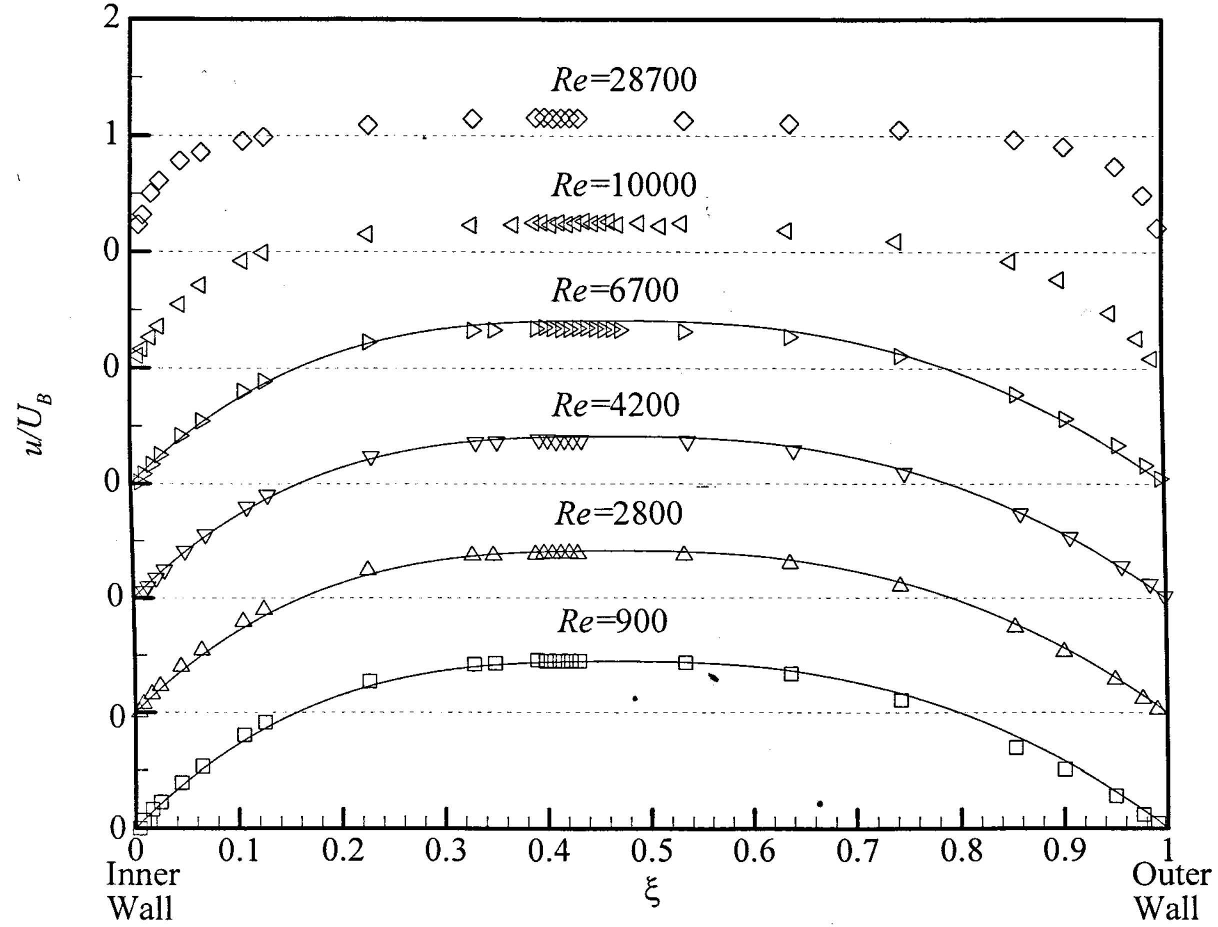

Figure 6.25: Velocity profiles for different Reynolds numbers within the laminar, transition and turbulent regimes, including the numerical data from Fluent (continuous lines) for 0.07%XG

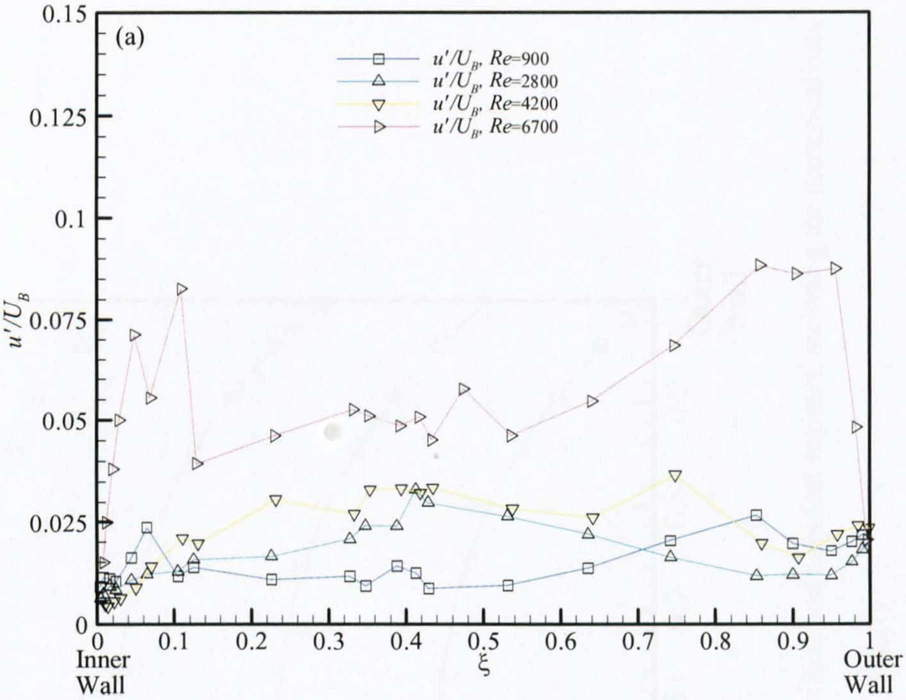

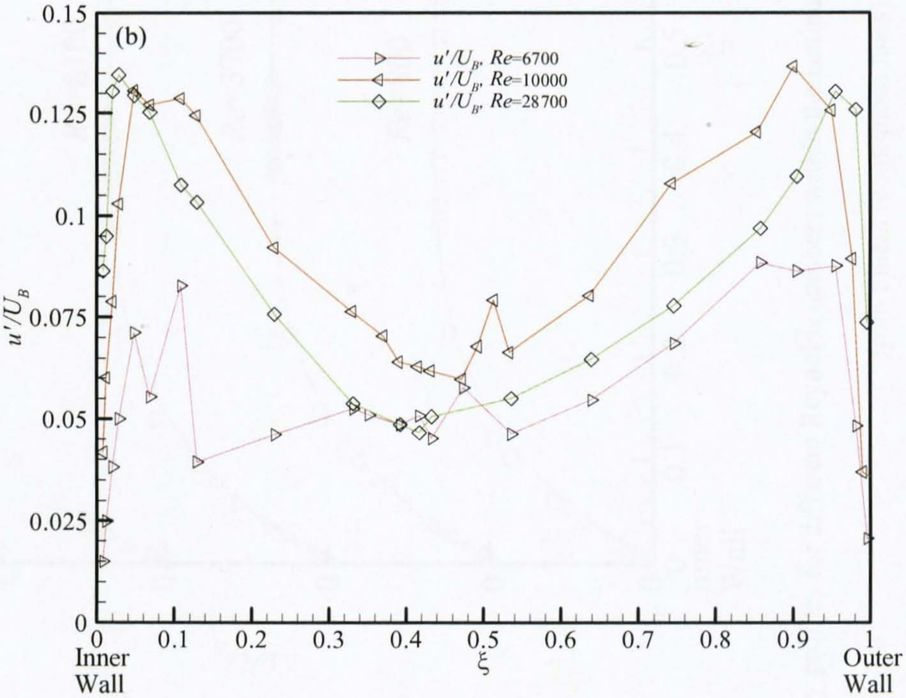

Figure 6.26(a-b): Axial velocity fluctuation component (u'/U_B) for different Reynolds numbers within the laminar, transition and turbulent regimes for 0.07%XG

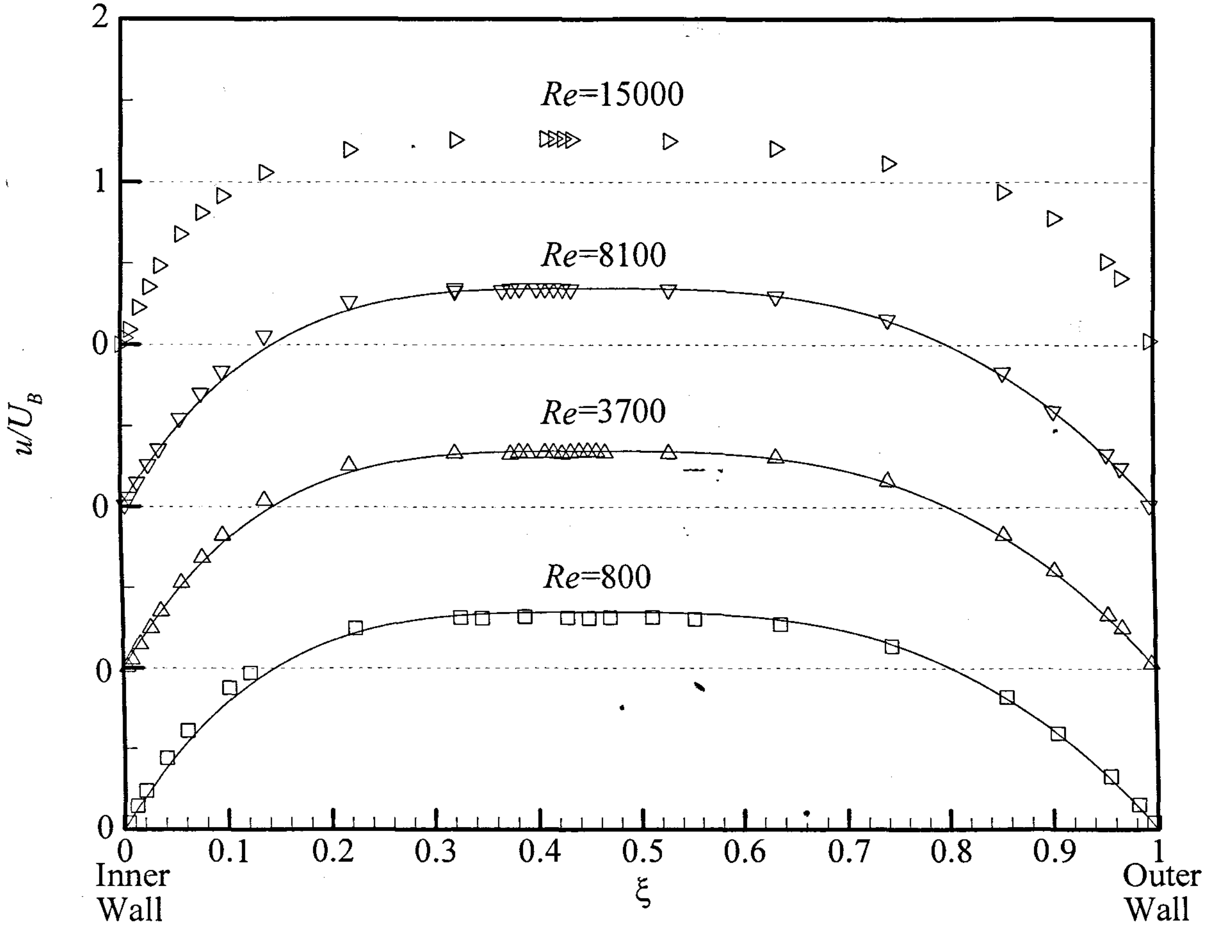

Figure 6.27: Velocity profiles for different Reynolds numbers within the laminar, transition and turbulent regimes, including the numerical data from Fluent (continuous lines) for 0.15%XG

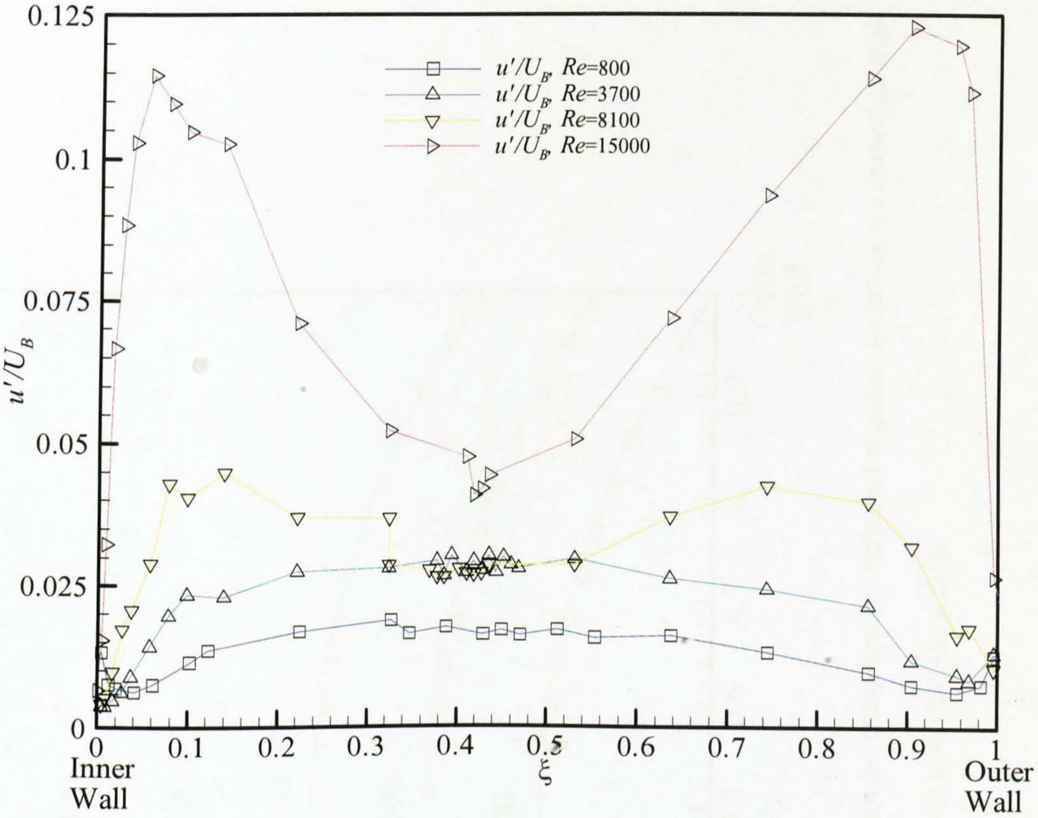

Figure 6.28: Axial velocity fluctuation component (u'/U_B) for different Reynolds numbers within the laminar, transition and turbulent regimes for 0.15%XG

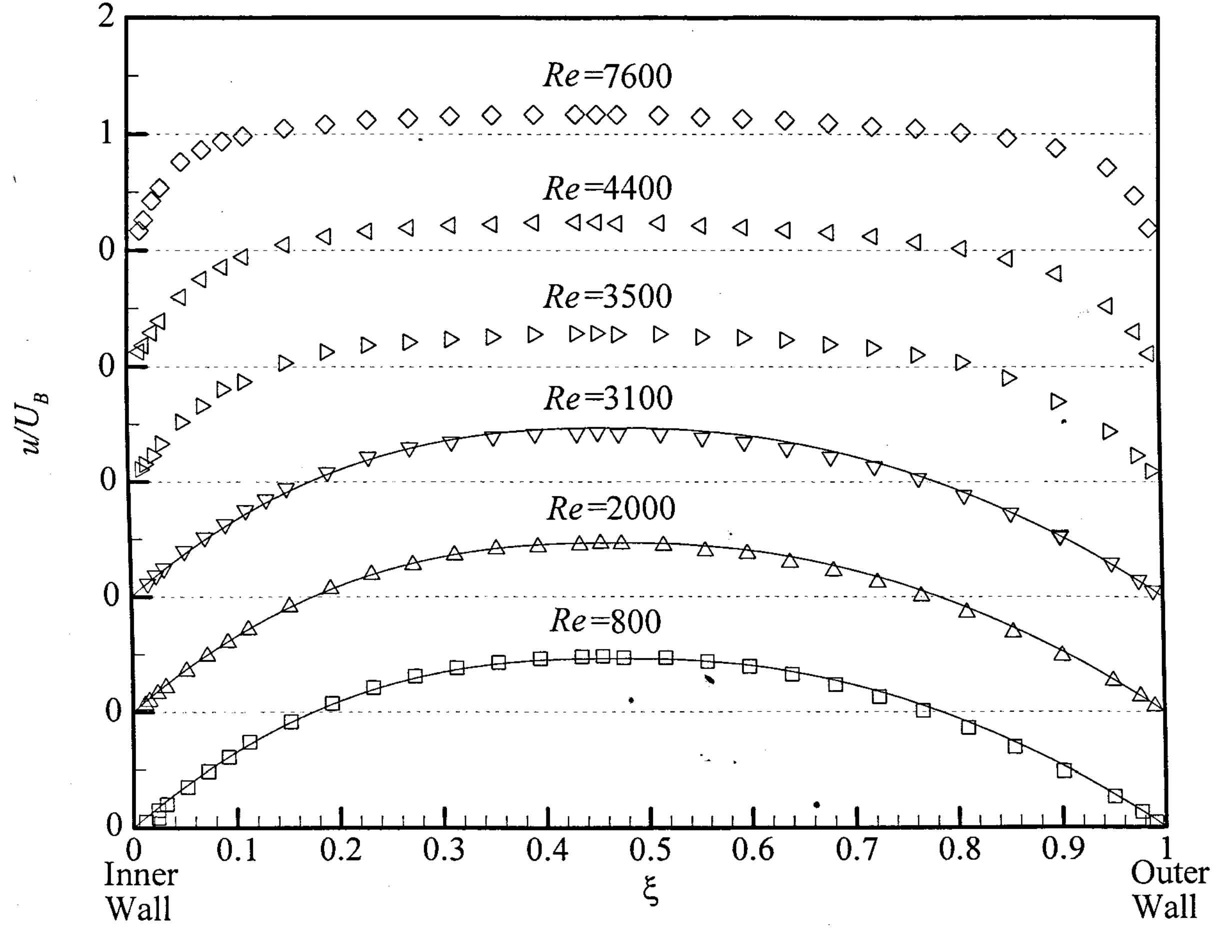

Figure 6.29: Velocity profiles for different Reynolds numbers within the laminar, transition and turbulent regimes, including the numerical data from Fluent (continuous lines) for 0.065%CARBOPOL

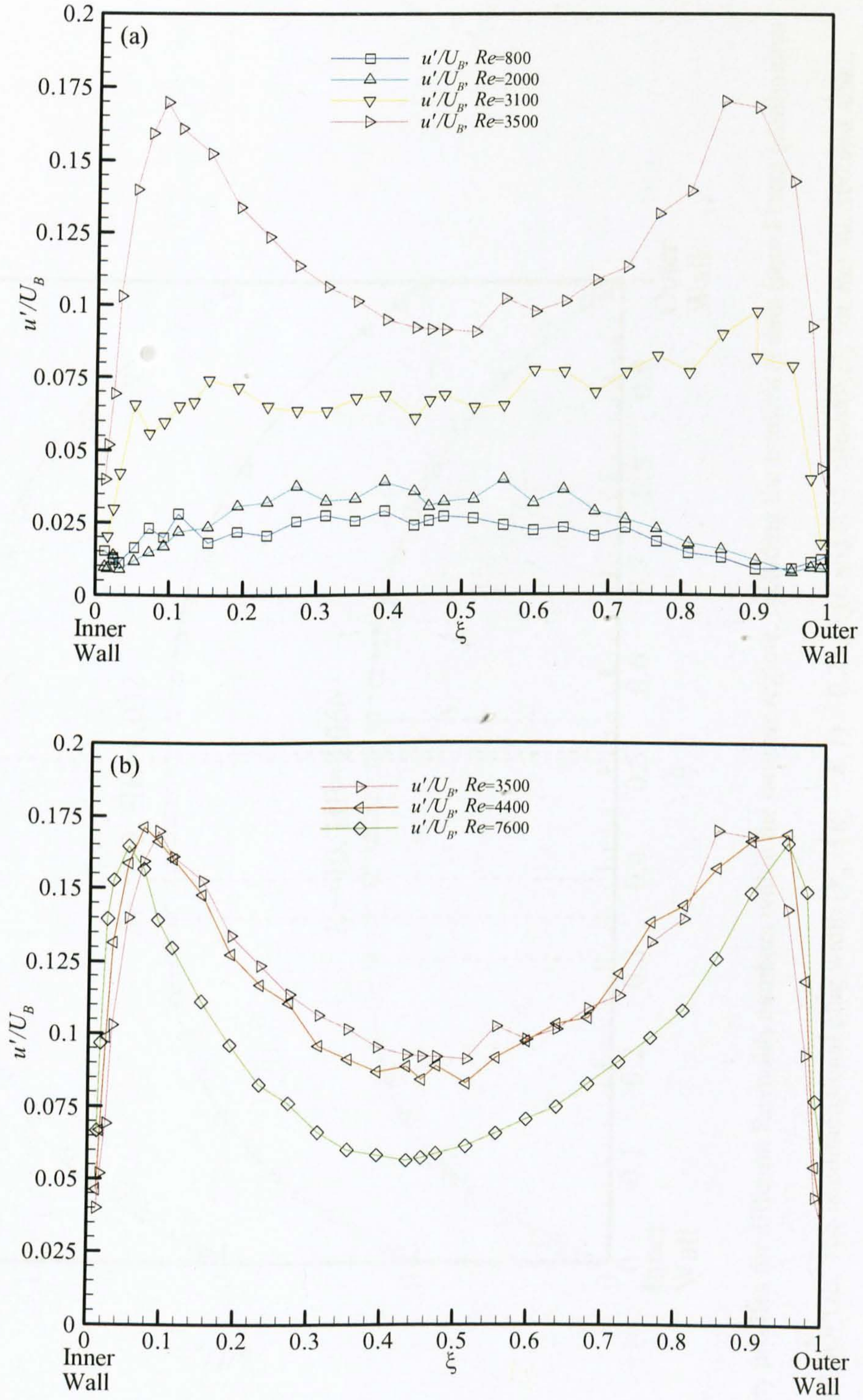

Figure 6.30(a-b): Axial velocity fluctuation component (u'/U_B) for different Reynolds numbers within the laminar, transition and turbulent regimes for 0.065%CARBOPOL

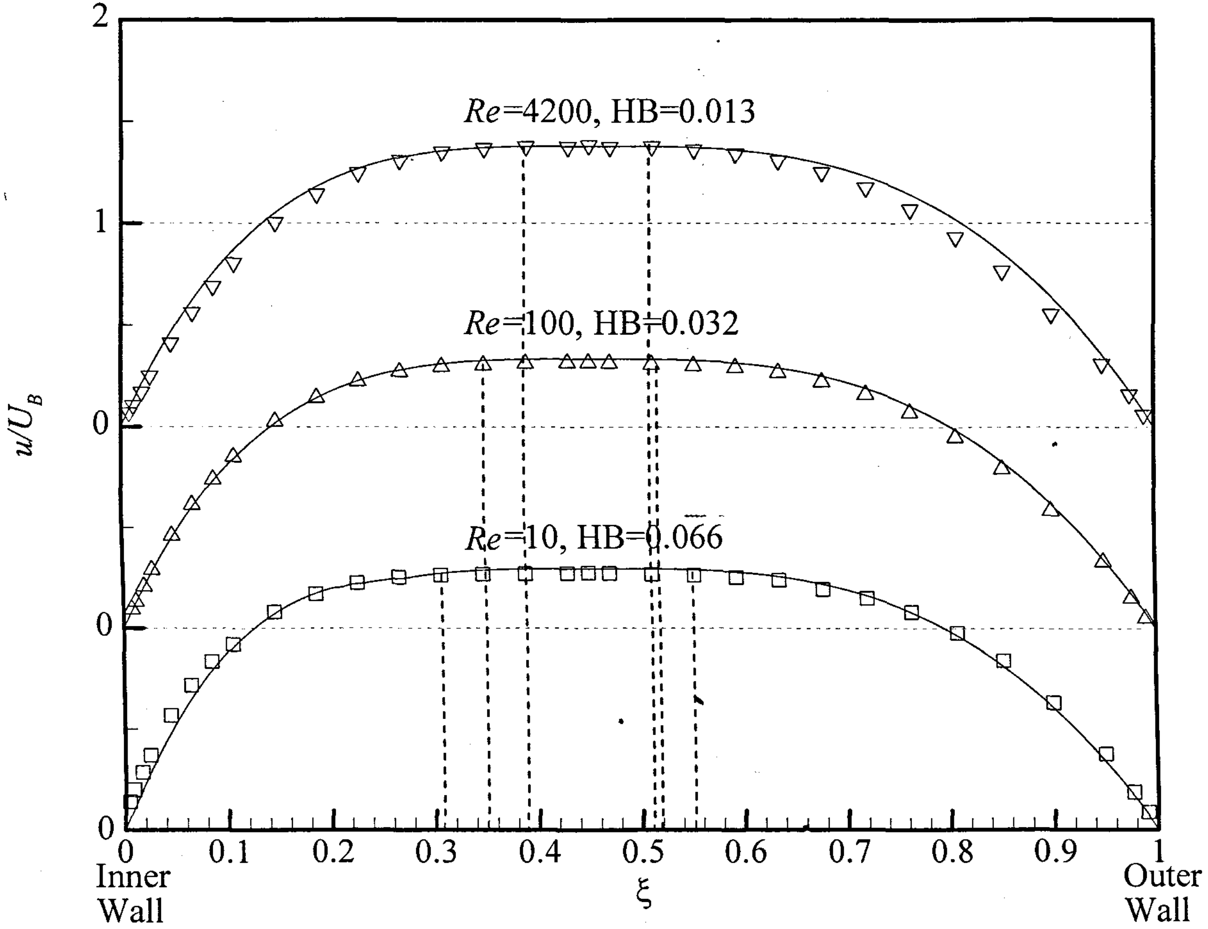

Figure 6.31: Velocity profiles for different Reynolds numbers within the laminar regime, including the numerical data from Fluent (continuous lines) for 0.1%CARBOPOL. The nondimensional plug width ($r_p/(R_o - R_i)$) = 0.25, 0.16 and 0.11 respectively for *Re*=10, 100 and 4200.

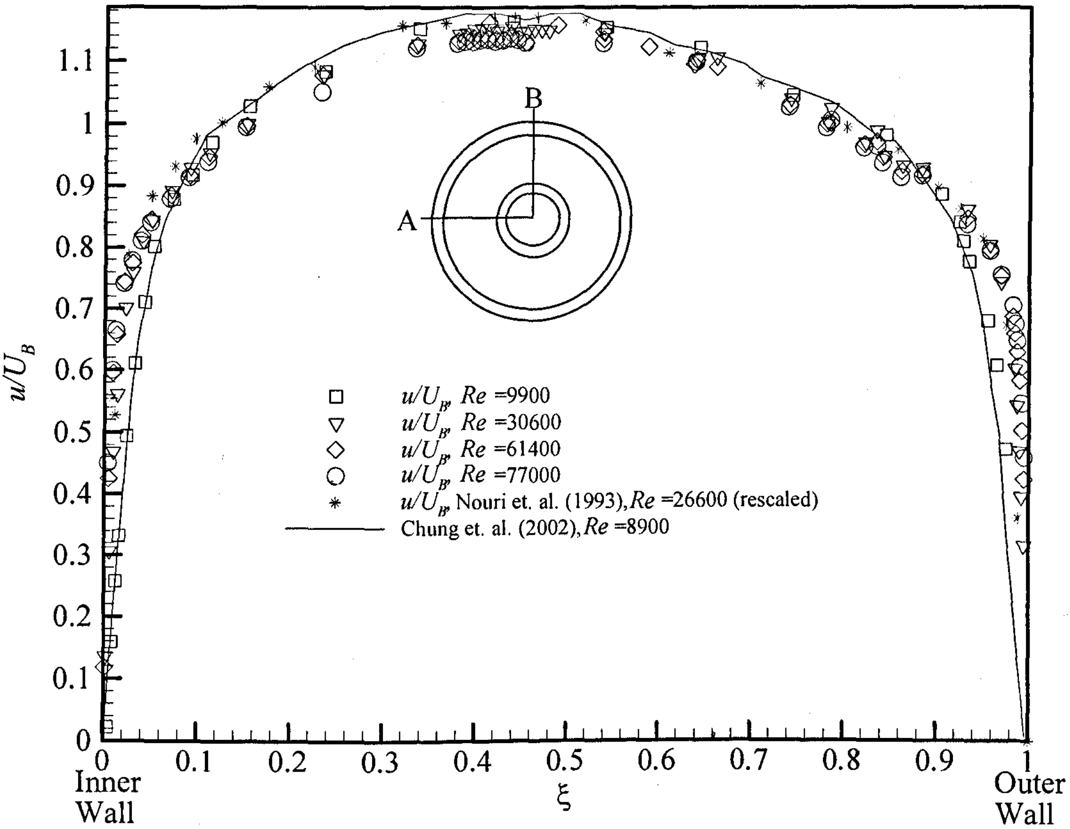

Figure 6.32: Normalized mean velocity distribution at various Reynolds numbers for water measured in Plane B in the annulus

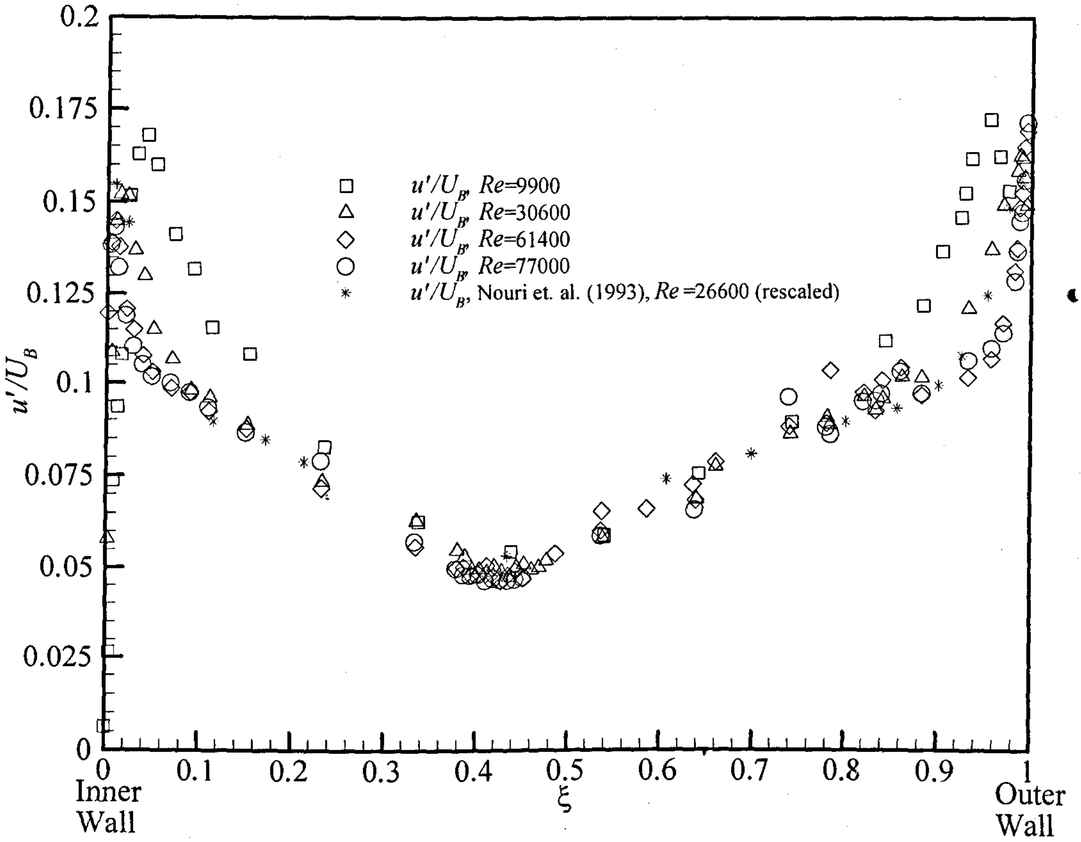

Figure 6.33: Normalized axial velocity component at various Reynolds numbers for water measured in Plane B

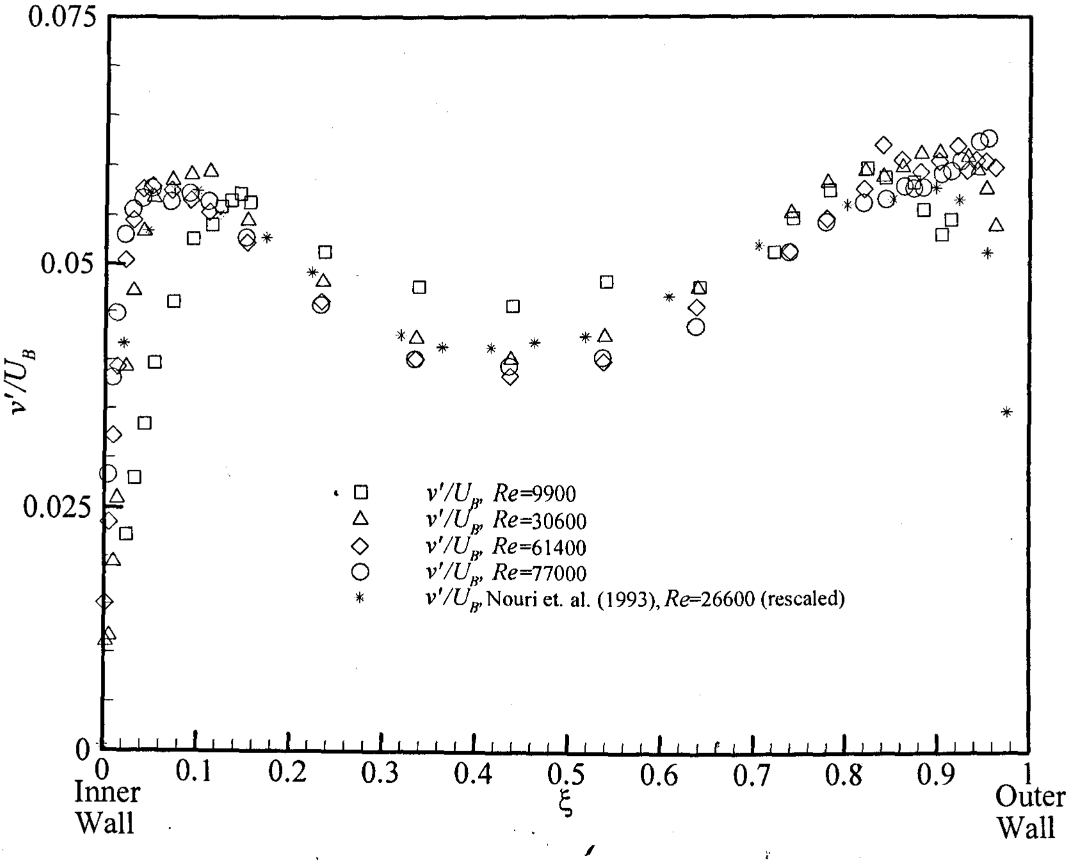

Figure 6.34: Normalized radial velocity component at various Reynolds numbers for water

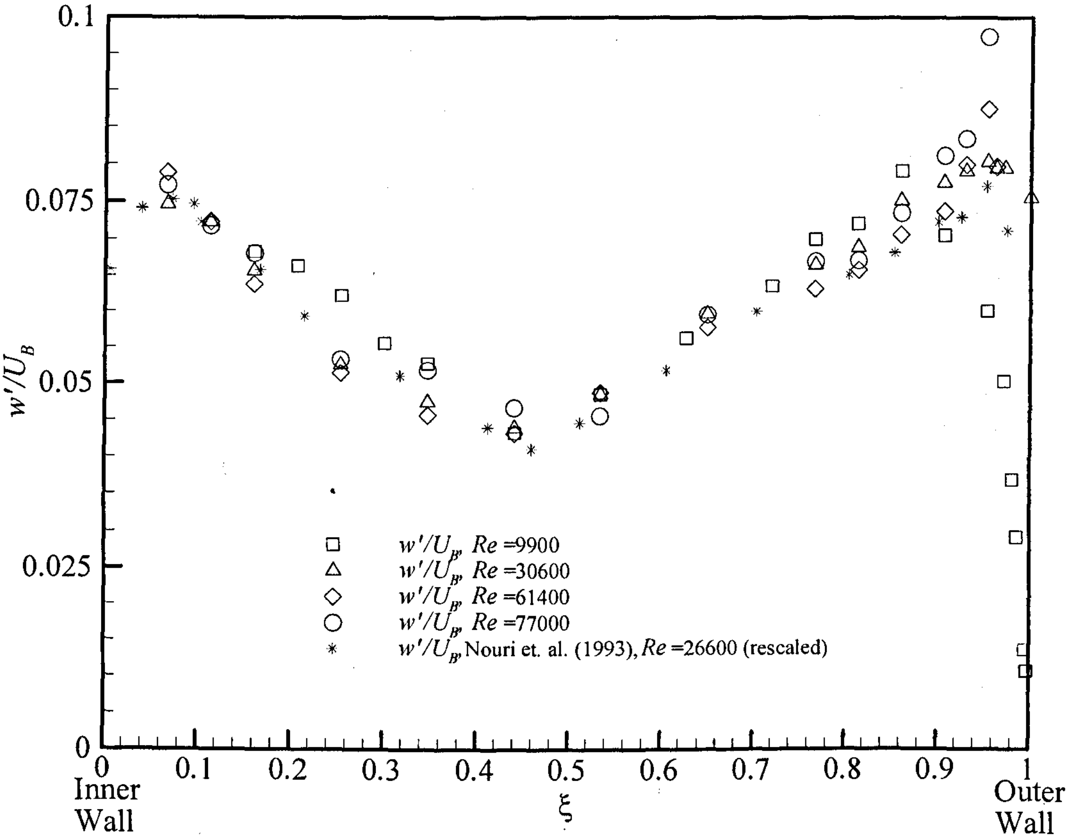

Figure 6.35: Normalized tangential velocity component at various Reynolds numbers for water

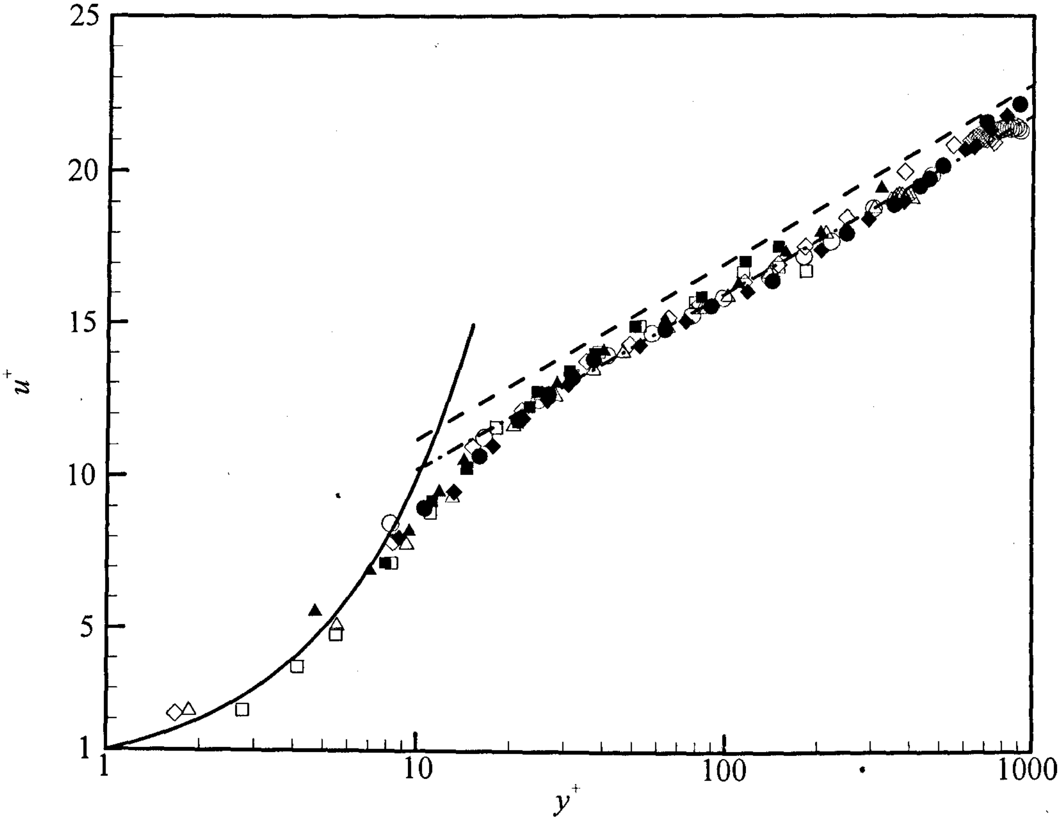

Figure 6.36: Universal mean velocity distribution for water. —: $u^+=y^+$; - - -: $u^+=2.5\ ln\ y^+ +5.5$; - · -: $u^+=2.5\ ln\ y^+ +4.9$ (Clauser); □: Water (Inner), *Re*=9900; ■: Water (Outer), *Re*=9900; Δ: Water (Inner), *Re*=30600; ▲: Water (Outer), *Re*=30600; ◇: Water (Inner), *Re*=61400; ◆: Water (Outer), *Re*=61400; ○: Water (Inner), *Re*=77000; ●: Water (Outer), *Re*=77000.

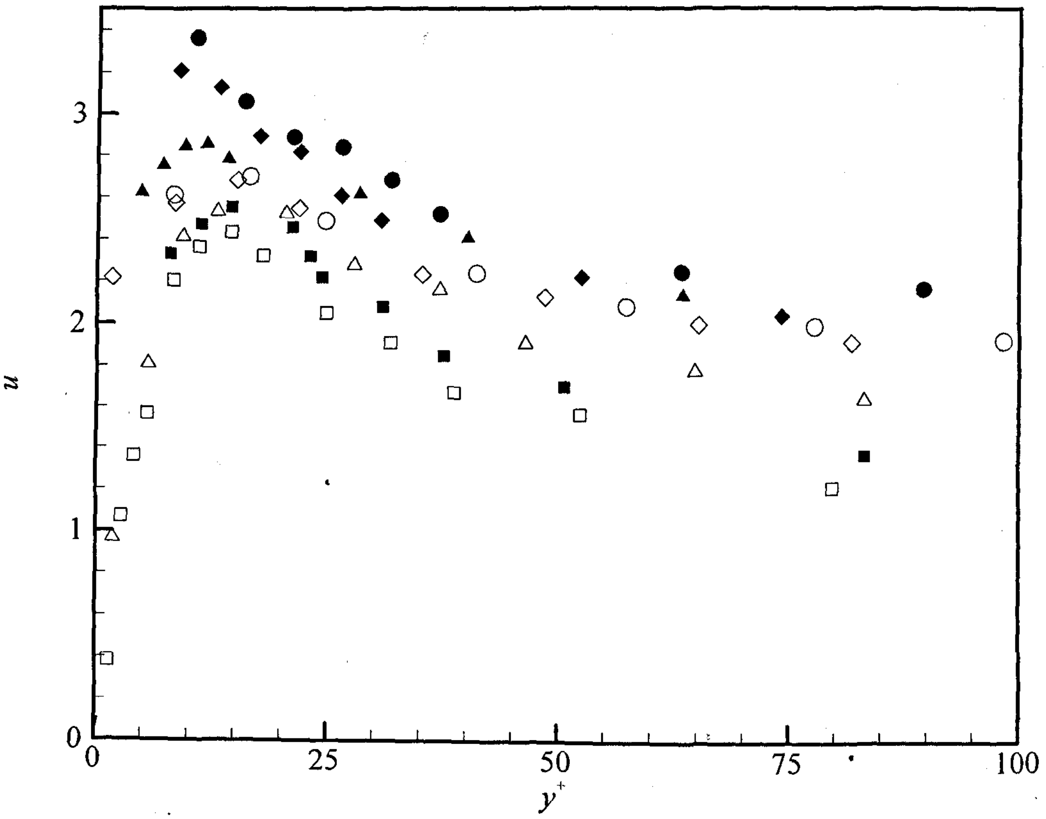

Figure 6.37: Axial rms fluctuation levels in wall coordinates for water. □: Water (Inner), *Re*=9900, u'^+_{max} =2.44; ■: Water (Outer), *Re*=9900, u'^+_{max} =2.63; Δ: Water (Inner), *Re*=30600, u'^+_{max} =2.53; ▲: Water (Outer), *Re*=30600, u'^+_{max} =2.86; ◇: Water (Inner), *Re*=61400, u'^+_{max} =2.68; ◆: Water (Outer), *Re*=61400, u'^+_{max} =3.21; ○: Water (Inner), *Re*=77000, u'^+_{max} =2.70; ●: Water (Outer), *Re*=77000, u'^+_{max} =3.37.

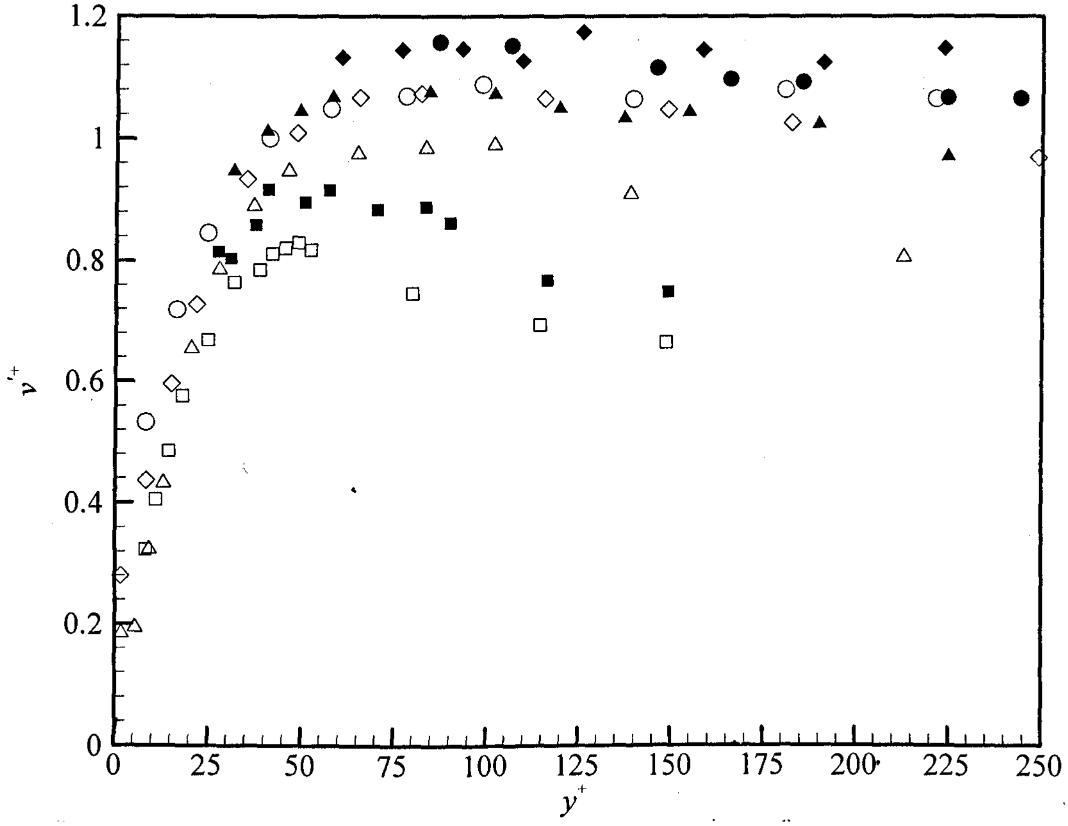

Figure 6.38: Radial rms fluctuation levels in wall coordinates for water. □: Water (Inner), *Re*=9900, v'^+_{max}=0.83; ■: Water (Outer), *Re*=9900, v'^+_{max}=0.92; Δ: Water (Inner), *Re*=30600, v'^+_{max}=0.99; ▲: Water (Outer), *Re*=30600, v'^+_{max}=1.08; ◇: Water (Inner), *Re*=61400, v'^+_{max}=1.07; ◆: Water (Outer), *Re*=61400, v'^+_{max}=1.18; ○: Water (Inner), *Re*=77000, v'^+_{max}=1.09; ●: Water (Outer), *Re*=77000, v'^+_{max}=1.16.

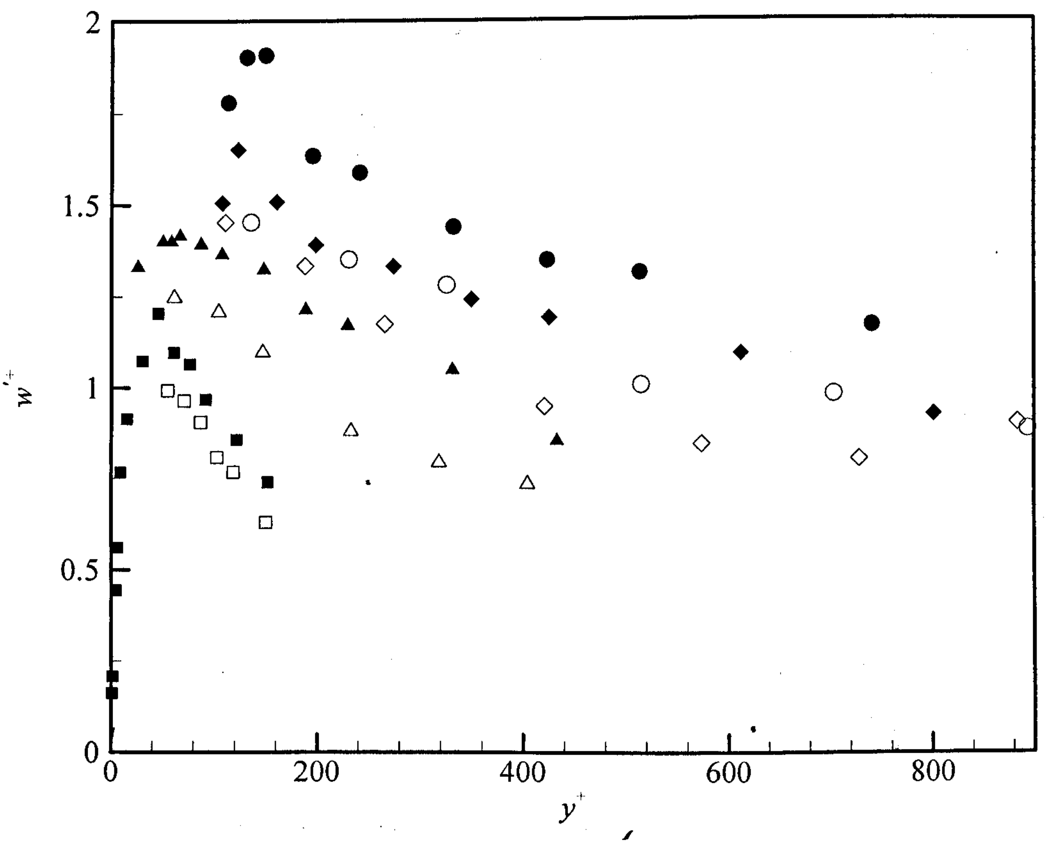

Figure 6.39: Tangential rms fluctuation levels in wall coordinates for water. □: Water (Inner), *Re*=9900, w'^+_{max} =0.99; ■: Water (Outer), *Re*=9900, w'^+_{max} =1.20; Δ: Water (Inner), *Re*=30600, w'^+_{max} =1.25; ▲: Water (Outer), *Re*=30600, w'^+_{max} =1.42; ◇: Water (Inner), *Re*=61400, w'^+_{max} =1.45; ◆: Water (Outer), *Re*=61400, w'^+_{max} =1.65; ○: Water (Inner), *Re*=77000, w'^+_{max} =1.45; ●: Water (Outer), *Re*=77000, w'^+_{max} =1.91.

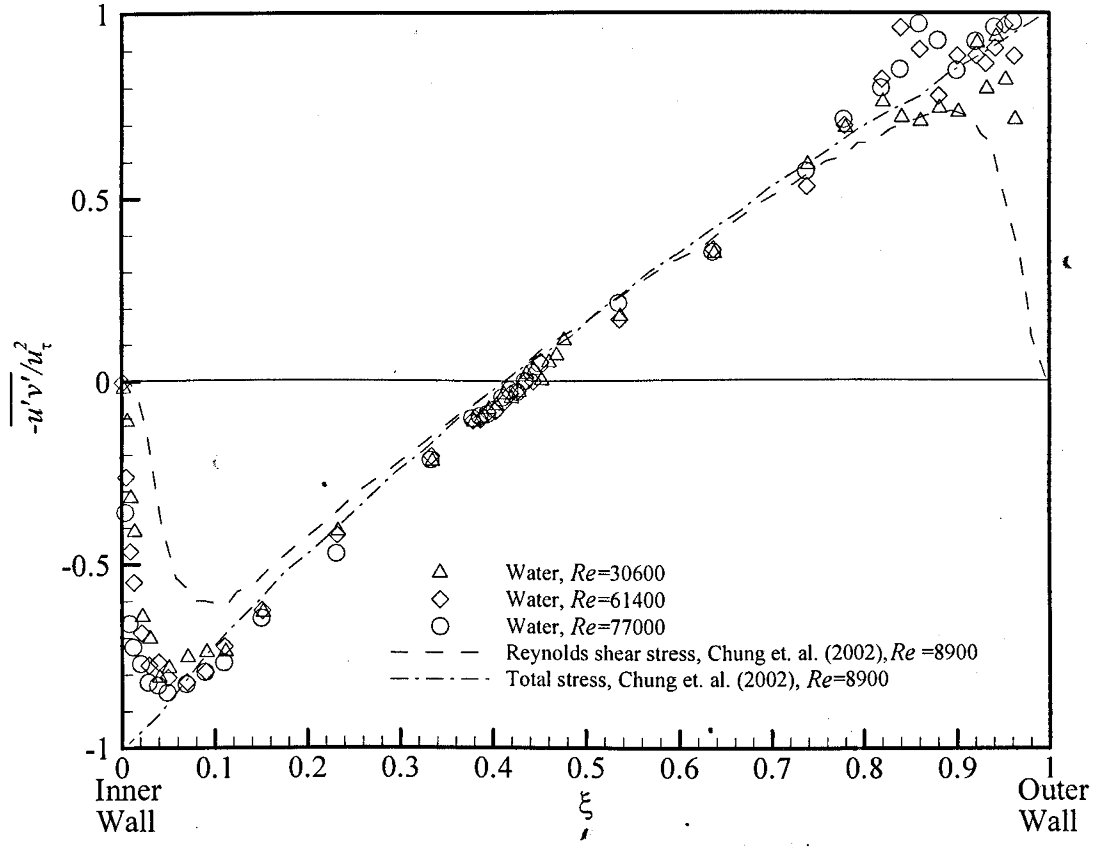

Figure 6.40: Reynolds shear stress normalized with the friction velocity for water

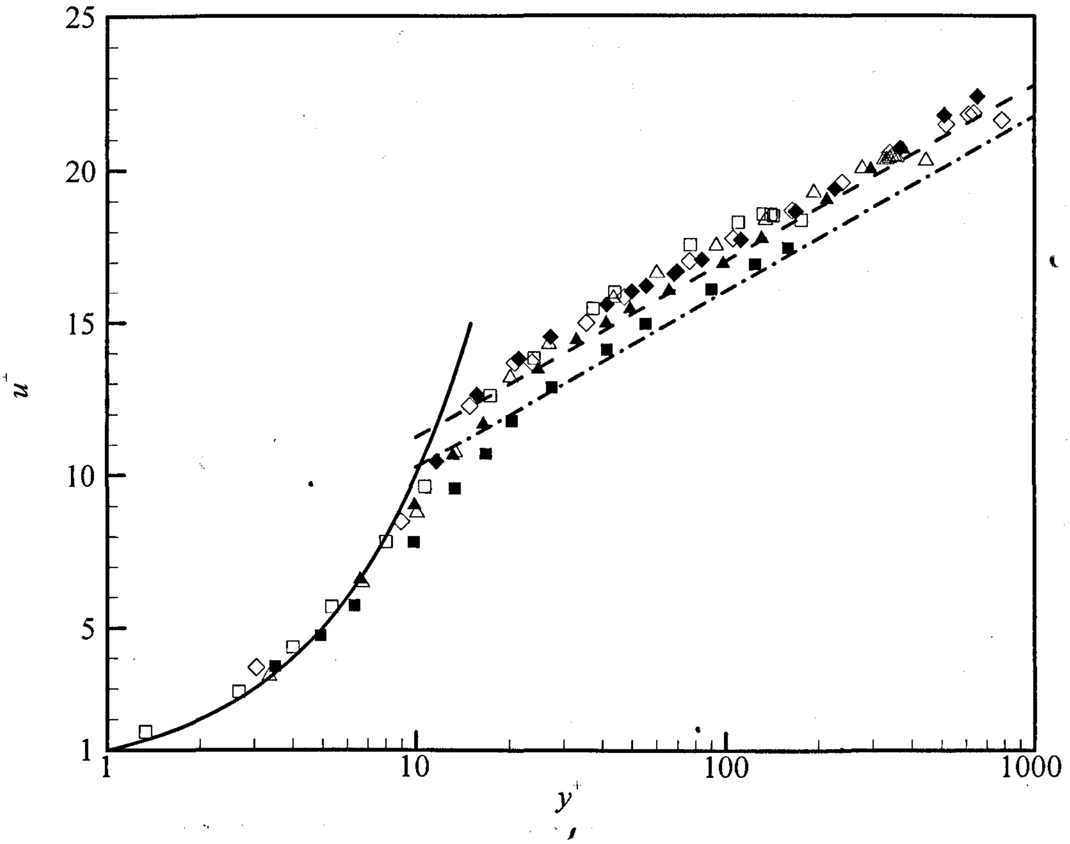

Figure 6.41: Universal mean velocity distribution for 0.0124%XG. —: $u^+=y^+$; - - -: $u^+=2.5\ ln\ y^+ +5.5$; - · -: $u^+=2.5\ ln\ y^+ +4.9$ (Clauser); □: 0.0124%XG (Inner), *Re*=10600, DR=3.2%; ■: 0.0124%XG (Outer), *Re*=10600, DR=3.2%; Δ: 0.0124%XG (Inner), *Re*=30300, DR=10.3%; ▲: 0.0124%XG (Outer), *Re*=30300, DR=10.3%; ◇: 0.0124%XG (Inner), *Re*=57600, DR=11.6%; ◆: 0.0124%XG (Outer), *Re*=57600, DR=11.6%.

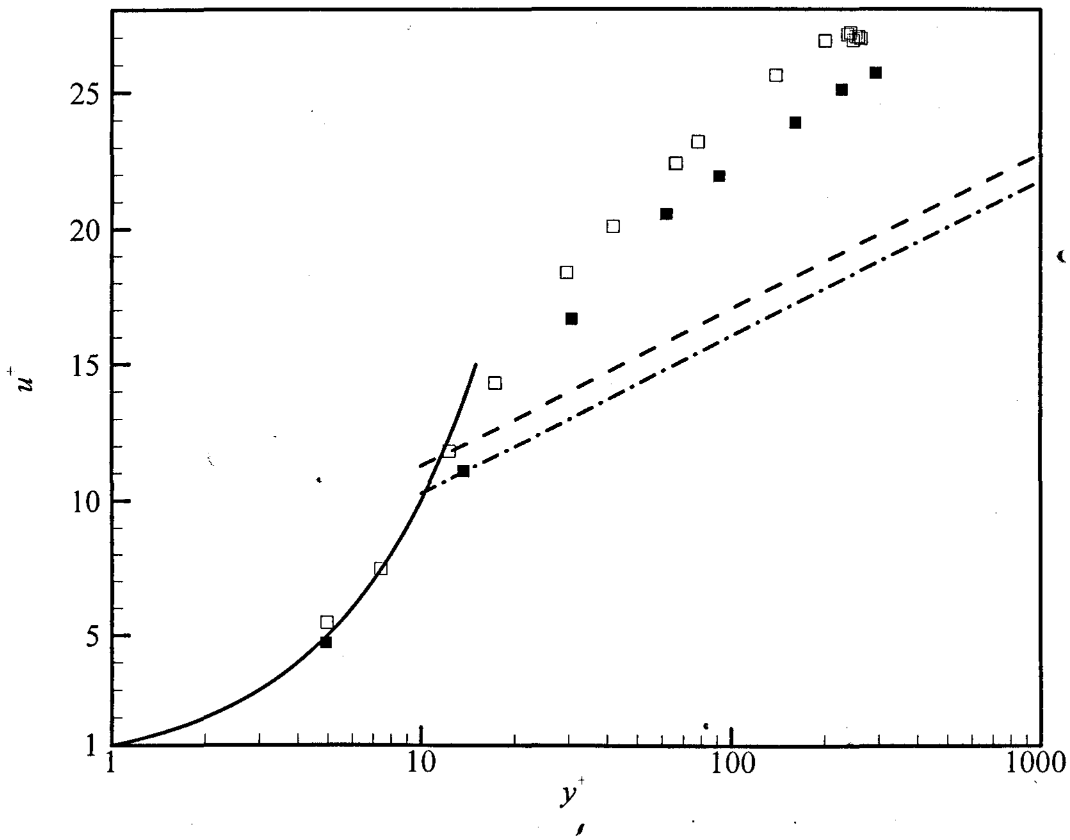

Figure 6.42: Universal mean velocity distribution for 0.07%XG. —: $u^+=y^+$; - - -: $u^+=2.5\ ln\ y^+ +5.5$; - · -: $u^+=2.5\ ln\ y^+ +4.9$ (Clauser); □: 0.07%XG (Inner), *Re*=28700, DR=42.3%; ■: 0.07%XG (Outer), *Re*=28700, DR=42.3%.

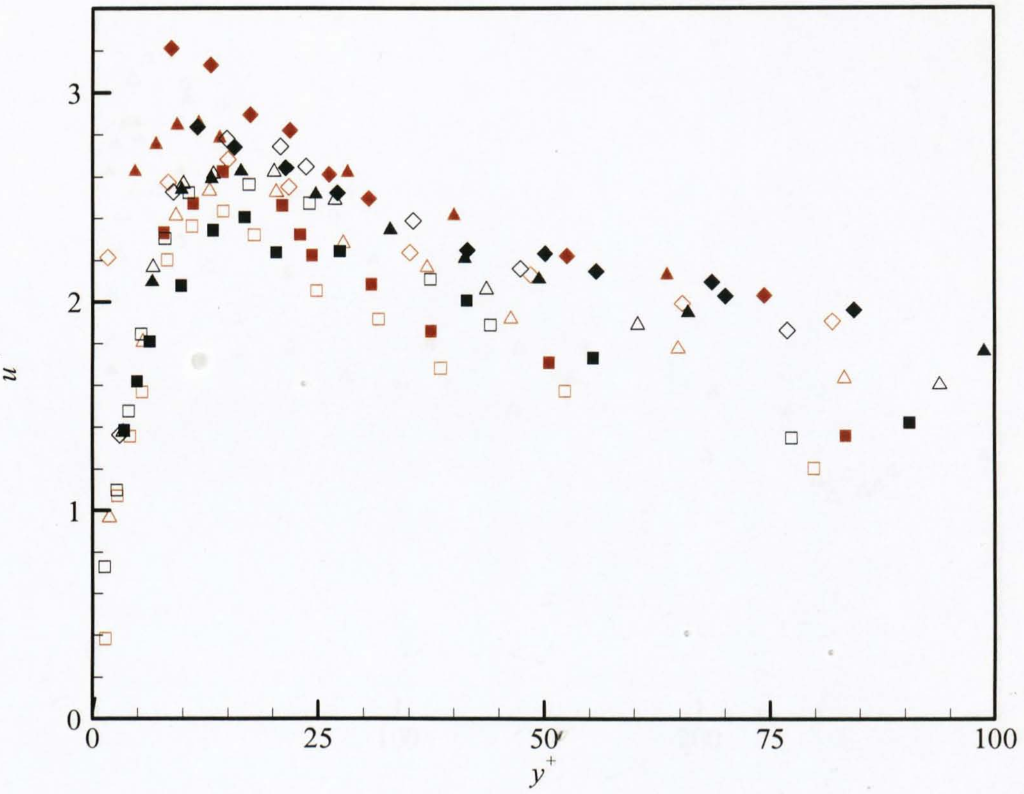

Figure 6.43: Axial rms fluctuation levels in wall coordinates for water and 0.0124%XG. □: Water (Inner), *Re*=9900, u'^+_{max}=2.44; ■: Water (Outer), *Re*=9900, u'^+_{max}=2.63; Δ: Water (Inner), *Re*=30600, u'^+_{max}=2.53; ▲: Water (Outer), *Re*=30600, u'^+_{max}=2.86; ◇: Water (Inner), *Re*=61400, u'^+_{max}=2.68; ◆: Water (Outer), *Re*=61400, u'^+_{max}=3.21; □: 0.0124%XG (Inner), *Re*=10600, u'^+_{max}=2.57; ■: 0.0124%XG (Outer), *Re*=10600, u'^+_{max}=2.41; Δ: 0.0124%XG (Inner), *Re*=30300, u'^+_{max}=2.63; ▲: 0.0124%XG (Outer), *Re*=30300, u'^+_{max}=2.63; ◇: 0.0124%XG (Inner), *Re*=57600, u'^+_{max}=2.78; ◆: 0.0124%XG (Outer), *Re*=57600, u'^+_{max}=2.84.

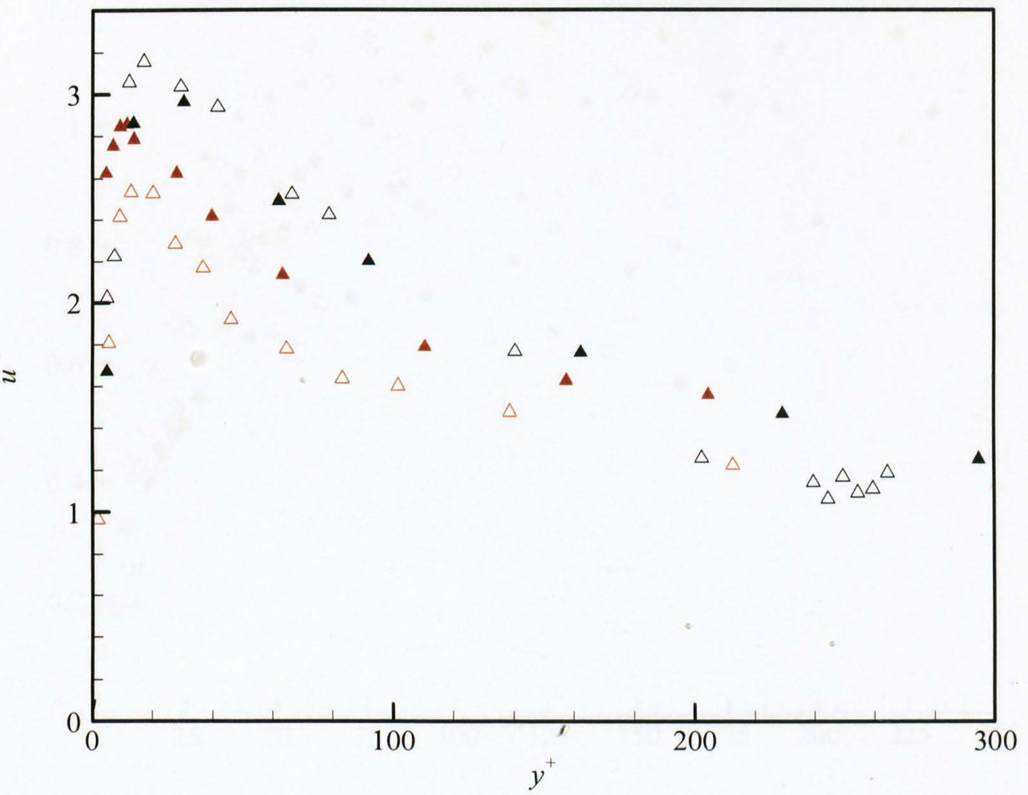

Figure 6.44: Axial rms fluctuation levels in wall coordinates for water and 0.07%XG. △: Water (Inner), *Re*=30600, u'^+_{max}=2.53; ▲: Water (Outer), *Re*=30600, u'^+_{max}=2.86; △: 0.07%XG (Inner), *Re*=28700, u'^+_{max}=3.16; ▲: 0.07%XG (Outer), *Re*=28700, u'^+_{max}=2.96.

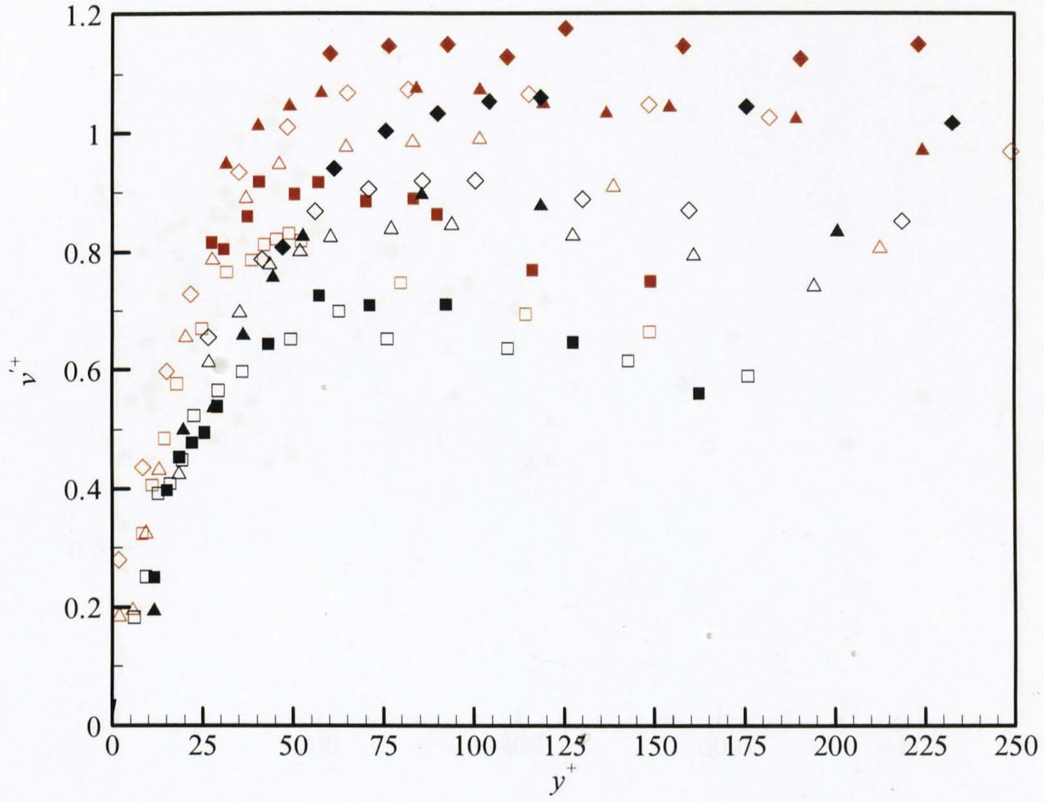

Figure 6.45: Radial rms fluctuation levels in wall coordinates for water and 0.0124%XG. □: Water (Inner), *Re*=9900, v'^+_{max} =0.83; ■: Water (Outer), *Re*=9900, v'^+_{max} =0.92; Δ: Water (Inner), *Re*=30600, v'^+_{max} =0.99; ▲: Water (Outer), *Re*=30600, v'^+_{max} =1.08; ◇: Water (Inner), *Re*=61400, v'^+_{max} =1.07; ◆: Water (Outer), *Re*=61400, v'^+_{max} =1.18; □: 0.0124%XG (Inner), *Re*=10600, v'^+_{max} =0.70; ■: 0.0124%XG (Outer), *Re*=10600, v'^+_{max} =0.72; Δ: 0.0124%XG (Inner), *Re*=30300, v'^+_{max} =0.85; ▲: 0.0124%XG (Outer), *Re*=30300, v'^+_{max} =0.90; ◇: 0.0124%XG (Inner), *Re*=57600, v'^+_{max} =0.92; ◆: 0.0124%XG (Outer), *Re*=57600, v'^+_{max} =1.06.

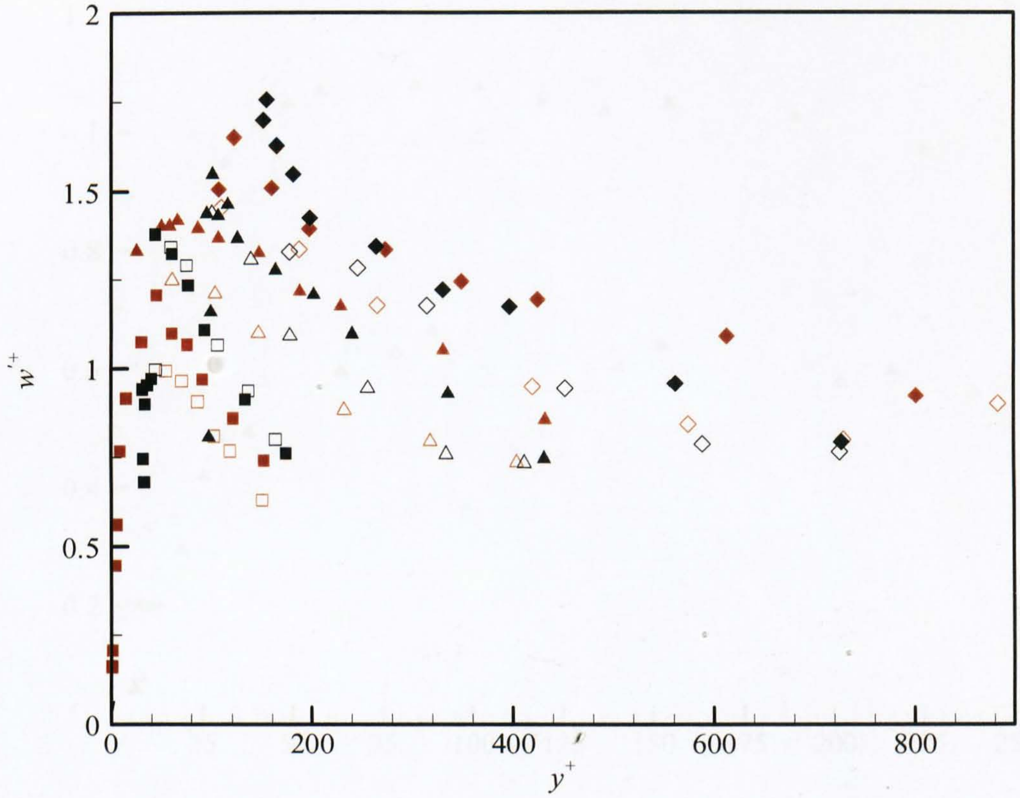

Figure 6.46: Tangential rms fluctuation levels in wall coordinates for water and 0.0124%XG. □: Water (Inner), *Re*=9900, w'^+_{max} =0.99; ■: Water (Outer), *Re*=9900, w'^+_{max} =1.20; Δ: Water (Inner), *Re*=30600, w'^+_{max} =1.25; ▲: Water (Outer), *Re*=30600, w'^+_{max} =1.42; ◇: Water (Inner), *Re*=61400, w'^+_{max} =1.45; ◆: Water (Outer), *Re*=61400, w'^+_{max} =1.65; □: 0.0124%XG (Inner), *Re*=10600, w'^+_{max} =1.34; ■: 0.0124%XG (Outer), *Re*=10600, w'^+_{max} =1.38; Δ: 0.0124%XG (Inner), *Re*=30300, w'^+_{max} =1.44; ▲: 0.0124%XG (Outer), *Re*=30300, w'^+_{max} =1.55; ◇: 0.0124%XG (Inner), *Re*=57600, w'^+_{max} =1.33; ◆: 0.0124%XG (Outer), *Re*=57600, w'^+_{max} =1.76.

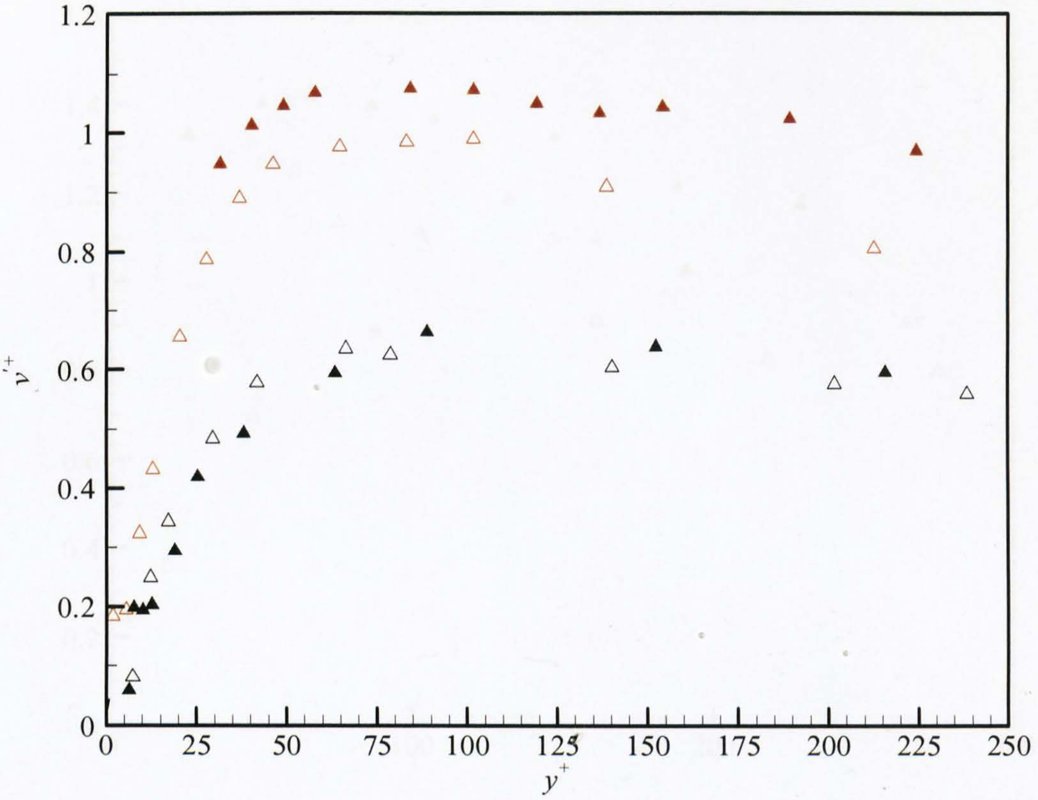

Figure 6.47: Radial rms fluctuation levels in wall coordinates for water and 0.07%XG. Δ: Water (Inner), *Re*=30600, v'^+_{max} =0.99; ▲: Water (Outer), *Re*=30600, v'^+_{max} =1.08; Δ: 0.07%XG (Inner), *Re*=28700, v'^+_{max} =0.63; ▲: 0.07%XG (Outer), *Re*=28700, v'^+_{max} =0.66.

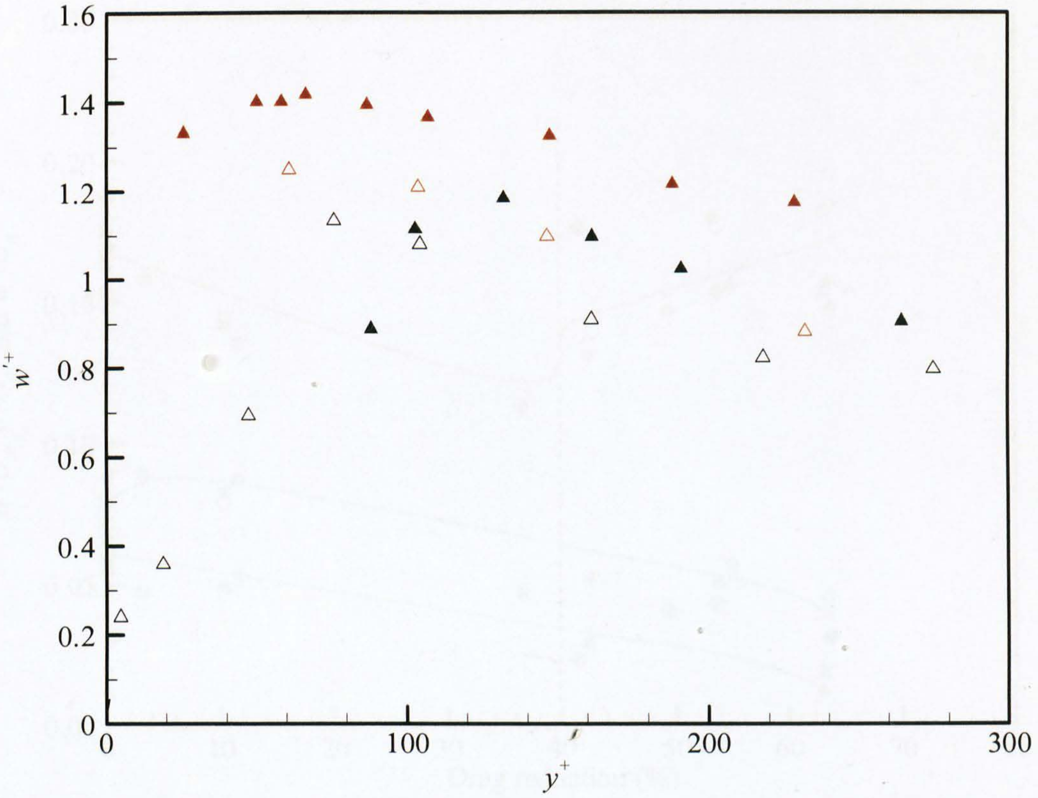

Figure 6.48: Tangential rms fluctuation levels in wall coordinates for water and 0.07%XG.

△: Water (Inner), *Re*=30600, w'^+_{max} =1.25; ▲: Water (Outer), *Re*=30600, w'^+_{max} =1.42; △: 0.07%XG (Inner), *Re*=28700, w'^+_{max} =1.13; ▲: 0.07%XG (Outer), *Re*=28700, w'^+_{max} =1.18.

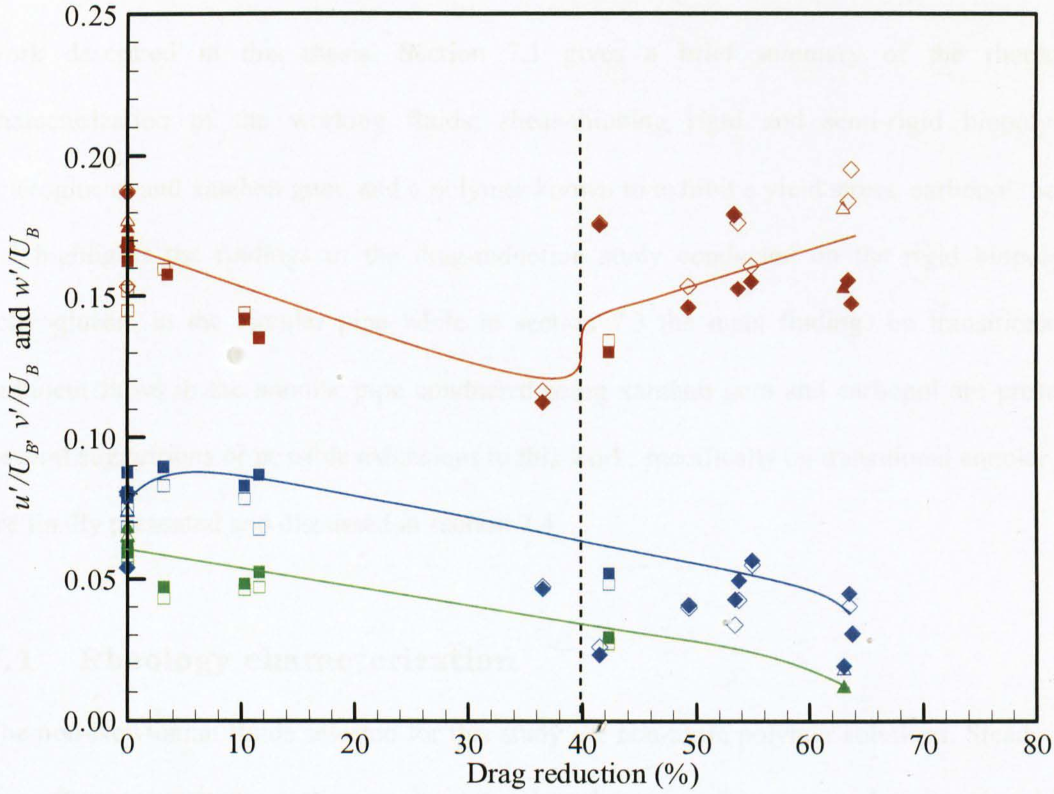

Figure 6.49: Peaks of axial, radial and tangential fluctuation components normalized with the bulk velocity, U_B, against drag reduction (□:current study, Δ: CMC (Nouri et. al., 1993), ◇: CMC, XG, LAPONITE/CMC (Escudier et. al., 1995a), Red: u'/U_B , Green: v'/U_B , Blue: w'/U_B , Hollow symbols: Inner wall, Filled symbols: Outer wall)

7 CONCLUSIONS

This chapter is divided into several sections which summarize the key findings of the research work described in this thesis. Section 7.1 gives a brief summary of the rheological characterization of the working fluids; shear-thinning rigid and semi-rigid biopolymers, scleroglucan and xanthan gum, and a polymer known to exhibit a yield stress, carbopol. Section 7.2 highlights the findings of the drag-reduction study conducted on the rigid biopolymer, scleroglucan, in the circular pipe while in section 7.3 the main findings on transitional and turbulent flows in the annular pipe conducted using xanthan gum and carbopol are presented. Several suggestions of possible extensions to this work, specifically on transitional annular flow, are finally presented and discussed in section 7.4.

7.1 Rheology characterization

The non-Newtonian fluids selected for this study are non-toxic polymer solutions. Steady-shear viscosity measurements on these polymers, scleroglucan, xanthan gum and carbopol, exhibited increased shear-thinning ability with increasing solution concentration. During these measurements, wall slip occurred in the carbopol solutions and the effects were minimized using a roughened parallel-plate geometry producing a very high first Newtonian plateau in the shear-viscosity data at very low shear stresses, typical of a "yield stress" fluid. The small amplitude oscillatory shear (SAOS) data showed that the loss modulus (G'') is greater than the storage modulus (G') until the crossover frequency, which decreases with concentration, indicating viscous dominance at low concentrations for scleroglucan and xanthan gum. Although the shear and SAOS properties of rigid and semi-rigid polymers were well-known before this study, no reliable information regarding their extensional properties was available. To fill this gap in understanding capillary break-up extensional viscosity measurements (CaBER) were conducted on the rigid and semi-rigid "rod-like" polymers, scleroglucan and xanthan gum. Newtonian-like linear filament-thinning behaviour was observed in the capillary-thinning experiments which has not been seen before in the flexible polymer solutions investigated using this technique in the literature. However, even though the filament thinning is Newtonian like, the magnitude of the Trouton ratio (>>3) confirms the non-Newtonian behaviour of these polymers in extensional flow. Although scleroglucan and xanthan gum have been classified in the literature as rigid and semi-rigid polymers, respectively, the CaBER results showed that these polymers in fact behave very similarly in extensional flows with the steady uniaxial extensional viscosity varying with concentration in the same power-law fashion for both polymers ($\eta_E \propto c^{1.2}$).

7.2 Pipe flow

For the first time detailed turbulence measurements in a pipe flow for a rigid rod-like polymer solution, scleroglucan, have been obtained. Although gross flow measurements, i.e. pressure drop versus Reynolds number, of this rigid polymer have been conducted before in a pipe (Sasaki, 1991), no information on the velocity field or turbulent statistics were available in the literature prior to this work. In fact the sole paper with detailed results for such polymer appears to be the boundary layer injection study of Paschkewitz et. al. (2005). The results presented in this thesis confirm that scleroglucan is drag reducing with the drag-reduction effectiveness, which increases with solution concentration, found to be only mildly dependent on the Reynolds number. Though slightly lower than the drag-reducing ability of flexible polymer solutions seen in the literature at the same concentrations the high degree of mechanical degradation resistance of the rigid rod-like polymer, even at very dilute concentrations, represents a potentially very significant practical benefit. For example, in the oil industry, the use of flexible polymers to reduce pumping power and to increase the bearing capacity of the drill cuttings may require constant addition of the polymer due to its fast degradation rate. Rigid polymer solutions represent a cost-effective and, as they are formed from biological processes, environmentally-friendly solution to this degradation problem.

The results in this study show that the mean axial and turbulence structure data exhibit behaviour typical of a low drag-reducing flexible polymer solution such as carboxymethylcellulose with increases in u'^{+} and decreases both in w'^{+} and v'^{+} generally when compared to that of the Newtonian flow at the same Reynolds number. The current results hence expand the previously extremely limited experimental database for rigid polymers in turbulent flow and provide a benchmark dataset for the validation of numerical simulations for rigid polymer flows, for example using direct numerical simulations (DNS).

7.3 Annular flow

Prior to this thesis no detailed experimental study had been conducted on the transitional flow within an annular pipe for non-Newtonian fluids. To address this deficit the transitional flow of a series of non-Newtonian fluids in an annulus of radius ratio $\kappa = 0.5$ have been investigated. By monitoring the axial rms fluctuation level at fixed radial locations close to the inner and outer walls (ξ=0.1 and 0.9) a larger Reynolds number range during which transitional flow can be observed is seen for the more shear-thinning fluids in comparison to the Newtonian control case. Time traces of the mean axial velocity at these non-dimensional radial locations provided further insight of the transitional flow within the annular pipe. Contrary to what is observed for the Newtonian fluid, glycerine in this case, the higher shear stress on the inner wall compared to the outer wall does not lead to earlier transition for shear thinning and yield stress fluids. For these fluids higher turbulent activity in terms of a greater number of high and low velocity spikes in the time traces is observed at the outer wall region, a transitional flow characteristic which is not clearly seen by monitoring the axial rms fluctuation level alone. The earlier transition to turbulence of the inner wall region seen in the experiments for the Newtonian fluid flow is in agreement with the theoretical predictions of Hanks and Bonner (1971). A slight shift (~5%) of the maximum velocity location towards the outer pipe wall was detected in the transitional regime only for the Newtonian fluid. For the non-Newtonian fluids, where the flattening of the velocity profiles due to shear thinning makes peak identification more difficult anyway, and for Newtonian laminar and turbulent regimes ($Re<Re_{crit}$ and $Re>Re_2$), the maximum velocity is located close to the inner pipe wall at a fixed location of $\xi=0.44$.

The transitional-flow analysis described within this thesis further allows identification of drag-reduction onset within the transitional flow regime. For these drag-reducing flows drag reduction is not observed immediately after the onset of transition to turbulence (Re_1) but at some delayed Reynolds number between the critical Reynolds number obtained from the time traces of the axial velocity (Re_{crit}) and the limit where the maximum value of turbulent intensity is reached (Re_2). This new finding further supports the Type B drag-reduction mechanism discussed by Virk et. al. (1997) for rigid polymers. A qualitative analysis of the peak values of the turbulent fluctuation levels (normalized with U_B) shows a decreasing trend of the axial component below 40% drag reduction. Above this drag-reduction "limit", the peak levels seemed to increase, generally, with drag reduction. Apart from a slight increase of the normalized tangential component for DR$\leq$12%, the normalized radial and tangential rms fluctuating components remained below the Newtonian values for all drag-reducing flows, with the peak value decreasing with increasing drag reduction, similar to what is observed in the pipe-flow study. These current limited results would then indicate a different turbulent structure between the low and high drag-reducing annular flow than what is observed in the literature for pipe and channel flows.

In addition to providing a detailed experimental database which can be used to aid the development of turbulence models for non-Newtonian fluids (see for example Cruz and Pinho, 2003 and Pinho et. al., 2008), the findings presented within this thesis have shown that the biopolymers studied are capable of drag reduction. As all synthetic polymers are flexible polymers the rigid and semi-rigid biopolymers studied here could be suitable substitutes to these synthetic polymers and have many potential applications especially, but not exclusively, in the oil industry in terms of mechanical degradation resistance, biodegradability, sustainability and low toxicity. Furthermore the results presented here have expanded the fundamental understanding of the flow behaviour specifically within the transitional and turbulent regimes of non-Newtonian fluid flows, which captures the essentials of the drilling fluid dynamics during the oil and gas drilling process. Although in the actual application the annulus departs from the ideal conditions, which are concentric, steady and isothermal, the results obtained here, in an annulus with a radius ratio close to that used in conventional drilling, could be utilized, at least as a starting point, in the study of drill cuttings management.

7.4 Recommendations for future work

It has been shown that rigid and semi-rigid polymers have the same drag-reduction characteristics as low drag-reducing flexible polymers in pipe flow and, in a slightly different manner, in the annular-flow geometry. It is also well-known that they possess greater resistance to mechanical degradation than flexible polymers. However the problem of how these polymers reduce the drag - whether the same mechanism for flexible polymer applies to rigid and semi-rigid polymers - remains poorly understood. Hence further work should involve the study of the rigid polymer-turbulent interactions, be it through direct numerical simulations using suitable constitutive equations or experimental work using other measuring systems capable of providing additional insight such as stress birefringence.

Further investigation may be useful to fully understand the transitional flow phenomena in the annular pipe. Monitoring the time traces of the axial velocity at just two fixed non-dimensional radial locations of $\xi = 0.1$ and $\xi = 0.9$ as a means of estimating flow transition only gives information at these locations. It is therefore difficult to make any overall conclusions of the transitional behaviour throughout the whole annular pipe. The use of time-resolved particle image velocimetry (PIV) to monitor the whole flow-field would be useful in this regard. The time ratio method utilized in detecting transition to turbulence is also not ideal because of the high degree of uncertainty in its determination with the LDA data. A more advanced method of intermittency estimation can be applied, through the square of the first derivative method for example, if the data rate is high enough (> 1kHz).

Further work is also required to overcome the difficulty in obtaining two-component velocity measurements particularly very close to the wall to determine the Reynolds shear stress component ($\overline{u'v'}$). With the current slit module box, use of a thin layer of material with a refractive index close to that of the working fluids over the cross-slit to provide a solid surface would probably be the simplest solution.

REFERENCES

Afzal, N., 2001, "Power law and log law velocity profiles in turbulent boundary layer flow: equivalent relations at large Reynolds numbers", Acta Mechanica, 151, 195-216.

Alderman, N.J., Ram Babu, D., Hughes, T.L., Maitland, G.C., 1988, "The rheological properties of oil well drilling fluids", Proc Xth Int. Cong. Rheology, Sydney, 140-142.

Allan, J.J., Greated, C.A., McComb, W.D., 1984, "Laser Doppler anemometer measurements of turbulent structure in non-Newtonian fluids", Journal of Physics D-Applied Physics., 17(3), 533-549.

Amarouchene, Y., Bonn, D.; Kellay, H., Lo, T.S., L'vov, V.S., Procaccia, I., 2008, "Reynolds number dependence of drag reduction by rodlike polymers", Physics of Fluids, 20, 065108.

Apel, S.M., 1997, "Viscoelastic behaviour of aqueous polyethylene oxide and xanthan gum solutions", MSc Thesis, California State University, USA.

Azouz, I., Shirazi, S.A., 1997, "Numerical simulation of drag reducing turbulent flow in annular conduits", Journal of Fluids Engineering, 119, 838-846.

Bais, D., Trevisan, A., Lapasin, R., Partal, P., Gallegos, C., 2005, "Rheological characterization of polysaccharide-surfactant matrices for cosmetic O/W emulsions", Journal of Colloid and Interface Science, 290, 546-556.

Barnes, H.A. Hutton, J.F., Walters, K., 1989, "An Introduction to Rheology", Elsevier, Amsterdam, ISBN 0-444-87469-0.

Barnes, H.A., 2000, "A handbook of elementary rheology", The University of Wales Institute of Non-Newtonian Fluid Mechanics, ISBN 0-9538032-0-1.

Benzi, R., Ching, E.S.C., Lo, T.S., L'vov, V.S., Procaccia, I., 2005, "Additive equivalence in turbulent drag reduction by flexible and rodlike polymers", Physical Review, E72, 016305.

Benzi, R., Ching, E.S.C., Angelis, E.D., Procaccia, I., 2008, "Comparison of theory and direct numerical simulations of drag reduction by rodlike polymers in turbulent channel flows", Physical Review, E77, 046309.

Berman, N.S., 1978, "Drag reduction by polymers", Annual Review of Fluid Mechanics, 10, 47-64.

Berman, N.S., 1980, "Evidence for molecular interactions in drag reduction in turbulent pipe flows", Polymer Engineering and Science, 20(7), 451-455.

Berman, N.S., George W.K., Jr., 1974, "Onset of drag reduction in dilute polymer solutions", Physics of Fluids, 17(1), 250-251.

Bewersdorff, H.W., Singh, R.P., 1988, "Rheological and drag reduction characteristics of xanthan gum solutions", Rheologica Acta, 27, 617-627.

Bicen, A.F., 1982, "Refraction correction for LDA measurements in flows with curved optical boundaries", TSI Quarterly, VII (2), 10-12.

Bird, R.B., Armstrong, R.C., Hassager, O., 1977 "Dynamics of Polymeric Liquids-Volume 1, Fluid Mechanics", John Wiley and Sons, ISBN 0-471-07375-X.

Boger, D.V., 1977, "Highly elastic constant-viscosity fluid", Journal of Non-Newtonian Fluid Mechanics, 3(1), 87-91.

Brighton, J.A., Jones, J.B., 1964, "Fully developed turbulent flow in annuli", Journal of Basic Engineering, 86, 835.

Brown, J.L., 1989, "Geometric bias and time coincidence in 3-dimensional laser Doppler velocimeter systems", Experiments in Fluids, 7, 25-32.

Buchhave, P., George Jr., W.K., Lumley, J.L., 1979, "The measurement of turbulence with the laser-Doppler anemometer", Annual Review of Fluid Mechanics, 11, 443-503.

Carrington, S., Odell, J., Fisher, L., Mitchell, J., Hartley, L., 1996, "Polyelectrolyte behaviour of dilute xanthan solutions: salt effects on extensional rheology", Polymer, 37(13), 2871-2875.

Casas, J.A., Santos, V.E., Garcia-Ochoa, F., 2000, "Xanthan gum production under several operational conditions: molecular structure and rheological properties", Enzyme and Microbial Technology, 26, 282-291

Ching, E.S.C., Lo, T.S., Procaccia, I., 2006, "Turbulent drag reduction by flexible and rodlike polymers: Crossover effects at small concentrations", Physical Review, E74, 026301.

Chung, J.S., Graebel, W.P., 1971, "Laser anemometer measurements of turbulence in non-Newtonian pipe flows", Physics of Fluids, 15(4), 546-554.

Chung, S.Y., Rhee, G.H., Sung, H.J., 2002, "Direct numerical simulation of turbulent concentric annular pipe flow, Part 1: Flow field", International Journal of Heat and Fluid Flow, 23, 426-440.

Clauser, F.H., 1956, "The turbulent boundary layer", Advances in Applied Mechanics, 4, 1-51.

Cruz, D.O.A., Pinho, F.T., 2003, "Turbulent pipe flow predictions with a low Reynolds-number $k-\varepsilon$ model for drag-reducing fluids", Journal of Non-Newtonian Fluid Mechanics, 114, 109-148.

Curran, S.J., Hayes, R.E., Afacan, A., Williams M.C., Tanguy, P.A., 2002, "Properties of Carbopol solutions as models for yield-stress fluids", Journal of Food Science, 67, 176-180.

den Toonder, J.M.J., Nieuwstadt, F.T.M., Kuiken, G.D.C., 1995, "The role of elongational viscosity in the mechanism of drag reduction by polymer additives", Applied Scientific Research, 54, 95-123.

den Toonder, J.M.J., Hulsen, M.A., Kuiken, G.D.C., Nieuwstadt, F.T.M., 1997, "Drag reduction by polymer additives in a turbulent pipe flow: Numerical and laboratory experiments", Journal of Fluid Mechanics, 337, 193-231.

den Toonder, J.M.J., Niewstadt, F.T.M., 1997, "Reynolds number effects in a turbulent pipe flow for low to moderate Re", Physics of Fluids, 9(11), 3398-3408.

Dimotakis, P.E., 1976, "Single scattering particle laser-Doppler measurements of turbulence", Symposium on Non-Intrusive Instrumentation in Fluid Flow Research, Agard-CP-193, paper 10.1-14.

Doi, M., Edwards, S.F., 1986, "The theory of Polymer Dynamics", Oxford Science Publications, ISBN 0-19-851976-1.

Draad A.A., 1996, "Laminar-turbulent transition in pipe flow for Newtonian and non-

Newtonian fluids", PhD thesis, Delft University of Technology, The Netherlands.

Draad, A.A., Kuiken, G.D.C., Nieuwstadt, F.T.M., 1998, "Laminar-turbulent transition in pipe flow for Newtonian and non-Newtonian fluids", Journal of Fluid Mechanics, 377, 267-312.

Durao, D.F.G., Laker, J., Whitelaw, J.H., 1980, "Bias effects in laser Doppler anemometry", Journal of Physics E-Scientific Instruments, 13, 442-445.

Durst, F., Melling, A., Whitelaw, J.H., 1981, "Principles and practice of laser-Doppler anemometer", Academic Press, ISBN 0-12-225260-8.

Durst, F., Ray, S., Unsal, B., Bayoumi, O.A., 2005, "The development lengths of laminar pipe and channel flows", Journal of Fluids Engineering, 127, 1154-1160.

Escudier, M.P., Gouldson, I.W., Jones, D.M., 1995a, "Flow of shear-thinning fluids in a concentric annulus", Experiments in Fluids, 18, 225-238.

Escudier, M.P., Gouldson, I.W., 1995b, "Concentric annular flow with centerbody rotation of a Newtonian and a shear thinning liquid", International Journal of Heat and Fluid Flow, 16, 156-162.

Escudier, M.P., Presti, F., 1996, "Pipe flow of a thixotropic liquid", Journal of Non-Newtonian Fluid Mechanics, 62, 291-306.

Escudier, M.P., Presti, F., Smith, S., 1999, "Drag reduction in turbulent pipe flow of polymers", Journal of Non-Newtonian Fluid Mechanics, 81, 197-213.

Escudier, M.P., Gouldson, I.W., Pereira, A.S., Pinho, F.T., Poole, R.J., 2001, "On Reproducibility of the Rheology of Shear Thinning Liquids", Journal of Non-Newtonian Fluid Mechanics, 97, 99-124.

Escudier, M.P., Oliveira, P.J., Pinho, F.T., Smith, S., 2002a, "Fully developed laminar flow of non-Newtonian liquids through annuli: comparison of numerical calculations and experiments", Experiments in Fluids, 33, 101-111.

Escudier, M.P., Oliveira, P.J., Pinho, F.T., 2002b, "Fully developed laminar flow of purely viscous non-Newtonian liquids through annuli, including the effects of eccentricity and inner cylinder rotation", International Journal of Heat and Fluid Flow, 23, 52-73.

Escudier, M.P., Nickson, A.K., Poole, R.J., 2009a, "Turbulent flow of viscoelastic shear-thinning liquids through a rectangular duct: quantification of turbulence anisotropy", Journal of Non-Newtonian Fluid Mechanics, 160, 2-10.

Escudier, M.P., Rosa, S., Poole, R.J., 2009b, "Asymmetry in transitional pipe flow of drag-reducing polymer solutions", Journal of Non-Newtonian Fluid Mechanics, 161(1-3), 19-29.

Farina, J.I., Sineriz, F., Molina, O.E., Perotti, N.I., 2001, "Isolation and physicochemical characterization of soluble scleroglucan from Sclerotium rolfsii. Rheological properties, molecular weight and conformational characteristics", Carbohydrate Polymers, 44, 41-50.

Ferziger, J.H., Peric, M., 2002, "Computational Methods for Fluid Dynamics", Springer, New York, ISBN 3-540-42074-6.

Fredrickson, A.G., Bird, R.B., 1958, "Non-Newtonian flow in annuli", Industrial and Engineering Chemistry, 50(3), 347-353.

Gasljevic, K., Aguilar, G., Matthys, E.F., 2001, "On two distinct types of drag-reducing fluids, diameter scaling and turbulent profiles", Journal of Non-Newtonian Fluid Mechanics, 96, 405-425.

Gillissen, J.J.J., Boersma, B.J., Mortensen, P.H., Andersson, H.I., 2008, "Fibre-induced drag reduction", Journal of Fluid Mechanics, 602, 209-218.

Gouldson, I.W., 1997, "The flow of Newtonian and non-Newtonian fluids in an annular geometry", PhD thesis, University of Liverpool.

Graham, M.D., 2004, "Drag reduction in turbulent flow of polymer solutions", Rheology Reviews, eds. D. M. Binding and K. Walters, British Society of Rheology, 143-170.

Grassi, M., Lapasin, R., Pricl, S., 1996, "A study of the rheological behavior of Scleroglucan weak gel systems", Carbohydrate Polymers, 29, 169-181.

Gray, G.R., Darley, H.C.H., 1980, "Composition and properties of oil well drilling fluids", Gulf Publishing Company, ISBN 0-87201-129-1.

Gucuyener, I.H., Mehmetoglu, T., 1996, "Characterization of flow regime in concentric annuli and pipes for yield-pseudoplastic fluids" Journal of Petroleum Science and

Engineering, 16, 45-60.

Hamed, S.B., Belhadri, M., 2009, "Rheological properties of biopolymers drilling fluids", Journal of Petroleum Science and Engineering, 67 (3-4), 84-90.

Hanks, R.W., Bonner, W.F., 1971, "Transitional flow phenomena in concentric annuli", Industrial and Engineering Chemistry Fundamentals, 10(1), 105-113.

Hoyt, J.W., 1985, "Drag reduction in polysaccharide solutions", Trends in Biotechnology, 3 (1), 17-21.

Hoyt, J.W., 1986, "Drag reduction", Encyclopaedia of Polymer Science and Engineering, 5, Wiley, New York, 129-151.

Jensen, K.D., 2004, "Flow measurements", 10th Brazilian Congress of Thermal Sciences and Engineering, Vol. XXVI (4), October-December.

Jones, D.M., Walters, K., Williams, P.R., 1987, "On the extensional viscosity of mobile polymer solutions", Rheologica Acta, 26 (1), 20-30.

Jones, O.C., Leung, J.C.M., 1981, "An improvement in the calculation of turbulent friction in smooth concentric annuli", Journal of Fluids Engineering, 103, 615-623.

Jonsson, V.K., Sparrow, E.M., 1966, "Experiments on turbulent-flow phenomena in eccentric annular duct", Journal of Fluid Mechanics, 25(1), 65-86.

Jovanovic, J., Pashtrapanska, M., Frohnaphel, B., Durst, F., Koskinen, J., Koskinen, K., 2006, "On the mechanism responsible for turbulent drag reduction by dilute addition of high polymers: Theory, experiments, simulations and predictions", Journal of Fluids Engineering, 128, 118-130.

Katzbauer, B., 1998, "Properties and applications of xanthan gum", Polymer Degradation and Stability, 59, 81-84

Kays, W.M., Leung, E.Y., 1963, "Heat transfer in annular passages – hydrodynamically developed turbulent flow with arbitrarily prescribed heat flux", International Journal of Heat and Mass Transfer, 6, 537-557.

Keegan, F., 2009, "Experimental investigation into non-Newtonian fluid flow through gradual contraction geometries",PhD thesis, University of Liverpool.

Keller, F.J., Wang, T., 1995, "Effects of criterion functions on intermittency in heated transitional boundary-layers with and without streamwise acceleration", Journal of Turbomachinery, 117(1), 154-165.

Kim, C., Yoo, B., 2006, "Rheological properties of rice starch-xanthan gum mixtures", Journal of Food Engineering, 75, 120-128

Knudsen, J.G., Katz, D.L., 1958, "Fluid dynamics and heat transfer", The McGraw-Hill Companies, ISBN 0882759175.

Kok, M.V., Alikaya, T., 2005, "Effects of polymers on the rheological properties of *KCl/Polymer* type drilling fluids", Energy Sources, 27, 405-415.

Lapasin, R., Pricl, S., 1995, "Rheology of industrial Polysaccharides: Theory and Applications", Blackie Academic and Professional, ISBN 0 7514 0211 7.

Lawn, C.J., Elliott, C.J., 1972, "Fully developed turbulent flow through concentric annuli", Journal Mechanical Engineering Science, 14(3), 195-204.

Lee, H., 2001, "Rheology of concentrated isotropic and anisotropic rigid polysaccharide solutions: xanthan and scleroglucan", PhD thesis, University of California, USA.

Lumley, J.L., 1969, "Drag reduction by additives", Annual Review of Fluid Mechanics, 1, 367-384.

Lumley, J.L., 1973, "Drag reduction in turbulent flow by polymer additives", Journal of Polymer Science : Macromolecular Reviews, 7, 263-290.

Luo, Y., Peden, J.M., 1987, "Flow of drilling fluids through eccentric annuli", Presented at 62nd Annual Technical Conference and Exhibition of Society of Petroleum Engineers.

McComb, W.D., Rabie, L.H., 1982, "Local drag reduction due to injection of polymer-solutions into turbulent-flow in a pipe. 1. Dependence on local polymer concentration", AIChE Journal, 28(4), 547-557.

McComb W.D., Chan, K.T., 1985, "Laser Doppler anemometer measurements of turbulent structure in drag reducing fibre suspensions", Journal of Fluid Mechanics, 152, 455-478.

McEachern, D.W., 1969, "Laminar-nonlaminar transition for non-Newtonian flow in annuli", AIChE Journal, 15(6), 885-889.

McKinley, G.H., Brauner, O., Yao, M., 2001, "Filament stretching rheometry and the extensional viscosity of dilute and concentrated polymer solutions", Proc. 1st International Symposium on Applied Rheology.

Metzner, A.B., Reed, J.C., 1955, "Flow of non-Newtonian fluids – correlation of laminar, transition and turbulent flow regions", AIChE Journal, 1(4), 434-440.

Milas, M., Rinaudo, M., Knipper, M., Schuppiser, J.L., 1990, "Flow and Viscoelastic Properties of xanthan gum Solutions", Macromolecules, 23, 2506-2511.

Mishra, I.M., Mishra, P., 1980, "Transition from laminar to turbulent flow of purely viscous non-Newtonian fluids in concentric annuli", Indian Chemical Engineer, XXII (4), 39-41.

Mishra, P., Tripathi, G., 1971, "Transition from laminar to turbulent flow of purely viscous non-Newtonian fluids in tubes", Chemical Engineering Science, 26, 915-921.

Mizushina, T., Usui, H., 1977, "Reduction of eddy diffusion for momentum and heat in viscoelastic fluid flow in a circular tube", Physics of Fluids, 20(10), s100-s108.

Moller, P.C.F., Mewis, J., Bonn, D., 2006, "Yield stress and thixotropy: on the difficulty of measuring yield stresses in practice", Soft Matter, 2, 274-283.

Moresi, M., Presti, S.L., Mancini, M., 2001, "Rheology of scleroglucan dispersions", Journal of Food Engineering, 50, 235-245.

Moussa, T., Tiu, C., 1994, "Factors affecting polymer degradation in turbulent pipe flow", Chemical Engineering Science, 49 (10), 1681-1692.

Munson, B.R., Young, D.F., Okiishi, T.H., 2002, "Fundamentals of Fluid Mechanics", John Wiley and Sons, Inc., ISBN 0-471-44250-X.

Nakano, A., Minoura, Y., 1975, "Effect of solvent and concentration on scission of polymers with high-speed stirring", Journal of Applied Polymer Science, 19(8), 2119-2130.

Naqwi, A.A., Durst, F., 1991, "Light scattering applied to LDA and PDA measurements. Part 1: Theory and numerical treatments", Particle and Particle Systems Characterization, 8(4), 245-258.

Nieuwstadt, F.T.M., den Toonder, J.M.J., 2001, "Drag reduction by additives: a review, in Turbulence structure and motion" Editors: A. Soldati and R. Monti, 269-316, Springer Verlag, Book Chapter.

Nouri, J.M., Umur, H., Whitelaw, J.H., 1993, "Flow of Newtonian and non-Newtonian fluids in concentric and eccentric annuli", Journal of Fluid Mechanics, 253, 617-641.

Nouri, J.M., Whitelaw, J.H., 1994, "Flow of Newtonian and non-Newtonian fluids in a concentric annulus with rotation of the inner cylinder", Journal of Fluids Engineering, 116, 821-827.

Noveon, 2008, "Neutralizing Carbopol and Pemulen Polymers in Aqueous and Hydroalcoholic Systems", http://www.lubrizol.com/PersonalCare/Products/Carbopol/980.html, accessed - 15 Febuary 2009.

Oliveira, M.S.N., Yeh, R., McKinley, H., 2006, "Iterated stretching, extensional rheology and formation of beads-on-string structure in polymer solutions", Journal of Non-Newtonian Fluid Mechanics, 137 (1-3), 137-148.

Ooms, G., Kampman-Reinhartz, B.E., 1996, "Influence of drill pipe rotation and eccentricity on pressure drop over borehole during drilling", European Journal of Mechanics B-Fluid, 15(5), 695-711.

Palleschi, A., Bocchinfuso, G., Coviello, T., Alhaique, F., 2005, "Molecular dynamics investigations of the polysaccharide scleroglucan: first study on the triple helix structure", Carbohydrate Research, 340, 2154-2162.

Park, J.T., Mannheimer, R.J., Grimley, T.A., Morrow, T.B., 1989, "Pipe flow measurements of a transparent non-Newtonian slurry", Journal of Fluids Engineering, 111, 331-336.

Paschkewitz, J.S., Dubief, Y., Dimitropoulos, C.D., Shaqfeh, E.S.G., Moin, P., 2004, "Numerical simulation of turbulent drag reduction using rigid fibres", Journal of Fluid Mechanics, 518, 281-317.

Paschkewitz, J.S., Dimitriropoulus, C.D., Hou, Y.X., Somandepalli, V.S.R., Mungal, M.G., Moin, P., 2005, "An experimental and numerical investigation of drag reduction in a turbulent boundary layer using a rigid rodlike polymer", Physics of Fluids, 17, 085101-1-16.

Paschkewitz, J.S., Dubief, Y., Shaqfeh, E.S.G., 2005, "The dynamic mechanism for turbulent drag reduction using rigid fibers based on Lagrangian conditional statistics", Physics of Fluids, 17, 063102-1-18.

Peixinho, J., Nouar, C., Desaubry, C., Theron, B., 2005, "Laminar transitional and turbulent flow of yield stress fluid in a pipe", Journal of Non-Newtonian Fluid Mechanics, 128(2-3), 172-184.

Petrie, C.J.S., 2006, "Extensional viscosity: A critical discussion", Journal of Non-Newtonian Fluid Mechanics, 137, 15-23.

Pinho F.T., Whitelaw, J.H., 1990, "Flow of non-Newtonian fluids in a pipe", Journal of Non-Newtonian Fluid Mechanics, 34, 129-144.

Pinho, F., 1990, "Velocity characteristics of polymer solutions in ducts"; PhD thesis, Imperial college of Science, technology and medicine.

Pinho. F.T., Li, C.F., Younis, B.A., Sureshkumar, R., 2008, "A low Reynolds number turbulence closure for viscoelastic fluids", Journal of Non-Newtonian Fluid Mechanics, 154, 89-108.

Poggi, D., Porporato, A., Ridolfi, L., 2002, "An experimental contribution to near-wall measurements by means of a special laser Doppler anemometry technique", Experiments in Fluids, 32, 366-375.

Poole, R.J., Ridley, B.S., 2007, "Development-length requirements for fully developed laminar pipe flow of inelastic non-Newtonian liquids", Journal of Fluids Engineering, 129, 1281-1287.

Poole, R.J., 2009, "Development length requirements for fully-developed laminar flow in concentric annuli", Submitted to the Journal of Fluids Engineering.

Pope, S.B., 2000, "Turbulent flows", Cambridge University Press, ISBN 0-521-59886-9.

Presti, F., 2000, "Investigation of transitional and turbulent pipe flow of non-Newtonian fluids", PhD thesis, University of Liverpool.

Ptasinski, P.K., Nieuwstadt, F.T.M., Van Den Brule, B.H.A.A., Hulsen, M.A., 2001, "Experiments in turbulent pipe flow with polymer additives at maximum drag reduction", Flow, Turbulence and Combustion, 66, 159-182.

Ptasinski, P.K., 2002, "Turbulent flow of polymer solutions near maximum drag reduction: Experiments, simulations and mechanisms", PhD thesis, TU-Delft, The Netherlands.

Quarmby, A., 1967, "An experimental study of turbulent flow through concentric annuli", International Journal of Mechanical Sciences, 9(4), 205-221.

Rehme, K., 1974, "Turbulent flow in smooth concentric annuli with small radius ratio", Journal of Fluid Mechanics, 64(2), 263-287.

Rehme, K., 1975, "Turbulence measurements in smooth concentric annuli with small radius ratios", Journal of Fluid Mechanics, 72(1), 189-206.

Roberts, G.P., Barnes, H.A., 2001, "New measurements of the flow-curves for Carbopol dispersions without slip artefacts", Rheologica Acta, 40, 499-503.

Rochefort, W.E., Middleman, S., 1987, "Rheology of xanthan gum: Salt, Temperature, and strain Effects in Oscillatory and Steady Shear Experiments", Journal of Rheology, 31(4), 337-369.

Rodd, A.B., Dunstan, D.E., Boger, D.V., 2000, "Characterisation of xanthan gum Solutions using Dynamic Light Scattering and Rheology", Carbohydrate Polymers, 42, 159-174.

Rodd, L.E., Scott, T.P., Cooper-White, J.J., McKinley, G.H., 2005, "Capillary break-up rheometer of low-viscosity elastic fluids", Applied Rheology, 15, 12-27.

Rosa, S., 2008, "Transitional pipe flow of drag-reducing polymer solutions", PhD thesis, University of Liverpool, UK.

Rothfus, R.R., Monrad, C.C., Senecal, V.E., 1950, "Velocity distribution and fluid friction in smooth concentric annuli", Industrial and Engineering Chemistry, 42(12), 2511-2520.

Rothfus, R.R., Monrad, C.C., Sikchi, K.G., Heideger, W.J., 1955, "Isothermal skin friction in flow through annular sections", Industrial and Engineering Chemistry, 47 (5), 913-918.

Rubin, Y., Wygnanski, I.J., Haritonidis, J.H., 1979, "Further observations on transition in a pipe", Eppler, R., Fasel, H., (eds), Laminar-Turbulent transition, IUTAM symposium Stuttgard, Germany, 17-26.

Sasaki, S., 1991, "Drag reduction effect of rod-like polymer solutions. I. Influence of polymer concentration and rigidity of skeltal back bone", Journal of the Physical Society of Japan, 60(3), 868-878.

Schlichting, H., 1987, "Boundary-layer theory", The McGraw-Hill Companies, ISBN 0-070-553343.

Schummer, P., Thielen, W., 1980, "Structure of turbulence in viscoelastic fluids", Chemical Engineering Communications, 4(4-5), 593-606.

Schlumberger, 2009, "Oilfield glossary – spacer fluid", http://www.glossary.oilfield.slb.com/Display.cfm?Term=spacer%20fluid, accessed – 26 November 2009.

Sear, P.R., 1997, "Phase behaviour of a thermal mixtures of rigid-rod and flexible polymers", Journal De Physique II, 7, 877-886.

Seyer, F.A., Metzner, A.B., 1969, "Turbulence phenomenon in drag reducing system", AIChE Journal, 15(3), 426-434.

Stelter, M., Brenn, G., 2002, "Elongational rheometry for the characterization of viscoelastic fluid", Chemical Engineering and Technology, 25(1), 30-35.

Stokke, B.T., Christensen, B.E., Smidsrod, O., 1992, "Degradation of multistranded polymers: effects of interstrand stabilization in xanthan and scleroglucan studied by a Monte Carlo method", Macromolecules, 25, 2209-2214.

Stokke, B.T., Elgsaeter A., Bjornstad E.O., Lund, T., 1992, "Rheology of xanthan and scleroglucan in synthetic seawater", Carbohydrate Polymers, 17, 209-220.

Tabor M., de Gennes, P.G., 1986, "A cascade theory of drag reduction", Europhysics

Letters, 2(7), 519-522.

Tanner, R.I., Walters, K., 1999, "Rheology: a historical perspective", Rheology series 7, Elsevier, ISBN 0-444-82946-6.

Tennekes H., Lumley J.L., 1972, "A first course in turbulence", The MIT Press, ISBN 978-0-262-20019-6.

Tiederman, W.G., 1990, "The effect of dilute polymer solutions on viscous drag and turbulence structure", In Structure of turbulence and drag reduction, ed. A Gyr, Berlin: Springer Verlag, 187-200.

Toms, B.A., 1977, "On the early experiments on drag reduction by polymers", Physics of Fluids, 20(10, Pt. 2), S3-S5.

Tracy, M.A., Pecora, R., 1992, "Dynamics of rigid and semirigid rodlike polymers", Annual Review of Physical Chemistry, 43, 525-557.

Tropea, C., 1995, "Laser Doppler anemometry: recent developments and future challenges", Measurement Science and Technology, 6, 615-619.

Trouton, F.T., 1906, "On the coefficient of viscous traction and its relation to that of viscosity", Proceedings of The Royal Society A, 77, 426-440.

Vinod, P.S., 1994, "Effect of fluid rheology on hole cleaning in highly deviated wells", PhD thesis, Rice University.

Virk, P.S., Baher, H., 1970, "The effect of polymer concentration on drag reduction", Chemical Engineering Science, 25, 1183-1189.

Virk, P.S., Mickley, H.S., Smith, K.A., 1970, "The ultimate asymptote and mean flow structure in Tom's phenomenon", Journal of Applied Mechanics, 37, 488-493.

Virk, P.S., 1975, "Drag reduction fundamentals", AIChE Journal, 21 (4), 625-653.

Virk, P.S., Sherman, D.C., Wagger, D.L., 1997, "Additive equivalence during turbulent drag reduction", AIChE Journal, 43(12), 3257-3259.

Walker, J.E., Rothfus, R. R., 1958, "Transitional velocity patterns in a smooth concentric annulus", AIChE. Journal, 5(1), 51-54.

Walters, K., Bhatti, A.Q., Mori, N., 1990, "The influence of polymer conformation on the rheological properties of aqueous polymer solutions", Recent Developments in Structured Continua, 2.

Wang, T., Zhou, D., 1998, "Conditionally sampled flow and thermal behaviour of a transitional boundary layer at elevated free-stream turbulence", International Journal of Heat and Fluid Flow, 19, 348-357.

Warholic, M.D., 1997, "Modification of turbulent channel flow by passive and additive devices", PhD thesis, University of Illinois at Urbana-Champaign.

Warholic, M.D., Massah, H., Hanratty, T.J., 1999, "Influence of drag-reducing polymers on turbulence: Effects of Reynolds number, concentration and mixing", Experiments in Fluids, 27, 461-472.

White F.M., 2005, "Viscous fluid flow", The McGraw-Hill Companies, ISBN 0-071-24493-X.

White, C.M., Mungal, M.G., 2008, "Mechanics and prediction of turbulent drag reduction with polymer additives", Annual Review of Fluid Mechanics, 40, 235-256.

Wikipedia, 2005, "Tobacco mosaic virus",
http://en.wikipedia.org/wiki/Tobacco_mosaic_virus, accessed – 20 November 2009.

Willmarth, W., Wei, T., Lee, C.O., 1987, "Laser anemometer measurements of Reynolds stress in a turbulent channel with drag reducing polymer additives", Physics of Fluids, 30, 933-935.

Wygnanski, I.J., Champagne, F.H., 1973, "On transition in a pipe. Part 1. The origin of puffs and slugs and the flow in a turbulent slug", Journal of Fluid Mechanics, 59(2), 281-335.

Wygnanski, I.J., Sokolov, M., Friedman, D., 1975, "On transition in a pipe. Part 2. The equilibrium puff", Journal of Fluid Mechanics, 69(2), 283-304.

Yanta, W.J., Smith, R.A., 1973, "Measurements of turbulence-transport properties with a laser Doppler velocimeter", AIAA 11th Aerospace Science Meeting.

Yasuda, K., Armstrong, R.C., Cohen, R.E., 1981, "Shear flow properties of concentrated solutions of linear and star branched polystyrenes", Rheologica Acta, 20, 163-178.

Zagarola, M.V., Smits, A.J., 1998, "Mean-flow scaling of turbulent pipe flow", Journal of Fluid Mechanics, 373, 33-79.

Zakin, J.L., Ni, C.C., Hansen, R.J., 1977, "Laser Doppler velocimetry studies of early turbulence", Physics of Fluids, 20(10-2), 85-89.

Zhang, D.H., Chew, Y.T., Winoto, S.H., 1996, "Investigation of intermittency measurement methods for transitional boundary layer flows", Experimental Thermal and Fluid Sciences, 12, 433-443.

Zhu, H., Kim, Y.D., Kee, D.D., 2005, "Non-Newtonian fluids with a yield stress", Journal of Non-Newtonian Fluid Mechanics, 129, 177-181.

Zirnsak, M.A., Boger, D.V., Tirtaatmadja, V., 1999, "Steady shear and dynamic rheological properties of xanthan gum solutions in viscous solvents", Journal of Rheology, 43, 627-650.

Turbulent Pipe Flow of "Rod-Like" Polymer Solutions

A. Japper-Jaafar, M.P. Escudier and R.J. Poole

Department of Engineering, University of Liverpool, Brownlow Street, Liverpool, L69 3GH United Kingdom

Abstract. In this study the drag reduction of an aqueous solution of a rigid "rod-like" polymer, scleroglucan, at a concentration of 0.01% w/w in a 100-mm diameter, 23-m long circular pipe-flow facility was experimentally investigated. Pressure-drop measurements were conducted via a differential pressure transducer and compared to that of the Newtonian solvent. Mean axial velocity and complete Reynolds normal stress data, i.e. *u'*, *v'* and *w'* were measured by means of a laser Doppler anemometer at three different Reynolds numbers, all in the turbulent-flow regime. Newtonian control runs, also within the turbulent-flow regime, were also performed for comparison.

Keywords: turbulent, pipe flow, rod-like polymer.
PACS: 40, 80

INTRODUCTION

Turbulent drag reduction of "rod-like" or "rigid" polymer solutions has received considerably less attention than "flexible" polymer solutions partly because they appear not to be as effective at reducing drag at a given concentration [1]. Compared to flexible polymer solutions, where the drag-reduction mechanisms are already well explored and understood [2,3,4], the effect of rigid-rod polymer solutions on the turbulent structure is still largely unstudied (with the notable exception of the boundary-layer experiments of [1]). In this study the drag-reducing behavior of an aqueous solution of a rigid-rod polymer, scleroglucan (SG, Cargill Inc.), at a concentration of 0.01% w/w was investigated experimentally in a circular pipe-flow facility.

EXPERIMENTAL

A 23-m long circular pipe-flow facility was utilized. The test pipe comprised of a number of precision-bore borosilicate glass tubes, each about 1 m in length, with an average internal diameter of 100.4 mm. The fluid was driven from a 500-l capacity stainless-steel tank by a progressive cavity pump (Mono-type, E101 with a maximum flowrate of 0.025 m^3/s). Three pulsation dampers located immediately after the pump outlet acted to remove pulsations resulting from the rotation of the mono pump. A Coriolis mass flowmeter (Promass 63 manufactured by Endress + Hauser) was also incorporated in the system. The pressure drop was measured by means of a differential pressure transducer, GE Druck (LPX9381), capable of measuring up to 5000 Pa and an uncertainty of less than 1.5%, over a distance of 72D, starting 140D downstream of the inlet. The reading of the transducer under no-flow conditions was made at the beginning and at the end of each measurement to account for any drift. Velocity profiles and turbulent fluctuation levels, performed at 220D downstream of the inlet of the pipe test section, were determined using a Dantec Fibreflow laser Doppler anemometer (LDA) system supplied by Dantec Electronic Ltd, UK, comprising of 60×10 probe and a Dantec 55×12 beam expander in conjunction with a Dantec Burst Spectrum Analyzer signal processor (model 57N10). Only one component of velocity could be obtained at any one time due to the refraction of the beams at the curved surface of the pipe wall. At each location across the pipe cross section, 10,000 data samples were collected and the data was processed using a simple ensemble-averaging method. The flowrates obtained from integration of the LDA mean velocity profiles were found to be within 1.5% of the value provided by the flowmeter. In order to increase the signal-to-noise ratio and the data rate for the LDA measurements, seeding particles (Timiron MP-1005, mean dia. $\approx 20\mu m$) were also added at a concentration of 1ppm.

CP1027, *The XVth International Congress on Rheology, The Society of Rheology 80th Annual Meeting*
edited by A. Co, L. G. Leal, R. H. Colby and A. J. Giacomin

RESULTS AND DISCUSIONS

Polymer Characterization

The scleroglucan used in this study is a non-ionic polysaccharide produced by the fungi of genus sclerotium with a molecular weight reported by the supplier to be in excess of 10^6 g/mol. The rigid behavior of the polymer is attributable to the long persistent length of the molecule originating from its triple helical structure [1,5]. Steady-shear measurements were conducted over a wide range of concentrations (0.01% - 0.75% w/w) using a TA Instrument Rheolyst AR 1000N controlled-stress rheometer. Plotting η_o, which is the viscosity in the zero shear rate plateau against the solution concentration, c, provided a way of estimating the so-called critical overlap concentration, c^*, which for this particular SG was found to be 0.057% (570 ppm). Small amplitude oscillatory measurements and capillary break-up extensional behavior measurements were also conducted but were only possible for higher concentration solutions ($c \geq 0.075\%$).

Pressure-Drop Measurements

The experimental pressure-drop results are displayed in Fig. 1, as the Fanning friction factor, f versus Reynolds number, Re. The Reynolds number is defined based on the bulk velocity, pipe diameter and the dynamic viscosity at the wall which was obtained from a Carreau-Yasuda model fit [6] to the steady-shear viscosity measurements, using a known average wall shear stress determined from the pressure-drop measurements. The friction factor showed deviations away from that of the Newtonian solvent (water) towards Virk's "maximum drag reduction asymptote" [2] as the solution concentration was increased from 0.01% to 0.02%. However, the average drag reduction was found to plateau to an approximately constant value as the concentration was further increased to 0.05%. The average drag reductions, calculated from the friction factor of the polymer solutions and that of the Newtonian solvent at the same Re, for all solutions studied were only weakly dependent on the Reynolds number in marked contrast to flexible polymers [2].

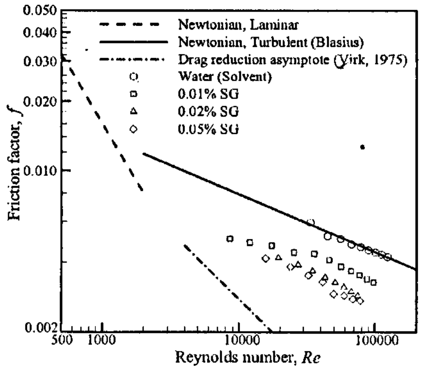

FIGURE 1. f-Re data for various scleroglucan concentrations in a circular pipe

Mean Flow and Turbulence Velocity Measurements

The onsets of the shifts of the polymer-solution data in Fig. 2(a) were found to be independent of Re occurring at a constant y^+ location of about 15. The magnitudes of the shifts were also found to be independent of Re. The axial fluctuation turbulent profile in Fig. 2(b) exhibits increased values, compared to the Newtonian data, towards the wall with the peaks found to be close to the onset of the shifts in the mean profiles ($y^+ \approx 15$). Fig. 2(c) and (d) exhibit suppression of the radial and tangential turbulence components with significant reductions in the peaks of the tangential turbulence velocity component compared to that of the Newtonian solvent.

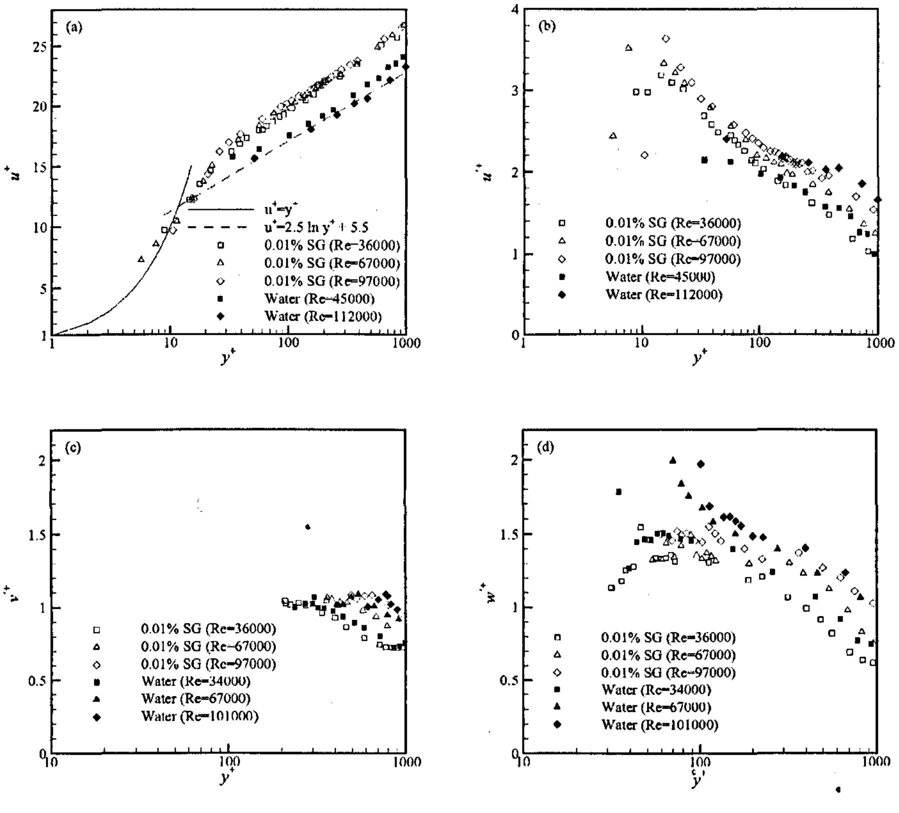

FIGURE 2. (a) Universal mean velocity distributions, (b) universal axial turbulence component at various Reynolds numbers, (c) Universal radial turbulence, (d) universal tangential turbulence components at various Reynolds numbers

CONCLUSIONS

Our data confirm that so-called rigid-rod polymer solutions are effective as drag-reducing agents. The mean axial and turbulence structure data presented here for a rigid-rod polymer solution, scleroglucan, exhibited behavior typical of a low drag-reducing *flexible* polymer solution with increases in u'^{+} and concomitant decreases in v'^{+} and w'^{+}.

REFERENCES

1. J.S. Paschkewitz, C.D. Dimitriropoulus, Y.X. Hou, V.S.R. Somandepalli, M.G. Mungal, P. Moin, "An experimental and numerical investigation of drag reduction in a turbulent boundary layer using a rigid rod-like polymer", Physics of Fluids, **17**, 2005, 085101-1-16.
2. P.S. Virk, "Drag reduction fundamentals", AIChE Journal, **21** (4), 1975, pp. 625-653.
3. C. M. White, M. G. Mungal, "Mechanics and prediction of turbulent drag reduction with polymer additives", Annual Review Fluid Mechanics, **40**, 2008, pp. 235-256.
4. J. Jovanovic, M. Pashtrapanska, B. Frohnaphel, F. Durst, J. Koskinen, K. Koskinen, "On the mechanism responsible for turbulent drag reduction by dilute addition of high polymers: Theory, experiments, simulations and predictions", Transactions of ASME, **128**, 2006, pp. 118-130.
5. S. Sasaki, "Drag reduction effect of rod-like polymer solutions. I. Influence of polymer concentration and rigidity of skeltal back bone", Journal of the Physical Society of Japan, **60**(3), 1991, pp. 868-878.
6. K. Yasuda, R.C., Armstrong, R.E. Cohen, "Shear flow properties of concentrated solutions of linear and star branched polystyrenes", Rheol. Acta, **20**, 1981, pp. 163-178.

J. Non-Newtonian Fluid Mech. 161 (2009) 86–93

Contents lists available at ScienceDirect

Journal of Non-Newtonian Fluid Mechanics

journal homepage: www.elsevier.com/locate/jnnfm

Turbulent pipe flow of a drag-reducing rigid "rod-like" polymer solution

A. Japper-Jaafar, M.P. Escudier, R.J. Poole *

Department of Engineering, University of Liverpool, Brownlow Street, Liverpool, L69 3GH United Kingdom

ARTICLE INFO

Article history:
Received 18 November 2008
Received in revised form 24 April 2009
Accepted 27 April 2009

Keywords:
Drag reduction
Pipe flow
Rigid-rod polymer solutions
LDA

ABSTRACT

Fully developed turbulent pipe flow of an aqueous solution of a rigid "rod-like" polymer, scleroglucan, at concentrations of 0.005% (w/w) and 0.01% (w/w) has been investigated experimentally. Fanning friction factors were determined from pressure-drop measurements for the Newtonian solvent (water) and the polymer solutions and so levels of drag reduction for the latter. Mean axial velocity u and complete Reynolds normal stress data, i.e. u', v' and w', were measured by means of a laser Doppler anemometer at three different Reynolds numbers for each fluid. The measurements indicate that the effectiveness of scleroglucan as a drag-reducing agent is only mildly dependent on Reynolds number. The turbulence structure essentially resembles that of flexible polymer solutions which also lead to low levels of drag reduction.

1. Introduction

The phenomenon of drag reduction, often referred to as "Tom's phenomenon", has been the subject of extensive reviews by Lumley [1], Virk [2], Berman [3], Hoyt [4], Nieuwstadt and den Toonder [5], Graham [6] and many others, and the behaviour of flexible polymer solutions as drag-reducing agents is now fairly well understood. A notional limit of drag reduction of 40% has been found below which, the flow is categorized as "low" drag-reducing and above which, "high" drag-reducing (e.g. Warholic et al. [7] and Escudier et al. [8]). There are marked differences between these two categories. For "low" drag-reducing flows, the normalized mean velocity in law-of-the-wall form (u^+) remains parallel to the Newtonian data but is upshifted [7,8]. In addition, the peak value of the normalized axial velocity fluctuations (u'^+) increases, the peak values of the radial (v'^+) and tangential (w'^+) velocity fluctuations decrease together with a monotonic decrease of the Reynolds shear stress ($\rho\overline{u'v'}$) [7]. Different trends are observed for high drag-reducing flows where there is a significant increase in the slope of the universal mean velocity profile [7]. At such high levels of drag reduction the normalized axial velocity fluctuation levels are ultimately suppressed with concomitant decreases of the Reynolds shear stress, to almost zero levels close to the maximum drag reduction asymptote [2], with corresponding increases in the so-called "polymer stress".

The drag-reducing mechanisms of "rigid" or "rod-like" polymers are far from as well studied or understood as is the case for flexible polymers. The limited literature on these polymers has shown that the polymer solutions are also capable of drag reduction but possibly to a lesser degree than flexible polymer solutions (e.g. the boundary-layer (polymer injection) work of Paschkewitz et al. [9]). However, while high molecular weight flexible polymer solutions are very prone to mechanical degradation, an advantage of rigid polymer solutions is that they are more resistant (Paschkewitz et al. [9], Hoyt [4]). An additional advantage of rigid polymers is that they tend to be biopolymers, derived through biological fermentation.

Berman [3] found that rigid structures and polyelectrolytes were not effective drag reducers until the concentration was "high enough" which was also confirmed by his later study [10]. Using collagen and carrageenan, the ratio of circumscribed volume of the molecules to the actual volume (the lengths of the rod-like molecules were used as diameters to calculate the circumscribed volume) was found to be at least 30 for the solution to be drag-reducing. Through pressure-drop measurements it was observed that the rigid polymer solutions were drag-reducing but did not show any drag reduction onset (i.e. there appeared to be no critical wall shear stress before drag reduction occurred). Although exhibiting drag reduction, the slopes of the friction factor, f, against the Reynolds number, Re, plotted in log–log coordinates remained parallel to that for the Newtonian fluid flow. In contrast to polyelectrolytes and flexible polymer solutions, no diameter effect was observed for these rigid polymer solutions [10].

Bewersdorff and Singh [11] studied the drag reduction of xanthan gum solutions, in which molecule rigidity was varied by the addition of salt to increase flexibility. Without salt addition, the f–Re data of the xanthan gum solutions (again plotted in log–log coordinates) exhibited drag reduction but the curves remained parallel to that for the Newtonian fluid. The greater flexibility due to the addition of salt resulted in greater drag reduction. These results are in disagreement with the observations of both Sasaki [12] and Virk et

---

* Corresponding author. Fax: +44 151 7944848.
E-mail addresses: a.jaafar@liv.ac.uk (A. Japper-Jaafar), escudier@liv.ac.uk (M.P. Escudier), robpoole@liv.ac.uk (R.J. Poole).

0377-0257/$ – see front matter © 2009 Elsevier B.V. All rights reserved.
doi:10.1016/j.jnnfm.2009.04.008

Nomenclature

a	Carreau–Yasuda parameter
b	diameter of CaBER plates (4 mm)
c	polymer concentration (%, w/w)
c^*	critical overlap concentration (%, w/w)
D	pipe diameter (m)
D_{CaBER}	filament diameter in CaBER (mm)
D_0	midpoint filament diameter in CaBER following cessation of stretch deformation (mm)
DR	drag reduction (%), $\left(\equiv (f_n - f_p)/f_n \times 100\right)$
f	Fanning friction factor, $(\equiv 2\tau_{\mathrm{W}}/\rho U_{\mathrm{B}}^2)$
G'	storage modulus (Pa)
G''	loss modulus (Pa)
h	distance between plates in CaBER (mm)
L	pipe length over which the pressure drop was measured (m)
m	slope of linear fitting to CaBER data (mm/s)
n	power-law index
Δp	pressure drop (Pa)
$\dot{Q}$	volumetric flowrate (m^3/s)
Re	Reynolds number $(\equiv \rho U_{\mathrm{B}} D/\eta_{\mathrm{W}})$
t	time (s)
T_{B}	filament breakup time in CaBER (s)
Tr	Trouton ratio, $(\equiv \eta_{\mathrm{E}}(\sqrt{3}\dot{\varepsilon})/\eta(\dot{\gamma}))$
u	mean axial velocity (m/s)
u^+	mean axial velocity normalised by friction velocity $(\equiv u/u_\tau)$
u_τ	friction velocity (m/s), $(\equiv \sqrt{\tau_{\mathrm{W}}/\rho})$
u'	RMS axial velocity fluctuation (m/s)
u'^+	RMS axial velocity fluctuation normalised by friction velocity $(\equiv u'/u_\tau)$
$\overline{u'v'}$	Reynolds shear stress (m^2/s^2)
U_{B}	bulk velocity (m/s), $(\equiv 4\dot{Q}/(\pi D^2))$
v'	RMS radial velocity fluctuation (m/s)
v'^+	RMS radial velocity fluctuation normalised by friction velocity $(\equiv v'/u_\tau)$
w'	RMS tangential velocity fluctuation (m/s)
w'^+	RMS tangential velocity fluctuation normalised by friction velocity $(\equiv w'/u_\tau)$
y	distance from pipe wall (m)
y^+	distance from pipe wall normalised by friction velocity $(\equiv \rho y u_\tau/\eta_{\mathrm{W}})$

Greek letters

$\dot{\gamma}$	shear rate (1/s)
$\dot{\gamma}_{\mathrm{W}}$	shear rate at the wall (s^{-1})
$\dot{\varepsilon}$	strain rate determined from CaBER (1/s), $\left(\equiv -\frac{4}{D_0}\frac{\mathrm{d}D_{\mathrm{CaBER}}}{\mathrm{d}t}\right)$
η	shear viscosity (Pa s)
η_{E}	uniaxial extensional viscosity (Pa s)
η_0	zero-shear rate viscosity (Pa s)
η_{W}	wall shear viscosity obtained from τ_{W} and $\dot{\gamma}_{\mathrm{W}}$ via Carreau–Yasuda fit (Pa s)
η_∞	infinite-shear rate viscosity (Pa s)
λ	characteristic relaxation time in CaBER (s)
λ_{CY}	Carreau–Yasuda constant representing onset of shear thinning (s)
ρ	fluid density (kg/m^3)
τ_{W}	wall shear stress (Pa) $(\equiv \Delta p D/4L)$
ω	angular frequency (rad/s)

Subscripts

N	Newtonian
P	polymer
W	wall

Superscripts

+	"wall" coordinates

al. [13] however. Virk et al. [13] found that increasing the flexibility of hydrolyzed polyacrylamide reduced the drag reduction ability of the polymer solution. Sasaki [12] also studied the drag-reducing ability of what he termed a "strictly rigid" polymer solution, scleroglucan, and found the trend to be in close agreement with that of a semi-rigid xanthan gum solution without salt addition.

Benzi et al. [14] postulated through theoretical considerations that the slope of the maximum drag reduction asymptote (*f*–*Re* plot) discovered by Virk [2] applies to both flexible and rigid polymers. However, their work showed that the dynamics of these polymers upon approaching the asymptote are different. They found that the degree of drag reduction for a rigid polymer is dependent only on the concentration while it is well known that for a flexible polymer, it is a function of concentration, Reynolds number and the Deborah number [1–5]. For flexible polymers, the asymptote is reached even for low concentrations and then a crossover back to the Newtonian core is found. For rigid polymers, maximum drag reduction is approached gradually as concentration is increased. Paschkewitz et al. [15] conducted direct numerical simulations of non-Brownian fibres (no elasticity) in a turbulent channel flow. At 15% drag reduction, the mean axial and turbulence structure data are found to be similar to that of low drag-reducing flexible polymer solutions leading to the conclusion that elasticity is not necessary for drag reduction. The Reynolds shear stress is reduced throughout the entire channel and the polymer stress shows large values closer to the wall suggesting that fibres most strongly affect the flow in the near-wall region ($y^+ < 100$). Similar observations were also made by Benzi et al. [16]. The drag reduction effectiveness is also found to increase with increasing aspect ratio of the fibres (Paschkewitz et al. [15], Gillissen et al. [17]).

To date, with the notable exception of the boundary-layer experiments of Paschkewitz et al. [9], there is no experimental information on the mean velocity and on the turbulence statistics of rigid polymer solutions in fully developed pipe flow, or indeed any pure shear flow. The present paper aims to address this deficit by studying the effects of concentration and Reynolds number on the degree of drag reduction of a "strictly rigid" polymer solution, scleroglucan, in a large-scale circular pipe flow facility (i.e. the same polymer as studied in [9] and [12]). Measurements on the Newtonian solvent, at Reynolds numbers close to that of the polymer solution flow, were also performed for comparison. As has been pointed out by den Toonder and Nieuwstadt [18] the turbulent fluctuation components for Newtonian pipe flow, normalized with the friction velocity (u_τ), are Reynolds number dependent. Hence, it is important, as we ensure here, that the flow measurements for the Newtonian fluid are conducted at the same Reynolds number as that of the polymer solutions. The Reynolds number is defined here based on the bulk velocity, pipe diameter and the fluid viscosity at the wall ($Re = \rho U_{\mathrm{B}} D/\eta_{\mathrm{W}}$).

2. Experimental arrangement

The measurements were carried out in a 23-m long circular pipe flow facility, which is essentially an extended version of the flow loop described in detail in [19] (Fig. 1). The test pipe (1) comprised of

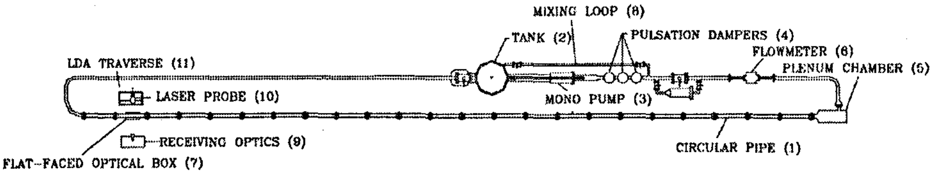

Fig. 1. Schematic diagram of the flow loop.

21 precision-bore borosilicate glass tubes, each about 1029 ± 2 mm long, a single glass tube 656 mm in length and one PVC plastic pipe, 1060 mm long, at the test section entrance. The internal diameter of the tubes is 100.4 ± 0.1 mm. The fluid was driven from a 500-l capacity stainless steel tank (2) by a progressive cavity pump (3) (Monotype, E101 with a maximum flowrate of 0.025 m^3/s). Three pulsation dampers (4) located immediately after the pump outlet acted to remove pulsations resulting from the rotation of the mono pump. A cylindrical plenum-chamber (5) upstream of the pipe test section minimizes swirl and suppresses disturbances with the intention of providing a smooth uniform inflow into the pipe. A Coriolis mass flowmeter (6) (Promass 63, manufactured by Endress + Hauser) was also incorporated in the experimental rig. The pressure drop was measured by means of a differential pressure transducer, GE Druck (LPX9381) with a range of 5000 Pa and an uncertainty of less than 1.5%, over a distance of 7.2 m (72 D) starting 14 m (140 D) downstream of the inlet. Readings of the transducer under no-flow conditions were made at the beginning and end of each measurement to account for any drift where the zero flowrate readings were monitored and subsequent readings were corrected accordingly.

Mean velocity profiles and turbulent fluctuation levels, were measured 22 m (220 D) downstream of the inlet of the pipe test section, using a Dantec Fiberflow laser Doppler anemometer (LDA) system comprising of a 60X10 probe and a Dantec 55X12 beam expander in conjunction with a Dantec Burst Spectrum Analyzer signal processor (model 57N10). The lens focal length is 160 mm and the measured half angle between the laser beams is 8.4° which produces a measuring volume with a diameter of 40 μm and a length of 0.27 mm in air, calculated using the procedure of Buchhave et al. [20]. The axial and tangential velocities and the respective radial locations were corrected as suggested by Bicen [21]. The radial velocity measurements were conducted with a flat-faced optical box (7), filled with water, placed on the test section to minimize the amount of refraction of the beams making it possible to obtain data closer to the wall. The radial velocities and locations were corrected using the ray-tracing method outlined by Presti [22].

At each radial location 10,000–20,000 data samples were collected and processed using a simple ensemble-averaging method. Processing the data using a transit-time weighting method [23] to account for velocity-biasing effects produced minimal differences compared with processing the data using a simple ensemble-averaging method (differences of less than 2% in the RMS fluctuation levels). The maximum statistical error, for a 95% confidence interval, was less than 0.5% in mean velocity and less than 1.5% in the turbulence intensity based on the method of Yanta and Smith [24]. The flowrates obtained from integration of the LDA mean velocity profiles were found to be within 1.5% of the value provided by the flowmeter.

Approximately 700 l of tap water was used as the solvent for the test fluid. Mixing of part of the solvent with the polymer powder was achieved by recirculating the polymer solution within the mixing loop (8) at a low pump speed for at least 5 h before the mixing loop was opened and the solution was circulated in the flow loop, allowing further mixing with the rest of the solvent in the pipe for at least another 5 h, until the solutions appeared to be visibly homogeneous. The homogeneity of the solution was also checked by comparing the viscometric data with a small sample solution prepared separately of the same concentration. Formaldehyde was added to the polymer solution at a concentration of 100 ppm to retard bacteriological degradation. The polymer solution was then left to hydrate in the rig for at least 24 h prior to commencing the LDA measurement. Measurements of fluid rheology were conducted prior to and after each LDA profile to check for signs of mechanical and bacteriological degradation. In order to increase the signal-to-noise ratio and the data rate for the LDA measurements, seeding particles (Timiron MP1005, mean diameter ≈5 μm) were added at a concentration of about 1 ppm.

3. Working fluid characterization

The scleroglucan (Actigum^{TM} CS, provided by Cargill Incorporated and hereafter referred to as SG) used in this study is a non-ionic polysaccharide produced by the fungi of genus Sclerotium with a molecular weight reported by the supplier to be about 5.4×10^5 g/mol. The rigid structure of the polymer is attributable to the long persistence length ([25]) of the molecule originating from its triple helical structure ([12,9]).

Steady-shear measurements and small-amplitude oscillatory-shear measurements (SAOS) were conducted over a wide range of concentrations (0.005–0.5% (w/w) for steady-shear and 0.075–0.5% (w/w) for SAOS) at 20 °C using a TA-Instruments Rheolyst AR 1000 N controlled-stress rheometer. The plot of shear viscosity against shear rate in Fig. 2 shows increased dependence of the shear viscosity, η on shear rate, $\dot{\gamma}$ with increasing concentration, i.e. increased shear thinning. The Carreau–Yasuda model ([26]) was used to fit the data

$$\frac{\eta - \eta_0}{\eta_0 - \eta_\infty} = \frac{1}{[1 + (\lambda_{CY}\dot{\gamma})^a]^{n/a}} \tag{1}$$

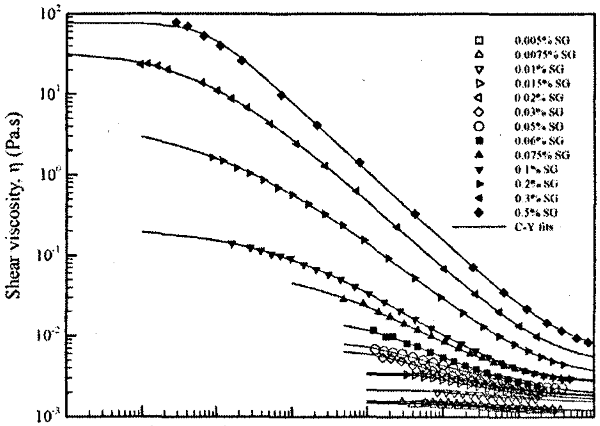

Fig. 2. Viscometric data for various scleroglucan concentrations together with the Carreau–Yasuda fits.

Table 1
Carreau–Yasuda parameters for scleroglucan solutions.

Scleroglucan concentration, c % (w/w)	Zero-shear viscosity, η_0 (Pa s)	Infinite-shear viscosity, η_∞ (Pa s)	Constant which represents onset of shear thinning, λ_{CY} (s)	Power-law index, n	Carreau–Yasuda parameter, a
0.005	1.48×10^{-3}	1.12×10^{-3}	1.70×10^{-1}	0.30	5.82
0.0075	1.56×10^{-3}	1.12×10^{-3}	1.71×10^{-1}	0.31	5.84
0.01	2.14×10^{-3}	1.41×10^{-3}	1.73×10^{-1}	0.31	5.78
0.015	3.33×10^{-3}	1.49×10^{-3}	2.04×10^{-1}	0.42	5.63
0.02	3.45×10^{-3}	1.67×10^{-3}	1.26×10^{-1}	0.50	5.15
0.03	6.59×10^{-3}	1.73×10^{-3}	6.17×10^{-1}	0.55	1.62
0.05	8.48×10^{-3}	1.74×10^{-3}	7.21×10^{-1}	0.47	1.27
0.06	1.52×10^{-2}	1.73×10^{-3}	8.19×10^{-1}	0.59	1.24
0.075	7.42×10^{-2}	2.51×10^{-3}	2.08×10^{0}	0.73	0.90
0.1	2.24×10^{-1}	2.59×10^{-3}	5.01×10^{0}	0.78	0.55
0.2	5.33×10^{0}	3.07×10^{-3}	4.99×10^{1}	0.82	0.45
0.3	3.48×10^{1}	4.22×10^{-3}	1.46×10^{2}	0.86	0.62
0.5	7.70×10^{1}	5.53×10^{-3}	1.37×10^{2}	0.87	1.86

where η_0 and η_∞ are the viscosities in the zero-shear and infinite-shear plateaus while λ_{CY}, n and a are constants which represents the inverse shear rate at the onset of shear thinning, the power-law index and a parameter introduced by Yasuda et al. [26], respectively. Table 1 lists the Carreau–Yasuda parameters for the fits. These model parameters were obtained using the methodology of Escudier et al. [27].

A plot of zero-shear rate viscosity, η_0, against the solution concentration, c (Fig. 3), provides a way of estimating the critical overlap concentration, c^*, which is regarded as the point at which individual polymer molecules begin to interact with each other ([25]), and for this particular scleroglucan is about 0.054% (540 ppm).

Fig. 4 shows the storage (G') and loss (G'') moduli plotted against frequency for higher solution concentrations ($c \geq 0.075\%$) measured in SAOS. Data for lower concentrations are not included as the G' data fell within 50% of the instrument/geometry limit data. The limit data was based on an oscillatory test conducted on water: non-zero values of G' obtained in such a test are a consequence of inertia and represent a limit of the instrument. As shown, the loss modulus, G'' is greater than the elastic modulus G' prior to the crossover for the lower concentration solutions. The crossover frequency decreases with concentration indicating viscous dominance at low concentrations compared to that at high concentrations. For the 0.5% solution, the elastic component plays a dominant role, at least for the frequency range tested. The dependence of both moduli on frequency reducing with concentration is indicative of structure build-up as suggested by Rochefort and Middleman [28] and Lee [29]. At the highest concentration (0.5%) the solution is essentially gel-like.

Much as was the case for the SAOS data, extensional property measurements were only possible for higher concentration solutions ($c \geq 0.1\%$) and were carried out using a Capillary Breakup Extensional Rheometer ("CaBER") supplied by Thermo Electron GmbH in conjunction with a high-speed camera. The CaBER utilizes a laser micrometer, with a resolution of around 10 μm, to monitor the diameter of the thinning elongated filament, which evolves under the action of viscous, inertia, gravitational and elastocapillary forces. High-speed digital imaging of the process was captured by a Dantec Dynamics Nano Sense MKIII high-speed camera with a Nikon 60 mm f/2.8 lens at 2000 frames per second.

A sample of about 25 mm^3 was loaded using a syringe between the 4 mm plates of the instrument, making sure that it was totally homogeneous with no bubbles within the sample. The initial aspect ratio ($\equiv h/b$) of 0.5 was chosen based on the recommendation by Rodd et al. [30] to minimize the effects of reverse squeeze flow and sagging. A uniaxial step strain was then applied, resulting in the formation of an elongated filament. A linear stretching deformation was employed as the mode of the step strain. The stretch time was set to 50 ms. The final aspect ratio was varied with solution concentration such that filament thinning was still observed between the 4 mm plates. For example, a final aspect ratio of 1.4 was chosen for 0.1% SG in order to observe filament thinning over a timeframe of about 10 ms.

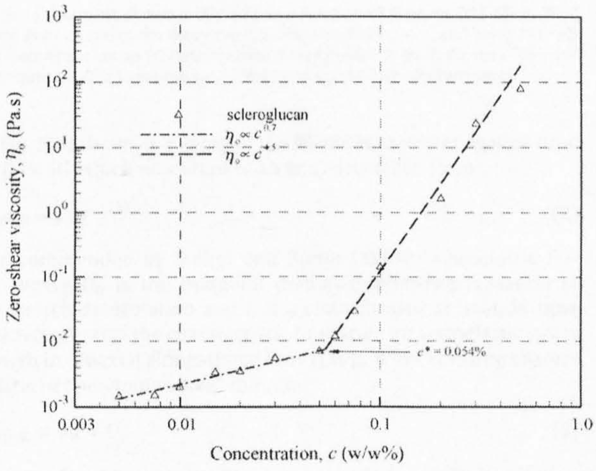

Fig. 3. Zero-shear viscosity versus SG concentration.

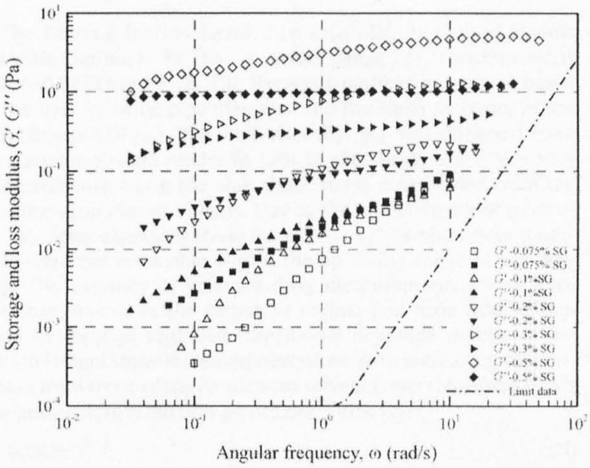

Fig. 4. Storage (G') and loss (G'') modulus versus angular frequency (ω) for various SG concentrations.

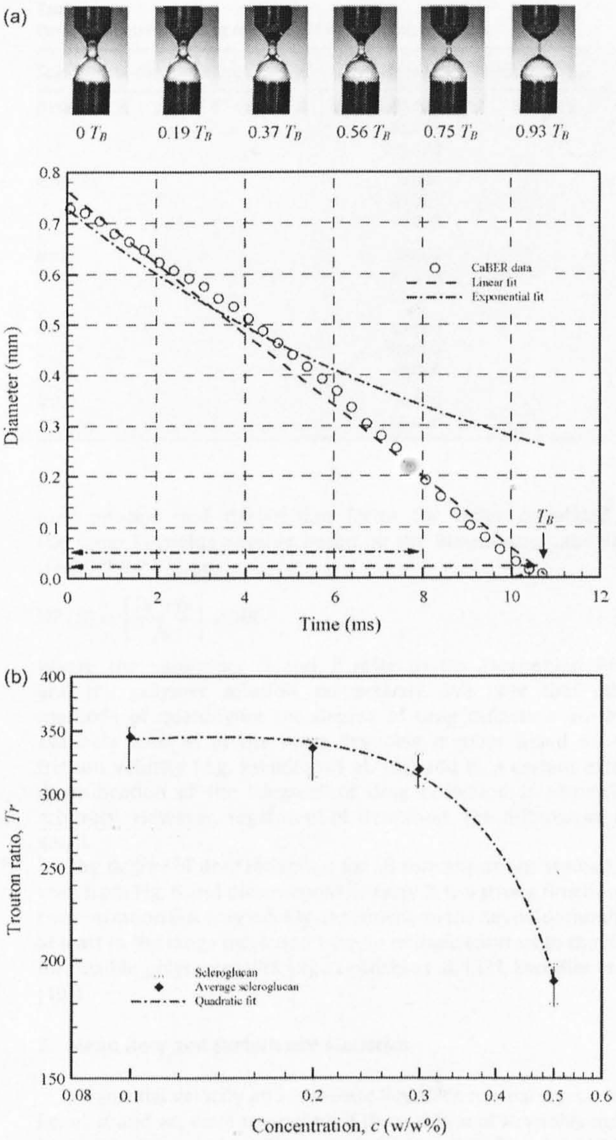

Fig. 5. (a) Filament diameter thinning as a function of time for 0.1% SG at 20 °C (arrow lines represent the time period for exponential fit (-·-) and linear fit (--)) (b) Trouton ratio versus SG concentration (fit is provided to guide the eye). The error bars represent data variations calculated from at least four measurements.

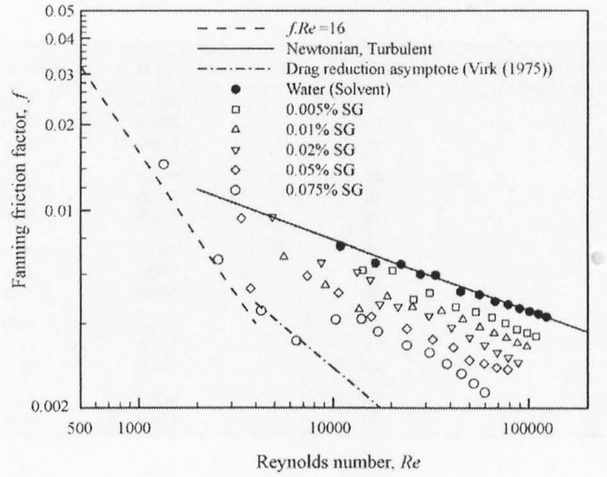

Fig. 6. f–Re data for various SG concentrations.

Fig. 5(a) shows the decay of the filament diameter against time for 0.1% SG which was fitted to an equation of the form

$$D_{\mathrm{CaBER}} = D_0 e^{-t/3\lambda} \tag{2}$$

as recommended by Stelter and Brenn [31] for viscoelastic fluids, where D_0 is the midpoint diameter following cessation of the stretch deformation and λ is a characteristic relaxation time which represents the characteristic time scale for viscoelastic stress growth in uniaxial elongational flow ([30]). A linear fitting characteristic of "Newtonian-like" thinning

$$D_{\mathrm{CaBER}} = mt + D_0 \tag{3}$$

was also fitted to the data. The Trouton ratio was calculated using the equation recommended by Pelletier et al. [32]

$$T_r = \frac{\eta_E(\sqrt{3}\dot{\varepsilon})}{\eta(\dot{\gamma})} \tag{4}$$

with the strain rate calculated from

$$\dot{\varepsilon} = -\frac{4}{D_0}\frac{\mathrm{d}D_{\mathrm{CaBER}}}{\mathrm{d}t} \tag{5}$$

Newtonian linear thinning was observed over the entire time to breakup with a slope of about 70 mm/s. Linear fitting the last six data points prior to breakup, where the sample most closely resembles the uniform cylindrical shape used in deriving Eqn. (2) and (3), gave a slope within 10% of the global fit. Linear thinning was also observed for higher concentrations. Despite this apparent Newtonian behaviour, the Trouton ratio plotted against concentration in Fig. 5(b) confirms the non-Newtonian behaviour of this scleroglucan as the magnitude for all the concentrations studied was significantly greater than that of a Newtonian fluid, i.e. $T_r \gg 3$. Although, due to instrument limitations, CaBER data could not be obtained for concentrations at which the fluid-dynamic measurements were carried out, it can be seen that across a wide range of concentration (0.1–0.3%) the Trouton ratio remains approximately constant at a value of 340 ± 10.

4. Pressure-drop measurements

The Fanning friction factor, $f\ (\equiv 2\tau_W/\rho U_B^2)$ is plotted against Reynolds number Re for a wide range of concentrations (0.005–0.075%) in Fig. 6. The Reynolds number is defined based on the bulk velocity, pipe diameter and the shear viscosity at the wall ($Re \equiv \rho U_B D/\eta_W$). The wall viscosity, η_W was obtained from the Carreau–Yasuda model fit [26] to the steady-shear viscosity measurements, using the wall shear stress determined from the pressure-drop measurements. Due to the low viscosity of most of the solutions, especially those for which $c < c^*$, laminar flow conditions were not attainable within the operating range of the flow loop. The majority of pressure-drop measurements taken were therefore limited to the turbulent regime and little information could be gleaned regarded transitional Reynolds numbers. The friction factors show increased deviations with increasing concentration from those of the Newtonian solvent (water) towards Virk's "maximum drag reduction asymptote" (Virk [2])

$$f = 0.58Re^{-0.58} \tag{6}$$

The drag reduction figures quoted in Table 2 at several Reynolds numbers, are calculated based on the friction factor of the poly-

Table 2
Flow parameters and drag reduction of scleroglucan solutions.

Scleroglucan concentration, c % (w/w)	Reynolds number, $\rho U_B D/\eta_W$	U_B (m/s)	u_τ ($\equiv \sqrt{\tau_W/\rho}$) (m/s)	Drag reduction (%) $(f_N - f_P)/f_N \times 100$
0.005	31,000	0.38	0.019	13
	65,000	0.76	0.035	15
	109,000	1.26	0.053	17
0.01	36,000	0.50	0.024	24
	67,000	0.88	0.038	25
	97,000	1.01	0.043	27
0.02	35,000	0.05	0.023	37
	67,000	1.01	0.040	39
	75,000	1.14	0.044	40
0.05	33,000	0.63	0.026	40
	69,000	1.14	0.042	43
	78,000	1.26	0.047	42
0.075	31,000	0.76	0.030	47
	60,000	1.26	0.042	55

mer solution and the friction factor for water calculated at the same Reynolds number based on the Blasius approximation ($f = 0.079Re^{-1/4}$), i.e.

$$\mathrm{DR}\,(\%) = \left[\frac{f_N - f_P}{f_N}\right] \times 100 \qquad (7)$$

where the subscripts N and P refer to the Newtonian fluid, and the polymer solution, respectively. We note that other methods of quantifying the degree of drag reduction are also available such as at the same Reynolds number based on the friction velocity (e.g. Escudier et al. [8]) and to a certain extent quantification of the "degree" of drag reduction is somewhat arbitrary. However, regardless of definition, the differences are small.

The degree of drag reduction for all concentrations studied, as seen from Fig. 6 and documented in Table 2, is a strong function of concentration but only weakly dependent on the Reynolds number, at least in the range measured here, in marked contrast to the data for flexible polymers (Virk [2], Ptasinski et al. [33], Escudier et al. [19]).

5. Mean flow and turbulence statistics

Mean axial velocity and complete Reynolds normal stress data, i.e. u', v' and w', were measured at three different Reynolds numbers, all in the turbulent-flow regime for both 0.005% and 0.01% SG. Only one component of velocity could be obtained at any one time due to the refraction of two beam pairs of different wavelengths at the curved surface of the pipe wall resulting in the measuring volumes of the beam pairs occupying different spatial locations. As a consequence, it was not possible to measure the Reynolds shear stress, $\overline{u'v'}$. LDA measurements for higher concentrations were not possible due to the higher opacity of the solutions. Control runs with a Newtonian fluid, also within the turbulent-flow regime at approximately identical Reynolds numbers, were also performed as a basis for comparison.

5.1. Mean flow

The mean flow data is shown in wall coordinates (i.e. u^+ against y^+) in Fig. 7. For the Newtonian fluid, good agreement is observed with the well-known log law (see e.g. Tennekes and Lumley [34]). The data close to the wall are also in good agreement with that expected for the viscous sublayer (i.e. ($y^+ \leq 10$) $u^+ = y^+$). The SG data in the viscous sublayer also follow $u^+ = y^+$ while in the Newtonian core region, the data are shifted upward from, but remain essentially parallel to, the Newtonian data as expected for low drag-reducing flows ([7,19]). The onsets of the shifts of the SG data were found to be independent of Reynolds number, occurring at a constant y^+ location of about 15. In physical units, this implies that the distance of onset location from the wall decreases with increasing Reynolds number. The magnitude of the shifts is a function of drag reduction but is only mildly dependent on Reynolds number.

5.2. Turbulence structure

The RMS fluctuation levels of the axial velocity u', again plotted in wall coordinates, u'^+ (y^+), and shown in Fig. 8, show that closer to the wall ($y^+ < 30$), the water data collapse and are independent of the Reynolds number, in agreement with the observations of den Toonder and Nieuwstadt [18]. Closer to the pipe centreline there are clear Reynolds number trends, again in agreement with previous results [18]. Compared to the data for a Newtonian fluid at the same Reynolds number, both concentrations of SG showed increased values of u'^+ close to the wall with the location of the peaks found to be within the region of the onset of the shifts in the mean velocity profiles ($y^+ \approx 15$), i.e. in the buffer region. Close to the pipe centre the fluctuation levels are essentially identical to the water data at comparable Reynolds numbers.

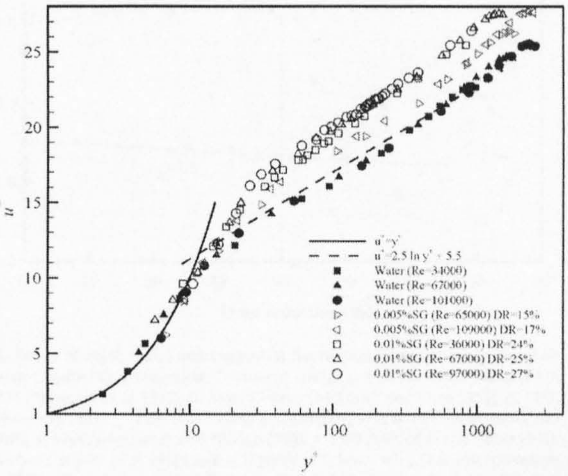

Fig. 7. Universal mean velocity distribution for water, 0.005% SG and 0.01% SG.

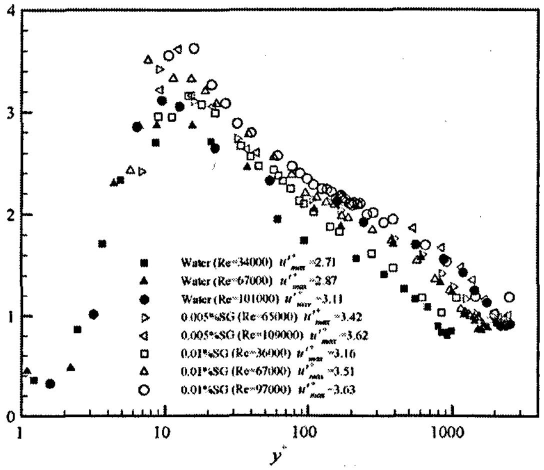

Fig. 8. Axial turbulence intensities in wall coordinate for water, 0.005% SG and 0.01% SG.

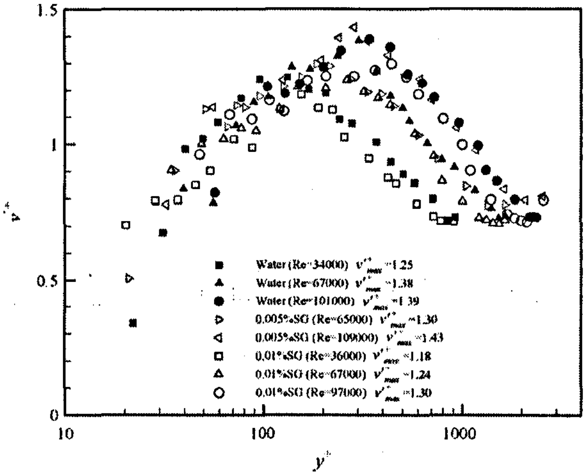

Fig. 9. Radial turbulence intensities in wall coordinate for water, 0.005% SG and 0.01% SG.

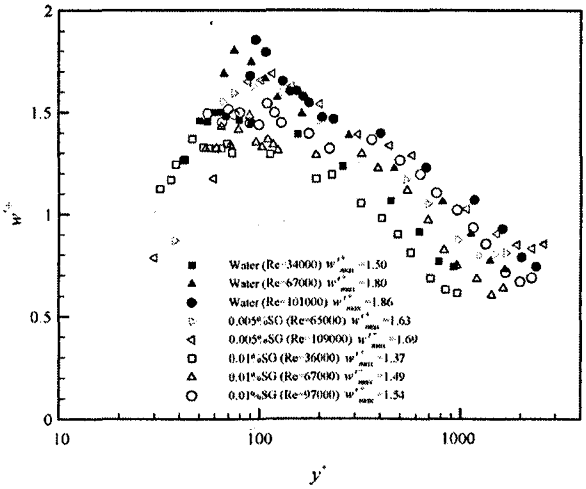

Fig. 10. Tangential turbulence intensities in wall coordinate for water, 0.005% SG and 0.01% SG.

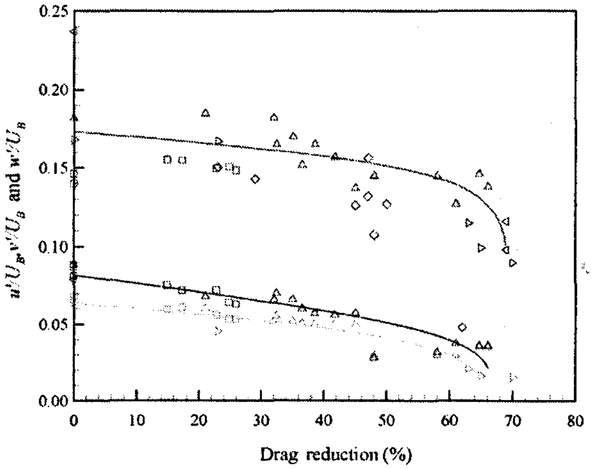

Fig. 11. Peaks of axial, radial and tangential fluctuation components normalized with the bulk velocity, U_B, against drag reduction (□: current study, △: PAA, XG, CMC (Presti [22]), ▷: HPAM (Ptasinski et al. [33]), ◁: Macro Fibres (McComb and Chan [35]), ◇: PEO, PAA (Allan et al. [36]), red: u'/U_B, green: v'/U_B, blue: w'/U_B). (For interpretation of the references to colour in this figure legend, the reader is referred to the web version of the article.)

Figs. 9 and 10 show that the RMS radial and tangential turbulent fluctuations for the Newtonian solvent are globally much lower than for the axial component, but exhibit increases with Reynolds number with the peaks situated further away from the wall. The SG results show increased suppression of the tangential and radial fluctuation levels with drag reduction with the exception of the peak of the radial fluctuation level at the highest Reynolds number measured for 0.005% SG.

In Fig. 11, the peak values of the turbulent fluctuation components, normalized with the bulk velocity, have been plotted against drag reduction together with selected data from the literature for comparison (Presti [22], Ptasinski et al. [33], McComb and Chan [35], Allan et al. [36], Chung and Graebel [37], Mizushina

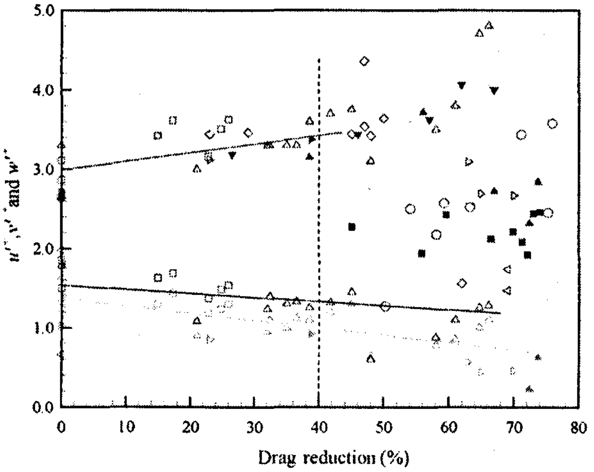

Fig. 12. Peaks of axial, radial and tangential fluctuation components in the wall coordinates against drag reduction (□: current study, △: PAA, XG, CMC (Presti [22]), ▷: HPAM (Ptasinski et al. [33]), ◁: Macro Fibres (McComb and Chan [35]), ◇: PEO, PAA (Allan et al. [36]), ○: PEO, PAA (Chung and Graebel [37]), ■: PEO (Mizushina and Usui [38]), ▲: PAA (Schummer and Thielen [39]), ▼: PEO (McComb and Rabie [40]), ▶: PAA (den Toonder et al. [41]), red: u'^+, green: v'^+, blue: w'^+). (For interpretation of the references to colour in this figure legend, the reader is referred to the web version of the article.)

and Usui [38], Schummer and Thielen [39], McComb and Rabie [40] and den Toonder et al. [41]). It can be seen that the data for the rigid-rod-like polymer from the current study agree well with the trend of decreasing normalized peaks with increasing drag reduction, similar to what is observed for two-dimensional channel flow [8]. In Fig. 12 the same data are plotted with the peak values are now normalized with the friction velocity, u_τ, and the trend is for a decrease in the radial and tangential peak levels but an increasing trend of axial peak level below 40% drag reduction with more complex behaviour at higher drag reduction. The lines in figures are included to guide the eye where clear trends are apparent.

6. Conclusions

The data presented here confirm that so-called rigid, rod-like polymer solutions, in our case a scleroglucan, are effective as drag-reducing agents. The drag reduction effectiveness increases as the solution concentration is increased and is only mildly dependent on Reynolds number but is still relatively lower than that for flexible polymer solutions. The mean axial and turbulence structure data exhibit behaviour typical of a low drag-reducing flexible polymer solution such as carboxymethylcellulose with increases in u'^+ and decreases both in w'^+ and v'^+ generally, except for 0.005% SG at the highest Reynolds number. It is suggested that in order to fully understand the mechanism of drag reduction for such rigid-rod polymer solutions, for example whether the same mechanism for a flexible polymer applies to rigid-rod polymers, direct numerical simulations using suitable constitutive equations will play a key role. Our aim with the current results is to provide an experimental database of low-order statistics to assist in the validation of such simulations and guide the development of turbulence modelling.

References

[1] J.L. Lumley, Drag reduction in turbulent flow by polymer additives, J. Polym. Sci. Macromol. Rev. 7 (1973) 263–290.
[2] P.S. Virk, Drag reduction fundamentals, AIChE J. 21 (4) (1975) 625–653.
[3] N.S. Berman, Drag reduction by polymers, Ann. Rev. Fluid Mech. 10 (1978) 47–64.
[4] J.W. Hoyt, Drag reduction, Encyclopedia of Polymer Science and Engineering, vol. 5, Wiley, New York, 1986, pp. 129–151.
[5] F.T.M. Nieuwstadt, J.M.J. den Toonder, Drag reduction by additives: a review, in: A. Soldati, R. Monti (Eds.), Turbulence Structure and Motion, Springer Verlag, 2001, pp. 269–316 (Book Chapter).
[6] M.D. Graham, Drag reduction in turbulent flow of polymer solutions, in: D.M. Binding, K. Walters (Eds.), Rheology Reviews, British Society of Rheology, 2004, pp. 143–170.
[7] M.D. Warholic, H. Massah, T.J. Hanratty, Influence of drag-reducing polymers on turbulence: effects of Reynolds number, concentration and mixing, Exp. Fluids 27 (1999) 461–472.
[8] M.P. Escudier, A.K. Nickson, R.J. Poole, Turbulent flow of viscoelastic shear-thinning liquids through a rectangular duct: Quantification of turbulence anisotropy, J. Non-Newtonian Fluid Mech 160 (2009) 2–10.
[9] J.S. Paschkewitz, Y. Dubief, E.S.G. Shaqfeh, The dynamic mechanism for turbulent drag reduction using rigid fibers based on Lagrangian conditional statistics, Phys. Fluids 17 (2005), 063102-1-18.
[10] N.S. Berman, Evidence for molecular interactions in drag reduction in turbulent pipe flows, Polym. Eng. Sci. 20 (7) (1980) 451–455.
[11] H.W. Bewersdorff, R.P. Singh, Rheological and drag reduction characteristics of xanthan gum solutions, Rheol. Acta 27 (1988) 617–627.
[12] S. Sasaki, Drag reduction effect of rod-like polymer solutions. I. Influence of polymer concentration and rigidity of skeletal back bone, J. Phys. Soc. Jpn. 60 (3) (1991) 868–878.
[13] P.S. Virk, D.C. Sherman, D.L. Wagger, Additive equivalence during turbulent drag reduction, AIChE J. 43 (12) (1997) 3257–3259.
[14] R. Benzi, E.S.C. Ching, T.S. Lo, V.S. L'vov, I. Procaccia, Additive equivalence in turbulent drag reduction by flexible and rodlike polymers, Phys. Rev. E 72 (2005) 016305.
[15] J.S. Paschkewitz, Y. Dubief, C.D. Dimitropoulos, E.S.G. Shaqfeh, P. Moin, Numerical simulation of turbulent drag reduction using rigid fibres, J. Fluid Mech. 518 (2004) 281–317.
[16] R. Benzi, E.S.C. Ching, E.D. Angelis, I. Procaccia, Comparison of theory and direct numerical simulations of drag reduction by rodlike polymers in turbulent channel flows, Phys. Rev. E77 (2008) 046309.
[17] J.J.J. Gillissen, B.J. Boersma, P.H. Mortensen, H.I. Anderson, Fibre-induced drag reduction, J. Fluid Mech. 602 (2008) 209–218.
[18] J.M.J. den Toonder, F.T.M. Nieuwstadt, Reynolds number effects in a turbulent pipe flow for low to moderate Re, Phys. Fluids 9 (11) (1997) 3398–3408.
[19] M.P. Escudier, F. Presti, S. Smith, Drag reduction in turbulent pipe flow of polymers, J. Non-Newtonian Fluid Mech. 81 (1999) 197–213.
[20] P. Buchhave, W.K. George, J.L. Lumley, The measurements of turbulence with the laser-Doppler anemometer, Ann. Rev. Fluid Mech. 11 (1979) 443–503.
[21] A.F. Bicen, Refraction correction for LDA measurements in flows with curved optical boundaries, TSI Quater. VII (2) (1982) 10–12.
[22] F. Presti, Investigation of transitional and turbulent pipe flow of non-Newtonian fluids, PhD thesis, University of Liverpool, 2000.
[23] C. Tropea, Laser Doppler anemometry: recent developments and future challenges, Meas. Sci. Technol. 6 (1995) 605–619.
[24] W.J. Yanta, R.A. Smith, Measurements of turbulence-transport properties with a laser Doppler velocimeter, AIAA 11th Aerospace Science Meeting, 1973.
[25] R. Lapasin, S. Pricl, Rheology of Industrial Polysaccharides: Theory and Applications, Blackie Academic and Professional, 1995.
[26] K. Yasuda, R.C. Armstrong, R.E. Cohen, Shear flow properties of concentrated solutions of linear and star branched polystyrenes, Rheol. Acta 20 (1981) 163–178.
[27] M.P. Escudier, I.W. Gouldson, A.S. Pereira, F.T. Pinho, R.J. Poole, On reproducibility of the rheology of shear-thinning liquids, J. Non-Newtonian Fluid Mech. 97 (2001) 99–124.
[28] W.E. Rochefort, S. Middleman, Rheology of xanthan gum: salt, temperature, and strain effects in oscillatory and steady shear experiments, J. Rheol. 31 (4) (1987) 337–369.
[29] H. Lee, Rheology of concentrated isotropic and anisotropic rigid polysaccharide solutions: xanthan and scleroglucan, PhD thesis, University of California, USA, 2001.
[30] L.E. Rodd, T.P. Scott, J.J. Cooper-White, G.H. McKinley, Capillary break-up rheometry of low-viscosity elastic fluids, Appl. Rheol. 15 (2005) 12–27.
[31] M. Stelter, G. Brenn, Elongational rheometry for the characterization of viscoelastic fluid, Chem. Eng. Technol. 25 (1) (2002) 30–35.
[32] E. Pelletier, C. Viebke, J. Meadows, P.A. Williams, A rheological study of the order-disorder conformational transition of xanthan gum, Biopolymers 59 (2001) 339–346.
[33] P.K. Ptasinski, F.T.M. Nieuwstadt, B.H.A.A. Van Den Brule, M.A. Hulsen, Experiments in turbulent pipe flow with polymer additives at maximum drag reduction, Flow Turbul. Combust. 66 (2001) 159–182.
[34] H. Tennekes, J.L. Lumley, A First Course in Turbulence, The MIT Press, 1972.
[35] W.D. McComb, K.T. Chan, Laser Doppler anemometer measurements of turbulent structure in drag reducing fibre suspensions, J. Fluid Mech. 152 (1985) 455–478.
[36] J.J. Allan, C.A. Greated, W.D. McComb, Laser Doppler anemometer measurements of turbulent structure in non-Newtonian fluids, J. Phys. D: Appl. Phys. 17 (1984) 533–549.
[37] J.S. Chung, W.P. Graebel, Laser anemometer measurements of turbulence in non-Newtonian pipe flows, Phys. Fluids 15 (4) (1971) 546–554.
[38] T. Mizushina, H. Usui, Reduction of eddy diffusion for momentum and heat in viscoelastic fluid flow in a circular tube, Phys. Fluids 20 (10) (1977) s100–s108.
[39] P. Schummer, W. Thielen, Structure of turbulence in viscoelastic fluids, Chem. Eng. Commun. 4 (4–5) (1980) 593–606.
[40] W.D. McComb, L.H. Rabie, Local drag reduction due to injection of polymer-solutions into turbulent-flow in a pipe. 1. Dependence on local polymer concentration, AIChE J. 28 (4) (1982) 547–557.
[41] J.M.J. den Toonder, M.A. Hulsen, G.D.C. Kuiken, F.T.M. Nieuwstadt, Drag reduction by polymer additives in a turbulent pipe flow: numerical and laboratory experiments, J. Fluid Mech. 337 (1997) 193–231.